

This file is part of the following work:

Lindsay, Mark J. (2006) *The structural and hydrothermal evolution of intrusion-related gold mineralisation at the Brewery Creek Mine, Yukon, Canada*. PhD Thesis, James Cook University.

Access to this file is available from:

<https://doi.org/10.25903/1vkw%2Dn009>

Copyright © 2006 Mark J. Lindsay

The author has certified to JCU that they have made a reasonable effort to gain permission and acknowledge the owners of any third party copyright material included in this document. If you believe that this is not the case, please email

researchonline@jcu.edu.au

**THE STRUCTURAL AND HYDROTHERMAL EVOLUTION
OF INTRUSION-RELATED GOLD MINERALISATION AT
THE BREWERY CREEK MINE, YUKON, CANADA.**

Thesis submitted by

Mark J. Lindsay B.Sc. (Hons.), MAIG

May 2006

for the degree of Doctor of Philosophy (geology) in the School of
Earth Sciences at James Cook University of North Queensland.

I dedicate this thesis to my grandmother, Eva Marie Weeks.

Statement of access

I, the undersigned, the author of this work, understand that James Cook University will make this thesis available for use within the University library and, via the Australian Digital Theses network, for use elsewhere.

I understand that, as an unpublished work, a thesis has significant protection under the Copyright Act and I do not wish to place any further restriction on access to this work.

.....

Statement of sources and declaration

I declare that this thesis is my own work and has not been submitted in any other form for another degree or diploma at any university or other institute of tertiary education. Information derived from the published or unpublished work of others has been acknowledged in the text and a list of references is given.

.....

Electronic Copy

I, the undersigned, the author of this work, declare that the electronic copy of this thesis provided to the James Cook University Library is an accurate copy of the print thesis submitted, within the limits of the technology available.

.....

Acknowledgements

Looking at the list of people I need to thank and remembering how they helped me it seems as if a PhD is far from a project completed by an individual, but rather a team effort. An agglomerate of ideas, problems, and solutions generated by many people and added to by many more. If it weren't for the help from the people below then completing this project would have been very difficult indeed.

Firstly I'd like to thank my supervisors Tim Baker and Nick Oliver for setting up the project, guidance, and especially their patience during my repeated excursions back to properly paid work. I would also like to thank Craig Hart from the Yukon Geology Survey for helping to set up the project, obtain funding, and several reviews of my earlier work. Rick Diment, Vivian Park, Beth Scott, Andrea Samuels, and Jeff Smith from Viceroy are thanked for their great help in the field, numerous discussions about the geology of Brewery Creek and introduction to many Yukon characters and rituals.

Thank-you to the people in various labs around Australia who helped me process my samples in particular the staff at the Advanced Analytical Centre, Alan, Kevin and Gordon, Keith Harris from the University of Tasmania and Norman Pearson from Macquarie University. Julian Stephens is also thanked for many technical discussions and for being a hassle free office mate.

The Yukon Geology Survey, Viceroy Minerals Corporation and James Cook University provided the primary funds for the project. The USGS kindly allowed my isotope samples to be processed in their labs after hours. The Society of Economic Geologists provided a cash grant (Hugh E. McKinstry Grant) for fieldwork expenses and the Mineral Deposits Research Unit at the University of British Columbia sponsored me to attend the Cordilleran Round-up.

Finally, I would like to thank my family and especially Karen, the support that you gave me while I was writing finalising the thesis was wonderful.

Abstract

Vein, fracture and disseminated Au-As-Sb mineralisation at Brewery Creek is principally hosted by Tombstone Plutonic Suite (TPS) monzonite sills that have intruded Palaeozoic sedimentary and volcanic rocks of the Selwyn Basin and the Earn Group. The overall architecture of the property is that of a broad NNE trending arch of thrust sheets, with the rocks in each thrust sheet deformed into upright to steeply inclined, open to tight, variably NE, E, NW trending and plunging folds. Middle Cretaceous intrusive rocks including monzonite, syenite and hornblende gabbro cut the thrust faults and folds. The monzonite intrusive rocks crop out through the centre of the Brewery Creek property as a series of elongate, E oriented sills that have been subsequently deformed by numerous, variably oriented normal faults

The paragenetic history of Brewery Creek can be resolved into three main stages: pre-, syn- and post- TPS intrusion. The pre-TPS intrusion stage encompasses sedimentary rock hosted disseminated and massive pyrite, carbonate veins and breccia infill, quartz veins, and stylolites. The TPS intrusion stage comprises the emplacement of TPS intrusions and the development of their contact aureoles and the post-TPS intrusion includes pyrite \pm quartz \pm carbonate \pm roscoelite veins, quartz only veins, gold bearing arsenopyrite-quartz-carbonate veins, several stages of brecciation and stibnite \pm quartz \pm carbonate \pm kaolinite veins.

Gold assay analysis and vein measurements from the open pits along the Reserve Trend highlight two distinct mineralised orientations, E and NE. These orientations are paralleled by numerous metre-scale, steeply dipping post-TPS faults and mineralisation is bound at depth by a moderately dipping, E-striking normal fault, termed the Basal Fault. The observed normal displacement, which is evident on all of the post-TPS faults, combined with steeply dipping E-trending gold bearing veins is best explained by mineralisation occurring during a period of local extension.

Gold mineralisation at Brewery Creek is characterised by an Au-As-Sb \pm Ag, Pb geochemical signature with elevated As (> 1000 ppm) being the best indicator of Au > 1 ppm. High concentrations of Sb in intrusive rocks and elevated levels of Ag and Sb in sedimentary rocks provide further indication of Au. Alteration is characterised by enrichment of CO₂, K₂O, MnO, and SO₃ and depletion of Na₂O. This element mobility can be directly correlated to pervasive carbonate, pyrite and arsenopyrite alteration of

feldspar and biotite in monzonite sills. CaO and Fe₂O₃ are comparatively immobile, which suggests that the Ca and Fe required to form calcite and pyrite respectively was sourced from destruction of feldspars and biotite.

The highest Au concentrations at Brewery Creek are hosted by arsenopyrite crystals with lower but significant levels of Au also found in arsenopyrite overgrowths on pyrite and pyrite overgrown by arsenopyrite. Gold is preferentially distributed into arsenopyrite and pyrite phases hosted by carbonate and clay altered wall rock. Vein-hosted sulphide minerals are volumetrically minor and contain lower concentrations of gold.

Hydrothermal fluids associated with mineralisation were reduced, CO₂ rich and near neutral in pH. Gold was likely to have been transported as a bisulphide complex and the predominance of Au-bearing wall rock arsenopyrite and arsenian pyrite emphasise the importance of sulphidation reactions as a Au precipitation mechanism.

Isotope data provide evidence for significant input of magmatic fluids into the mineralising system at Brewery Creek. The calculated fluid compositions are consistent with an initial mixed magmatic and crustal (sedimentary) source that is replaced over time by a mixed magmatic and evolved meteoric fluid source. A genetic model for mineralisation is described that is based on emplacement of felsic magma and subsequent cooling of the associated hydrothermal system.

Table of contents

Dedication	i
Statement of access	ii
Statement of sources and declaration	iii
Electronic Copy	iv
Acknowledgements	v
Abstract	vi
Table of contents	viii
List of figures	x
List of tables	xiii
List of appendices	xiv
 Chapter 1 - Introduction	 1 - 1
1.1 General introduction	1 - 2
1.2 Location and access	1 - 3
1.3 Aims	1 - 5
1.4 Methodology	1 - 5
 Chapter 2 - Regional geology	 2 - 1
2.1 Chapter overview	2 - 2
2.2 Stratigraphic setting of the central Yukon	2 - 3
2.3 Tectonic and structural history	2 - 9
2.4 Intrusive rocks	2 - 11
2.5 Gold Mineralisation in the Yukon – the Tintina Gold Belt	2 - 16
2.6 Intrusion-related gold mineralisation	2 - 19
 Chapter 3 - Property geology	 3 - 1
3.1 Chapter overview	3 - 2
3.2 Property stratigraphy	3 - 3
3.3 Intrusive rocks	3 - 17
3.4 Metamorphism	3 - 24
3.5 Deformation	3 - 30
3.6 Correlation of the deformation at Brewery Creek to elsewhere in the Selwyn Basin	3 - 39

Chapter 4 - Mineralisation	4 - 1
4.1 Chapter overview	4 - 2
4.2 Gold mineralisation at Brewery Creek	4 - 3
4.3 Paragenesis of mineralisation along the Reserve Trend	4 - 8
4.4 Orientation and structural controls on the distribution of gold mineralisation	4 - 27
Chapter 5 - Geochemistry	5 - 1
5.1 Chapter overview	5 - 2
5.2 Element distribution and correlations	5 - 3
5.3 The geochemistry of mineralisation and alteration	5 - 33
5.4 Geochemistry of the main sulphide phases at Brewery Creek	5 - 47
Chapter 6 - Oxygen, carbon, and sulphur stable isotopes	6 - 1
6.1 Chapter overview	6 - 2
6.2 Quartz, biotite, and roscoelite oxygen isotope analyses	6 - 6
6.3 Pyrrhotite, pyrite, arsenopyrite, and stibnite sulphur isotope analyses	6 - 8
6.4 Carbonate carbon and oxygen isotope analyses	6 - 10
6.5 Temperature estimates	6 - 12
6.6 Fluid $\delta^{18}\text{O}$ estimates from quartz	6 - 17
6.7 Fluid $\delta^{18}\text{O}$ and $\delta^{13}\text{C}$ estimates from carbonates	6 - 19
6.8 Fluid $\delta^{34}\text{S}$ estimates	6 - 22
Chapter 7 - Discussion and conclusions	7 - 1
7.1 Chapter overview	7 - 2
7.2 Structural controls on mineralisation	7 - 3
7.3 Lithological and mineralogical constraints on fluid oxidation state and pH	7 - 8
7.4 Hydrothermal transport and deposition of gold	7 - 10
7.5 Isotopic constraints on fluid source	7 - 14
7.6 A genetic model for mineralisation at Brewery Creek	7 - 20
7.7 Classification of the Brewery Creek gold deposit	7 - 27
7.8 Further exploration	7 - 30
7.9 Conclusions	7 - 33

References

Appendices

List of figures

Figure 1.1	A map of the Yukon showing the location of Brewery Creek.	1 - 4
Figure 2.1	Structural controls on the distribution of Selwyn Basin and Earn Group lithologies in the west-central Yukon.	2 - 4
Figure 2.2	A stratigraphic column displaying the relationships, composition, and age of rocks comprising the Selwyn Basin and overlying Earn Group.	2 - 5
Figure 2.3	Distribution of plutonic suites in the Yukon.	2 - 13
Figure 2.4	Distribution of the Tombstone and McQuesten plutonic suites within the Selwyn Basin.	2 - 14
Figure 2.5	The Tintina Gold Belt in the Yukon Territory and Alaska.	2 - 17
Figure 2.6	A schematic model of an intrusion-related gold system.	2 - 21
Figure 3.1	A map and cross-section summarising the geology of the Brewery Creek property.	3 - 4
Figure 3.2	Stratigraphic columns displaying the relationships, composition, and age of rocks comprising the Selwyn Basin, and rocks outcropping at Brewery Creek.	3 - 5
Figure 3.3	Calcareous phyllite of the Rabbitkettle Formation.	3 - 6
Figure 3.4	Photos of selected lithologies from the Menzie Creek volcanic unit.	3 - 8
Figure 3.5	Photographs of the Duo Lake Formation in outcrop.	3 - 10
Figure 3.6	Rocks of the Steel Formation.	3 - 11
Figure 3.7	Photographs of selected lithologies from the Brewery unit.	3 - 14
Figure 3.8	Photographs of selected lithologies from the Earn Group.	3 - 16
Figure 3.9	The geochemical signature of TPS intrusive rocks at Brewery Creek.	3 - 18
Figure 3.10	Photographs of quartz - biotite monzonite.	3 - 21

Figure 3.11	Examples of biotite monzonite.	3 - 22
Figure 3.12	Examples of syenite.	3 - 23
Figure 3.13	Examples of hornblende gabbro.	3 - 25
Figure 3.14	Examples of contact metamorphosed rocks.	3 - 26
Figure 3.15	Relict andalusite porphyroblasts in Earn Group carbonaceous shale.	3 - 29
Figure 3.16	A schematic diagram illustrating the structural development of the rocks underlying the Brewery Creek property.	3 - 31
Figure 3.17	Graphic illustration of D-stage 1 folding at North Slope.	3 - 32
Figure 3.18	Graphic illustration of D-stage 3 folding across the Brewery Creek property.	3 - 34
Figure 3.19	A graphic illustration of D-stage 7 normal faults.	3 - 37
Figure 4.1	A cross-section through the Classic Zone.	4 - 6
Figure 4.2	A cross section through North Slope.	4 - 7
Figure 4.3	Photographs of P-stage 1.1 to 1.4.	4 - 11
Figure 4.4	Photographs of P-stage 2.1 intrusive rocks.	4 - 13
Figure 4.5	Stereonets and photographs of P-stage 3.1 pyrite \pm quartz \pm carbonate \pm roscoelite veins.	4 - 15
Figure 4.6	A ternary diagram and photographs illustrating P-stage 3.1 pyrite \pm quartz \pm carbonate \pm roscoelite veins.	4 - 16
Figure 4.7	Photographs and of P-stages 3.2 and 3.3.	4 - 18
Figure 4.8	Stereonets, photographs and a photomicrograph illustrating P-stage 3.4 arsenopyrite \pm quartz \pm carbonate \pm gold veins.	4 - 20
Figure 4.9	A ternary diagram and two photomicrographs illustrating P-stage 3.4 arsenopyrite \pm quartz \pm carbonate \pm gold.	4 - 21
Figure 4.10	Photographs and a photomicrograph of P-stages 3.5, 3.6, and 3.7.	4 - 22
Figure 4.11	Photographs, stereonets and a ternary diagram illustrating P-stage 3.8 stibnite \pm quartz \pm carbonate \pm feldspar.	4 - 25
Figure 4.12	Photomicrographs illustrating the timing of P-stage 3.8.	4 - 26
Figure 4.13	Gold Assay trends in the open pits.	4 - 28
Figure 4.14	Cross-sections through the eastern and western ends of Kokanee Pit.	4 - 29
Figure 4.15	A photograph of a wall in the Fosters Pit.	4 - 30

Figure 5.1	Cross-sections through the Golden pit (21760E) illustrating the distribution of elements that comprise factor 3, lithology, and the factor 3 scores.	5 - 18
Figure 5.2	Cross-sections through the Blue pit (18470E) illustrating the distribution of elements that comprise factor 3, lithology, and the factor 3 scores.	5 - 26
Figure 5.3	A photograph illustrating proximal and distal alteration around an arsenopyrite-quartz-carbonate-gold vein as defined for geochemical sampling.	5 - 34
Figure 5.4	Element enrichment and depletion associated with P-stage 3.1 pyrite-carbonate-quartz proximal and distal alteration of monzonite.	5 - 40
Figure 5.5	Element enrichment and depletion associated with P-stage 3.4 arsenopyrite-carbonate-quartz-gold proximal and distal alteration of monzonite.	5 - 43
Figure 5.6	Element enrichment and depletion associated with P-stage 3.4 arsenopyrite-carbonate-quartz-gold proximal and distal alteration of monzonite.	5 - 45
Figure 5.7	A schematic diagram illustrating the distribution of pyrite and pyrrhotite grains analysed by LA-ICP-MS.	5 - 50
Figure 5.8	A schematic diagram illustrating the distribution of sulphides analysed by LA-ICP-MS in samples MJL 56-63.	5 - 51
Figure 5.9	Scanning electron microprobe backscatter images of pyrite overgrown by arsenopyrite.	5 - 56
Figure 5.10	Histograms of gold grades in various sulphide morphologies at Brewery Creek.	5 - 59
Figure 5.11	A graph illustrating the variation in Au concentration with respect to alteration zones and sulphide morphology.	5 - 60
Figure 5.12	Graphs illustrating the relationship between Au and As.	5 - 62
Figure 5.13	Graphs illustrating the relationship between Au and various trace elements.	5 - 63
Figure 6.1	$\delta^{18}\text{O}$ values from quartz, biotite and roscoelite mineral separates.	6 - 7
Figure 6.2	$\delta^{34}\text{S}$ values of pyrite, pyrrhotite, arsenopyrite and stibnite mineral separates and in-situ laser ablation of sulphide grains.	6 - 9

Figure 6.3	$\delta^{18}\text{O}$ and $\delta^{13}\text{C}$ values of carbonate mineral separates.	6 - 11
Figure 6.4	Oxygen isotope fractionation curves used to calculate temperature.	6 - 15
Figure 6.5	A pH – log $f\text{O}_2$ diagram for stage 3.1 mineralisation	6 - 23
Figure 7.1	A schematic structural model for mineralisation	7 - 6
Figure 7.2	Calculated δO^{18} fluid values	7 - 16
Figure 7.3	Calculated δC^{13} fluid values	7 - 18
Figure 7.4	Calculated δS^{34} fluid values	7 - 19
Figure 7.5	A photograph of a sulphidised monzonite sill	7 - 21
Figure 7.6	A genetic model for mineralisation at Brewery Creek	7 - 23

List of tables

Table 3.1	Fossil age dates for Brewery Creek lithologies.	3 - 12
Table 3.2	Correlation of structural features identified at Brewery Creek to structures elsewhere in the Selwyn Basin.	3 - 40
Table 4.1	Known gold resources at Brewery Creek	4 - 4
Table 4.2	Paragenetic history of Reserve Trend mineralisation.	4 - 9
Table 5.1	Summary of descriptive statistics applied to the Viceroy exploration fire assay data base.	5 - 6
Table 5.2	A summary of maximum As values and relative As enrichments in various lithologies.	5 - 9
Table 5.3	A summary of element correlations versus rock type.	5 - 10
Table 5.4	A summary of elements that show a significant correlation to gold.	5 - 12
Table 5.5	Factor analysis of the multi-element data set.	5 - 14
Table 5.6	Description of samples selected for major element oxide and trace element geochemistry.	5 - 35
Table 5.7	Major element oxide and trace element geochemistry of selected samples from Brewery Creek.	5 - 37
Table 5.8	Converted data for isocon diagrams.	5 - 38
Table 5.9	Description of samples used for LA-ICP-MS analysis.	5 - 52
Table 5.10	Mean, median, minimum and maximum values of various trace elements in arsenopyrite, pyrite, pyrrhotite and stibnite at Brewery Creek.	5 - 54

Table 5.11	Atomic % of the major components in arsenopyrite, pyrite, pyrrhotite, and stibnite.	5 - 57
Table 6.1	^{18}O , ^{13}C , and ^{34}S isotope data tabulated according to paragenetic stage.	6 - 3
Table 6.2	$\delta^{18}\text{O}_{\text{fluid}}$ estimates from quartz mineral separates.	6 - 18
Table 6.3	$\delta^{18}\text{O}_{\text{fluid}}$ estimates from carbonate mineral separates.	6 - 20
Table 6.4	$\delta^{13}\text{C}_{\text{fluid}}$ estimated from carbonate mineral separates.	6 - 21
Table 6.5	$\delta^{34}\text{S}_{\text{fluid}}$ estimated from sulphur mineral separates and laser ablation.	6 - 25

List of appendices

Appendix 1	James Cook University catalogue numbers
Appendix 2	Analytical methodology
Appendix 3	Intrusion geochemistry
Appendix 4	Microprobe data
Appendix 5	Viceroy Exploration fire assay data
Appendix 6	Drill hole and trench collar location
Appendix 7	Blast-hole assay data
Appendix 8	Viceroy lithology logs and lithology codes
Appendix 9	Viceroy ICP data
Appendix 10	Descriptive statistics
Appendix 11	Correlation matrices
Appendix 12	Factor scores for all data
Appendix 13	Factor scores by major rock type
Appendix 14	Factor scores by mineralised zone
Appendix 15	LA-ICP-MS data

CHAPTER ONE

Introduction



A photograph taken during summer of the Tombstone Mountains to the North of Brewery Creek. The pink flower is fireweed, which grows in areas that have been burnt by bushfires.

1.1 General Introduction

Recent gold exploration successes in the Yukon and Alaska have delineated a newly defined gold province termed the Tintina Gold Belt (Smith, 2000). This belt, which extends for more than 1000 km across central Alaska through the Yukon and into the westernmost Northwest Territories, encompasses deposits such as Pogo (Smith et al., 2000), Fort Knox (Bakke et al., 1995), Donlin Creek (Goldfarb et al., 2004), Brewery Creek (Lindsay et al., 2000, 2001; Diment and Craig, 1999), and Dublin Gulch (Maloof et al., 2001). Much of the gold mineralisation along the TGB is temporally and spatially coincident with mid-Cretaceous (i.e. 90-100 Ma) intrusions and a genetic link to magmatism has been postulated for many of these gold deposits.

Research over the last decade on the gold deposits of the TGB and other similar deposits worldwide has led to the delineation of a new class of deposit termed intrusion-related gold deposits (Lang et al., 1997, 2000; Thompson et al., 1999; Thompson and Newberry, 2000; Lang and Baker, 2001). Intrusion-related gold deposits are characterised by (1) gold as a principal commodity, (2) a spatial, temporal and genetic association with metaluminous, sub-alkalic intrusions of intermediate to felsic composition, (3) the presence of carbonic hydrothermal fluids, (4) aereally restricted alteration haloes, (5) a low sulphide mineral content, (6) a reduced ore mineral assemblage that typically includes arsenopyrite, pyrrhotite and pyrite and lacks magnetite or hematite, and (7) a continental setting well inboard of inferred or recognized convergent plate boundaries.

Brewery Creek has been classified as an intrusion related gold deposit by several authors (Poulsen et al., 1997; Thompson et al., 1999; Hart et al., 2000; Lang et al., 2000 a and b). However, no clear links between mineralisation and magmatism were established by these workers and the geological and geochemical signature of Brewery Creek contrasts with better-documented intrusion-related gold deposits.

The Brewery Creek mine was chosen for research as:

1. There had been limited previous research on Brewery Creek despite the significant contribution the mine has made to the Yukon economy.

2. There are few detailed descriptions of gold deposits that comprise the Tintina Gold Belt despite a significant increase in resources of this region over the last 15 years.
3. There have been few deposit specific investigations of intrusion-related gold systems and thus the detailed information required to thoroughly understand this new class of gold deposit is lacking.
4. Brewery Creek has been previously classified as an intrusion-related gold deposit but shows many differences to better-defined intrusion-related gold deposits such as Fort Knox and Dublin Gulch.

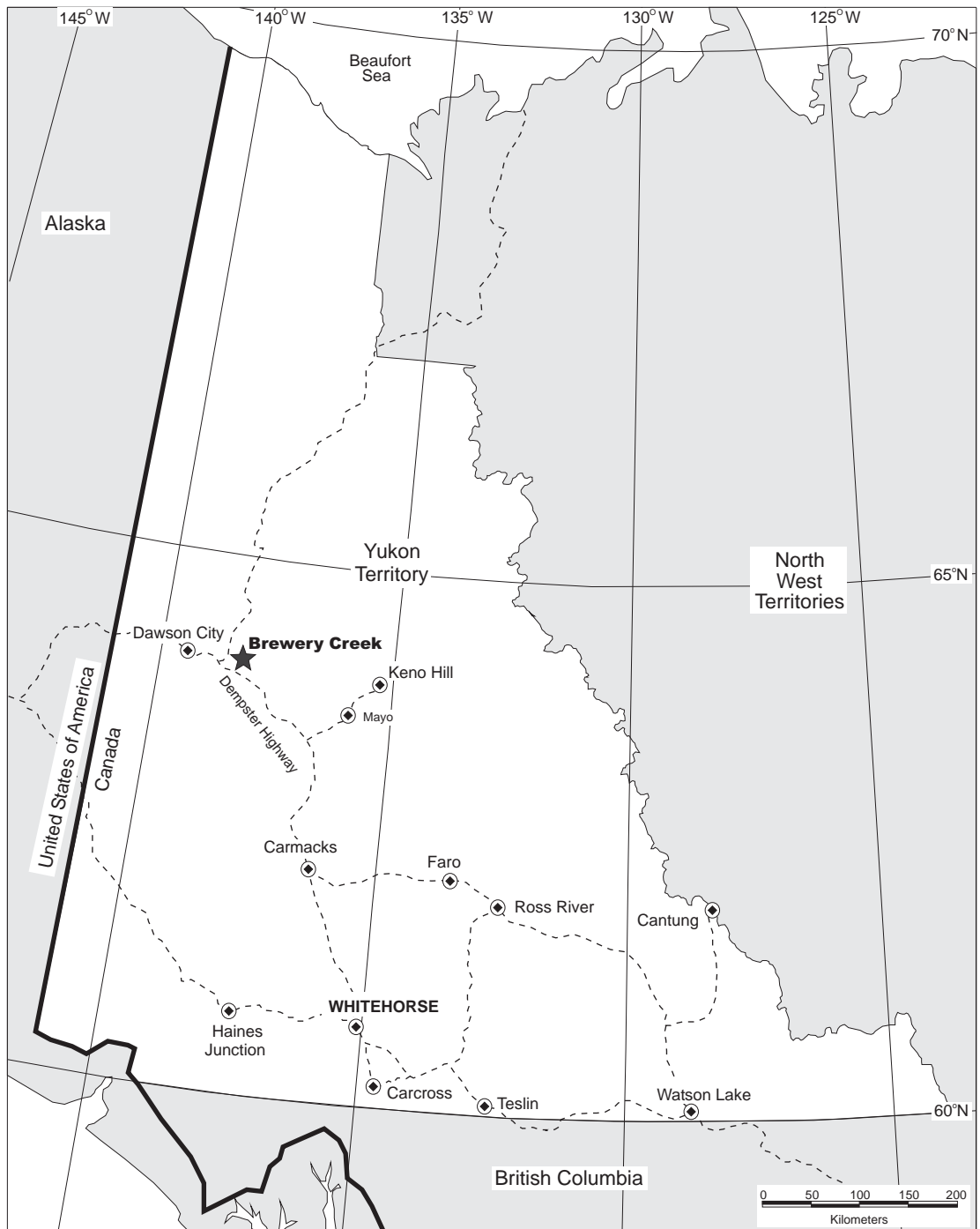
1.2 Location and access

The Brewery Creek gold mine was a bulk tonnage, heap leach operation located 57 km East of Dawson City, Yukon, Canada (Figure 1.1). The deposit was discovered by Noranda Limited in 1989, at a time when gold resources in the Yukon and Alaska rose from 31 tons or 1 Moz to 370 tons or 70 Moz (Flannigan et al., 2000). Loki Gold subsequently bought the deposit from Noranda, and a merger in 1996 saw the ownership of the claim transfer to Viceroy Resources Ltd (Diment and Craig, 1999).

During the summer months the mine can be accessed by conventional vehicle along the North Fork Road via the Dempster Highway, which links Dawson City to the capital of the Yukon, Whitehorse. Access to exploration areas around the mine is by four-wheel drive vehicle or all-terrain vehicle. Natural outcrop of rock across the property is limited by dense vegetation to less than 1 %.

There are a number of open pits at Brewery Creek; from west to east these are Pacific, Blue, Moosehead, Canadian, Upper and Lower Fosters, Kokanee (K1 to K4) Golden and Lucky (see Chapter 3 and 4). In addition a number of mineralised zones have been delineated, these include East and West Big Rock, North Slope, Classic, Schooner and Bohemian. Access was available to all open pits and mineralised zones except for Canadian, Upper Fosters and Lower Fosters, as these pits had been back filled. In 1998 Brewery Creek had a global geological resource of 43 million tonnes @ 1.03 g/t Au and a reserve of 13.3 million tonnes @ 1.44g/t Au. Mining at Brewery Creek focussed on oxide ore only and mining operations ceased in the summer of 2000. Prior to the mine closure Brewery Creek was the only operating hard rock gold mine in the Yukon and significantly contributed to the Yukon economy.

Figure 1.1. A map of the Yukon showing the location of Brewery Creek.



1.3 Aims

The objectives of this PhD project were to:

1. Evaluate the key controls on mineralisation through geological mapping with an emphasis on structural and host rock controls.
2. Evaluate alteration and mineralisation mineral paragenesis.
3. Investigate the hydrothermal fluid evolution and the relationship of hydrothermal fluids to magmatism.
4. Constrain the geochemical signature of gold mineralisation.
5. Clearly resolve the mineralogical location of gold.
6. Investigate the chemistry of mineralising fluids.
7. Develop a genetic model for mineralisation.
8. Compare Brewery Creek with other deposit types and classify Brewery Creek.

1.4 Methodology

To fulfil the aims listed above the following methods were used:

1. Detailed property and open pit structural mapping.
2. Paragenetic logs of drill core.
3. Thin section, microprobe, and general area detector diffractor system (GADDS) investigation of mineral phases.
4. Geochemical analysis of altered and unaltered rock samples using inductively coupled plasma - mass spectrometry (ICP-MS) / optical emission spectrometry (ICP-OES) / atomic emission spectrometry (ICP-AES), fire assay, and x-ray fluorescence (XRF) procedures.
5. Laser ablation - inductively coupled plasma - mass spectrometry (LA-ICP-MS) investigation of various sulphide phases.
6. O, C, and S isotope analysis (mineral separates and in-situ ablation) of samples from various paragenetic stages.

Note that representative portions of any sample remaining after analysis has been stored in the James Cook University (JCU) rock store. The samples and their corresponding JCU catalogue number are tabulated in Appendix 1. The methodology of all analytical methods used is described in Appendix 2.

CHAPTER TWO

Regional geological setting of the Brewery Creek gold deposit



A photograph of the famous Klondike River close to Dawson City

2.1 Chapter overview

The Brewery Creek gold mine is situated within sedimentary and volcanic rocks of the Selwyn Basin and Earn Group that were deposited along the North American margin in a passive, off-shelf setting (Gabrielse and Yorath, 1991). Sedimentation in the Selwyn Basin was interrupted by several episodes of Palaeozoic rifting, and was terminated in the Middle-Jurassic as compressional deformation commenced with the accretion of exotic terranes along the North American margin (Templeman-Kluit, 1979). Accretion-related deformation initially resulted in the development of moderate to tight NW trending folds (Gordey and Anderson, 1993). Subsequent brittle-ductile deformation partitioned the rocks of the Selwyn Basin into three tectonic sheets that are separated by the Dawson, Tombstone and Robert Service Thrusts. The hanging-wall of the Tombstone Thrust hosts several kilometres of highly strained rocks that comprise the Tombstone High Strain Zone (Murphy, 1997; Stephens et al., 2000). The broad McQuesten Antiform folds all of the structural features described above about an east-trending, west-plunging axis.

The Selwyn Basin and Earn Group are host to several middle Cretaceous plutonic suites. These intrusive rocks display distinct metallogenic associations that include Au, Ag, Bi, Mo, W, Sn, Cu and other base metals (Lang et al., 2000; Mortensen et al., 2000). Recent gold exploration and exploitation has focussed on Tombstone Plutonic Suite (TPS) rocks that have intruded the northern Selwyn Basin and outcrop at Brewery Creek. Mineralisation associated with TPS intrusions lies within a broader gold province termed the Tintina Gold Belt (TGB). The TGB is an approximately 250 km wide belt of gold mineralisation and spatially associated middle Cretaceous granitic intrusive rocks that extends for more than 1000 km from Alaska through the Yukon and into the Northwest Territories. Gold deposits in the TGB include Pogo (9.0 Mt @ 17.8 g/t Au for 5.2 Moz Au; Smith et al., 2000), Fort Knox (169 Mt @ 0.93 g/t Au for 4.6 Moz Au; Bakke et al., 1995), Brewery Creek (43.8 Mt @ 1.03g/t Au for 1.4 Moz Au; Park, 1999) and Dublin Gulch (99 Mt @ 1.1 g/t Au for 3.5 Moz Au; Smit et al., 1996).

2.2 Stratigraphic setting of the central Yukon

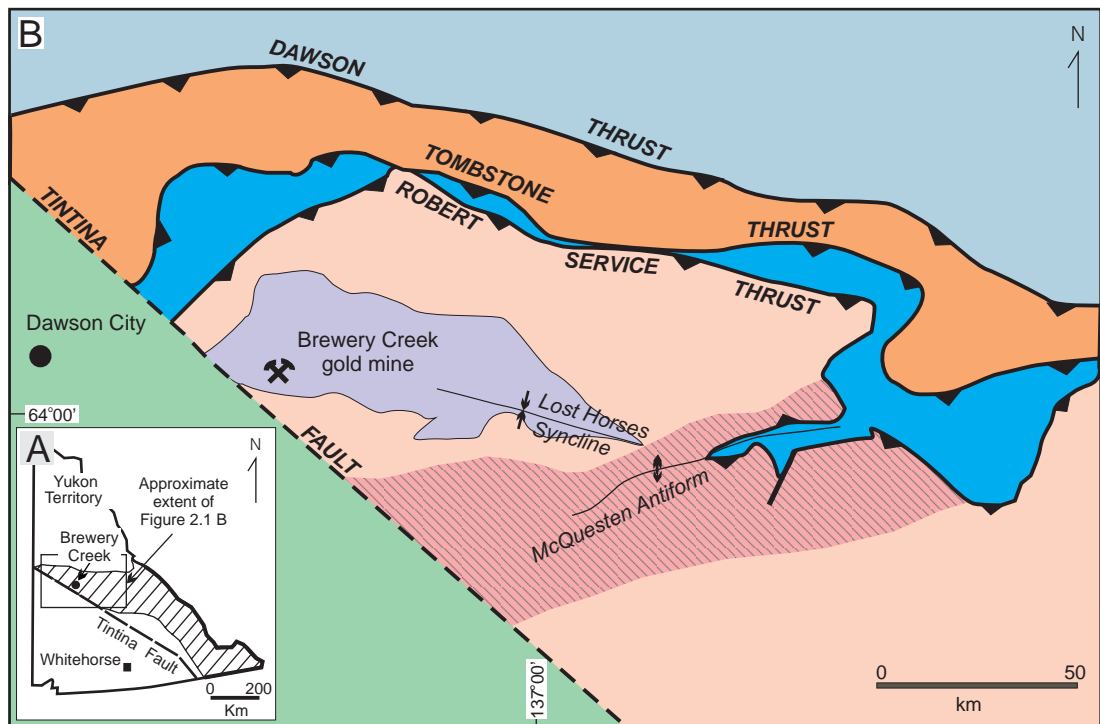
Neoproterozoic to Middle Devonian, deep-water offshore sedimentary rocks of the Selwyn Basin and Late Devonian to early Carboniferous clastic shelf sedimentary rocks of the Earn Group occur throughout the central Yukon as a 900 km long and up to 300 km wide northwest trending tract of rock. To the north and west the Dawson Thrust separates the Selwyn Basin and Earn Group from time-equivalent carbonate dominated strata of the Mackenzie Platform. To the east rocks of the Selwyn Basin and Mackenzie Platform are interstratified due to lateral movement of basin margins, and to the south the Tintina Fault juxtaposes deformed and metamorphosed rocks of the Yukon-Tanana terrane against the Selwyn Basin and Earn Group (Figure 2.1).

Rocks of the Selwyn Basin have been partitioned into two Groups and six Formations (Figure 2.2); from oldest to youngest these are the Hyland Group (comprising the Yusezyu and Narchilla Formations), Gull Lake Formation, Rabbitkettle Formation, and Road River Group (comprising the Duo Lake and Steel Formations). The Earn Group unconformably overlies the rock types comprising the Selwyn Basin (Gordey and Anderson, 1993).

Hyland Group

Meta-sedimentary rocks of the Hyland Group are widely distributed throughout the Selwyn Basin. Gordey and Anderson (1993) partitioned rocks of the Hyland Group into two formations, the Yusezyu Formation and the Narchilla Formation. The Yusezyu Formation consists of variably metamorphosed gritty, quartz-rich, fine- to coarse-grained succession of evenly interbedded sandstone and shale capped by a thin discontinuous limestone member. Sedimentary fabrics and overall morphology suggest that deposition of this Formation most likely occurred as a result of sedimentary gravity flows in an upper or mid submarine fan setting in water of shallow to moderate depth (Gordey and Anderson, 1993). Primitive trace fossils suggest that the Yusezyu Formation is upper Proterozoic in age and may constitute the oldest strata in the Selwyn Basin (Fritz et al., 1983). A structural thickness for the Yusezyu Formation of at least seven kilometres occurs on the northern limb of the Lost Horses Syncline (Murphy, 1997), however, Gordey and Anderson (1993) estimated a stratigraphic thickness of approximately three kilometres.

Figure 2.1. Structural controls on the distribution of Selwyn Basin and Earn Group lithologies in the west-central Yukon. (A) Note the distribution of the Selwyn Basin in the Yukon. (B) The Dawson thrust bounds the Selwyn Basin to the north and the Tintina Fault juxtaposes the Selwyn Basin against rocks of the Yukon Tanana Terrane to the southwest. The axial trace of the Lost Horses Syncline trends toward Brewery Creek however this structure was not identified on the property. Note the location of the Brewery Creek mine. Figure modified from Murphy, (1997).










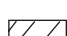
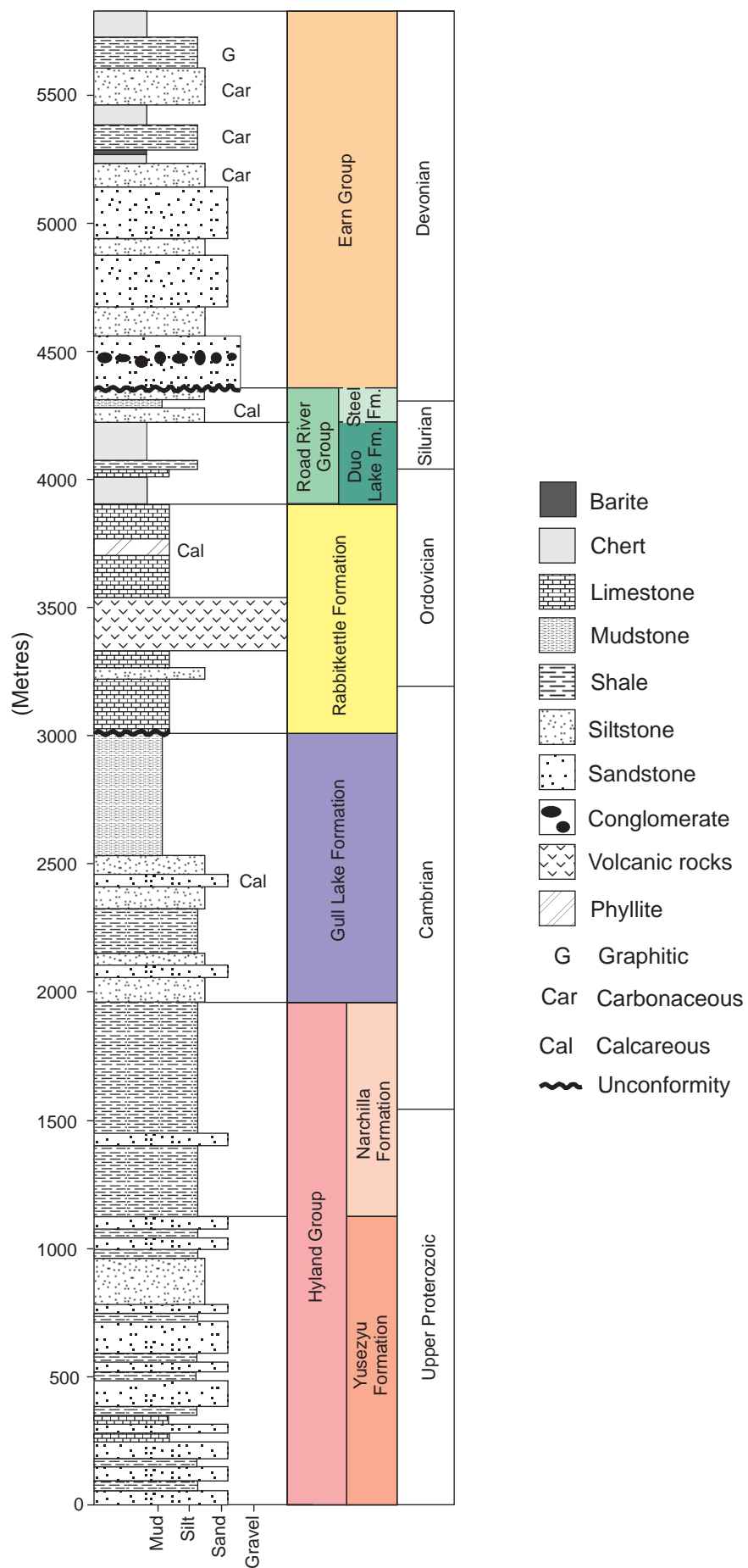
- | | |
|--|---|
|  Mackenzie Platform |  Hyland Group |
|  Chiefly Road River Group and Rabbitkettle Formation |  Yukon Tanana Terrane |
|  Chiefly Earn Group and Keno Hill Quartzite. |  Tombstone High Strain Zone |
|  Gull Lake Formation and Earn Group |  Approximate extent of the Selwyn Basin within the Yukon |

Figure 2.2. A stratigraphic column displaying the relationships, composition, and age of rocks comprising the Selwyn Basin and overlying Earn Group. Note the unconformity at the base of the Earn Group. Data used to compile the stratigraphic column was sourced from Cecile (1982, 1997), Fritz et al. (1991), Gordey et al. (1982), Gordey and Irwin (1987), Gordey and Anderson (1993), Jennings and Jilson (1986), Murphy (1997), and Roots (1988).



Recessive, commonly variegated maroon to dark grey/green shale and sandstone of the Narchilla Formation conformably overlies the Yusezyu Formation. Gordey and Anderson (1993) reported that this Formation displays sedimentary structures that are consistent with deposition from sedimentary gravity flows, most probably turbidites and suggested that the Narchilla Formation was probably deposited below wave base in relatively deep water. The Narchilla Formation is late Precambrian to Early Cambrian in age based on trace fossils in the lower 20 m of the Formation (Fritz et al., 1983) and Archaeocyathids in the overlying unit (Cecile and Abbott, 1992; Cecile, 1997). The Narchilla Formation has been interpreted to have a maximum stratigraphic thickness of approximately 800 m (Gordey and Anderson, 1993), however in structurally complex areas the thickness of the Formation has been measured at more than three kilometres (Murphy, 1997).

Gull Lake Formation

The Gull Lake Formation sharply and conformably overlies the Hyland Group and is intermittently preserved throughout the Selwyn Basin (Murphy, 1997). The type section of the Gull Lake Formation has been partitioned into three members: (1) a basal, discontinuous, archaeocyathid-bearing limestone conglomerate, (2) a middle member comprising locally bioturbated slate, siltstone, and very fine-grained sandstone, and (3) an upper locally wispy laminated and bioturbated siltstone and mudstone member (Gordey and Anderson, 1993). Elsewhere in the Selwyn Basin this Formation also comprises massive greenstone, volcano-lithic conglomerate, pebbly sandstone, siltstone, mudstone, limestone, shale, chert, quartzite, and phyllite (Abbott and Roots, 1992, 1993a, b; Abbott, 1993; Cecile and Abbott, 1992; Cecile, 1997; Jennings and Jilson, 1986; Murphy, 1997; Roots et al., 1995a, b).

Gordey and Anderson (1993) suggested that the Gull Lake Formation was most likely deposited below wave base in an off shelf, quiet water setting and interpreted the limestone conglomerate at the base of the Formation to represent a debris flow. However, Murphy (1997) indicated that mafic volcanic rocks not seen in the type area, combined with clean quartzite might reflect the presence of local rifting, uplift and erosion of first cycle sediments deposited on basin flanks. Fossil evidence suggests that the age of the Gull Lake Formation is Early to Late Cambrian (Gordey and Anderson, 1993). The type section of the Gull Lake Formation has a stratigraphic thickness of approximately one kilometre, however, up to three kilometres of structurally thickened section has been measured (Murphy, 1997).

Rabbitkettle Formation

The Rabbitkettle Formation is a laterally continuous white weathering carbonate marker unit that occurs extensively throughout the Selwyn Basin and unconformably overlies the Gull Lake Formation (Gabrielse et al., 1973; Fritz et al., 1991; Abbot et al., 1986). The Rabbitkettle Formation primarily consists of limestone, siltstone and calcareous phyllite with locally occurring quartz-sandstone, limestone pebble meta-conglomerates, nodular limestone, carbonaceous shale, marble, carbonaceous phyllite, chloritic phyllite, volcanic tuff, tuffaceous shale, pillow basalts, subaqueous debris flows and submarine tuff (Cecile, 1982, 2000; Gordey and Anderson, 1993; Jennings and Jilson, 1986; Roots, 1988; Thompson, 1995)

Fine lamination, lack of traction features and position west of correlative, shallow water carbonate strata led Gordey and Anderson (1993) and Cecile (2000) to suggest that the Rabbitkettle Formation was deposited in a quiet water, sub-wave base, offshore setting. The exact age of the Rabbitkettle Formation in the central Yukon is unclear; Thompson et al. (1992) reported Cambro-Ordovician fossils from a similar unit in the southeastern Dawson map area while Gordey and Anderson (1993) documented a middle Ordovician age. At its type locality, the Rabbitkettle Formation was estimated to be at least 1200 m thick (Gabrielse et al., 1973).

Road River Group

The Road River Group conformably overlies the Rabbitkettle Formation and crops out extensively throughout the Northern Cordillera. Gordey and Anderson (1993) partitioned the Road River Group into the Duo Lake Formation and Steel Formation. The Duo Lake Formation (Cecile, 1982) comprises black graptolitic shale and chert combined with lesser phyllite and limestone. The carbonaceous, fine-grained and cherty nature of the Duo Lake Formation suggests that it was deposited in a quiet, sub-wave base, exilic, off-shelf setting starved of sediment input (Gordey and Anderson, 1993; Murphy, 1997). Graptolite faunas indicate that the Duo Lake Formation is Early Ordovician to Late Silurian in age (Green, 1972; Cecile, 2000). The stratigraphic thickness of the Duo Lake Formation is approximately 300 metres (Gordey and Anderson, 1993).

The Steel Formation (Gordey and Anderson, 1993) conformably overlies the Duo Lake Formation and is characterized by tan weathering and wispy discontinuous lamination.

This Formation is composed of variably calcareous siltstone and mudstone, with lesser chert, argillite, sandstone and sandy limestone (Cecile, 2000; Diment, 1986; Diment and Craig, 1999; Gordey and Irwin, 1987; Murphy, 1997). Gordey and Anderson (1993) suggest that the rocks of the Steel Formation were deposited in a relatively quiet, sub-wave base, off-shelf setting. The presence of benthic fauna, as indicated by wispy lamination, suggests a change to oxygenated bottom waters from the reducing euxinic conditions that prevailed during the deposition of the Duo Lake Formation (Murphy, 1997).

The exact age of the Steel Formation is uncertain, graptolite fauna collected from the Steel Formation in the McQuesten River Region suggest a late Silurian to possibly Early Devonian age (Murphy, 1997), while elsewhere age estimates include mid Silurian to Early Devonian (Gordey and Anderson, 1993) and early Silurian to Early Devonian (Cecile, 1997). The type section of the Steel Formation was measured to be 140 m thick (Gordey and Anderson, 1993), however structural thicknesses of up to 350 m have been calculated (Murphy, 1997).

Earn Group

The Earn Group (Campbell, 1967) unconformably overlies the Road River Group throughout most of the Selwyn Basin and is typically comprised of variably carbonaceous shale interbedded with lesser chert, siltstone, sandstone, limestone, bedded barite, baritic limestone, and chert pebble conglomerate (Abbott et al., 1986; Cecile, 2000; Gordey et al., 1982; Gordey and Irwin, 1987; Gordey and Anderson, 1993; Murphy, 1997). Numerous authors have partitioned the Earn Group into a variety of units. At the type locality (Glenlyon map area) the Earn Group was mapped as four separate units (Campbell, 1967); Gordey and Irwin (1987) subdivided the Earn Group in the Sheldon Lake and Tay River map areas into five map units; in the Nahanni map area Gordey and Anderson (1993) described the Portrait Lake Formation and the Prevost Formation, and finally Cecile (2000) mapped the Earn Group in the Niddery Lake area as two Formations, the Misfortune Formation and the Thor Hills Formation. For the purposes of this discussion the Earn Group will be discussed as a single unit.

Deposition of the Earn Group probably occurred in a submarine fan complex located in a deep marine basin broken by tensional or trans-tensional rifts (Abbott et al., 1986; Gordey et al., 1987; Gordey and Anderson, 1993; Murphy, 1997). Thus the coarse clastic sedimentary rocks of the Earn Group may represent the first indication of Devonian tectonic instability in the Selwyn Basin area. Fossils preserved in Earn Group

strata include graptolites and conodonts that range in age from Early to Late Devonian in the Nahanni and Nidderly Lake map areas (Gordey and Anderson, 1993; Cecile, 2000) and Devonian to Carboniferous in the Glenlyon map area (Campbell, 1967). The thickness of the Earn Group varies dramatically, Gordey and Anderson (1993) suggest an average thickness of 100-300 m and a maximum of almost 1.5 km while structurally thickened portions have been reported to be several kilometres thick (Murphy, 1997).

2.3 Tectonic and structural history

Lower Palaeozoic rocks of the Cordilleran miogeocline, as defined by Gordey and Anderson (1993) as a westward thickening wedge of sedimentary rocks of mid-Proterozoic to Middle Jurassic age, were deposited in a passive, off-shelf setting overlying the rifted margin of ancestral North America (Gabrielse and Yorath, 1991). Two northwest-trending facies belts developed during late Precambrian to Middle Devonian time and consist of shallow water carbonate and sandstone to the north, referred to as the Mackenzie Platform (Lenz, 1972), and turbiditic sandstone, deep-water limestone, shale and chert to the south that comprise the Selwyn Basin (Gabrielse, 1967, 1976). A third facies belt composed of shallow water carbonate-clastic sedimentary rocks, the Cassiar Platform, developed during the Late Silurian to Middle Devonian along the southwestern side of the Selwyn Basin.

The formation of the facies belts was interrupted by several episodes of Palaeozoic extension or rifting (Tempelman-Kluit, 1979) and was terminated in the Early Devonian with a sudden influx of marine turbiditic rocks, including lithologies that comprise the Earn Group. Clasts of Duo Lake Formation within the Earn Group indicate that at least part of this turbidite sequence was sourced from uplifted portions of the Selwyn Basin (Gordey and Anderson, 1993). From the middle Carboniferous to Middle Jurassic normal marine shelf sedimentation resumed with the deposition of clastic and carbonate rocks (Bamber and Mamet, 1978; Gibson, 1975; Graham, 1973). In the Middle Jurassic a Mesozoic island arc terrane collided with the western margin of the North American plate ending sedimentation within the Cordilleran miogeocline (Templeman-Kluit, 1979). Subsequent orthogonal collision of the amalgamated Wrangellia / Chulach Super terrane with the North American plate coincided with subduction related magmatism at about 115 – 110 Ma. Later northward translation of the Wrangellia block along the dextral Denali-Farewell and Tintina - Kaltag fault systems was synchronous with the northwest migration of the magmatic arc and 95 –

90 Ma magmatism. Between 95 and 70 Ma the magmatic arc had migrated to the vicinity of present-day southwestern Alaska (Goldfarb et al. 2000).

Accretion of exotic terranes along the North American margin initiated compressional deformation of the Cordilleran miogeocline. Within an orogenic framework the western Selwyn Basin is thought to represent an immediate northeastern salient to the exhumed core (Mair et al., 2006). Imbrication and folding produced upright to locally inclined, moderate to tight northwest-trending folds that are evident throughout the miogeocline (Green, 1972; Gordey and Anderson, 1993; Murphy, 1997; Mair, 2000; Mair et al., 2006; Stephens et al., 2000; Thompson et al., 1992; Thompson, 1995). The style of deformation across the miogeocline was strongly influenced by the distribution of lower and middle Palaeozoic facies. The competent carbonate strata of the Mackenzie Platform were folded into large-scale open folds and form the Mackenzie Fold Belt (Gordey, 1981b). The largely incompetent strata of the Selwyn Basin were intensely folded by small- to large-scale open to tight folds (e.g. Lost Horses Syncline; Murphy, 1997) and comprise the Selwyn Fold Belt (Gordey and Anderson, 1993).

A number of thrust faults and steeply dipping normal and/or reverse faults have been documented throughout the Selwyn and Mackenzie Fold Belts. In the eastern Yukon, Gordey and Anderson (1993) note that many of the thrusts are spatially associated with folds. They suggest that the thrusts developed synchronously with folding possibly as a result of the 'room problem' that develops in an anticlinal core as the fold tightens. In the western Yukon the Dawson, Tombstone and Robert Service Thrusts (Figure 2.1) separate the rocks of the Selwyn Basin and overlying Earn Group into three tectonic sheets (Anderson, 1987; Green, 1972; Mair et al., 2006; Templeman-Kluit, 1970; Thompson et al., 1990; Roots, 1988). The hanging-wall of the Tombstone Thrust hosts several kilometres of highly strained rocks that comprise the Tombstone High Strain Zone (Murphy, 1997; Murphy and Heon, 1995a and b; Stephens et al., 2000). This zone crosscuts the Robert Service Thrust, however, its relationship to the Tombstone Thrust is unclear. The steeply dipping normal and/or reverse faults follow three main trends: north to northeast, northwest, and east (Gordey and Anderson, 1993; Lindsay et al., 2000; Murphy, 1997; Stephens et al., 2000, 2004). The most prominent of these faults is the Tintina Fault. Late Cretaceous dextral transcurrent movement along the Tintina Fault, the Northern Rocky Mountain Trench Fault, and related structures was at least 450 kilometres (Templeman-Kluit, 1979) and possibly as much as 650 kilometres (Gabrielse, 1985). The timing of initial movement on the Tintina Fault is uncertain.

Plafker and Berg (1994) modelled major movement on the Tintina Fault post-Late Cretaceous, while Flanigan et al (2000) suggest a maximum age of 55Ma.

Comparison of the Selwyn and Mackenzie Fold Belts to the northern and southern Canadian Rocky Mountains led Gordey (1981b), and Gordey and Anderson (1993), to interpret the overall structure of the region to be that of a thin-skinned detachment terrane. They suggested that all thrust faults and folds root into or die out above a basal decollement, below which underlying strata and /or basement remain unaffected by events that produced the Selwyn and Mackenzie Fold Belts.

Deformation of the western margin of the Cordilleran miogeocline began in the Middle Jurassic, however, it did not occur simultaneously across the fold belts. Gordey and Anderson (1993) suggested an Early Cretaceous age for deformation in the eastern portion of the miogeocline based on middle Cretaceous intrusions that cut folded stratigraphy, combined with Early Cretaceous folded strata in the Sekwi Mountain map area (Blusson, 1971). A similar Jura-Cretaceous age of thrusting (including the formation of the Tombstone High Strain Zone) in the miogeocline has been determined from the youngest offset lithology combined with intrusive rocks that cut thrust faults (Gordey and Anderson, 1993; Green and Roddick, 1962; Murphy, 1997; Poulton and Tempelman-Kluit, 1982). Collision related had ceased by ca. 100 Ma and was followed by a Late Cretaceous dextral transcurrent regime (Mair et al., 2006). The age and kinematic relationships of many of the steeply dipping normal and/or reverse faults to folding and thrusting across the miogeocline also varies. Some faults are truncated by middle Cretaceous intrusions while others cut the plutons. Those that cut the plutons likely developed in response to a younger stress regime.

2.4 Intrusive Rocks

Several phases of Early to Late Cretaceous felsic to intermediate plutonic rocks crop out across the Yukon. The intrusions are typically composed of granodiorite, monzodiorite, monzonite, or granite with less common syenite and diorite and have been variably classified by a number of authors. In the eastern Selwyn Basin, Gordey and Anderson (1993) described a distinctive group of compositionally restricted metaluminous to peraluminous, granite and granodiorite intrusions; the Selwyn Plutonic Suite (SPS). The SPS are generally circular in plan, vary from less than one km to more than 20 km in width, and intrude and metamorphose strata as young as Triassic.

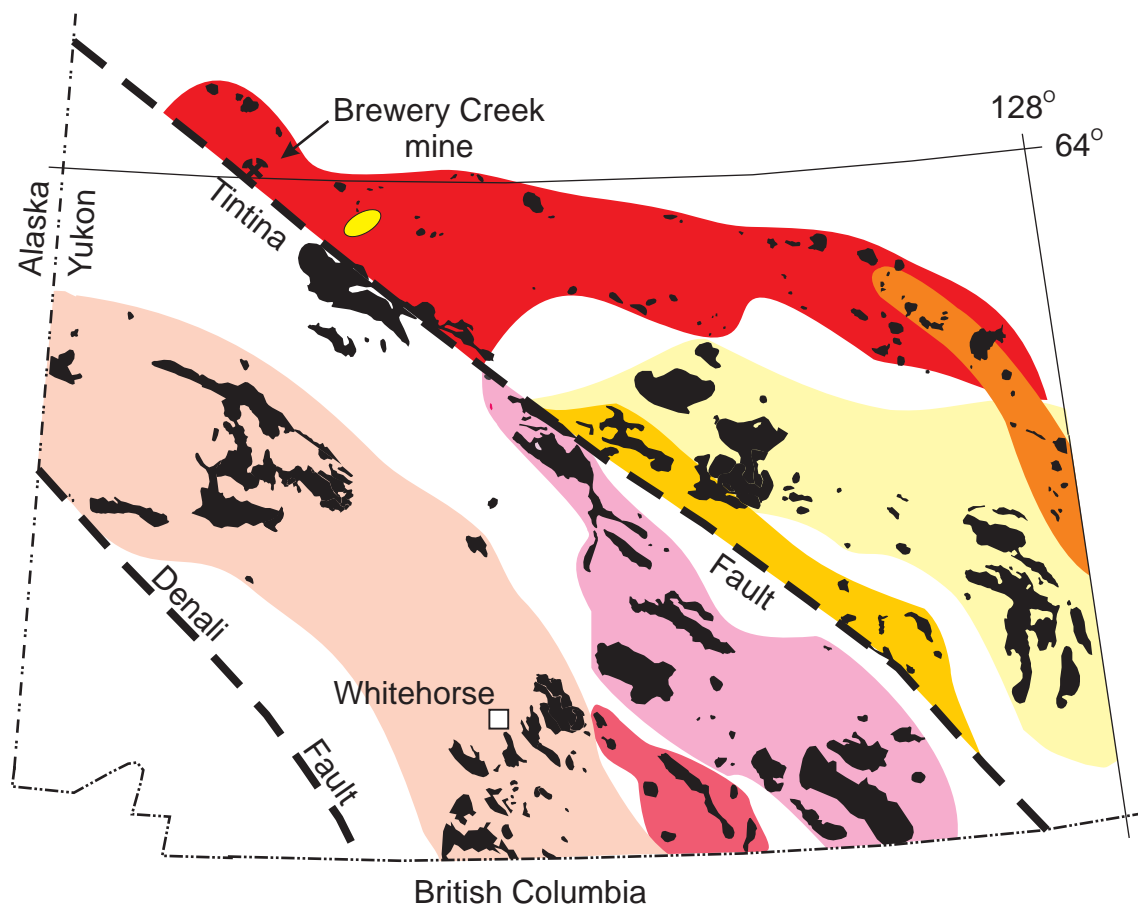
Gordey and Anderson (1993) partitioned the SPS using a threefold classification: (1) intrusions commonly containing hornblende, (2) intrusions with biotite and rarely containing hornblende, and (3) intrusions with biotite and muscovite. The SPS range in age from 106-80 Ma (Gordey and Anderson, 1993).

On the basis of age, lithology, mineralogy, geochemistry and distribution Mortensen et al. (1995, 2000) and Lang et al. (2000a, 2000b) partitioned the plutonic rocks in the Yukon into eight suites. These are the Teslin (123-115 Ma), Whitehorse-Coffee Creek (111-99 Ma), Cassiar (110-99 Ma), Anvil (112-100Ma), Tay River (98 – 96 Ma), Tungsten (97 – 92Ma), Tombstone (94 – 90 Ma) and the South Lansing (95 – 93 Ma) plutonic suites (Figures 2.3 and 2.4). A younger suite of intrusions, termed the McQuesten suite (70 – 65Ma), was documented by Murphy (1997), however, these plutons have only been recognised in the McQuesten River Region (Figure 2.4).

The name 'Tombstone plutonic suite' was originally applied to middle Cretaceous, alkalic intrusions in the Tombstone Mountains (Anderson, 1987). Recently the term 'Tombstone plutonic suite' has been used to refer to more than 110 stocks and plutons that are distributed along a 550 km long belt from the Tintina Fault at Dawson City eastwards to the Northwest Territories border and includes the intrusive rocks that crop out at Brewery Creek (Figure 2.3 and 2.4). The western continuation of the TPS has been dextrally offset approximately 450 km along the Tintina Fault and extends at least another 200 km southwest into Alaska to the Fairbanks mining district.

TPS intrusions are typically metaluminous, reduced, I-type, sub-alkaline to alkaline intrusions that range from less abundant mafic phases of pyroxenite, gabbro, and diorite, through to more common felsic end-members of granodiorite, quartz monzonite and granite (Mortensen et al., 1996, 2000; Lang et al., 2000). These intrusions are commonly porphyritic to K-feldspar megacrystic but equi-granular bodies are also present (Lang et al., 2000). TPS intrusions range in size from 5 km² to 100 km² and are variably shaped, however, elongate intrusions generally follow an east-west trend (Hart et al., 2000). Intrusions form simple to multiphase complexes that are generally homogenous and locally display concentric zoning (Abercrombie, 1989; Duncan et al., 1998; Lambert, 1966). Dykes and sills compositionally similar to major TPS intrusions occur in most systems including Brewery Creek (Diment, 1996; Diment and Craig, 1999; Lindsay 2000). Highly differentiated dykes, pegmatites and aplites are also ubiquitous within larger TPS intrusions but are volumetrically minor (Lang et al., 2000).

Figure 2.3. Distribution of plutonic suites in the Yukon as described by Mortensen et al. (1995, 2000) and Lang et al. (2000a, 2000b). The intrusive suites form broadly NW trending belts. Note the location of Brewery Creek mine within the area containing Tombstone plutonic suite intrusions.









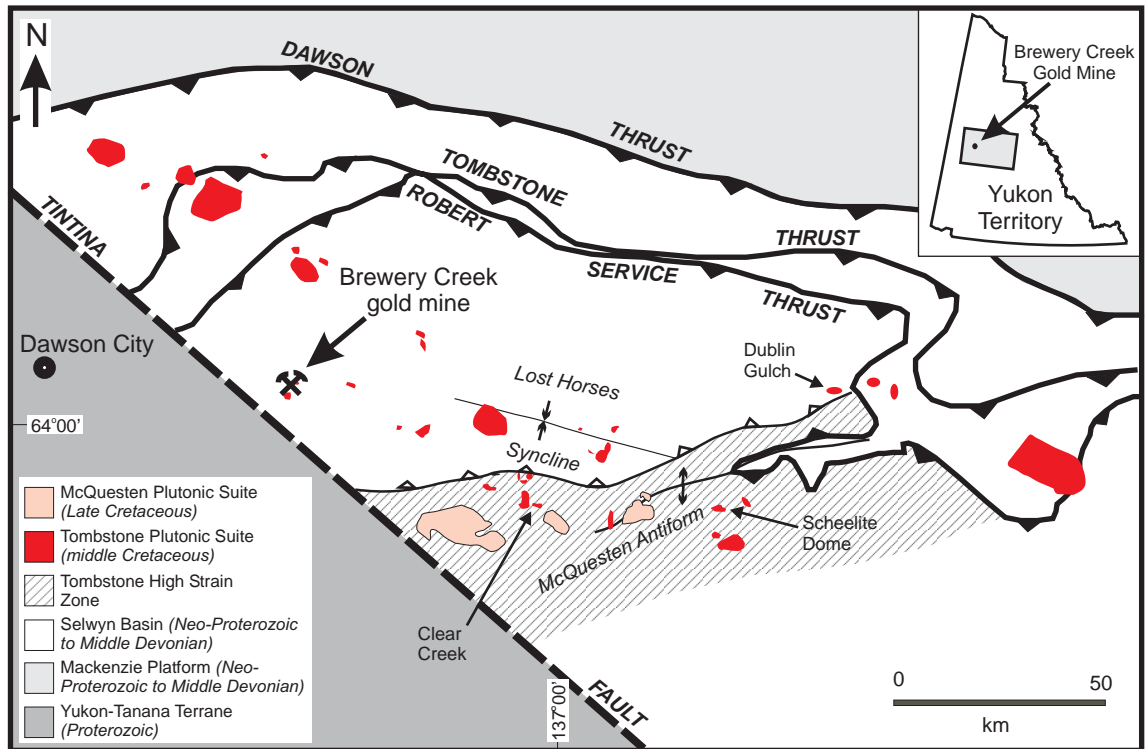
- | | | |
|---|---|--|
|  McQuesten
plutonic suite |  Tungsten
plutonic suite |  Cassiar
plutonic suite |
|  Tombstone
plutonic suite |  Tay River
plutonic suite |  Teslin
plutonic suite |
|  South Lansing
plutonic suite |  Anvil
plutonic suite |  Whitehorse-
Coffee Creek
plutonic suite |

Figure 2.4. Distribution of the Tombstone and McQuesten plutonic suites within the Selwyn Basin. Note that TPS intrusions crop out at Brewery Creek and that TPS intrusions cut the regional thrusts and the high strain zone. Figure modified from Murphy (1997).



Murphy (1997) noted that TPS intrusions post-date the major deformation events recognised in the Selwyn Basin and are also generally post-metamorphic.

Ilmenite or more rarely magnetite is common in TPS intrusive rocks indicating that most magmas have a low primary oxidation state. The low oxidation state and typically felsic nature give the plutons a low magnetic response (Hart et al., 2000), however, pyrrhotite-bearing intrusions exposed at Brewery Creek are an exception. The majority of TPS intrusions are enclosed by a contact metamorphic aureole that typically extends from 100 m up to several kilometres from the outcropping intrusive contacts and can envelope several small plutons (Poulsen et al., 1997). Murphy (1997) suggested that the predominant biotite-andalusite contact metamorphic mineral assemblage indicates formation at low to moderate pressures (< 3 kb) with emplacement depths estimated at between 3.3 and 11.6 km for the Tungsten plutonic suite (Gordey and Anderson, 1993). Contact aureoles commonly contain abundant pyrrhotite developed after pyrite that produces a characteristic doughnut shaped aeromagnetic signature (Poulsen et al., 1997; Hart et al., 2000).

The origin of the Cretaceous intrusive suites described above is presently unresolved. Most suites show geochemical and radiogenic isotope (e.g. Sr_i approximately 0.71; Armstrong, 1988) evidence indicating that they contain a large component of evolved continental crust (Gordey and Anderson, 1993; Mortensen et al., 2000), however, a mantle contribution was noted for middle Cretaceous TPS rocks (Mortensen et al., 1996). Lang et al. (2000) suggest that the distribution and geochemical characteristics of the Cretaceous intrusive rocks is consistent with their formation resulting from subduction related magmatism in a southwest facing continental magmatic arc. Thus they interpret the Whitehorse-Coffee Creek suite to represent an Andean-type arc built on continental crust with the Anvil and Cassiar suites emplaced coevally in a back arc position. The younger Tay River, Tungsten, Tombstone and South Lansing suites formed as a series of roughly orogen parallel magmatic belts that stepped successively north and northeast over a period of approximately 10 Ma.

The tectonic setting during the emplacement of middle Cretaceous intrusions in Alaska and the Yukon is also poorly understood. Flannigan et al. (2000) proposed a variation of structural style through space and time. They cite the Tombstone plutonic suite, the north-eastern most mid Cretaceous plutonic belt in the TGB, as comprising intrusions that were emplaced into old continental crust, most likely a back-arc or foreland environment, during an episode of local extension that followed movement on major

thrust faults (Murphy, 1997; Marsh et al., 1999; Stephens et al., 2004). In contrast, the Late Cretaceous intrusions in southwestern Alaska have a demonstrably more direct relationship to subduction processes. Despite uncertainties in tectonic setting most IRGS formed above or within 'old', typically cratonic continental crust (Thompson et al., 1999) in a setting well removed or distal from convergent margins active at the time of magmatism.

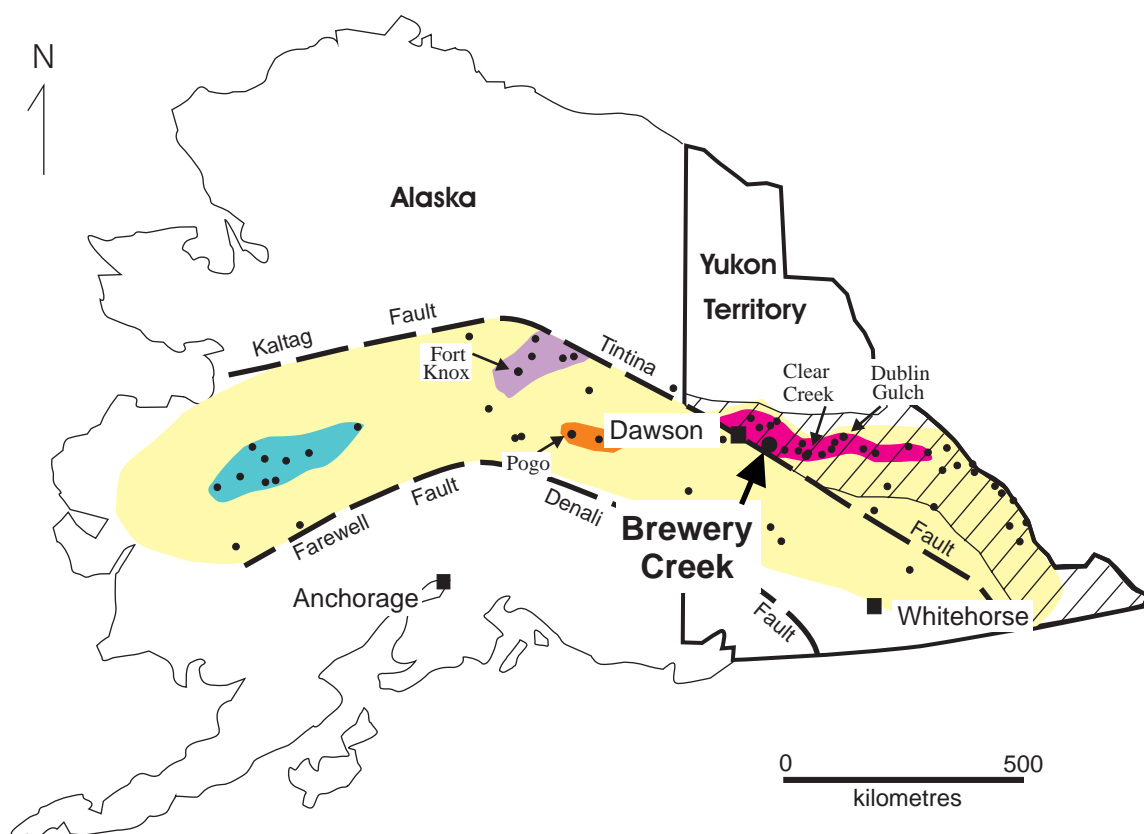
2.5 Gold Mineralisation in the Yukon - The Tintina Gold Belt

The Yukon Territory is host to a diverse range of mineralisation and has experienced a long mining history. The earliest activity centred on alluvial gold mining with a major gold rush to the world famous Klondike gold fields near Dawson City in the late 1800's. Subsequent discoveries have included significant deposits of gold, lead, zinc, silver, iron, tungsten, copper, nickel, molybdenum, PGE, barite and tin. Most recently, gold exploration, mining and research interests in the Yukon have focussed on intrusion-related gold deposits and a newly defined gold province termed the Tintina Gold Belt (TGB).

The TGB is an approximately 250 km wide and 1000 km long belt of gold mineralisation and spatially associated middle Cretaceous granitic intrusive rocks that extends through central Alaska, the Yukon and into the westernmost Northwest Territories. This belt comprises numerous smaller gold belts and districts, with the most significant being the Kuskokwim, Fairbanks and Goodpaster districts in Alaska and the Tombstone gold belt in the Yukon (Figure 2.5). Gold deposits in the TGB include Pogo (9.0 Mt @ 17.8 g/t Au for 5.2 Moz Au; Smith et al., 2000; Rhys et al., 2003), Fort Knox (169 Mt @ 0.93 g/t Au for 4.6 Moz Au; Bakke et al., 1995; Selby et al., 2002), Brewery Creek (43.8 Mt @ 1.03g/t Au for 1.4 Moz Au; Park, 1999) and Dublin Gulch (99 Mt @ 1.1 g/t Au for 3.5 Moz Au; Smit et al., 1996), and prospects such as Clear Creek and Scheelite Dome (Stephens et al., 2004). The TGB has a recently defined lode gold resource of ~ 35 Moz and past placer lode production of ~ 33 Moz. (Hart et al., 2002).

Smith (2000) suggested that the nature of gold deposits within the TGB is so variable that no specific geologic elements precisely define it. However mineralisation along the Tintina Gold Belt is typically characterised by (1) a spatial and/or temporal association with Cretaceous plutons, (2) distinct element associations, typically Au-Bi-W-Te in systems hosted by granitoid stocks and Au-As-Sb in systems hosted by meta-

Figure 2.5. The Tintina Gold Belt in the Yukon Territory and Alaska. The four major gold producing districts have been highlighted. Note the location of the Brewery Creek mine to the north of the Tintina Fault and the distribution of Selwyn Basin lithologies within the Yukon. Figure modified from Hart et al. (2000).



- | | | | |
|---|--|--|---|
| Tintina Gold Belt | Goodpaster District | Kuskokwim District | • Known occurrence of gold mineralisation |
| Tombstone Gold Belt | Fairbanks District | Approximate extent of the Selwyn Basin within the Yukon | |

sedimentary rocks, (3) minor base metals, (4) low sulphide content and reduced sulphide mineral assemblages, and (5) an Early to mid Cretaceous age (Hart et al., 2000; Goldfarb et al., 2000; McCoy et al., 1997; Newberry et al., 1995).

The TGB was originally considered as three discrete gold provinces; (1) porphyry, dyke, sill and stock related systems in the Kuskokwim district, southwestern Alaska (Bundtzen and Miller, 1997), (2) granitoid and metamorphic rock hosted gold deposits in the Fairbanks and other mining districts of east central Alaska (McCoy et al., 1997), and (3) the diverse styles of gold mineralisation in rocks of the Selwyn Basin in central Yukon (Poulsen et al., 1997). Despite the delineation of the TGB, Goldfarb et al. (2000) suggest that these provinces must still be differentiated as gold deposits within the provinces display distinct differences in structural styles, levels of deposit emplacement, ore-fluid chemistry and gold grades. Thus, Goldfarb et al. (2000) classified deposits in the southwestern Alaska as epithermal and/or porphyry style, in the east central Alaska as orogenic, and in the Selwyn Basin as intrusion-related. However, several authors suggest that many of the deposits in east-central Alaska may be classified as intrusion-related gold deposits as they display spatial and temporal relationships to Cretaceous intrusions (Thompson et al., 1999; Lang et al., 2000a; Lang and Baker, 2001).

Gold mineralisation within the Yukon portion of the Tintina Gold Belt is coincident with the mid-Cretaceous Tombstone plutonic suite (TPS) (see section 2.4). The TPS extends for approximately 550 km across central Yukon and commonly display a strong Au-Bi-W-As-Sb metal signature. Gold mineralisation around TPS intrusions occurs as quartz-sulphide veins, sheeted veins, stockwork, replacements, breccias, skarns and disseminated mineralisation in felsic intrusive rocks, and in both carbonate and non-carbonate meta-sedimentary rocks (Lang et al., 2000a; Mortensen et al., 2000; Poulson et al., 1997). These styles of gold mineralisation also display regional controls and are influenced by carbonate bearing strata of the Selwyn Basin and ENE oriented faults related to an interval of N-S directed extension (Poulsen et al., 1997; Stephens et al., 2004).

2.6 Intrusion-related gold mineralisation

Numerous authors have noted a spatial and temporal relationship of gold with granitoid intrusive rocks. Recently a new class of intrusion-related gold mineralisation has been defined and is variably referred to as porphyry gold deposits (Hollister, 1992; Bakke, 1995), intrusion-related stockwork disseminated deposits (Sillitoe, 1991), plutonic-related gold deposits (Newberry et al 1995; McCoy et al 1997), intrusion-related gold deposits (Thompson et al 1999) and intrusion-related gold systems (Lang et al., 2000; Lang and Baker, 2001; Thompson and Newberry, 2000). In this thesis the term intrusion-related gold system (IRGS) is used when referring to this class of deposit and intrusion-related gold deposit (IRGD) is used when referring to a single deposit.

IRGS along the TGB and elsewhere around the world have been well documented by several authors and are thought to include Fort Knox, Donlin Creek, Pogo, Dublin Gulch, and True North in North America as well as Mokorsko, Czech Republic, Vasilkovskoe, Kazakhstan, Salave, Spain, Korri Kollo, Bolivia and Kidston and Timbarra in Australia (Goldfarb et al., 2000; Lang and Baker, 2001; Lang et al., 1997, 2000a and b; McCoy et al., 1997; Thompson et al., 1999). This type of gold deposit is characterised by (1) gold as a principal commodity, (2) a common association with metaluminous, sub-alkalic intrusions of intermediate to felsic composition that span the magnetite-ilmenite series boundary, (3) a metal assemblage that predominantly includes Au, Bi, As, W, Mo, Te, and Sb, (4) the presence of carbonic hydrothermal fluids, (5) restricted alteration haloes, (6) a low sulphide mineral content, mostly less than 5% vol, with a reduced ore mineral assemblage that typically includes arsenopyrite, pyrrhotite and pyrite and lacks magnetite or hematite, (7) deposits that are commonly located within areas formerly recognised for tin and/or tungsten mineralisation, and (8) a continental setting well inboard of inferred or recognized convergent plate boundaries, where continental magmatism has combined intrusions of alkalic metaluminous calc alkalic and peraluminous compositions.

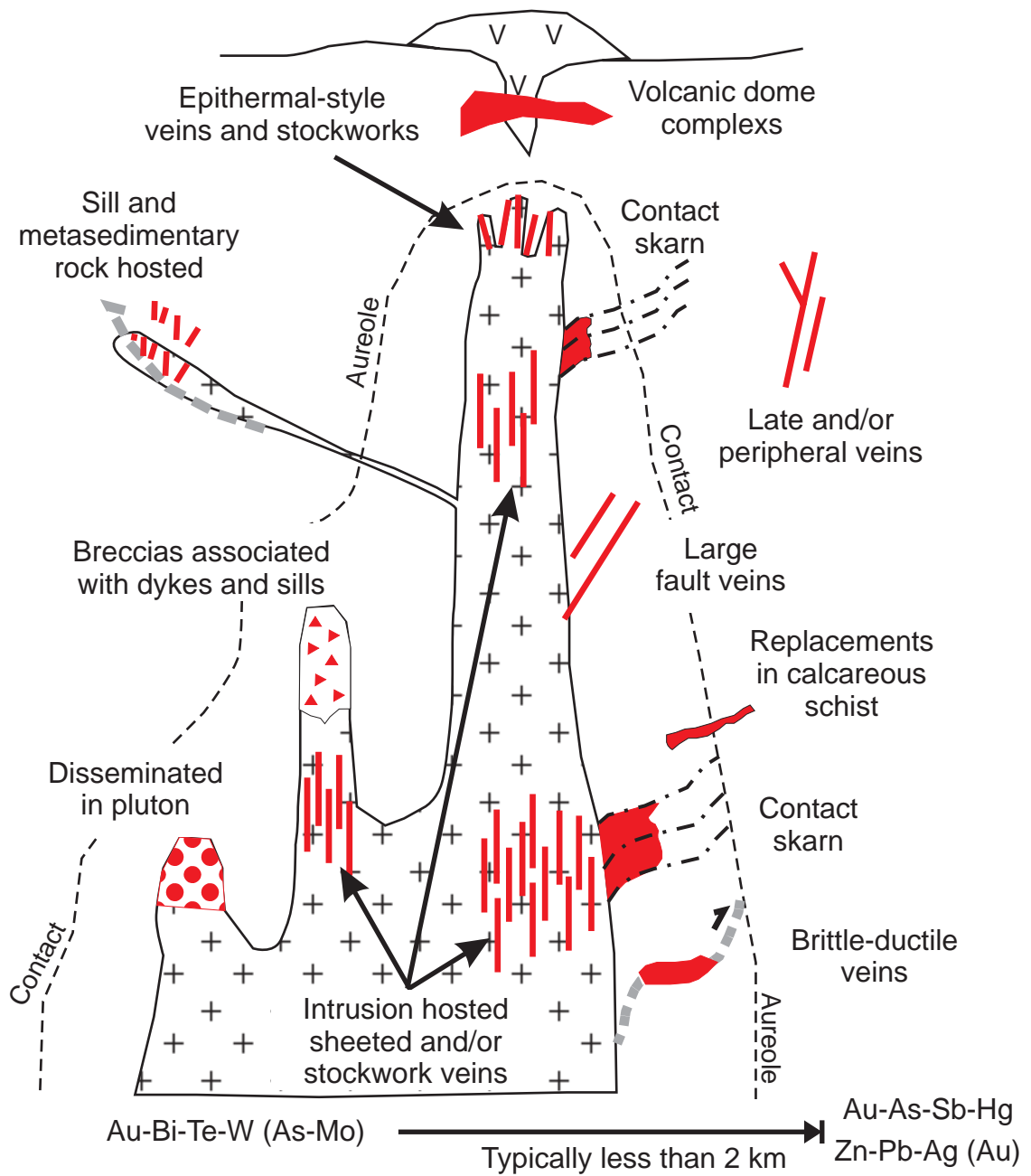
Igneous centres that form IRGS are typically multiphase complexes that were rapidly emplaced and cooled quickly. The complexes variably comprise batholiths, large or small plutons, irregular plugs, dome complexes, or swarms of dykes and sills (Lang et al., 2000; Newberry, 2000; Thompson et al., 1999). The composition of igneous rocks associated with IRGS varies greatly from pyroxenite, gabbro, and diorite, through to more common felsic end-members of granodiorite, quartz monzonite and granite

(Mortensen et al., 1996, 2000; Lang et al., 2000), however, the most common compositions are metaluminous, subalkalic, intermediate to felsic, I-type intrusions that span the magnetite-ilmenite series boundary (Thompson et al., 1999; Lang and Baker, 2001). In the Yukon Cretaceous intrusions associated with gold mineralisation are surrounded by contact metamorphic aureoles up to several kilometres wide that commonly encompass several discrete intrusive bodies (Poulsen et al., 1997).

Styles of gold deposits in IRGS are strongly influenced by depth of formation, host rock composition and the presence or absence of structures. Lang et al. (1999) proposed a model for IRGS that accounts for these controls and highlights the vertical and lateral zonation of ore environment and mineralisation styles with respect to a hypothetical central mineralising pluton (Figure 2.6). Based on their spatial relationship to intrusions, deposits of the IRGS model were further partitioned into three categories by Hart et al (2000). (1) Intrusion hosted deposits that comprise sheeted and stockwork vein deposits with a metal assemblage of $\text{Au-Bi} \pm \text{Te} \pm \text{As} \pm \text{Mo} \pm \text{W}$. (2) Proximal deposits are those that are located in host rocks adjacent to intrusions, within the contact metamorphic aureole. Proximal deposit types show a metal association of $\text{W} \pm \text{Cu} \pm \text{Au} \pm \text{Bi}$ and $\text{Cu-Bi-Au} \pm \text{W}$ and include skarns, sulphide replacement of calcareous rocks, Sn and Cu bearing breccias and diatremes, and veins and disseminated deposits in meta-sedimentary host rocks. (3) Distal deposits are sited outside the contact metamorphic aureole. They include auriferous, mesothermal to epithermal quartz sulphide veins along steep faults, hydrothermal breccias and base metal veins enriched in $\text{Ag} \pm \text{Au}$, and disseminated Au in variably calcareous and carbonaceous host rocks that have been likened to Carlin deposits (Poulsen, 1996). Distal deposits have a typical metal signature of $\text{Au-As-Sb} \pm \text{Hg}$.

Thompson et al. (1999) and Lang and Baker (2001) described alteration in IRGS as typically fracture controlled or limited to narrow envelopes around individual veins, pervasive alteration is rare but has been noted in shallowly emplaced (< 3 km) deposits. Felspathic and sericitic assemblages are the most common styles of alteration with rare occurrences of silicic, greisen, calc-silicate, and/or advanced argillic alteration. Gold and its associated minerals are most closely associated with late stage sericite alteration (Maloof et al., 2001; Mustard, 2001). The relative simplicity of alteration within IRGS may be partly explained by the fluid evolution of a developing IRGS. At the Emerald Lake pluton the fluid evolution appears to be unidirectional with

Figure 2.6. A schematic model of an intrusion-related gold system. The model illustrates how styles of intrusion related gold mineralisation vary with depth and distance from the mineralising pluton. Brewery Creek has been attributed to the sill and meta-sedimentary rock hosted style. Note the change in gold-metal associations across the system. Diagram adapted from Lang et al. (2000a).



little or no evidence for multiple pulses of fluid that typify porphyry systems (Duncan et al., 1998; Coulsen et al., 2001).

It should be noted that several authors have suggested that Brewery Creek may be classified as an intrusion related gold deposit (Poulsen et al., 1997; Thompson et al., 1999; Hart et al., 2000; Lang et al., 2000 a and b), however the specific links between magmatism and gold at this deposit have not been rigorously explored.

CHAPTER THREE

Local geological setting of the Brewery Creek gold deposit



A sunny day in the Yukon. The photo was taken at the North Slope zone looking east along the Tintina Gold Belt towards Clear Creek.

3.1 Chapter Overview

The Brewery Creek property is underlain by Palaeozoic sedimentary and volcanic rocks of the Selwyn Basin and the Earn Group. Outcropping lithologies include calcareous phyllite, basalt, dolerite, chert, calcareous sandstone, fossiliferous limestone, chert pebble conglomerate and variably carbonaceous sandstone, siltstone and shale. These lithologies have been cut by several generations of faults and folds. The overall architecture of the property is that of a broad NNE trending arch of thrust sheets. The rocks in each thrust sheet have been deformed into upright to steeply inclined, open to tight, variably NE, E, and NW trending folds.

Middle Cretaceous intrusive rocks including monzonite, syenite and hornblende gabbro cut the thrust faults and folds. These magmatic rocks were subsequently deformed by numerous, variably oriented normal faults, and host a variety of sulphide \pm gold bearing veins. The intrusions and mineralisation have been cut and dextrally offset approximately 1.5 km by the Classic Fault that trends sub parallel to the near-by Tintina Fault.

Previous work on the geology of Brewery Creek (Diment, 1996; Diment and Craig 1999) has briefly described some of the host rocks, however, no detailed descriptions have been given. This chapter addresses the following points:

- (1) Description of property stratigraphy and correlation to regional units.
- (2) Description of intrusive rocks
- (3) Description of structures and a structural history
- (4) Correlation of the structural history to elsewhere in the Selwyn Basin

All lithological descriptions and structural measurements described in this chapter were collected from road cuts, open pits and other man-made excavations, as there is less than 2% natural outcrop at Brewery Creek.

3.2 Property stratigraphy

Sedimentary and volcanic rocks of the Selwyn Basin and Earn Group underlie the Brewery Creek property. Six early Palaeozoic rock units have been recognised at Brewery Creek, from oldest to youngest they are the Rabbitkettle Formation, Menzie Creek Volcanic unit (informal), Road River Group (Duo Lake Formation and Steel Formation), Brewery unit (informal) and Earn Group (Figure 3.1 and 3.2). The lithologies comprising the Brewery unit are previously unrecognised at a similar stratigraphic position in the Selwyn Basin and are described in detail below.

Rabbitkettle Formation

Beds (0.5 to 1 cm thick) of cream to white weathered, fine grained calcareous siltstone and calcareous phyllite (Figure 3.3) interbedded with subordinate chert and mudstone (0.5 cm thick) crop out in a small area in the north-central part of the Brewery Creek property (Figure 3.1). The lithological characteristics and stratigraphic position of this unit suggests that it correlates with the Rabbitkettle Formation that occurs extensively throughout the Selwyn Basin (Gordey and Anderson, 1993; Murphy, 1997). At Brewery Creek, the Rabbitkettle Formation is thrust bound against the Earn Group to the west. Tight folding present in the Rabbitkettle Formation but absent in the Menzie Creek volcanic unit suggests that the eastern contact may be a fault or an unconformity, however, this relationship remains unresolved. No age indicators were identified at Brewery Creek, however, elsewhere in the Selwyn Basin the Rabbitkettle Formation is interpreted to be Cambro-Ordovician (Gordey, 1981; Thompson et al., 1992;) and locally as young as mid-Ordovician (Gordey and Anderson, 1993) in age. Sedimentary younging derived from local cross-lamination and graded bedding suggest that the Rabbitkettle Formation is upright. A minimum structural thickness of 50 m has been calculated from cross-section (Figure 3.1) for the Rabbitkettle Formation, however, this package of rocks has been intensely deformed by numerous tight, cm-scale folds of bedding and the lower contact was not observed.

Menzie Creek volcanic unit (MCV)

A thick succession of green to brown weathered, mafic volcanic rocks crop out at Brewery Creek along the northern margin of the map area and as two outcrops along the road toward the Classic Zone (Figure 3.1). Diment (1996) and Diment and Craig (1999) correlated these rocks to the Menzie Creek volcanic rocks that outcrop near Faro. Cambro-Ordovician mafic volcanic rocks sited in a similar stratigraphic position

Figure 3.1 **A map and cross-section summarising the geology of the Brewery Creek property.** Six sedimentary and volcanic rock units have been identified, namely the Rabbitkettle Formation, Menzie Creek volcanic unit, Duo Lake Formation, Steel Formation, Brewery unit (new), and Earn Group. The repetition of these units results from folding and thrusting as shown in cross-section A-A'. Plutons and stocks of syenite and sills and dykes of monzonite cut the folds and thrusts. Where these igneous rocks are in contact with Steel Formation and Brewery unit metamorphic aureoles several hundred metres wide are common. However there is only evidence of contact metamorphism where monzonite sills intrude the Earn Group. 80% of the gold mineralisation at Brewery Creek is hosted along the Reserve Trend, a roughly east-striking linear trend of mineralisation, sills and structure. Note that A0 sized versions of this map that display comprehensive geology, contours and streams can be found in the map pocket at the back of this thesis.

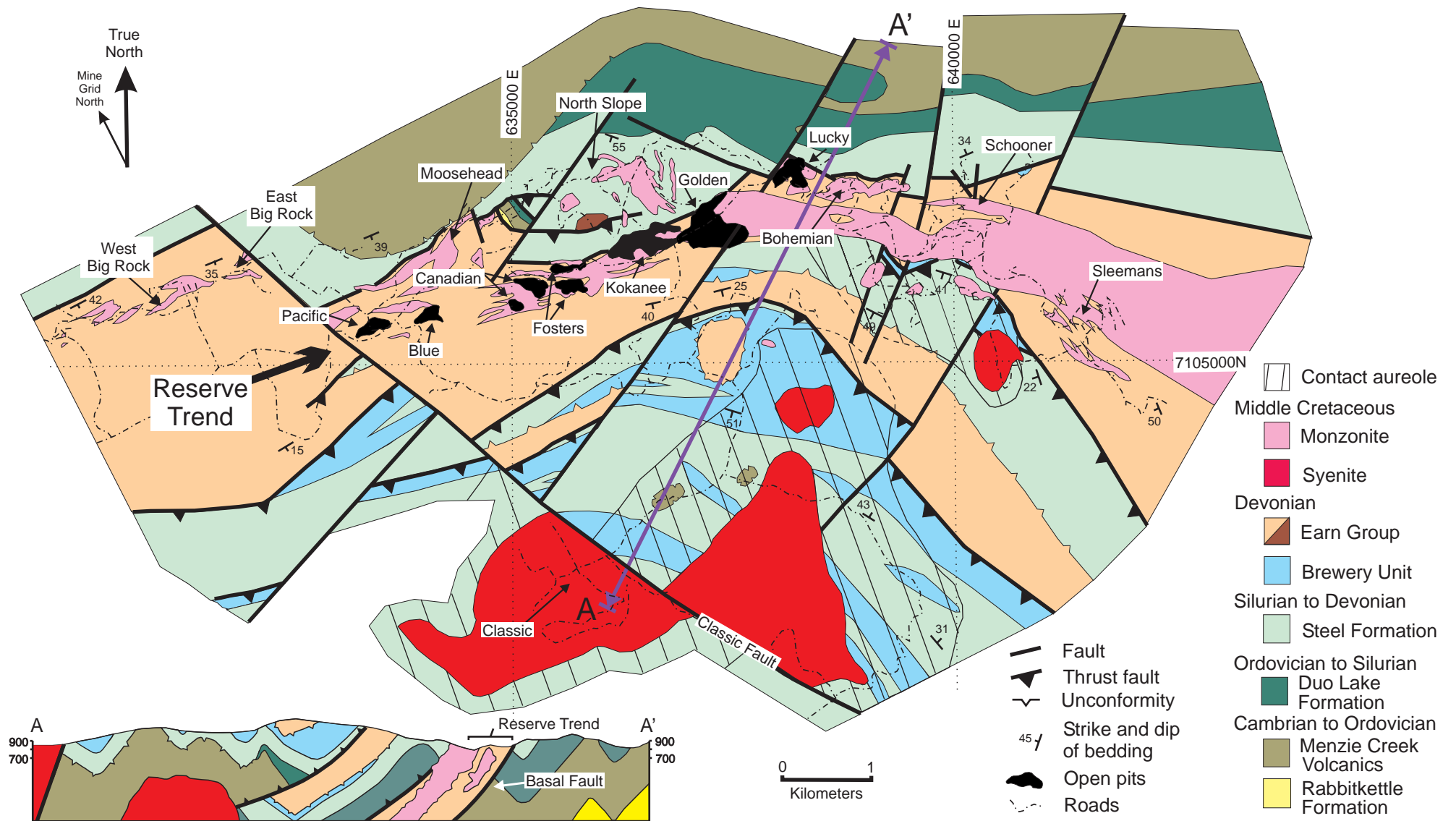


Figure 3.2 **Stratigraphic columns displaying the relationships, composition, and age of (A) rocks comprising the Selwyn Basin, and (B) rocks outcropping at Brewery Creek.** Note the location of the Brewery Unit and Menzie Creek volcanic unit in the stratigraphic column for Brewery Creek. Data used to compile column A was sourced from Cecile (1982, 1997), Fritz et al. (1991), Gordey et al. (1982), Gordey and Irwin (1987), Gordey and Anderson (1993), Jennings and Jilson (1986), Murphy (1997), and Roots (1988). Data for column B is sourced from field descriptions with the stratigraphic thickness measured from cross section.

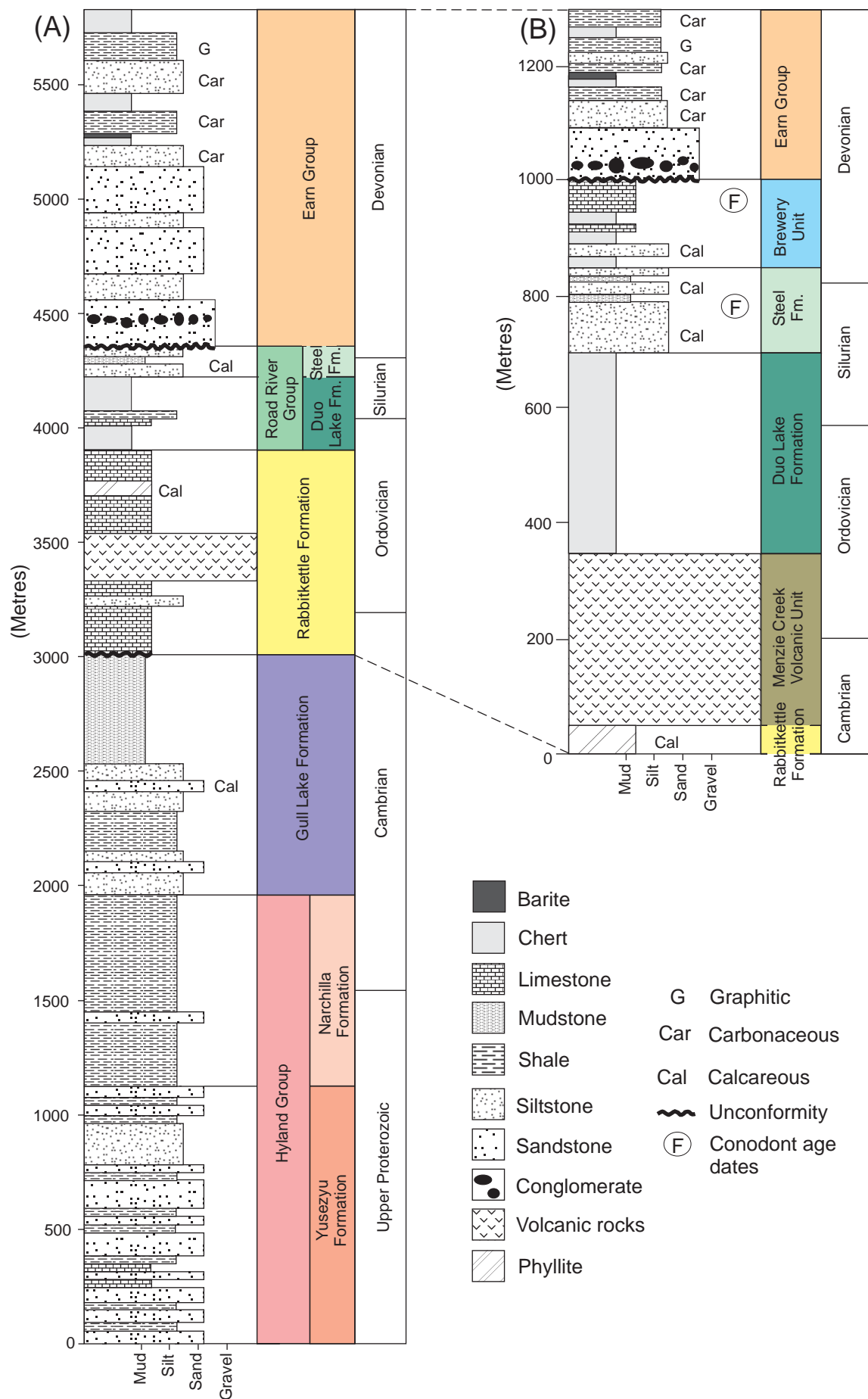
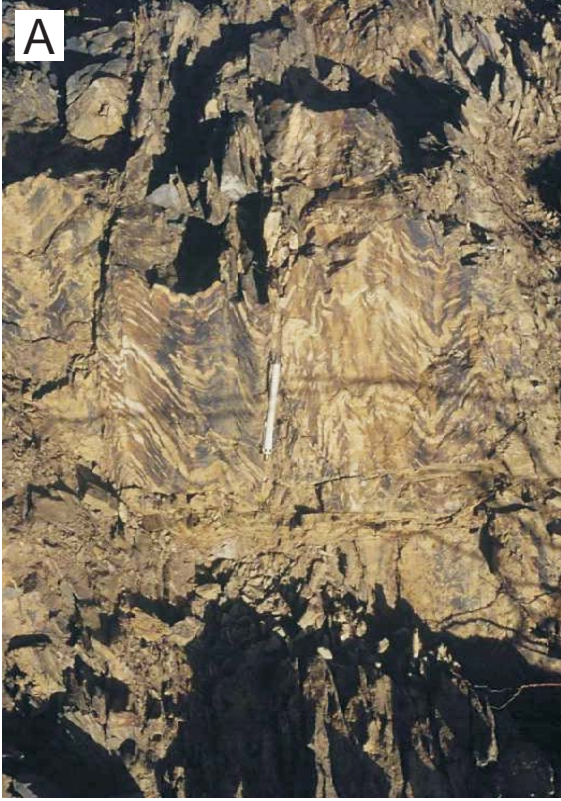


Figure 3.3 **Calcareous phyllite of the Rabbitkettle Formation.** (A) Outcrop on the road to North Slope (note pencil for scale). (B) Photograph of a hand specimen collected from the Moosehead Zone. Note that both outcrop and specimen show well-developed fold patterns that typify the Rabbitkettle Formation at Brewery Creek.



also occur in the Dawson and Hart River areas and include hyaloclastite breccias and pillow lavas. These features are common in the volcanic unit at Brewery Creek, however, given that neither occurrence of volcanic rocks have been formally recognised this thesis continues with previously established informal nomenclature (Diment, 1996; Diment and Craig, 1999) and refers to these lithologies as the Menzie Creek volcanic unit (MCV).

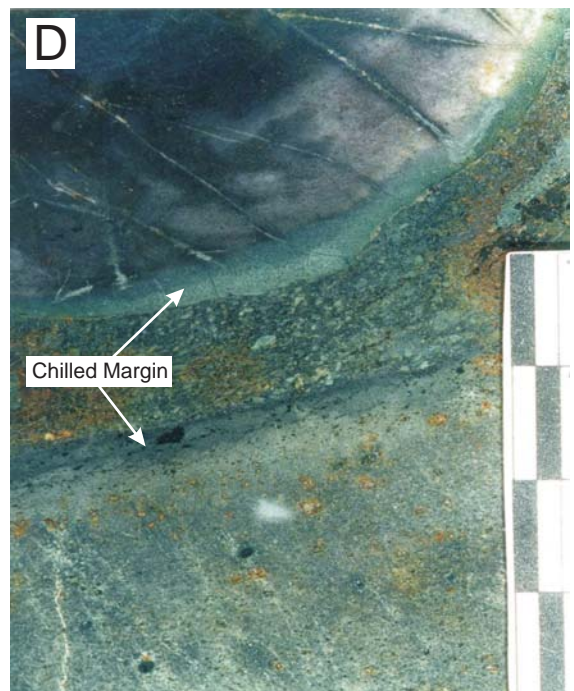
The MCV at Brewery Creek is comprised of chlorite- and carbonate-altered medium-grained dolerite, basalt, amygdaloidal basalt (amygdales filled with calcite), basaltic pillow lavas, hyaloclastite breccias and mafic volcanoclastics with clasts up to 8 cm across (Figure 3.4). The MCV is either fault bound or unconformable over the Rabbitkettle Formation, and both Duo Lake Formation and Steel Formation overlie the upper boundary of the MCV (Figure 3.1). The stratigraphic absence of the Duo Lake Formation can be explained by two contrasting mechanisms: (1) The outcrops of MCV may represent ancient topographic highs onto which the Steel Formation could have been deposited, thus this boundary would represent an unconformity. (2) The boundary may represent a post-sedimentation normal fault. The first interpretation is preferred because to the northeast of the Classic Zone beds of Steel Formation immediately overlie a thick sequence of MCV (R.Diment pers. comm.) Furthermore, an unconformity has been documented beneath the Steel Formation in other parts of the Selwyn Basin. Kilometre-scale normal faults have not been documented in the Selwyn Basin and thus the second interpretation is less likely.

No age determinations were made for the MCV at Brewery Creek, however Diment (1996) and Diment and Craig (1999) suggested a Late Cambrian to Early Ordovician age. This age is supported by mafic volcanic rocks that are intermittently associated with the Rabbitkettle Formation elsewhere in the Selwyn Basin (Gordey, 1981, 1983), and the stratigraphic position of the MCV (Figure 3.1 and 3.2). The MCV at Brewery Creek is moderately resistant to weathering and commonly forms ridges or hills. A minimum structural thickness of 150 m has been calculated from cross-section. However, extensive outcrop of this unit along the northern margin of the Brewery Creek property suggests that the MCV could be more than one km thick (Figure 3.1).

Road River Group

Across the Brewery Creek property the MCV are overlain by black chert and tan weathered, wispy laminated siltstone. Based on stratigraphic position and lithological characteristics Diment (1996) and Diment and Craig (1999) correlated these rocks

Figure 3.4 Photographs of selected lithologies from the Menzie Creek volcanic unit. (A) Vesicular basalt with vesicles infilled with chlorite, carbonate and epidote. (B) Equi-granular dolerite with pyroxene (dark green) and plagioclase (white). (C) Volcaniclastic breccia with clasts of vesicular basalt, chert and sandstone. (D) Pillow basalt displaying chilled margins.



respectively to the Duo Lake Formation (Cecile, 1982) and Steel Formation (Gordey and Anderson, 1993) of the Road River Group (Gabrielse et al., 1973).

Duo Lake Formation

The Duo Lake Formation crops out along the northeastern portion of the Brewery Creek property (Figure 3.1). This Formation comprises grey to black weathered chert and siliceous siltstone (Figure 3.5). Sedimentary layers are massive to thick-bedded and range in width from 2 – 100 cm but are generally 10 – 20 cm thick. Volcaniclastic and/or calcareous layers that characterise the MCV and Steel Formation respectively are absent in the Duo Lake Formation. This unit lies either unconformably or is fault bound above the MCV and conformably below the Steel Formation. The unconformity, or fault control, on the distribution of the Duo Lake Formation may explain the stratigraphic absence of this unit in the southern part of the property. No age dates were obtained from this Formation at Brewery Creek, however, elsewhere in the Selwyn Basin the age of the Duo Lake Formation is inferred to be Early Ordovician to Silurian (Green, 1972; Gordey and Anderson, 1993). The Duo Lake Formation at Brewery Creek is moderately resistant to weathering and commonly forms hills and ridges. The Duo Lake Formation has been intermittently deformed by close to tight folds with wavelengths above 30 cm and up to km-scale. A maximum structural thickness of 350 m has been calculated for the Duo Lake Formation from cross-section (Figure 3.1).

Steel Formation

The Steel Formation crops out throughout the Brewery Creek property and comprises more than 25% of the total map area (Figure 3.1). The Steel Formation is dominantly composed of tan weathered, wispy laminated, burrowed, calcareous siltstone, silty shale, and mudstone interbedded with minor chert and up to 10 m thick packages of black carbonaceous shale and siltstone (Figure 3.6). Carbonaceous shale beds are commonly boudinaged while adjacent calcareous siltstone beds remain competent. Beds range in thickness from 1 – 20 cm (generally 1 – 5 cm thick) and display rare cross lamination and grading. The Steel Formation conformably overlies the Duo Lake Formation and conformably underlies the Brewery Unit. Fossils from the upper part of the Steel Formation at Brewery Creek contain Silurian to Early Devonian conodonts (Table 3.1) which is consistent with ages documented elsewhere in the Selwyn Basin (Cecile, 1997).

Figure 3.5 **Photographs of the Duo Lake Formation in outcrop.** (A) Folded beds of chert probably representing syn-sedimentary deformation. The fold is parallel to the dashed line. Note the pencil in the centre of the photo for scale. (B) Beds of chert 5 - 20 cm thick that are typical of the Duo Lake Formation at Brewery Creek.



Figure 3.6 Rocks of the Steel Formation. Photographs display (A) tan-weathered wispy-laminated siltstone typical of the Steel Formation at Brewery Creek, (B) the wispy, discontinuous lamination results from bioturbation as evidenced by worm borrows, and (C) interbedded siltstone (tan) and shale (black).

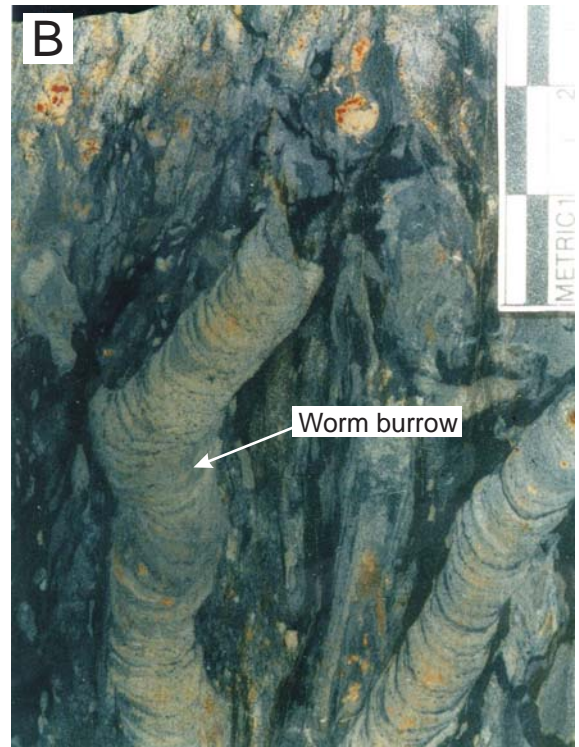
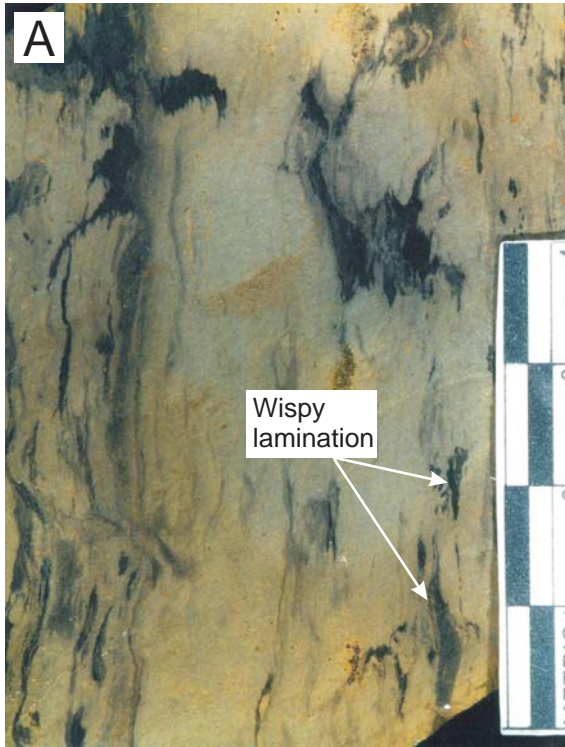


Table 3.1 Fossil age dates for Brewery Creek lithologies. Age data was sourced from Orchard (1993). T.J. Bremner collected the samples and recorded the lithology types. Sample sites are shown on figure 3.1.

GSC number	Sample location N E		UTM zone	Lithology	Mapped as	Fossils	Age
C-211101	7108500	635800	7	Limestone	Steel Fm.	Echinoderm fragments Stromatoporoid <i>Catenipora</i> sp. <i>Favosites</i> sp. <i>Palaeofavosites</i> sp. <i>?Striapore</i> sp. <i>"Thamnopora"</i> sp.	Silurian
C-211105	7106450	634600	7	Chert	Steel Fm.	Radiolarians <i>Entactinia</i> sp.	Silurian -Devonian
C-211108	7104600	637700	7	Limestone	Brewery unit	Conodonts <i>Polygnathus</i> sp.	Early Devonian
C-211110	7104800	636400	7	Limestone	Brewery unit	Conodonts <i>Panderodus</i> sp. <i>Pandorinellina exigua</i> <i>Polygnathus</i> sp.	Early Devonian
C-211111	7104600	636500	7	Limestone	Brewery unit	Conodonts <i>Icriodus</i> sp.	Devonian

The Steel Formation at Brewery Creek is moderately resistant to weathering and commonly forms hills and ridges. This Formation has been deformed by numerous open to tight folds with wavelengths from centimetres to 10's of metres. A structural thickness of 120 – 150 m has been estimated for the Steel Formation from cross-section (Figure 3.1).

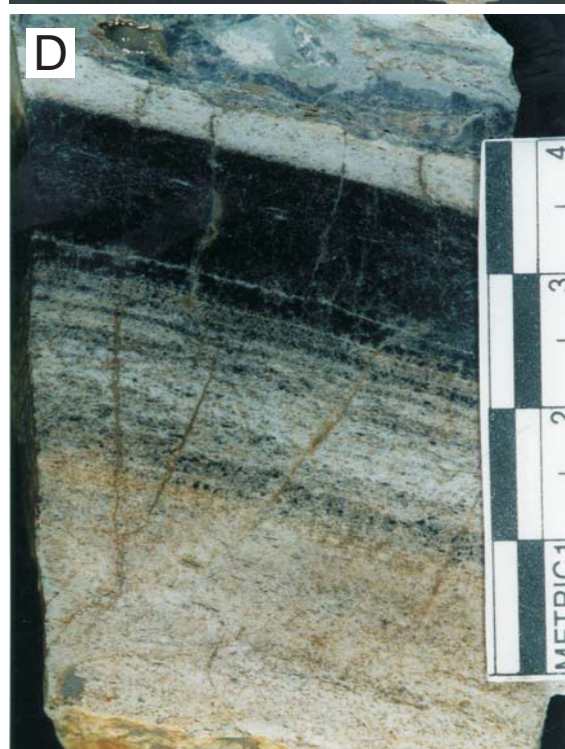
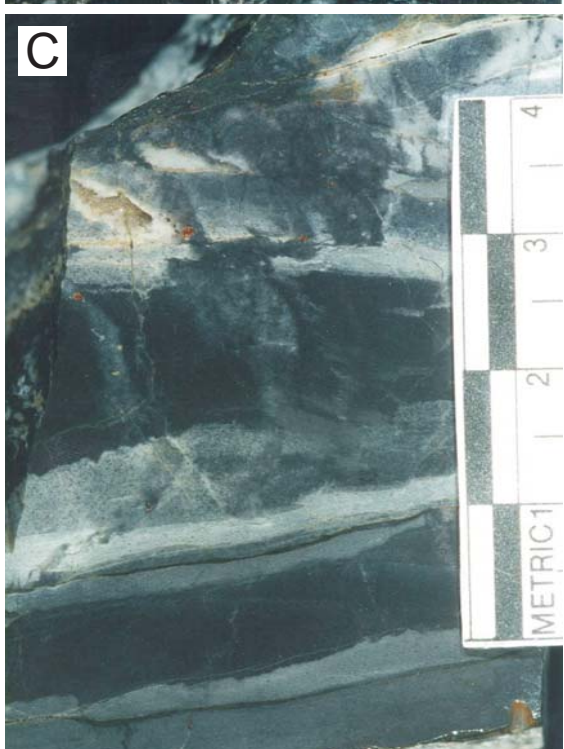
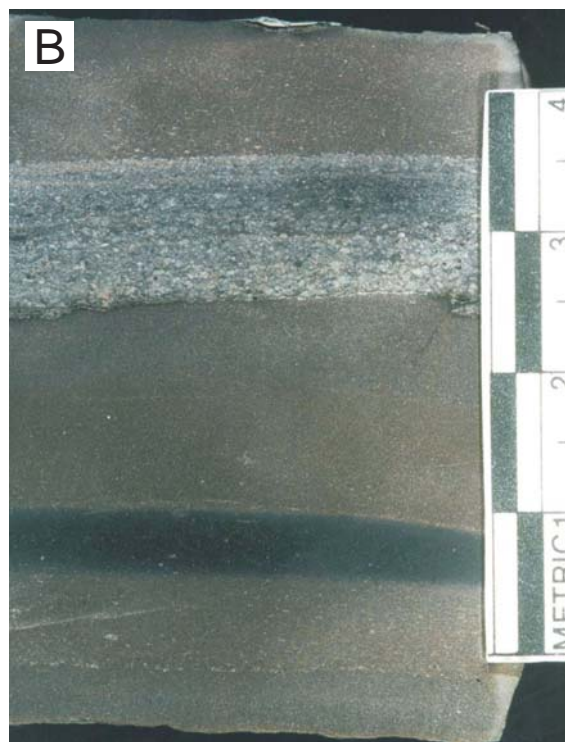
Brewery unit (New)

Tan weathered siltstone with interlayered beds of black chert and bioclastic limestone, black bioclastic limestone (beds 1 – 5 cm thick) containing segments of crinoid stems (1 - 2 mm in diameter), black bioclastic limestone with black chert layers (beds 1 – 5 cm thick), black chert with white fossiliferous/ calcareous layers that displays a distinctive banded appearance (beds 1 – 3 cm thick), and black chert (beds 1 – 7 cm thick) (Figure 3.7) occur throughout the southern part of the Brewery Creek property (Figure 3.1). These units were previously undocumented at Brewery Creek and are henceforth informally referred to as the Brewery unit.

The Brewery unit is previously unrecognised within the Selwyn Basin stratigraphy. This unit lies between the Steel Formation and Earn Group (Figure 3.2), an unconformity throughout much of the Selwyn Basin (Murphy, 1997; Gordey and Anderson, 1993), and display a marked contrast to the monotonous succession of tan weathered wispy laminated siltstone, shale and mudstone of the Steel Formation and the heterogeneous siliciclastic, and variably carbonaceous rocks of the Earn Group. This distinctive interval is named after Brewery Creek, which is a tributary of the South Klondike River and located to the east of the type section. A complete section of Brewery unit was not observed within the Brewery Creek property, thus the type section is defined as the units that outcrop along the road from Blue Pit to the Classic Zone between 7104800N - 63685E and 7104210N – 63768E (Figure 3.1).

The Brewery unit is interpreted to conformably overlie the Steel Formation with the transition characterised by wispy-laminated chert. The upper boundary of the Brewery unit was not seen, however, conglomerate in the overlying Earn Group and the absence of this unit elsewhere in the Selwyn Basin suggests that the contact is most likely unconformable. Rocks of the Brewery unit have been deformed by numerous m-scale tight to open folds. The structural thickness of this unit is uncertain but cross sections suggest that the Brewery unit may be up to 200 m thick (Figure 3.1). Conodonts identified in the Brewery unit suggest an Early Devonian age (Table 3.1).

Figure 3.7 **Photographs of selected lithologies from the Brewery unit.** (A) Clast supported limestone predominantly composed of segments of crinoid stems. (B) Interbedded calcareous sandstone (brown), chert (black), and limestone (white). (C) Interbedded layers of white and black chert. (D) Limestone (white) grading into chert (black). This example has been partly hornfelsed. Note the banding in photos B, C, and D, which is typical of the Brewery unit.



The formation and environment of deposition of the Brewery unit is largely constrained by the sedimentary units that surround this unit. Gordey and Anderson (1993) suggested that the Steel Formation and Earn Group were deposited in a quiet water, sub-wave base, oxygenated, off-shelf setting. They proposed that the nature of Earn Group clastic sediments is indicative of a submarine fan setting. In contrast to the clastic sediments of the Earn Group, the Brewery unit is rich with fossil fragments, mostly crinoid stems, interbedded with siltstone and chert layers. Thus, the absence of large sections of crinoid stem combined with the proposed depositional environment of the Steel Formation and Earn Group suggests that the fossiliferous layers of the Brewery unit may be bioclastic deposits derived from sedimentary gravity flows. Thus, the interbedded chert and limestone of the Brewery unit may have been deposited in an off-shelf submarine fan setting similar to the depositional setting of the Earn Group and may represent structural instability and minor uplift immediately prior to the major uplift associated with the deposition of the Earn Group.

Earn Group

A thick sequence of brown to black weathered, variably carbonaceous, siliciclastic rocks crop out through the centre of the Brewery Creek property (Figure 3.1). Diment (1996) and Diment and Craig (1999) correlated these lithologies to the Earn Group (Campbell, 1967; Gordey and Anderson, 1993; Murphy, 1997). The Earn Group at Brewery Creek primarily consists of shale (beds 0.5 - 1 cm thick, dark grey to black), siltstone (beds 0.5 – 5 cm thick, grey to brown), and fine to coarse grained sandstone (beds 1 - 30 cm thick, dark grey) interbedded with subordinate chert-pebble conglomerate (beds 20 cm thick to massive and contain multi-coloured sub-rounded pebbles up to 10 cm across of Duo lake Formation), chert (beds 1 to 100 cm thick, dark grey), argillaceous siltstone (beds 0.5 – 2 cm thick, dark grey to black), graphitic shale (beds 0.5 to 1 cm thick, black) and volumetrically minor bedded barite (beds 2 cm thick, white to light grey) (Figure 3.8).

Throughout much of the Selwyn Basin the Earn Group unconformably overlies the Steel Formation (Gordey and Anderson, 1993; Murphy, 1997), however, at Brewery Creek the Earn Group is interpreted to unconformably overlie the Brewery unit. The Earn Group is the youngest sedimentary unit outcropping at Brewery Creek. No age determinations were made for Earn Group strata at Brewery Creek but Campbell (1967) suggested that deposition of the Earn Group extended from the Devonian into the Early Carboniferous.

Figure 3.8 Photographs of selected lithologies from the Earn Group. (A)

Deformed argillaceous shale (black) interbedded with chert (tan). Thick sections of carbonaceous sediments are characteristic of the Earn Group. (B) Finely laminated siltstone. (C) Chert pebble conglomerate with multi-coloured clasts of chert. (D) Strongly folded bedded barite. This unit displays numerous tight folds that are otherwise only seen in the Rabbitkettle Formation at Brewery Creek.



The Earn Group at Brewery Creek is generally recessive, though more resistant portions (i.e. conglomerate) locally form hills and ridges. The Earn Group commonly contains muscovite, this mineral was not observed in the underlying sedimentary rocks. Earn Group strata have been highly disrupted by numerous, tight, cm- to km-scale folds and the destruction of the primary bedding fabric by strong shearing was noted in several locations. The minimum structural thickness of the Earn Group is interpreted from cross-section to be 300 m. However, extensive outcrop in the western portion of the Brewery Creek property suggests that the Earn Group may be more than 1 km thick (Figure 3.1).

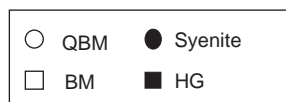
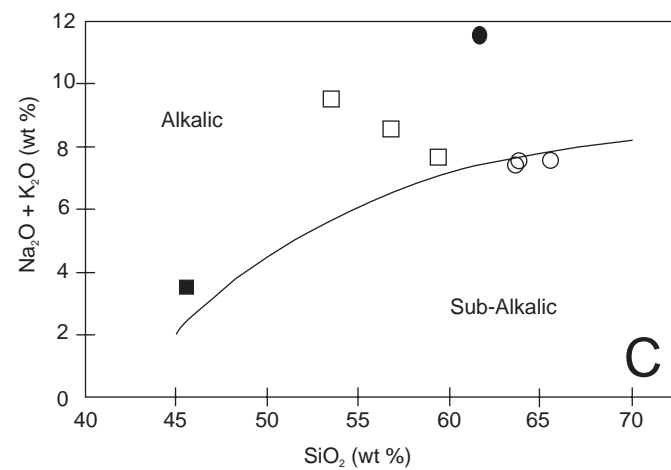
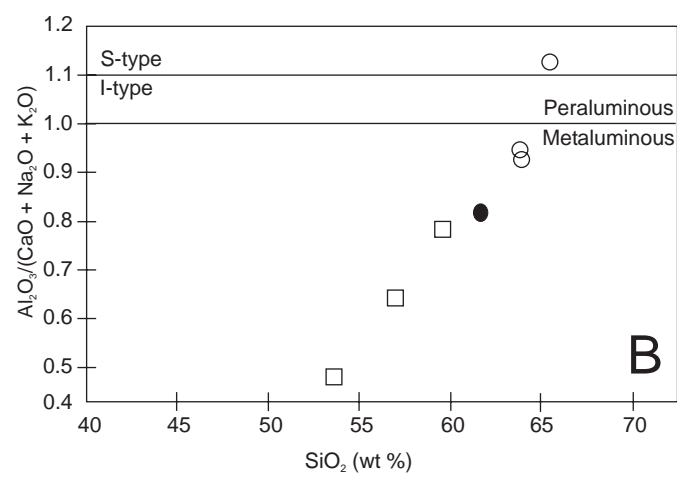
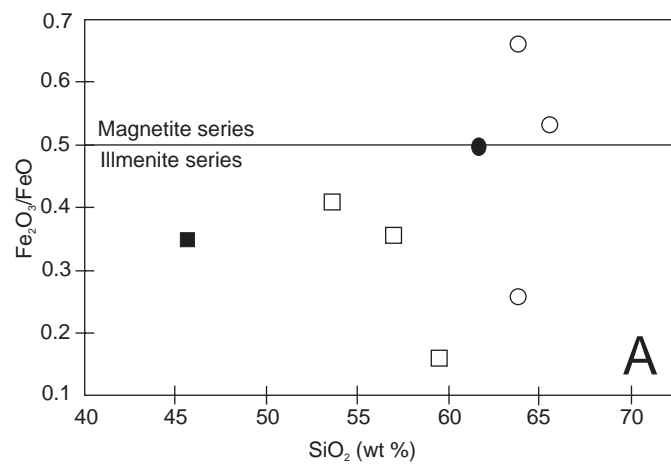
3.3 Intrusive rocks

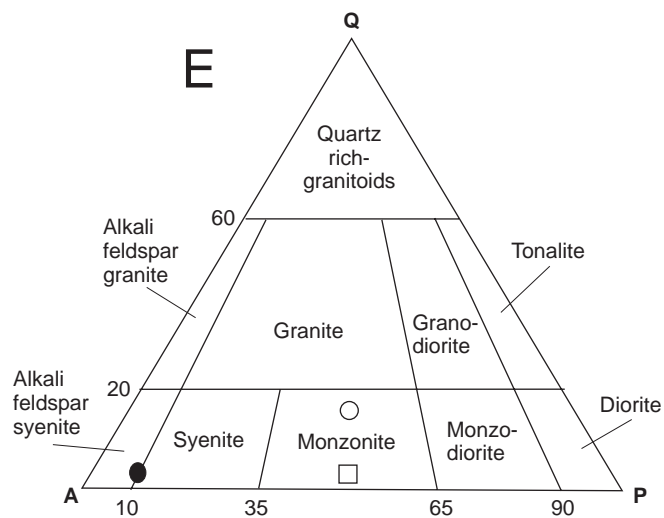
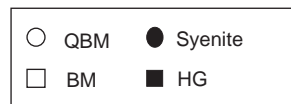
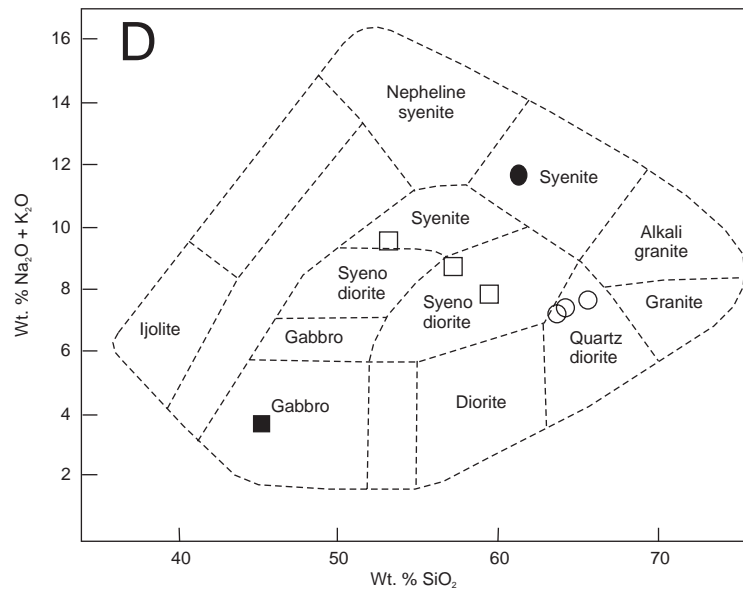
TPS magmatic rocks (ca. 94 – 90 Ma) have intruded along the northern Selwyn Basin (Figures 2.3 and 2.4) in a broadly east trending, 550 km long belt that extends from the Tombstone Range north of Dawson City to the Yukon and Northwest Territories border (Lang et al. 2000b; Mortensen et al., 2000). A number of predominantly reduced, alkalic, and metaluminous I-type intrusions (Figure 3.9 and Appendix 3) crop out across the Brewery Creek property. These intrusions can be classified using I.U.G.S. nomenclature (Anon, 1973) as monzonite, syenite, and hornblende gabbro or geochemically (Miyashiro, 1978) as syeno-diorite and quartz diorite, syenite and gabbro (Figure 3.9). The intrusive rocks at Brewery Creek are herein referred to as quartz - biotite monzonite, biotite monzonite, syenite and hornblende gabbro. The composition and age (ca. 90 – 92 Ma, Lang et al., 2000b; and 91.4 Ma, unpublished Geological Survey of Canada date) of these intrusions suggests that they are part of the Tombstone Plutonic Suite.

Quartz - biotite monzonite

Quartz - biotite monzonite (QBM) outcrops through the central part of the property as a series of NW and E trending sills that vary in thickness from less than 1 m to more than 1 km and extend for over 12 km along strike. The QBM sills are fine- to medium-grained and generally porphyritic but may also be megacrystic and locally equigranular. The sills have a fine-grained, grey to grey-green coloured groundmass that contains phenocrysts of plagioclase (25 - 30 % and up to 1 cm long; An₄₀₋₅₀), alkali (K) feldspar (20 - 25% and up to 3 cm long), biotite (20 - 25 % and 1 – 5 mm across), quartz (5 to 10 % up to 1 cm across), pyroxene (hedenbergite with lesser diopside; 5 - 10 % and up to 2mm long), hornblende (5 - 10 % and up to 5mm long), and trace

Figure 3.9 The geochemical signature of TPS intrusive rocks at Brewery Creek. Graphs A - C illustrate the variation in oxidation state (A), aluminium saturation index (B), and alkalinity (C) and respectively show that TPS intrusive rocks at Brewery Creek are typically reduced, metaluminous, and alkalic to sub-alkalic. Graphs D and E classify the intrusions geochemically (D; Miyashiro, 1978) and mineralogically by using the IUGS method (E; Anon, 1973). Geochemical data used to produce the graphs is presented in F. QBM = quartz -biotite monzonite, BM = biotite monzonite, HG = hornblende gabbro.





F	Syenite	QBM	QBM	QBM	BM	BM	BM	HG
SiO_2	61.66	64.05	65.74	64.10	56.66	53.45	59.48	45.07
TiO_2	0.56	0.58	0.54	0.57	0.89	0.85	0.76	1.88
Al_2O_3	15.90	14.72	14.95	14.64	13.58	12.48	14.95	14.74
FeO	3.04	2.57	2.74	3.25	5.31	5.61	5.33	9.13
Fe_2O_3	1.51	1.70	1.46	0.84	1.92	2.28	0.85	3.18
MnO	0.10	0.08	0.09	0.08	0.15	0.16	0.12	0.20
MgO	1.25	1.97	1.85	2.02	4.06	5.00	3.29	10.83
CaO	2.79	3.38	1.98	3.53	6.05	8.30	5.05	8.16
Na_2O	3.45	2.43	2.78	2.71	1.75	1.30	2.08	1.88
K_2O	8.16	4.99	4.70	4.60	6.67	8.16	5.79	1.54
P_2O_5	0.21	0.25	0.25	0.25	0.52	0.70	0.45	0.26
LOI	0.44	2.90	2.35	2.74	1.06	0.90	1.04	2.28
Total	99.07	99.63	99.44	99.33	98.62	99.19	99.19	99.15

titanite (Figure 3.10 and Appendix 4). In contrast to other intrusions at Brewery Creek QBM intrusions are typically oxidised, sub-alkalic intrusions that trend across the metaluminous-peraluminous boundary (Figure 3.9). The contacts between QBM sills and the host Earn Group sedimentary rocks are sharp but highly irregular and QBM intrusions commonly contain rafts of argillaceous sedimentary rock as xenoliths. The linear nature of these intrusions combined with intrusions hosted by shear zones suggests that sill emplacement may have been partly controlled by pre-existing or syn-intrusive structures.

Biotite monzonite

Biotite monzonite (BM) outcrops through the central part of the property as a series of NW and E trending sills and dykes that vary in thickness from less than 1 m to more than 200 m. BM sills and dykes are generally fine-grained and commonly porphyritic. These intrusions display a fine-grained, grey groundmass that contains phenocrysts of plagioclase (20 - 40% and up to 2 cm long; An₄₀₋₅₀), alkali (K) feldspar (10 - 40% and up to 2 cm long), biotite (20 - 35% and up to 5 mm across), hornblende (10 - 20% and up to 5 mm long), pyroxene (hedenbergite with lesser diopside; 5 - 10 % and up to 2 mm long), pyrrhotite (less than 2%), localised mafic xenoliths (up to 3 cm across) and rare quartz and apatite (Figure 3.11 and Appendix 4). BM intrusions are characterised by a paucity of quartz in hand specimen. These intrusions generally display regular margins and were not observed to enclose rafts of sedimentary rock. A notable feature of the BM intrusions is that they commonly contain pyrrhotite. This sulphide was not identified in the QBM sills and only rarely in syenite intrusions. In the Golden Pit a BM dyke crosscuts a QBM sill.

Syenite

Syenite plutons outcrop in several areas across the southern part of the Brewery Creek property. The largest mappable unit is approximately 4 km long by 2 km wide and may be more extensive at depth as indicated by a broad contact aureole (Figure 3.1). The syenite intrusions generally display a medium- to coarse-grained equi-granular texture, however, some outcrops contain alkali feldspar phenocrysts two or three times larger than other crystals in the rock. These intrusions are composed of alkali (K) feldspar (65 - 85% and 1 – 2 cm long), biotite (5 - 20% and up to 3 mm across), hornblende (5 - 20% and up to 3 mm long), pyroxene (diopside-hedenbergite; 5 – 10% and up to 4 mm across), plagioclase (less than 5%; An₄₁₋₄₆), titanite (less than 1%), and trace apatite and ilmenite (Figure 3.12 and Appendix 4). In several thin sections hornblende

Figure 3.10 Photographs of quartz - biotite monzonite intrusions. (A) Typical quartz - biotite monzonite with zoned plagioclase phenocrysts and quartz eyes. (B) Clasts of shale (black) within monzonite. (C) The pit walls of most of the pits at Brewery Creek are comprised of monzonite that contains large rafts of argillaceous shale. The scale bar in (C) has metre intervals.

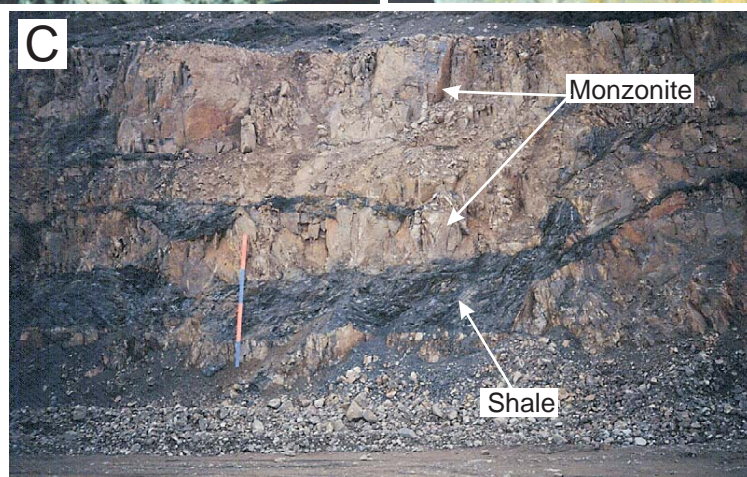
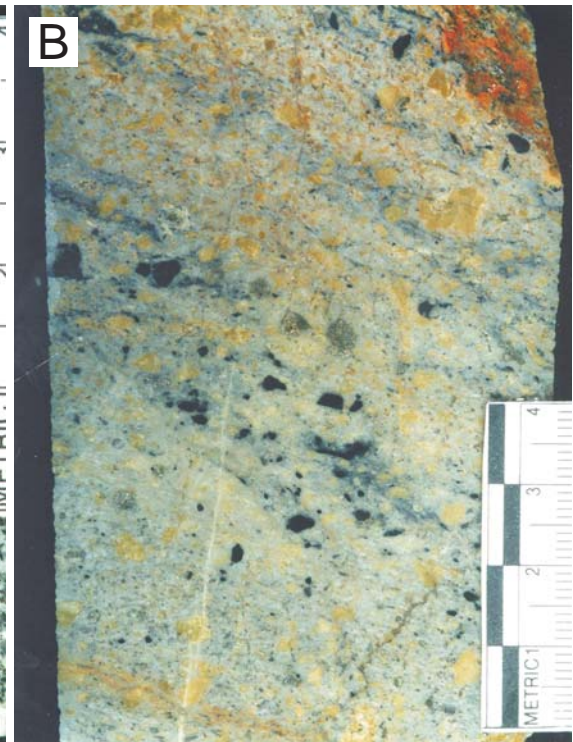
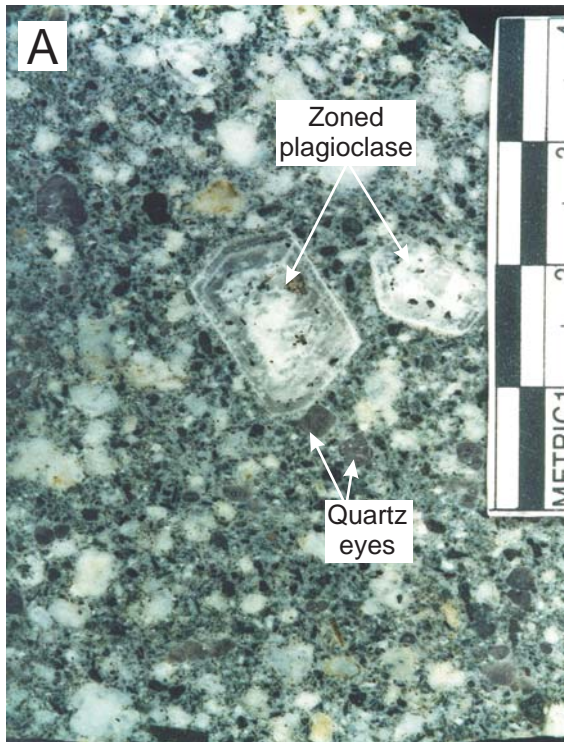


Figure 3.11 Examples of biotite monzonite. (A) A typical example of this variety of monzonite. Note the absence of quartz eyes. (B) Biotite rich xenoliths are a common feature of biotite monzonite. Photomicrographs in (C) cross polarised and (D) plane polarised light show the presence of zoned and twinned plagioclase, abundant biotite and minor pyroxene. Photomicrographs are of an area ~ 2 cm long.

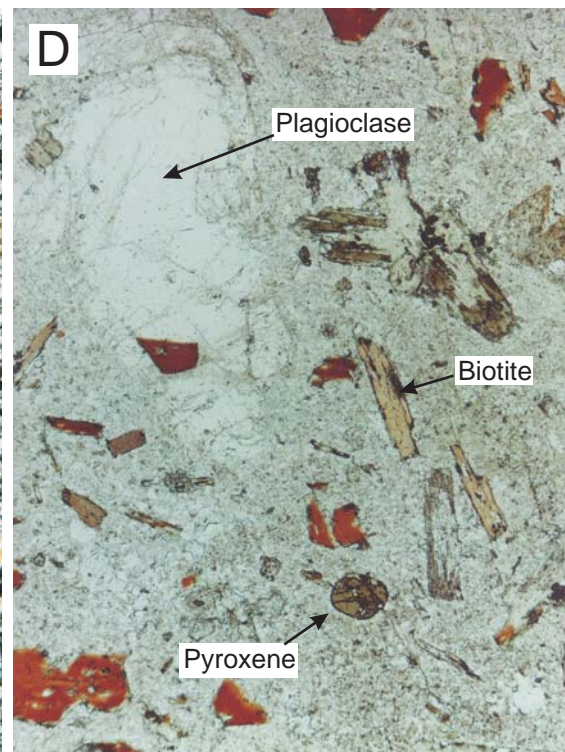
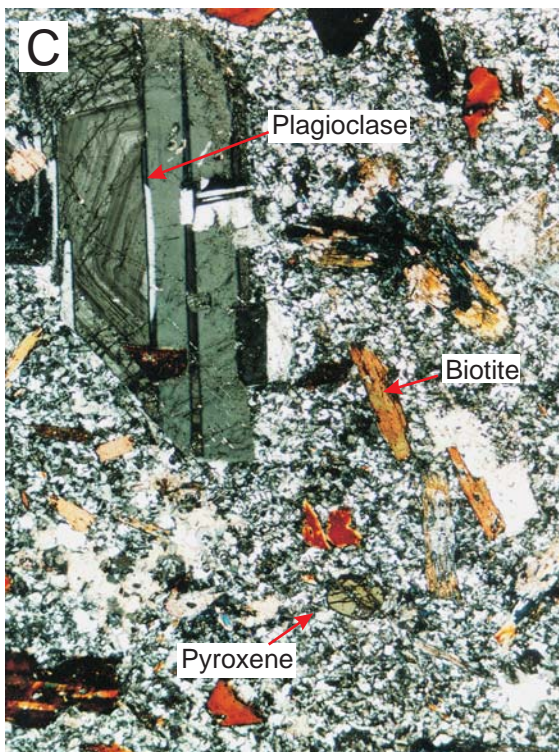
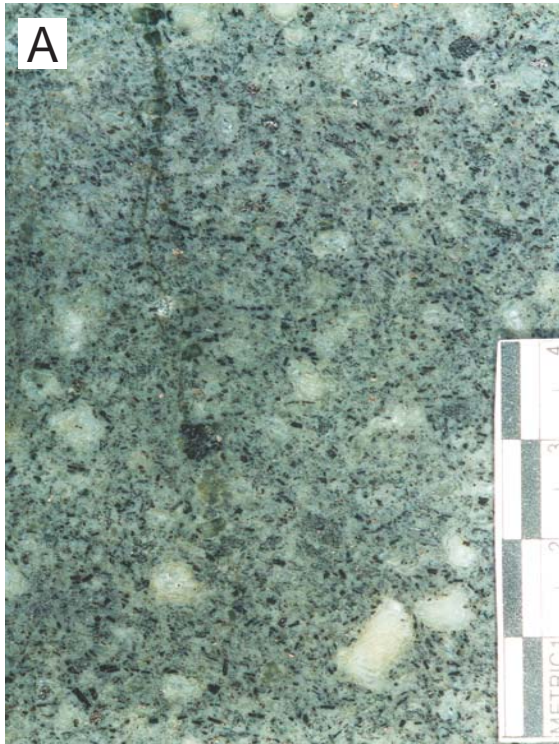
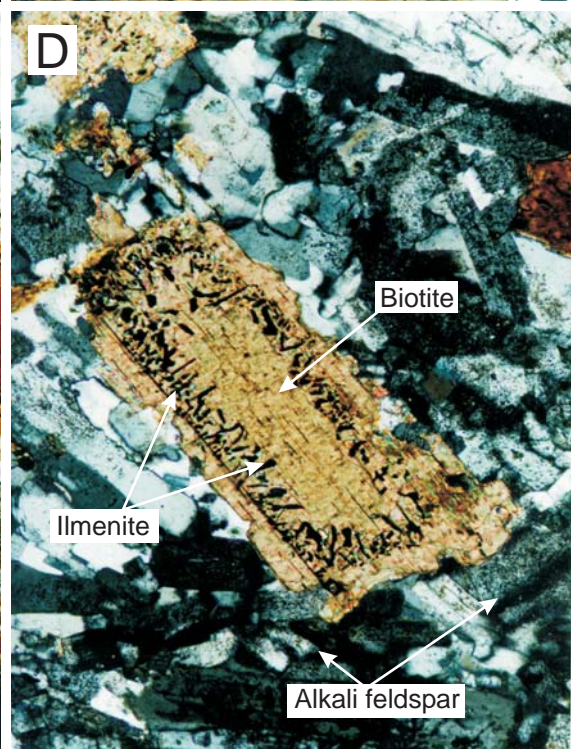
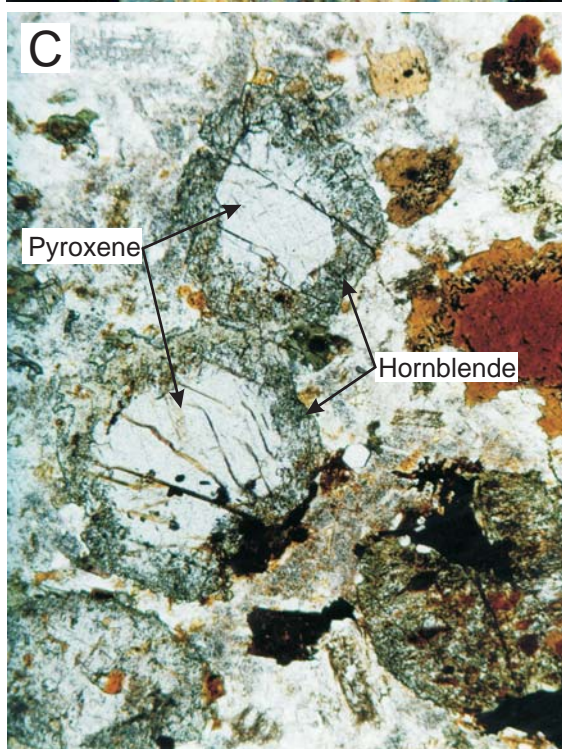
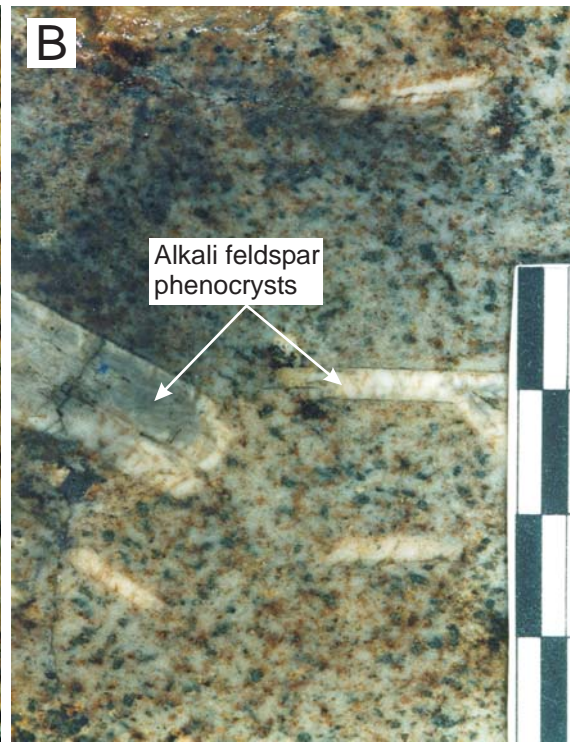
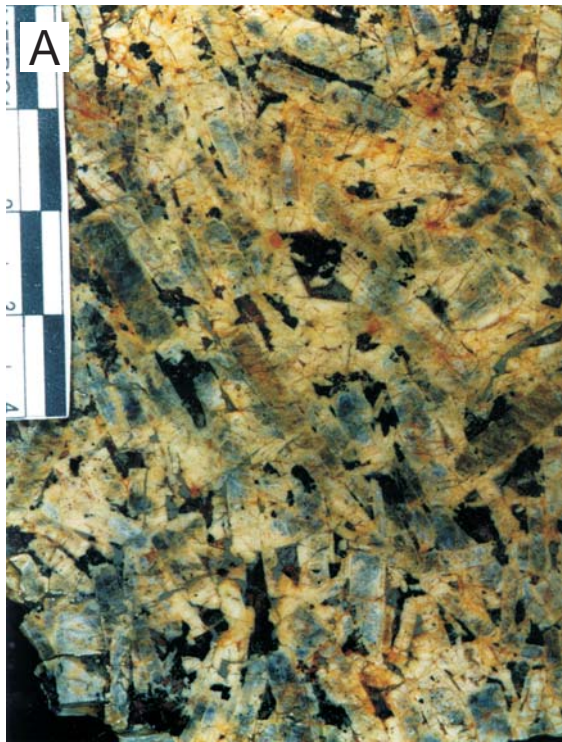


Figure 3.12 Examples of Syenite at Brewery Creek. (A) A photograph of syenite that is typical at Brewery Creek. (B) A photograph of porphyritic syenite with 2 – 3 cm long alkali feldspar phenocrysts. (C) A photomicrograph of hornblende overgrowing pyroxene (either diopside or hedenbergite). Field of view is approximately 1cm. (D) a photomicrograph of ilmenite hosted by a biotite crystal. The groundmass is dominated by alkali feldspar. Biotite crystal is approximately 1.5 mm long.



was observed to overgrow hedenbergite and/or diopside. Biotite phenocrysts containing numerous inclusions of ilmenite were also noted.

Syenite intrusions commonly contain large xenoliths of intensely hornfelsed sedimentary rock and display irregularly developed endoskarn (see section 3.4). A BM dyke was observed to crosscut a syenite pluton in the Classic Zone (R. Diment, pers. com., 1999), however, the relationship between the syenite intrusions and the QBM sills is uncertain.

Hornblende gabbro

Rare hornblende gabbro occurs as dykes up to 1 m thick in the Golden pit and locally in drill core. The gabbro dykes are fine-grained and equi-granular with phenocrysts typically 1 - 1.5 mm across. The hornblende gabbro dykes are aluminium and calcium rich and are composed of hornblende (alumno-tschermakite; 60 - 70 %), plagioclase (30 - 40 %; An₇₉₋₈₆), biotite (5 %), pyroxene (Hedenbergite; 1 %), trace apatite and titanite (Figure 3.13 and Appendix 4). Hornblende gabbro dykes were observed to crosscut both the QBM and BM, however, it is uncertain if this intrusive phase can be correlated to the TPS or if it represents a younger magmatic event.

3.4 Metamorphism

Sub-greenschist facies regional metamorphism and locally developed contact metamorphism occurs throughout the Selwyn Basin (Murphy, 1997; Stephens et al., 2000) with conodont colour alteration indices and metamorphism of organic matter indicating a maximum temperature of about 300°C (Gordey and Anderson, 1993). Across the Brewery Creek property, rocks that lie outside the contact aureoles of TPS intrusions show little to no metamorphism. The oldest rocks on the property, the Rabbitkettle Formation, have been locally metamorphosed to a talc-carbonate phyllite while younger rocks, including calcareous siltstone of the Steel Formation and limestone of the Brewery unit show no petrographic evidence of metamorphism.

In contrast, rocks of the Steel Formation and Brewery unit within the contact aureoles of TPS intrusions are generally strongly metamorphosed. The contact aureole of the syenite pluton in the southern portion of the property is characterised by a calc-silicate mineral assemblage that includes grossular garnet, diopside, titanite, scapolite, calcite, biotite, microcline, quartz, alkali feldspar, and chlorite (Figure 3.14 and Appendix 4).

Figure 3.13 Examples of Hornblende gabbro from Brewery Creek. (A) A photograph of a hornblende gabbro dyke (dark) cutting biotite monzonite in drill core. (B) A photomicrograph of the example described in (A) above with hornblende gabbro at the top. Note the sharp contact between the two intrusive rocks and the abundant hornblende in the hornblende gabbro. Photomicrograph is of an area ~ 2 cm long.

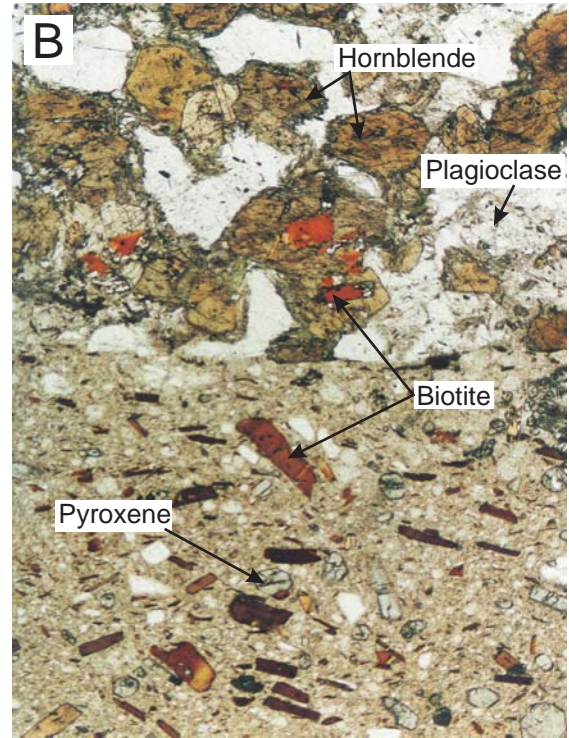
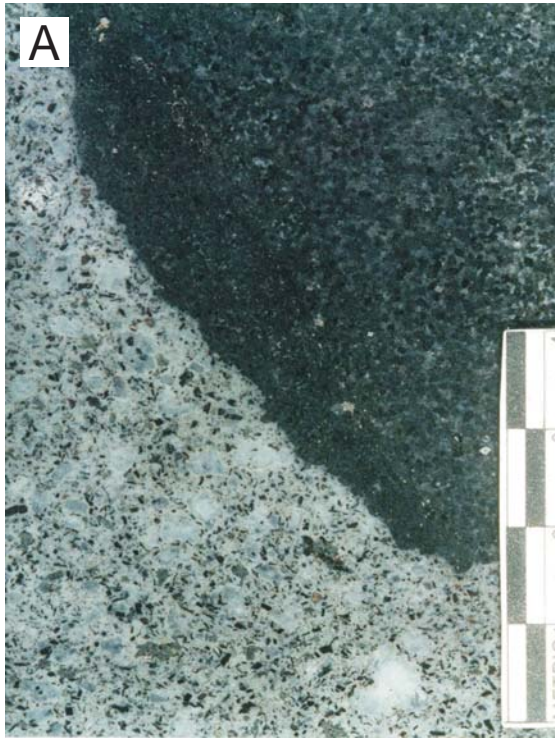
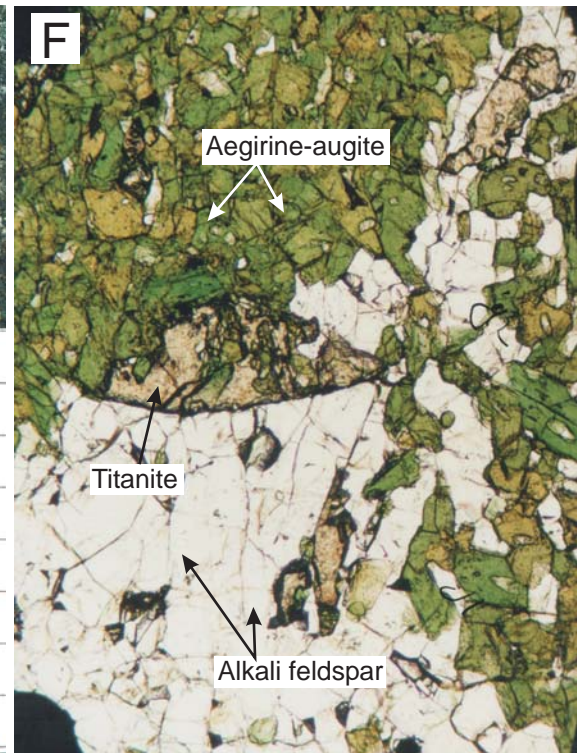
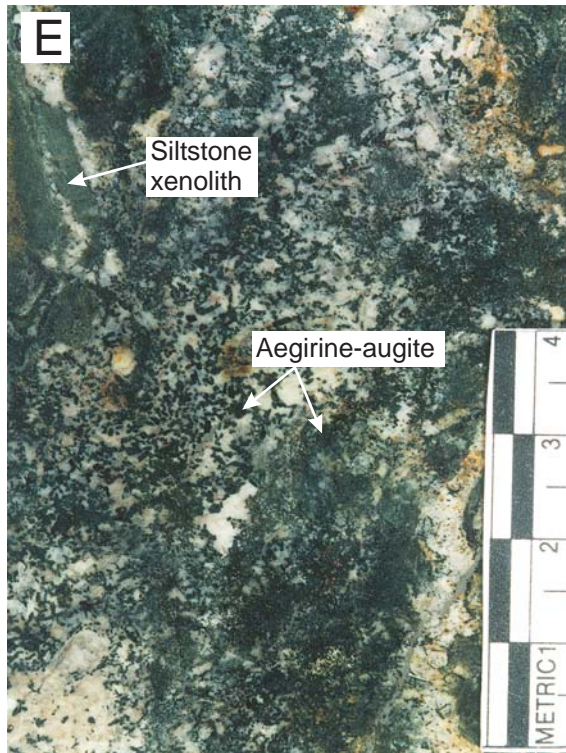


Figure 3.14 Examples of contact metamorphosed rocks at Brewery Creek. (A) and (B) are photographs of metamorphosed Steel Formation, the difference thought to result from the calcium content of the original sediment. The sample in (A) is dominantly comprised of quartz whilst (B) contains hedenbergite (green colour), wollastonite, titanite, microcline, quartz, calcite and tourmaline. (C) and (D) are photographs of metamorphosed Brewery unit and are composed of grossular garnet (red-pink colour), diopside (green colour), titanite, scapolite, calcite, biotite, microcline, quartz, and chlorite. Note the differences in morphology between metamorphosed Steel Formation and Brewery Unit. This helps with discrimination in the field. (E) and (F) are images of endoskarn from the Classic Zone syenite unit. Note the xenolith of siltstone in (E) and the numerous crystals of aegirine-augite. (F) A photomicrograph that shows titanite and abundant aegirine-augite in thin section. The field of view is ~ 1.5 cm.



The syenite pluton has also been metamorphosed to endoskarn and contains aegirine-augite, hornblende, titanite, microcline, calcite, alkali feldspar, and apatite. Elsewhere at Brewery Creek contact aureoles occur as distinct silicified or calc-silicate hornfels zones at the contact between monzonite intrusions and the Steel Formation (Figure 3.14). The aureoles commonly contain hedenbergite, wollastonite, titanite, microcline, quartz, calcite and rare pyrrhotite and tourmaline.

Along the Reserve Trend, several monzonite sills intrude siliciclastic and variably carbonaceous Earn Group sedimentary rocks. Open cut mining has exposed a number of contacts between monzonite sills and the Earn Group; however, most of these exposures show little evidence of contact metamorphism. One occurrence of contact metamorphosed Earn Group shale immediately adjacent to a monzonite sill was found in drill core from under the Fosters Pit and contained a number of relict andalusite porphyroblasts up to 1 cm long (Figure 3.15). The apparent lack of contact metamorphism in most of the Earn Group is best explained by the absence of minerals susceptible to the metamorphic processes (i.e. carbonate minerals, which are common in the Steel Formation and Brewery unit, or aluminosilicate minerals) that were operating during the emplacement of TPS intrusions. The one occurrence of Earn Group shale with andalusite porphyroblasts may represent a layer that contained a high percentage of aluminium. Furthermore, the marked difference between contact metamorphosed Steel Formation and Brewery Unit compared to the Earn Group probably results from the calcareous nature of the Steel Formation and Brewery Unit favourably reacting with heat and fluids from intrusions.

Elsewhere in the Selwyn Basin TPS intrusion contact aureoles are commonly characterised by the presence of abundant pyrrhotite (Hart et al., 2000). At Brewery Creek, TPS intrusion contact aureoles within the Steel Formation contain variable amounts of pyrrhotite and pyrite. A sample of hornfelsed siltstone collected from the Schooner Zone is comprised of approximately 5% pyrrhotite while most other samples of hornfelsed siltstone contain no sulphide minerals. Trace amounts of chalcopyrite and sphalerite were also identified in hornfelsed Steel Formation containing abundant tremolite.

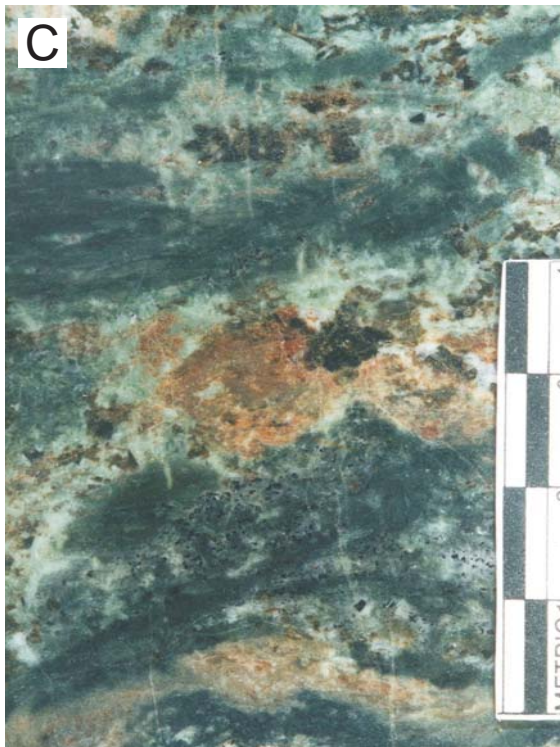
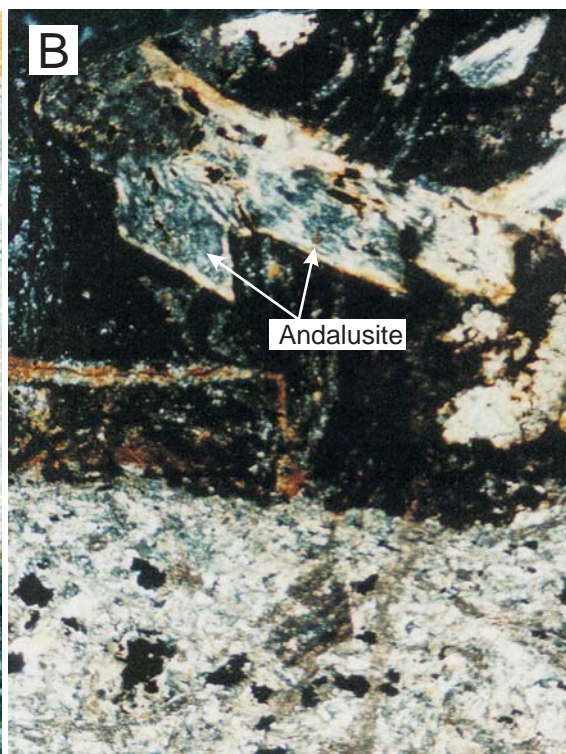
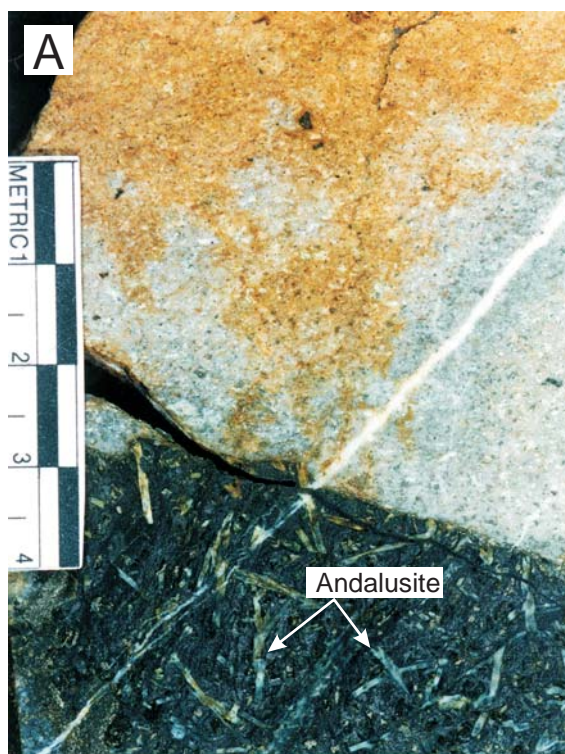


Figure 3.15 Relict andalusite porphyroblasts in Earn Group carbonaceous shale. (A) and (B) are images of the only petrographic evidence of contact metamorphosed Earn Group along the Reserve Trend. The porphyroblasts have been altered to carbonate but their distinctive shape in thin section is indicative of andalusite. The lighter coloured half of the samples is monzonite whilst the darker portion is carbonaceous Earn Group shale. The photomicrograph (B) is approximately 3 cm long.



3.5 Deformation

Sedimentary and volcanic rocks that crop out at Brewery Creek have been multiply deformed and record a structural history that has been punctuated by several episodes of brittle and ductile deformation. Faults and folds of all scales are present, however, low-grade (absent?) regional metamorphism combined with heterogeneous, mostly low strain resulted in poor development of cleavage or other micro-scale fabrics. The overall structure of the property is that of a NNE trending arch of thrust sheets. The rocks in each thrust sheet have been deformed into upright to steeply inclined, open to tight, variably NE, E, NW trending folds. Eight distinct structural events have been recognised at Brewery Creek (henceforth referred to as D-stages 1 to 8 to avoid confusion with mineral paragenesis stages); these are described below and their relationships are summarised in Figure 3.16. The age of events 1-6 can be constrained between the youngest deformed sedimentary rocks, the Devonian-Carboniferous Earn Group, and middle Cretaceous intrusive rocks that cut these events. D-stages 7 and 8 are post- middle Cretaceous as they cut TPS intrusive rocks; however, no upper age constraints were identified.

D-stage 1 - NW trending folds

The units comprising the SW-vergent thrust package described below are folded by upright to steeply inclined (72° to vertical) NW trending and variably NW and SE shallowly plunging ($0^\circ - 17^\circ$) folds (Figure 3.17). These folds are best seen in outcrop along the road from the Moosehead zone to North Slope. D-stage 1 folds may be open to tight with inter-limb angles of 112° to 14° . The folds vary in strike length from less 2 m to 500 m and in wavelength from 10 cm to 300 m. The units affected by D-stage 1 folding are bound by the D-stage 2 thrust fault, and trend perpendicular to the broad E-orientation of lithology immediately to the north and south of this fault. The original orientation of these folds is uncertain as they lie on the NW limb of a broad NNE trending open fold (D-stage 5 below). However, D-stage 1 trending folds do not show the effects of later D-stage 5 folding, probably as a result of the restricted distribution of D-stage 1 folds.

D-stage 2 - SW-vergent thrusting

The earliest faulting recognised at Brewery Creek is evidenced by the displacement of Rabbitkettle Formation, MCV, Duo Lake Formation and Steel Formation over the Earn Group at North Slope (Figure 3.1). The contact between the Devonian – Carboniferous

Figure 3.16 A schematic diagram illustrating the structural development of the rocks underlying the Brewery Creek property. (A) and (B) show two alternate hypotheses for juxtaposition of the Steel Formation against the Menzie Creek volcanic unit, which are an unconformity (A), or the development of a normal fault (B). (C) Illustrates property-scale folding (D-stage 3) of a pre-existing unconformity. (D) D-stage 3 folds are cut by thrust faults (D-stage 4). (E) The folds and thrusts are deformed into a broad fold (D-stage 5). (F) The development of strike slip faults (D-stage 6). (G) Emplacement of TPS intrusions. (H) Normal faulting (D-stage 7). (I) NW trending strike-slip faulting (D-stage 8). Note that D-stage 1 and D-stage 2 have are not illustrated on figure 3.16 as their occurrence is isolated and their relationships to deformations is uncertain.

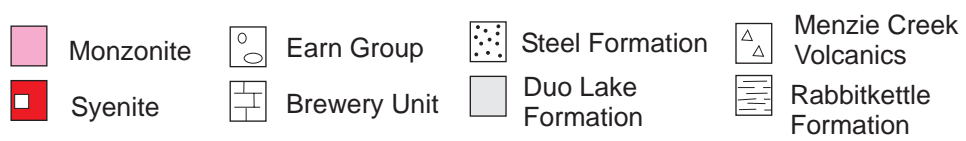
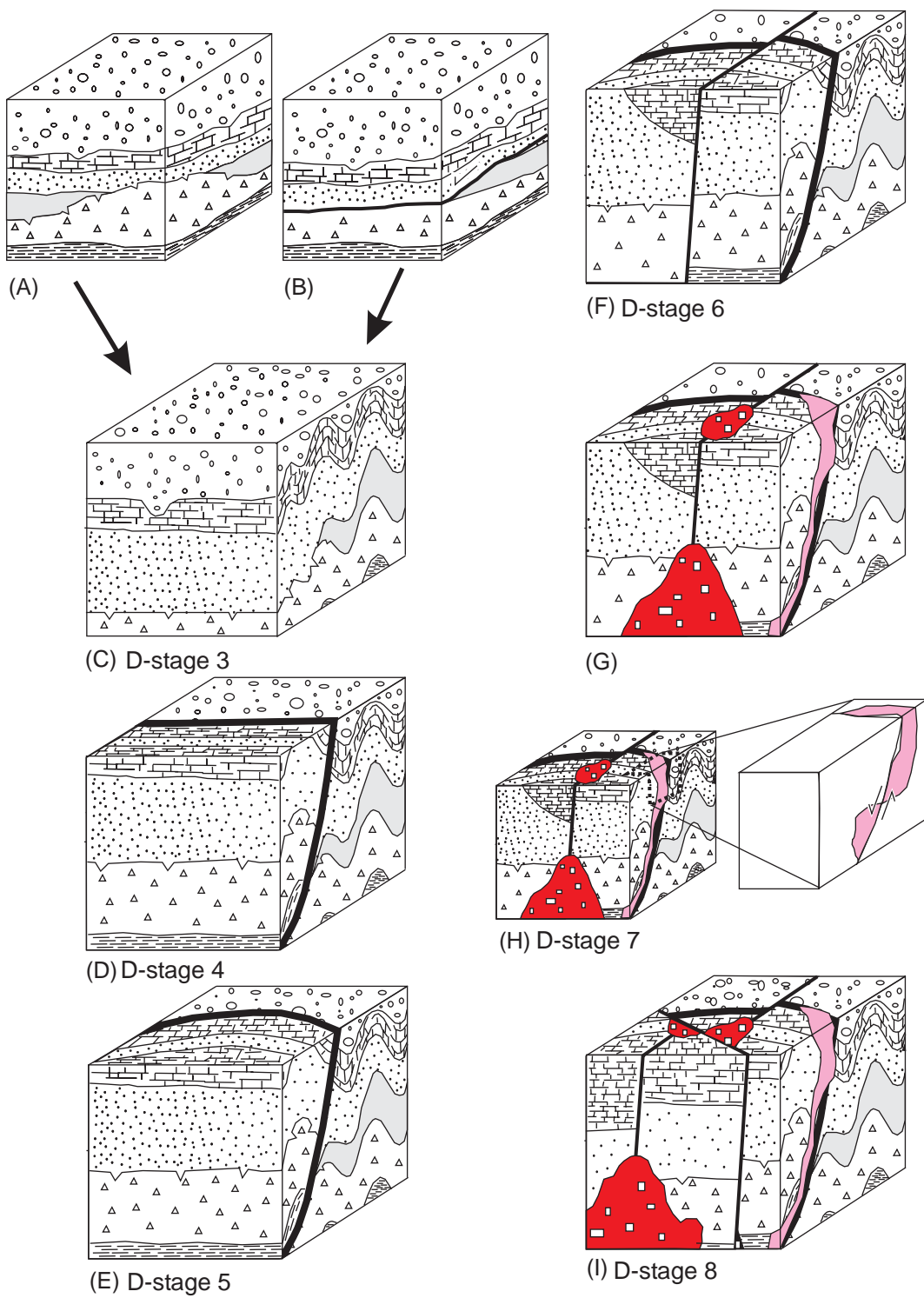
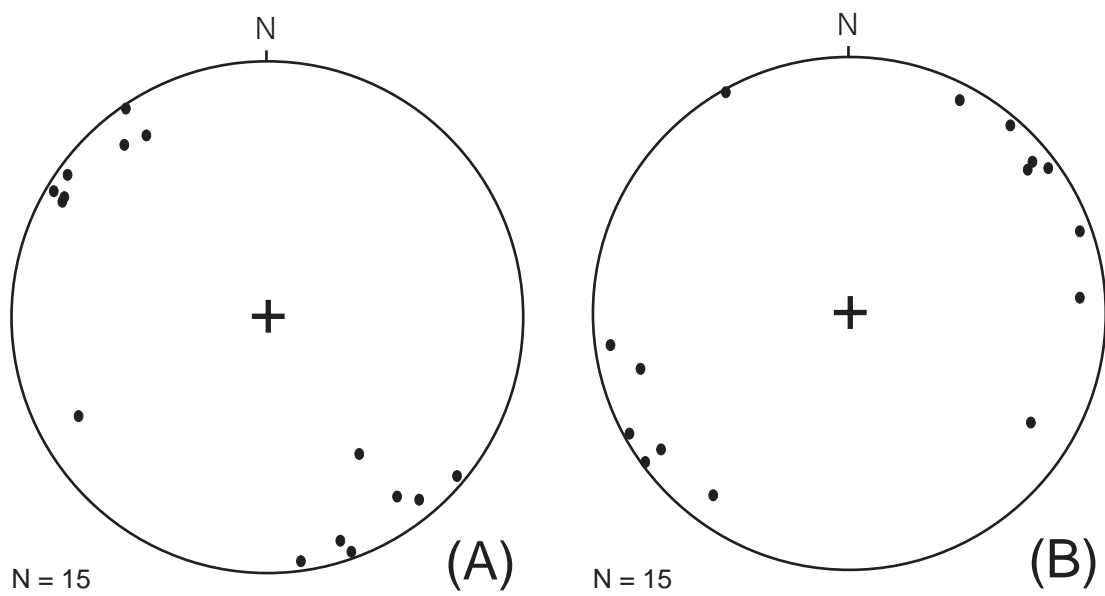


Figure 3.17 Graphic illustration of folding at North Slope (D-stage 1).

Stereographic plots show (A) the distribution of fold axis, and (B) the distribution of poles to axial planes of folds. The plots do not show any evidence of later folding that is obvious in Figure 3.18. A photograph of folded Rabbitkettle Formation is shown in (C). Note the geological hammer for scale.



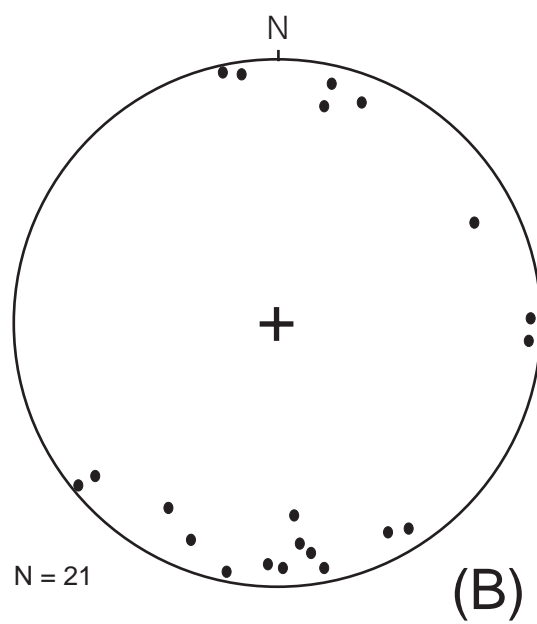
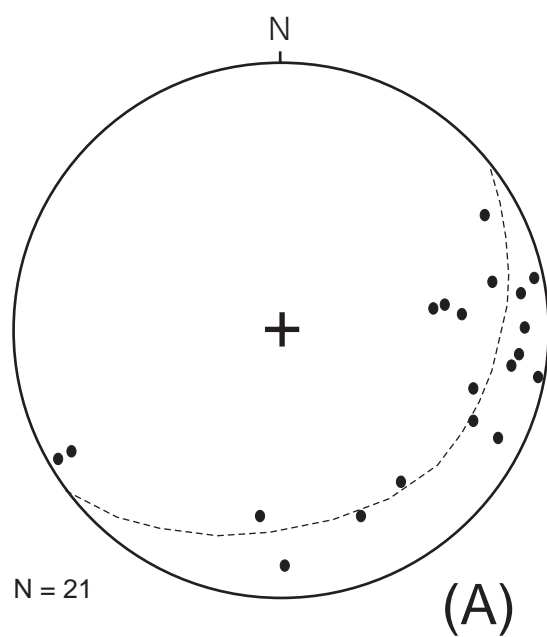
Earn Group and overlying Cambro-Ordovician Rabbitkettle Formation is interpreted to be a thrust fault. The present day orientation of this thrust package suggests SW vergence and is thus oriented perpendicular to other thrust faults identified on the property. The original orientation of this structure is uncertain as it lies on the NW limb of a broad NNE trending fold (D-stage 5 below). The contact of this thrust package with the underlying Earn Group displays a curved surface trace. Where exposed, the fault occurs as a 0.1-0.4 m wide zone of strongly brecciated and sheared rock that has been cut by several stages of quartz and carbonate veining. The thrust fault extends for more than 1 km along strike and is interpreted to dip moderately to the NE. The relative components of strike-slip and dip-slip movement along this thrust fault are unconstrained; however, lithological relationships (i.e. Rabbitkettle Formation overlying Earn Group) suggest an apparent dip-slip offset of approximately 800 m. The relationship of D-stage 1 and 2 to D-stage 3 below is uncertain because of limited exposure of rocks that have been affected by the earlier deformation.

D-stage 3 - km-scale folding

Steeply dipping (70° – 87°), NE-SW, E-W, and NW-SE trending (Figure 3.18), and shallow to moderate plunging (2° – 35°) folds deform most of the sedimentary and volcanic rocks at Brewery Creek. These folds were observed throughout the property with several examples of this fold type cropping-out along the road from the North Slope zone to the Lucky pit. At property-scale, D-stage 3 folds control much of the map pattern and have produced the km-scale repetition of lithologies and apparent structural thickening that is evident on Figure 3.1.

D-stage 3 folds may be tight to open with inter-limb angles of 26° to 90° . These folds vary in strike length from 5 m to 2 km and in wavelength from 50 cm to 600 m. D-stage 3 folds verge to the NW, N, and NE with respect to bedding which trends NE, E, and NW. The variation in D-stage 3 fold axis and axial plane trends is interpreted to result from later property-scale folding. Cleavage and other ductile micro-structural fabrics associated with this deformation were rarely observed, however, minor bedding parallel cleavage and boudinaged siltstone/sandstone beds in an argillaceous siltstone matrix were noted in some outcrops. Faults cutting the core of D-stage 3 folds are common. This deformation event also produced local overturning.

Figure 3.18 **Graphic illustration of D-stage 3 folding across the Brewery Creek property.** Stereographic plots show (A) the orientation of fold axes, and (B) the orientation of poles to axial planes of folds. Note that in (A) the fold axis lie on a great circle indicating that D-stage 3 folds have been folded. A photograph of Brewery unit folded by a D-stage 3 fold is shown in (C). Note the pencil for scale.



D-stage 4 - km-scale thrusting

At a number of places across the Brewery Creek property the Silurian Steel Formation overlies Early Devonian Brewery unit or Devonian Earn Group (see cross-sections B-B' and C-C' on Map 1). Upright sedimentary younging within these units combined with marked differences in unit thickness suggests the presence of property-scale thrust faults. D-stage 4 thrust faults were rarely observed in outcrop. The best exposure is along the dead-end road immediately to the north of the large chert-pebble conglomerate body in the centre of the property (see Figure 3.1). D-stage 4 also produced the strong deformation evident in the argillaceous shale, shale and siltstone that crops out along the Reserve Trend. Where exposed, the D-stage 4 thrust faults manifest as 0.5 – 2 m wide zones of strongly sheared and brecciated rock. These zones variably comprise discrete graphitic fault planes (2-10 mm thick), irregularly developed shear foliation and fault breccias, cm-scale folds of clasts of sedimentary rock, and areas of partial to complete textural destruction of the host rock. Quartz veins and monzonite sills and dykes have also invaded the thrust faults. These thrust faults extend for more than 12 km along strike and display curved surface traces, which are interpreted to be a result of D-stage 5 folding.

D-stage 4 thrust faults trend broadly parallel to bedding and D-stage 3 fold axes. However, along strike they are often bedding discordant and were observed to juxtapose units with opposing dip (Figure 3.1) indicating that the faults post-date D-stage 3. The D-stage 4 fault set is broadly NE vergent and is interpreted to dip moderately to the SW. Although the amount of strike-slip movement along D-stage 4 thrust faults is uncertain, an apparent dip-slip movement of between 50 and 250 m is suggested by stratigraphic relationships.

It is important to note that D-stage 4 faults may represent the initial structural preparation of the Reserve Trend. The linear nature of TPS monzonite intrusions, combined with intrusions hosted within shear zones (Figure 3.10) suggests sill emplacement was at least partly controlled by pre-existing structures. Monzonite sills trend parallel to D-stage 4 thrust faults and probably used these faults as structural pathways during emplacement. Normal reactivation of D-stage 4 faults may also provide a mechanism for the development of some of the D-stage 7 structures, and for localising mineralisation. This is further discussed in chapter 7.

D-stage 5 - NNE trending fold development

A broad NNE trending fold of previously deformed lithology controls the overall distribution of rocks at Brewery Creek. The stage 5 deformation has folded D-stage 3 folds and D-stage 4 thrust faults (Figures 3.1 and 3.18). The D-stage 5 fold or similarly oriented structures were not observed in outcrop, this event was only identified by the map-scale distribution of lithologies, and the orientation of D-stage 3 fold axis and D-stage 4 thrust faults.

D-stage 6 - NE-SW oriented property-scale faulting

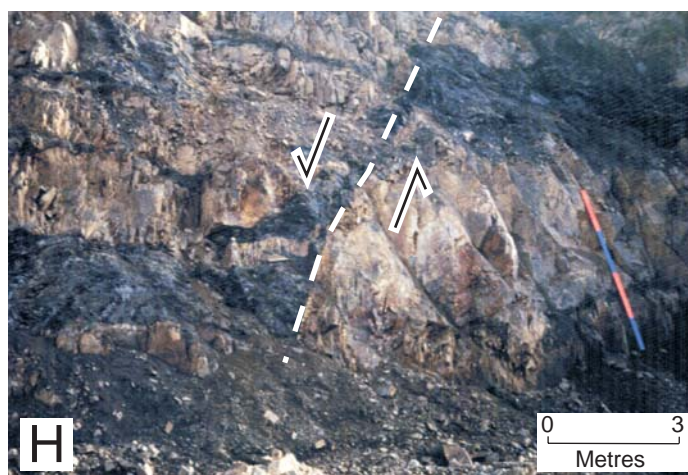
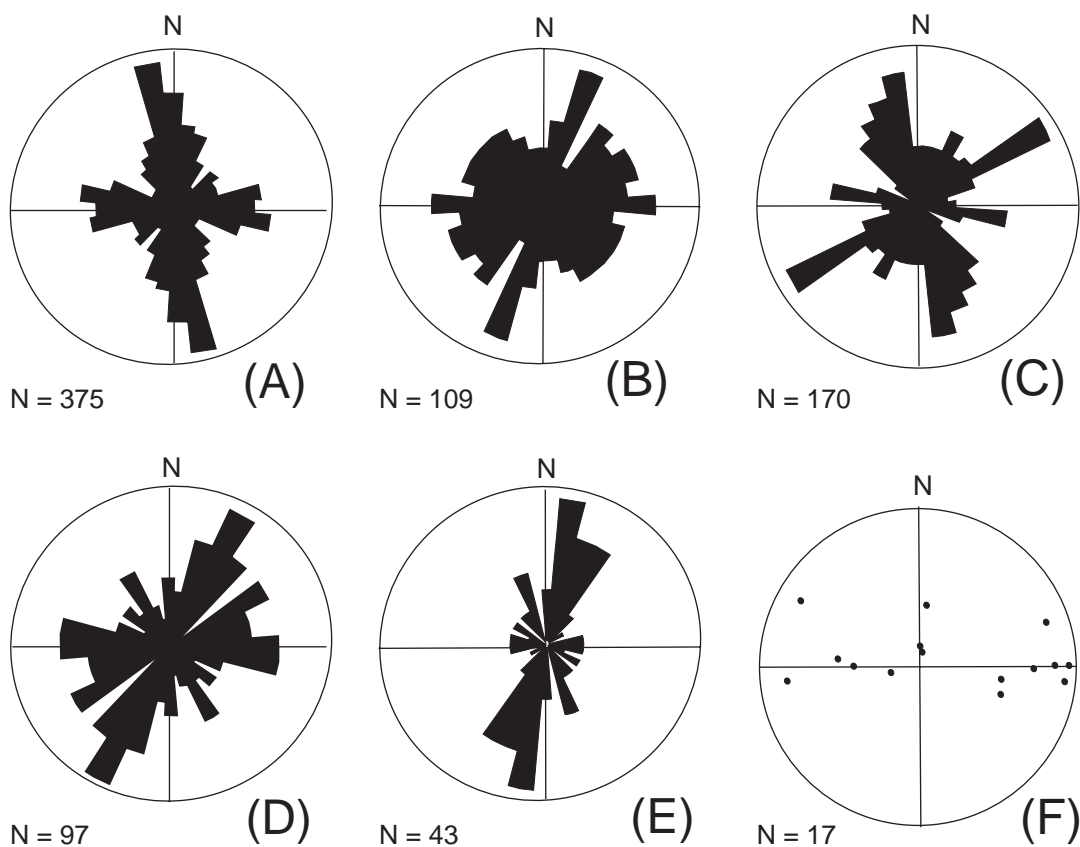
The broad fold created by D-stage 5 has been crosscut by property-scale NE trending faults (Figure 3.1). The best exposure of a D-stage 6 fault is in the road immediately to the west of the Lucky pit. Here the fault is manifest as a 0.5 - 1 m wide zone of strongly brecciated and sheared rock that contains large amounts of carbonaceous material. All primary bedding fabrics within the main shear have been destroyed. Quartz veins and clasts of quartz veins were also noted within the fault. The D-stage 6 faults have sub-linear surface traces that vary in strike length from 1.5 to 6 km. These faults display either apparent dextral or apparent sinistral movement of between 250 m and 1 km, however, the amount of dip-slip movement on these structures is unknown. The dip of D-stage 6 faults is also uncertain but is thought to be steep, as a steeply dipping NW oriented fault was mapped to the west of Lucky pit.

D-stage 7 - Normal faulting

The emplacement of TPS monzonite sills along the Reserve Trend annealed D-stage 6 strike-slip faults. TPS sills were subsequently crosscut by numerous, variably oriented normal faults. D-stage 7 faults are exposed in all of the open pits and can be seen in many of the pit walls (Figure 3.19). These structures typically crop out as discrete faults less than 1 cm wide or as a 5 - 10 cm wide swarm of hairline fractures that are comprised of carbonaceous material and/or clay, and display irregularly developed breccia and rare shear textures. Host rock textures immediately adjacent to D-stage 7 faults are generally preserved. In some instances the faults are poorly formed and show little evidence of offset. Atypical D-stage 7 faults up to 40 cm thick, containing moderately sheared and brecciated rock were also noted (e.g. the main fault in the Blue pit).

The D-stage 7 faults dominantly strike NW, NNE, NE, and E and have a steep to moderate dip (Figure 3.19). These faults are mutually crosscutting and display linear to

Figure 3.19 A graphic illustration of D-stage 7 normal faults. (A) – (E) are rose diagrams illustrating fault orientations measured in the Lucky, Golden, Kokanee, Blue, and Pacific Pits respectively. There are four dominant fault orientations, NW, NNE, NE, and E. Note the variation in fault orientations between pits. (F) Is a stereonet illustrating the orientation of slickenlines measured on D-stage 7 faults. Note that there is no preferred orientation indicating no predominant sense of movement. (G) and (H) are photos of apparent normal offset on D-stage 7 faults in the walls of the Blue and Golden Pits respectively.



sub-linear surface traces (confirming their steep dip) that commonly extend for more than 50 m along strike. Apparent offsets and asymmetrical curvature of marker beds around D-stage 7 faults predominantly indicate normal, dip-slip movement of generally no more than 15 m but occasionally up to 70 m. Rare reverse movement was also noted. Slickensides are uncommon and indicate variable movement vectors (Figure 3.19), however, the amount of strike-slip movement is interpreted to be minimal, as D-stage 7 strike-slip faults show no appreciable offset from one side of the Reserve Trend to the other.

The D-stage 7 faults commonly host pyrite-quartz-carbonate-roscoelite, arsenopyrite-quartz-carbonate-gold, and stibnite-quartz-carbonate-kaolinite veins. Quartz and carbonate alteration haloes were also noted around several of these faults. An E trending D-stage 7 fault, termed the Basal fault, bounds mineralisation at depth. Lithological asymmetries in the Fosters pit suggest that there was a component of normal dip-slip movement along the Basal Fault. The relationship between D-stage 7 faults and mineralisation is further discussed in chapters 4 and 7.

D-stage 8 - NW – SE strike-slip faulting

All of the events described above including the TPS intrusions and the mineralisation are cut by the steeply SW dipping, NW trending Classic Fault with an apparent strike-slip dextral offset approximately 1.5 kilometres (Figure 3.1). The Classic Fault crops out in trenches dug within the Classic zone. This fault is a 1 - 5 metre wide zone comprising well developed shear foliation, common crenulation cleavage, fault breccias with angular clasts of wall rock and quartz veins, centimetre wide discrete fault planes, and partial to complete textural destruction of the host rock. The Classic Fault has a sub-linear surface trace and extends for more than 10 km across the width of the property. The Classic Fault trends sub-parallel to the Tintina Fault and likely formed in response to movement along Tintina Fault. The relative movement on the Classic Fault is uncertain but strike-slip movement is likely to be dominant given the close spatial and geometric relationship to the Tintina Fault. The Classic Fault represents the youngest deformation event recognised at Brewery Creek. Sheeted quartz-carbonate-pyrite-gold veins that trend sub parallel to the Classic Fault cut the shear fabrics within the fault and also cut the rocks that host the fault.

3.6 Correlation of the deformation at Brewery Creek to elsewhere in the Selwyn Basin.

The distribution of rocks that crop out through the central Yukon shows complex patterns that are the result several episodes of deformation of both regional and local extent. Most of the recent structural work in the Selwyn Basin has focussed on rocks within the Tombstone High Strain Zone (Murphy, 1997; Murphy and Heon, 1993; Murphy et al., 1992; Mair, 2000; Mair et al., 2006; Stephens et al., 2000, 2004). These rocks are structurally complex and, though they record an extended deformation history, many of these events have not been recognised outside the Tombstone High Strain Zone.

Table 3.2 summarises the major structural features that have been described by various workers across the Selwyn Basin. The oldest feature recognised is the Selwyn Fold Belt. Fabrics associated with this Belt are evident throughout the Selwyn Basin and manifest as NW trending folds that verge to the SW and to the NE and are spatially associated thrust faults (Gordey and Anderson, 1993). Other structural features within the Basin include km-scale thrust faults, a high strain zone, NE-trending folds, several populations of local faults and the Tintina Fault.

At Brewery Creek eight structural events have been recognised. The relationship of D-stages 1 and 2 to regionally developed structures, and indeed to other structures at Brewery Creek, is uncertain. The main structural event (D-stage 3) produced kilometre-scale repetition of lithologies and apparent structural thickening that is evident throughout the property. Subsequent thrust faults (D-stage 4) trend parallel to, and display similar vergence to, stage 3 folds. Later NE trending warping (D-stage 5) has disrupted the original orientation of these folds and thrusts and prevents correlation with regionally developed structural fabrics based on the orientation of structures. However, the magnitude of the fold and thrust structural regime at Brewery Creek suggests that it probably correlates to the development of the Selwyn Fold Belt. Furthermore, Gordey and Anderson (1993) documented a similar spatial relationship between fold and thrust development in the eastern Selwyn Fold Belt.

Structural fabrics associated with the formation of the Robert Service Thrust, Tombstone High Strain Zone and Tombstone Thrust were not identified at Brewery Creek. It is possible that the development of D-stage 4 thrust faults may correspond to

Table 3.2 A table correlating structural features identified at Brewery Creek to structures elsewhere in the Selwyn Basin. Note that the stages 3 - 8 of deformation described at Brewery Creek have been documented elsewhere. Data to compile the table was sourced from Flannigan et al (2000), Gordey and Anderson (1983), Green (1972), Mair et al. (2000, 2006), Murphy (1997), Stephens et al. (2000, 2004), and Templeman-Kluit (1979).

Event	Trends	Structural Relationships	Age	Murphy (1997)	Mair et al. (2000)	Mair et al. (2006)	Stephens et al. (2000, 2004)	Tempelman-Kluit (1979)	Green (1972)	Gordey & Anderson (1993)	Brewery Creek
Local folding	NW?-trending, shallowly plunging folds	Oldest structure recognised at B.C.	?								Stage 1
Local thrusting	SW?-vergent, curve linear trace	Bounds folds described above	?								Stage 2
Fold belt development	NW fold axis, S-SW and/or NE vergent folds and thrust faults	Oldest regional structure recognised	Broadly Devonian - Cretaceous	Lost Horses Syncline		Lost Horses Syncline			2nd phase of folding	Selwyn Fold Belt	Stage 3 and 4?
Km-scale thrusting	Broadly E-trending, near planar fault	Unknown relationship to NW-trending folds	Jura-Cretaceous	Robert Service Thrust (RST)		Robert Service Thrust (RST)			Complex thrust structure		
THSZ development	N-NE vergent folds.	THSZ fabrics deform NW-trending folds and RST.	Jura-Cretaceous	Sp, Sp', Sc, Fc, Fc'	S1-S2		D2 - D4				
Km-scale thrusting	Broadly E-trending fault	Tombstone Thrust cuts THSZ fabrics	Jura-Cretaceous	Tombstone Thrust		Tombstone Thrust					
NE-trending folds	Axis trends NE plunges W-SW	Folds the RST, THSZ, and Tombstone Thrust.	Jura-Cretaceous	McQuesten Antiform	unresolved deformations	McQuesten Antiform	D5				Stage 5
Local faulting	NE-trending faults	Faults cut stage 5 fold at B.C. and are pre-TPS	Jura-Cretaceous				BFa-c				Stage 6
Normal faulting	NW, NE, and E - trending faults	Faults cut TPS monzonite sills	Post-Cretaceous	NE- to E-striking normal faults	N- and NW-striking faults		BFa-c			NE-trending faults?	Stage 7
Regional Faulting	NW-trending fault	Cuts mineralised TPS intrusions	Late Cretaceous Palaeogene?					Tintina Fault			Stage 8

regional shortening associated with one of the thrust events, however, no second-order thrust faults have been described in areas proximal to the Robert Service and Tombstone Thrusts.

At Brewery Creek a broad NE trending fold (D-stage 5) has deformed D-stage 3 folds and D-stage 4 thrust faults. In the McQuesten River region NE-trending folds (e.g. the McQuesten Antiform) deform fabrics of the Selwyn Fold Belt, the Robert Service and Tombstone Thrusts and the Tombstone High Strain Zone (Murphy, 1997; Mair et al., 2006). Thus the formation of the D-stage 5 fold at Brewery Creek can be correlated to the deformation event that produced the McQuesten Antiform and other similarly oriented folds.

Several populations of pre- (D-stage 6) and post-TPS (D-stage 7) faults cut the NE trending folds. Faults of a similar orientation and relative age (i.e. pre- or post-TPS) have been documented elsewhere in the Yukon (Gordey and Anderson, 1993; Murphy, 1997; Stephens et al, 2000 and 2004) suggesting that these structures may have developed contemporaneously and in response to a regional stress field. This is significant from an exploration point of view as D-stage 7 faults partly control the distribution of mineralisation at Brewery Creek.

The final stage of deformation at Brewery Creek (D-stage 8) is manifested as a steeply dipping NW trending fault termed the Classic Fault. The Classic Fault displays a similar orientation and movement sense to the nearby Tintina Fault (Gabrielse and Yorath, 1991) and most likely developed in response to movement along the Tintina Fault.

CHAPTER FOUR

Gold mineralisation at Brewery Creek



The Reserve Trend, looking east from the Blue pit.
The excavation in the saddle between the hills is Kokanee pit.

4.1 Chapter overview

The bulk of the gold mineralisation at Brewery Creek occurs along a linear zone of intrusions and faulting termed the Reserve Trend. Mineralisation along this Trend is hosted by TPS intrusions and sedimentary rocks of the Earn Group and can be partitioned into four broad paragenetic stages, (1) pre-TPS intrusion, (2) syn-TPS intrusion, (3) post-TPS intrusion (Au bearing stage), and (4) weathering. The pre-TPS intrusion stage encompasses sedimentary rock hosted disseminated and massive pyrite, carbonate veins and breccia infill, quartz veins, and stylolites. The syn-TPS intrusion stage comprises the emplacement of TPS intrusions and the development of their contact aureoles. Finally the post-TPS intrusion includes pyrite \pm quartz \pm carbonate \pm roscoelite veins, quartz only veins, gold bearing arsenopyrite \pm quartz \pm carbonate veins, several stages of brecciation and stibnite \pm quartz \pm carbonate \pm kaolinite veins.

Gold assay analysis and vein measurements from the open pits along the Reserve Trend highlight two distinct mineralised orientations, E and NE. These orientations are paralleled by a number of metre-scale, steeply dipping post-TPS faults and mineralisation is bound at depth by a moderately dipping, E striking normal fault, termed the Basal Fault.

This chapter addresses the following points:

- (1) The nature and location of mineralisation at Brewery Creek.
- (2) The paragenesis of mineralisation hosted along the Reserve Trend.
- (3) The orientation and structural controls on the distribution of mineralisation along the Reserve Trend

4.2 Gold mineralisation at Brewery Creek

The Brewery Creek mine was host to a global geological resource of 43.8 million tonnes at 1.03 grams per tonne gold for 1.45 million ounces of gold that has been defined from 13 mineralised zones (Table 4.1). The bulk of the gold mineralisation occurs as fracture and/or fault controlled disseminations and veins within Cretaceous monzonite sills. However, fracture and/or fault controlled disseminations and veins within non-carbonate sedimentary rocks, carbonate hosted mineralisation, and skarn style mineralisation is also present. In intrusive and sedimentary rocks gold occurs in association with arsenopyrite and arsenic rich pyrite grains (see Chapter 5).

Mineralisation at Brewery Creek can be partitioned into three main areas termed the Reserve Trend, Classic Zone, and North Slope (Figure 3.1). This thesis briefly describes all three of these areas but focuses on the Reserve Trend, as this trend is host to 80% of the gold resources at Brewery Creek (Table 4.1). Furthermore, poor outcrop and limited diamond drilling restricts more detailed investigations of mineralisation at the Classic and North Slope zones.

Reserve Trend

The Reserve Trend is located in the central part of the property (Figure 3.1) and is the main mineralised zone at Brewery Creek. Lindsay et al. (2000) described this area as a linear zone of faulting, monzonite sills and mineralisation that strikes broadly east for more than 12 km and has a moderate dip to the south. Mineralisation along the Reserve Trend is hosted by TPS BM and QBM sills, and variably carbonaceous, siliciclastic Earn Group sedimentary rocks. Within the monzonite sills gold dominantly occurs in association with steeply south dipping quartz-carbonate-arsenopyrite veins and their alteration haloes, whereas gold hosted by Earn Group sedimentary rocks is generally disseminated around steeply dipping faults and is associated with arsenopyrite. Gold mineralisation along the Reserve Trend is bound at depth by a moderately south dipping normal fault (see section 4.3).

There are a number of open pits and mineralised zones located along the Reserve Trend. From west to east these include; West Big Rock Zone, East Big Rock Zone, Blue Pit, Pacific Pit, Moosehead Zone, Canadian Pit, Fosters Pit, Kokanee Pit, Golden Pit, Lucky Pit, Bohemian Zone, Schooner Zone, and Sleemans Zone (Figure 3.1). Drilling along the Reserve Trend has returned intersections of up to 16 g/t Au over 6 m,

Table 4.1 Known gold resources at Brewery Creek. The data shows that the Reserve Trend (figures for Reserve Trend shaded in light yellow) hosts almost 80% of the total known resource at Brewery Creek. For locations of the various pits and mineralised zones see Figure 3.1. The data was sourced from Park (1999).

Deposit	Tonnes	g/t Au	Au (ounces)	% of resources
West Big Rock Zone	1,691,370	0.87	47,490	3.3
East Big Rock Zone	1,504,320	0.75	36,360	2.5
Blue Pit	2,930,560	1.27	119,870	8.3
Pacific Pit	1,298,880	1.03	43,020	3.0
Moosehead Pit	2,097,530	0.93	62,770	4.3
Canadian Pit	579,000	1.04	19,360	1.3
Fosters Pit	1,690,130	1.05	56,980	3.9
Kokanee Pit	6,013,430	0.99	190,860	13.2
Golden Pit	6,781,090	1.1	239,680	16.6
Lucky Pit	4,805,860	1.58	243,030	16.8
Bohemian Zone	1,305,600	1.42	59,430	4.1
Reserve Trend Total	30,697,770	1.14	1,118,850	77.4
Classic Zone	10,883,260	0.52	182,750	12.6
North Slope Zone	2,228,090	2.01	143,810	9.9
Total	43,809,120	1.03	1,445,410	100.0

7.5 g/t over 28 m, and 2.07 g/t Au over 50 m. The Reserve Trend contained a resource of 30.7 million tonnes at 1.14 g/t Au for 1.12 million ounces of Au (Park, 1999). Metallurgical testing commissioned by Viceroy International indicates that gold mineralisation hosted by intrusive rocks is dominantly associated with arsenopyrite. Little free gold or gold associated with other minerals was observed. However, up to 36% of the gold recovered from sedimentary rocks was free gold closely associated with carbonates, iron oxides and carbonaceous material, with the remaining gold associated with arsenopyrite (Laprenune, 1997). Due to complications with gold locked in sulphide grains only the weathered part of the mineralised system has been mined at Brewery Creek. The development of a deep weathering profile was aided by the absence of glaciation, which is common elsewhere in the Yukon.

Classic Zone

The Classic Zone is located in the southwestern part of the property (Figure 3.1). The bulk of the gold mineralisation is hosted by a syenite pluton (~ 4 km long and 2 km wide) that has been divided into two portions and dextrally offset 1.5 km by the NW trending Classic Fault. Gold mineralisation occurs as steeply SW dipping cm-scale sheeted quartz – pyrite – gold veins that trend NW sub-parallel to the Classic Fault (Figure 4.1). The mineralised zone also trends northwest, extends along strike for over 1 km and has a width of 200 to 600 m. Drilling across the Classic Zone has returned intersections of up to 0.57 g/t Au over 54 m and defined a resource of 10.9 million tonnes at 0.52 g/t Au for 180,000 ounces of Au (Park, 1999). Although this represents approximately 12% of the resources at Brewery Creek, the Classic Zone has not been mined due to its geographic location and low grade. Bottle roll test recoveries were similar for oxidised and un-oxidised rocks, suggesting that the gold in the Classic Zone is free (Park, 1999).

North Slope

North Slope is located approximately 500 m north of the Reserve Trend in the central part of the Brewery Creek property (Figure 3.1). Disseminated and fracture-controlled gold mineralisation is hosted by calcareous siltstone of the Steel Formation. Viceroy geologists have interpreted the mineralisation to occur as flat lying, moderately to shallowly south dipping mineralised zones that are generally 4 - 6 m thick (Figure 4.2). Decalcification, brecciation and silicification were also noted at North Slope, features that are typical characteristics of Carlin-style mineralisation (Poulsen et al., 1997). Thin section analysis of mineralised breccia has shown silica altered siltstone clasts in a

Figure 4.1 **A cross-section through the Classic Zone looking northwest (local grid north).** The sheeted veins that characterise mineralisation in the Classic Zone dip parallel to the mineralised zones illustrated. Note that these zones are also parallel to the Classic Fault, which accommodates 1.5 km of apparent strike slip offset. Mineralised reverse-circulation drill intersections are annotated on the figure.

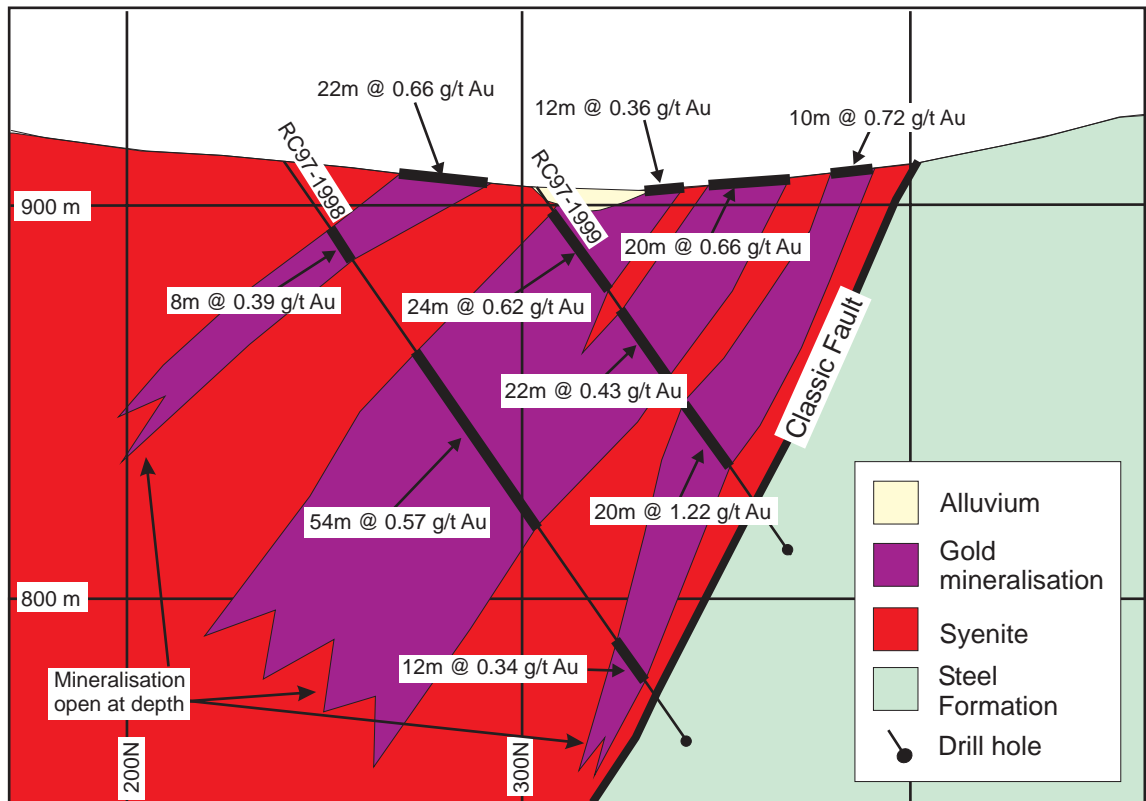
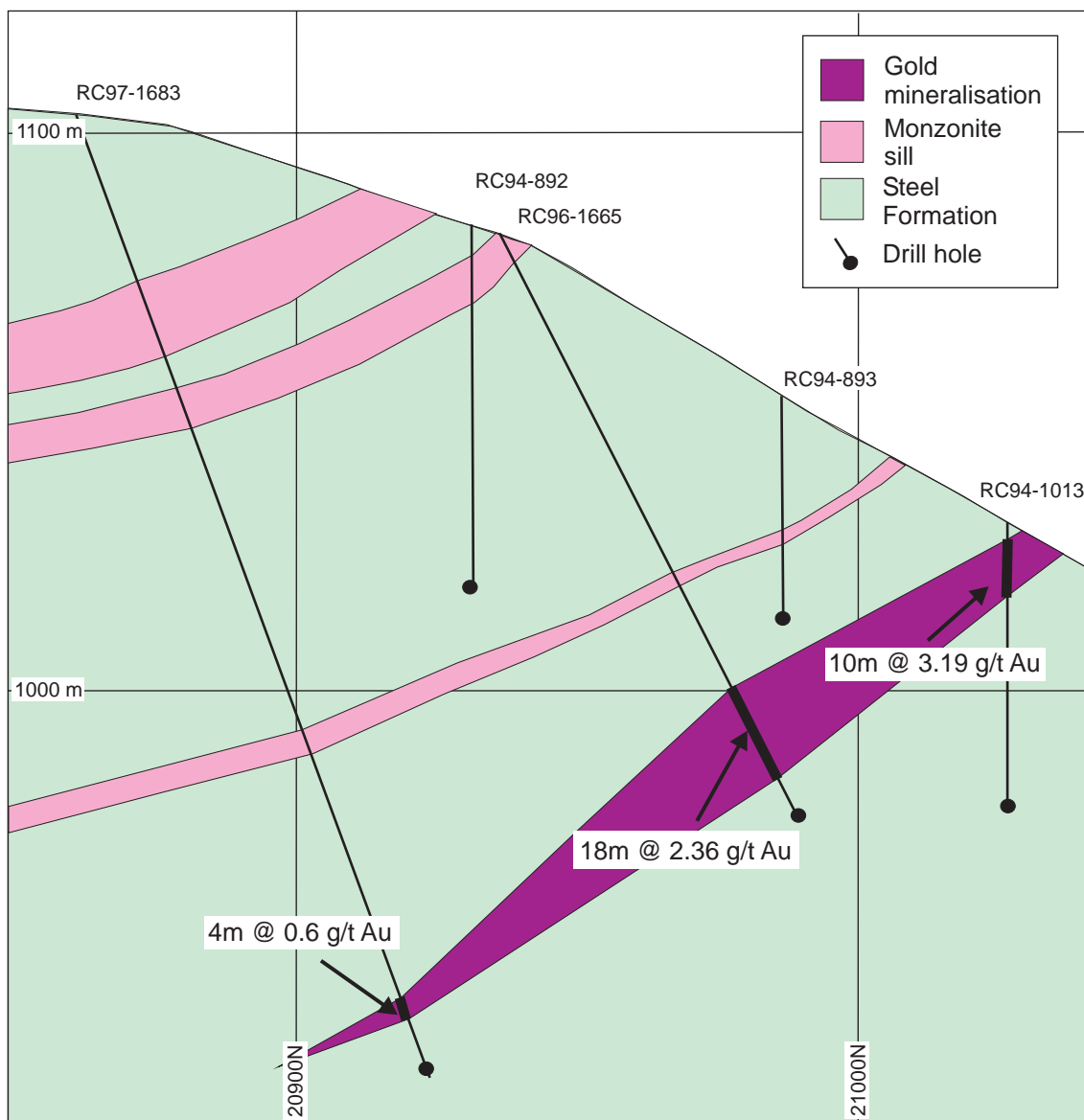


Figure 4.2 **A cross section through North Slope looking southwest (grid west).** Mineralisation is interpreted to dip moderately to the south, parallel to monzonite sills. This southward dip approximates bedding trends. Mineralised reverse-circulation drill intersections are annotated on the figure.



groundmass of clay. Micro-cavities formed through carbonate dissolution were also noted (Park, 1999). Alteration associated with mineralisation at North Slope is subtle with mineralised and un-mineralised samples typically visually indistinct. Drilling at North Slope has returned intersections of up to 2.67g/t Au over 14 m, 13.1g/t Au over 4 m and individual results of up to 22.06 g/t Au. The North Slope zone contains a resource of 2.2 million tonnes at 2.01g/t Au for 140,000 ounces of Au (Park, 1999). This represents approximately 8% of the resources at Brewery Creek, however, this area has not been mined.

4.3 Paragenesis of mineralisation along the Reserve Trend

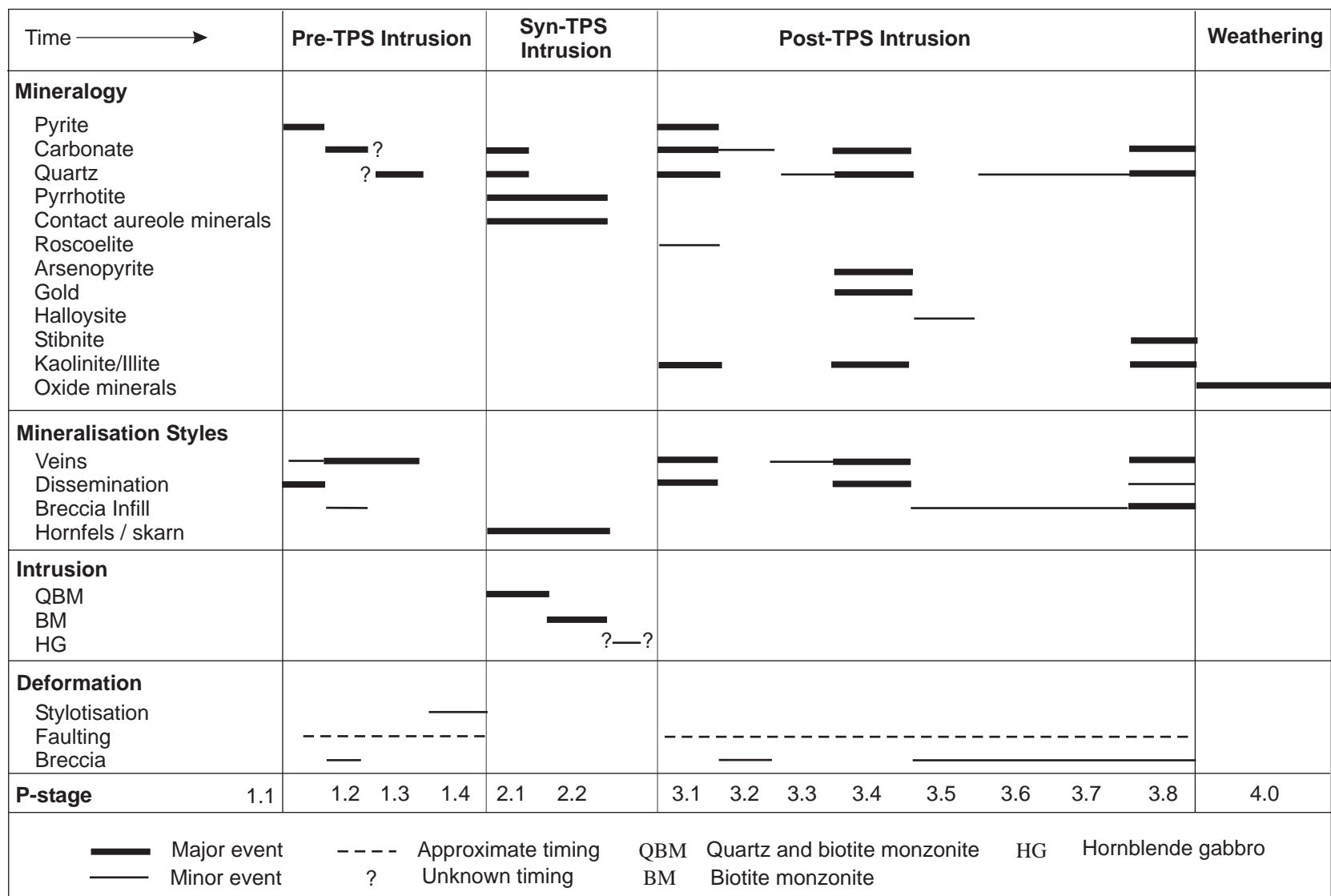
Logging of over 2700 m of drill core from the Reserve Trend combined with observations in the open pits was used to construct a detailed paragenetic history. The paragenesis can be partitioned into pre-, syn-, and post-TPS intrusion and weathering and is summarised in Table 4.2. To avoid confusion with deformation events, the paragenetic stages are referred to as 'P-stages'. A number of P-stages of quartz, carbonate and pyrite have been documented in the paragenesis. The relative timing of these events was aided by their relationship to intrusions (e.g. if a quartz vein is hosted by an intrusion then it must post-date the intrusion) and by associated minerals (e.g. arsenopyrite in an arsenopyrite-quartz-carbonate vein). However, where no additional information is available (e.g. two quartz veins hosted by sedimentary rock), the timing of the event is difficult to evaluate. This paragenesis describes the mineralisation history of the Reserve Trend and does not include data from the Classic and North Slope zones.

Polished thin-section and scanning electron microscope work on composite sulphide separates commissioned by Viceroy Exploration (Honea, 1997, A and B) identified trace amounts of marcasite, sphalerite, covellite, Ag-bearing tetrahedrite, boulangerite, and gersdorffite (a Ni-Co-As sulphide). The paragenetic timing of these minerals is uncertain, as they were not identified in this study.

P-stage 1 - Pre-TPS intrusion.

Four distinct stages of mineral growth and or vein formation/deformation have been documented prior to the emplacement of TPS intrusions, the evidence for the relative timing of these stages is discussed below.

Table 4.2 **Paragenetic history of mineralisation within the Reserve Trend.** The paragenesis has been partitioned into four stages; pre-, syn-, and post-TPS intrusion, and weathering. Note that there are only three sulphide bearing events post-TPS intrusions and that gold is associated with arsenopyrite. Contact aureole minerals include hedenbergite, wollastonite, sphene, microcline, quartz, calcite and rare tourmaline. Oxide minerals are goethite, limonite and jarosite after pyrite, scorodite after arsenopyrite, antimony ochre and kermesite after stibnite.



P-stage 1.1 - Early pyrite.

Pyrite occurs commonly as disseminated euhedral cubes, cm-scale nodules or as massive replacement of layers (Figure 4.3 A) randomly distributed in outcrops of the Menzie Creek Volcanic unit, Steel Formation and Earn Group and in gold-absent drill core of Earn group and Steel Formation from the Reserve Trend and North Slope.

P-stage 1.2 - Carbonate veins and breccia infill.

Carbonate veins were observed within all of the sedimentary and volcanic rocks that outcrop at Brewery Creek, and are particularly widespread within the calcareous Steel Formation. The carbonate veins vary in composition from high-iron dolomite to ankerite. These randomly oriented veins are generally less than 1 cm thick, with sharp margins and little visible alteration of the wall rocks in hand specimen. Hydrothermal and fault breccias with carbonate infill and strong carbonate alteration of clasts were also identified, however, the orientation and relationships between the carbonate veins and breccia is unknown. Carbonate veins cross cut P-stage 1.1 massive pyrite (Figure 4.3 B), which commonly occurs within clasts of carbonate-matrix breccias.

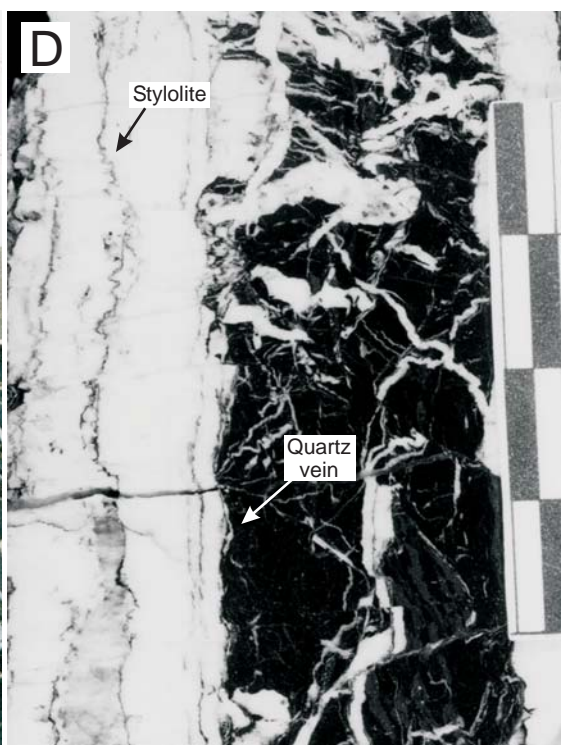
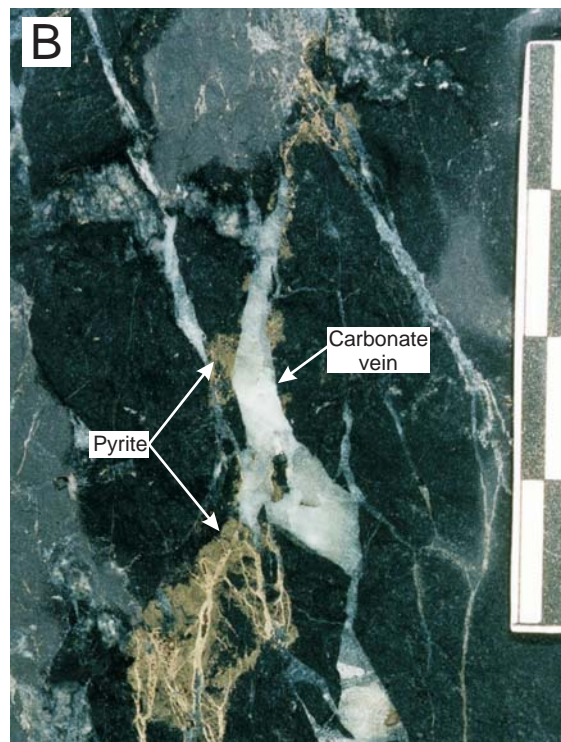
P-stage 1.3 - Quartz veins.

Quartz veins crosscut all of the Selwyn Basin lithologies that outcrop at Brewery Creek. These veins are massive, generally less than 1 cm thick, and have sharp margins. Alteration around these veins is rare but where present is manifested as weak silification. The quartz veins crosscut P-stage 1.2 carbonate veins as shown in Figure 4.3 C. A variety of stages of quartz veins displaying irregular orientations have been identified, however, compositional and textural similarity between veins makes further paragenetic partitioning difficult.

P-stage 1.4 - Stylolisation.

Stylolites were observed to crosscut a number of stages of quartz veins in drill core (Figure 4.3 D). The stylolites commonly trend parallel to vein walls, are composed of carbonaceous matter and are generally less than 1 mm thick. The trend of the stylolites is unknown as they were only observed in un-oriented drill core. The timing of stylolisation with respect to the emplacement of TPS sills is uncertain, but is interpreted to pre-date intrusive rocks as stylolites form in a compressive environment and the intrusive rocks were emplaced into an extensional regime. Furthermore, no stylolites were observed in the intrusive rocks.

Figure 4.3 Photographs of P-stage 1.1 to 1.4. (A) P-stage 1.1 pyrite replacing layers of Earn Group carbonaceous siltstone. (B) A P-stage 1.2 carbonate vein cutting P-stage 1.1 pyrite in Earn Group carbonaceous siltstone. (C) P-stage 1.3 quartz vein cutting P-stage 1.2 carbonate vein in Steel Formation siltstone. (D) P-stage 1.4 stylolites cutting P-stage 1.3 quartz veins in Earn Group carbonaceous shale. The scale bar in each photo has cm intervals.



P-stage 2 - Syn-TPS intrusion.

This stage encompasses the emplacement of TPS intrusions and the development of associated contact aureoles. TPS intrusions are interpreted to be younger than P-stage 1.3 quartz veins as suggested by a QBM sill that crosscuts a fault zone that contains numerous stages of quartz veins (Figure 4.4).

P-stage 2.1 - Emplacement of TPS intrusions.

Three phases of TPS intrusions have been identified along the Reserve Trend; QBM, BM, and hornblende gabbro (see section 3.3 for detailed descriptions of these intrusive rocks). A BM dyke was observed to crosscut a QBM sill in the Golden Pit (Figure 4.4) and in drill core a hornblende gabbro dyke cuts a BM sill. The monzonite intrusions crop out along the Reserve Trend as E-W oriented elongate sills that dip moderately to steeply to the south. Hornblende gabbro was only observed in outcrop in one location in the Golden Pit as a broadly NE trending, steeply dipping dyke. At hand specimen scale the margins of the monzonite sills are highly irregular while the hornblende gabbro dykes are relatively planar. The timing of the hornblende gabbro relative to the rest of the paragenesis is uncertain. The biotite monzonite sills and dykes also commonly contain pyrrhotite.

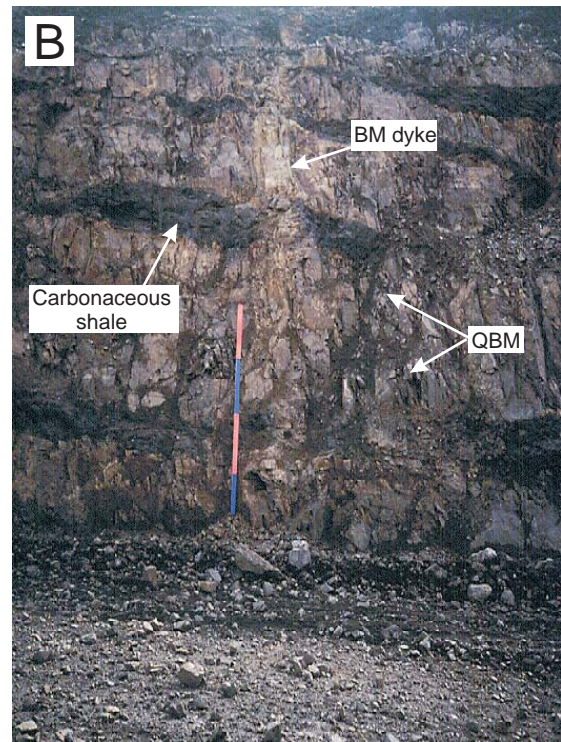
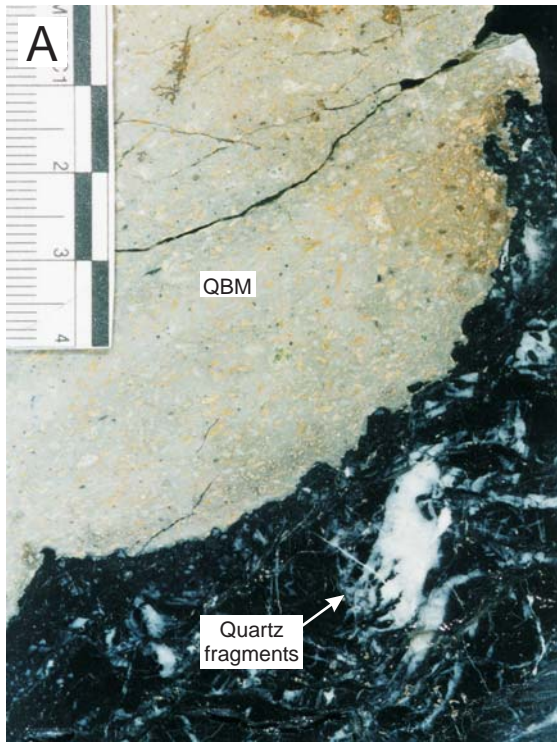
P-stage 2.2 - Development of contact aureoles and skarn.

The emplacement of TPS intrusions resulted in the development fine- to medium-grained skarn and calc-silicate hornfels (Figures 3.14 and 3.15) in the Steel Formation below the Basal Fault along the Reserve Trend and to the south of the Reserve Trend in the Schooner and Sleemans areas. The nature of these contact metamorphic rocks is discussed in section 3.4. In contrast to the Steel Formation, Earn Group rocks along the Reserve Trend show less clear evidence of contact metamorphism. Only one occurrence of obviously contact metamorphosed Earn Group shale was found in drill core from under the Fosters open pit and contained a number of relict andalusite porphyroblasts up to 1 cm long (Figure 3.16).

P-stage 3 - Post-TPS intrusion

A variety of vein and breccia stages crosscut the TPS monzonite sills (P-stage 2.1) that crop out along the Reserve Trend. Eight post-TPS stages have been recognised and are discussed below.

Figure 4.4 **Photographs of P-stage 2.1 intrusive rocks.** (A) A monzonite sill cuts a shear zone composed of carbonaceous Earn Group shale and clasts of quartz veins. Note that the margin of the intrusion is highly irregular and does not show any evidence of deformation. This indicates that the intrusion was emplaced following shear zone development. Scale bar has cm intervals. (B) A dyke of BM cutting QBM exposed in the wall of the Golden Pit. The QBM contains numerous xenoliths of carbonaceous shale. Scale bar has meter intervals.



P-stage 3.1 - Pyrite ± quartz ± carbonate ± roscoelite veins.

Pyrite ± quartz ± carbonate ± roscoelite (a vanadium-rich mica with the formula $K(V,Al,Mg)_2AlSi_3O_{10}(OH)_2$) veins occur within TPS intrusions and Earn Group sedimentary rocks along the length of the Reserve Trend. P-stage 3.1 veins are generally less than 5 mm in width and show vein abundances that range from randomly spaced singular veins up to sheeted arrays with vein densities on the order of 10 per metre. Vein orientations measured along the Reserve Trend show that pyrite ± quartz ± carbonate ± roscoelite veins dominantly trend E and dip steeply to the south (Figure 4.5 A and B). P-stage 3.1 veins typically comprise microcrystalline quartz and carbonate with lesser euhedral to subhedral pyrite (0.5 – 2 mm long) but also display variable mineralogy including pyrite only (Figure 4.5 C), pyrite – quartz, pyrite – carbonate (Figure 4.5 D), and pyrite – quartz – carbonate – roscoelite (Figure 4.5 E). Multiple generations of these veins were observed with pyrite – quartz – carbonate veins crosscutting and displacing other pyrite – quartz – carbonate veins, and with pyrite only veins crosscutting pyrite – carbonate veins.

Vein morphology is dependant on vein composition. Veins dominated by quartz and / or carbonate display sharp margins while veins dominated by pyrite have diffuse margins. Alteration associated with P-stage 3.1 veins is also dependant on vein composition with the composition of the vein approximating the alteration assemblage. Carbonate and clay (kaolinite and illite; identified using GADDS (General Area Detector Diffraction System) facilities at the Advanced Analytical Centre, James Cook University) alteration is most common with lesser, disseminated euhedral to sub-hedral pyrite and roscoelite and rare silicification. Oxygen isotope temperature estimates of > 400°C (see Chapter 6) suggests that muscovite and or sericite may have been stable initially and retrograded to illite and kaolinite. In monzonite sills carbonate has replaced phenocrysts of mafic minerals (hornblende, biotite and pyroxene) and with increasing alteration intensity both feldspar phenocrysts and the groundmass were replaced. Microprobe analysis indicates that both ankerite and dolomite are present in P-stage 3.1 veins and alteration (Figure 4.6 A and Appendix 4). Pyrite occurs as disseminated, generally euhedral, crystals, as framboidal aggregates and as massive replacement of both intrusive and sedimentary rocks (Figure 4.6 B). Disseminated pyrite in monzonite sills preferentially replaces carbonate altered mafic phenocrysts (hornblende, biotite and pyroxene), typically along mineral cleavage. Pyrite overgrowths on pyrite crystals and rare micro-scale zoning within pyrite were also noted. Roscoelite locally replaces biotite proximal (within 1cm) to the P-stage 3.1 veins within monzonite sills but was rarely observed in sedimentary rocks.

Figure 4.5 Stereonets and photographs of P-stage 3.1 pyrite \pm quartz \pm carbonate \pm roscoelite veins. (A) A rose diagram displaying dominant E orientation of veins. (B) Poles to veins highlighting the dominantly steep dip. (C – E) Various morphologies of P-stage 3.1 hosted by monzonite including (C) a pyrite-quartz-carbonate vein cut by a pyrite only vein, (D) sheeted pyrite-carbonate veins, and (E) pyrite-quartz-carbonate-roscoelite veins. The roscoelite (green) preferentially replaces biotite phenocrysts proximal to P-stage 3.1 veins. Note the grey alteration halos around the veins in C – E that represents disseminated pyrite and strong carbonate alteration. The scale bars in the photos have cm intervals.

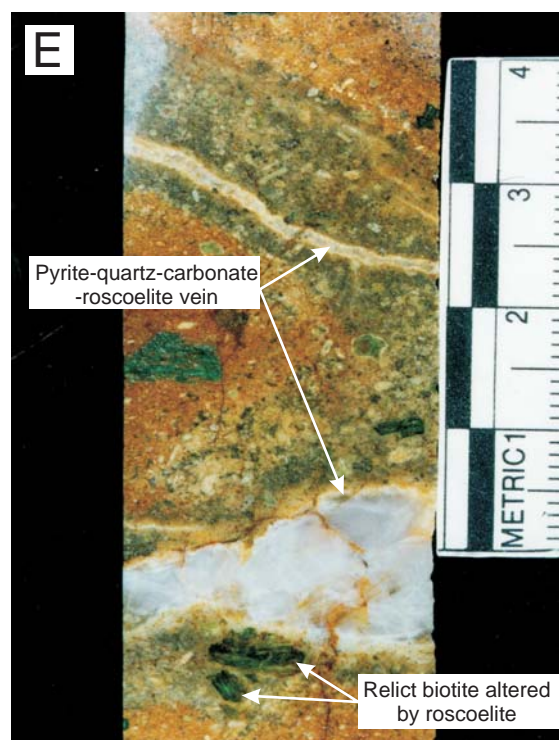
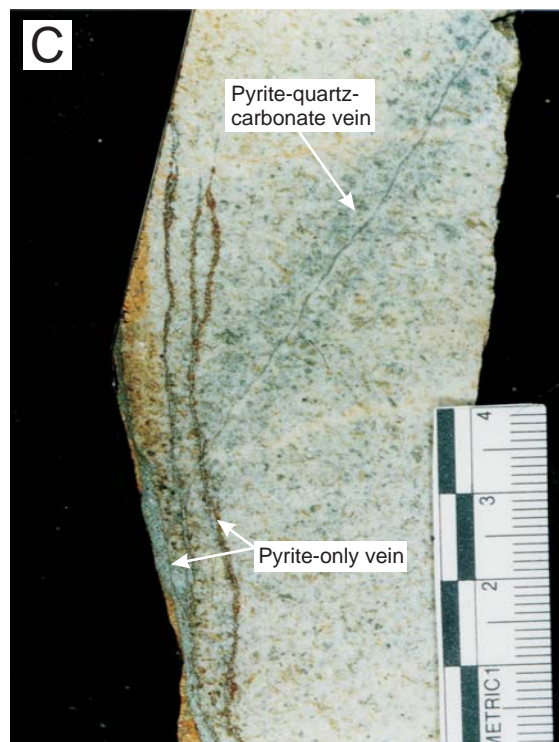
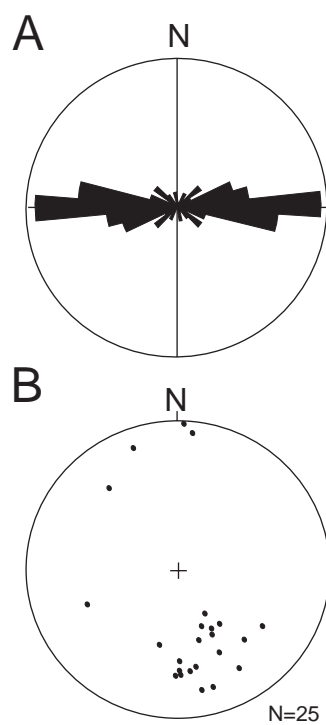
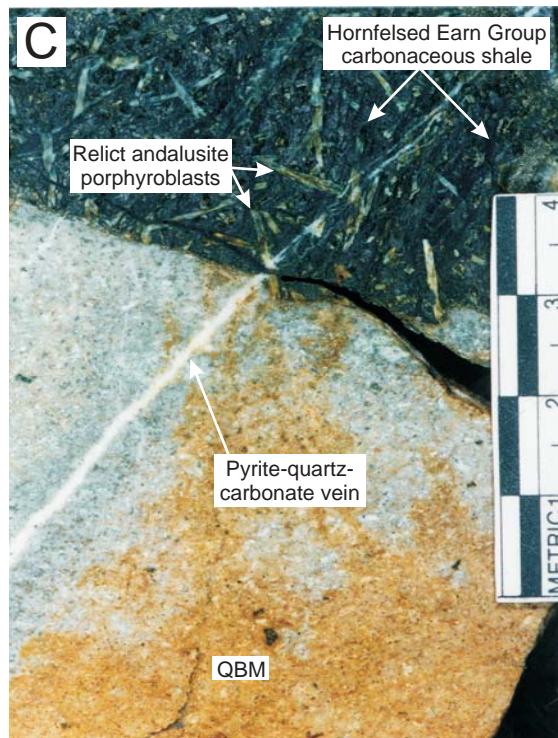
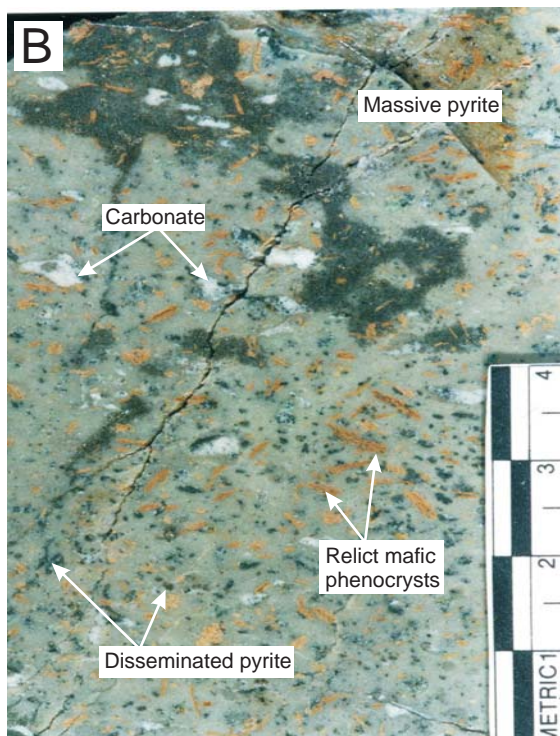
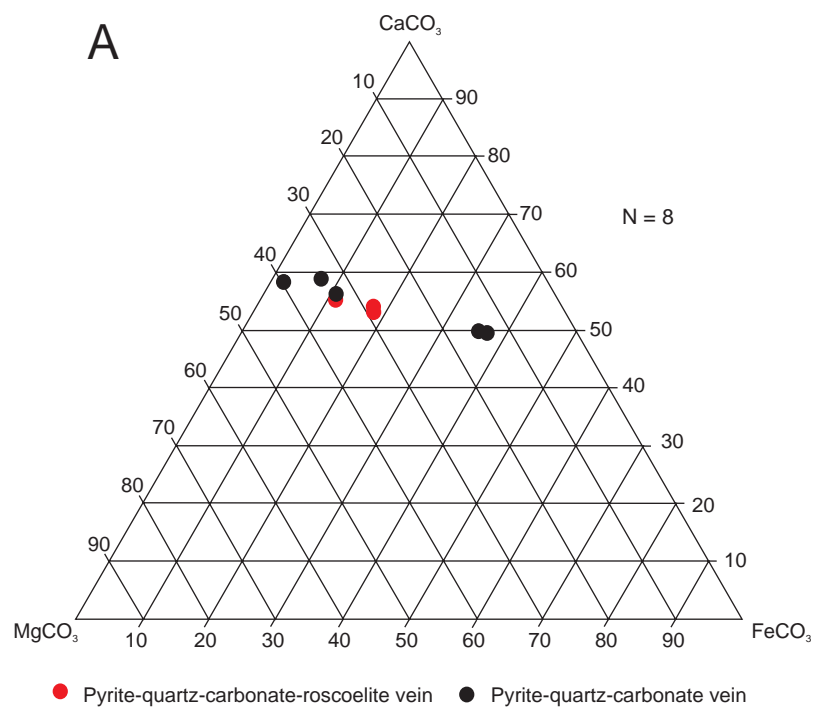


Figure 4.6 **A ternary diagram and photographs illustrating P-stage 3.1 pyrite \pm quartz \pm carbonate \pm roscoelite veins.** (A) A ternary diagram illustrating the composition of carbonate in P-stage 3.1 veins. Note that there are both high-Mg (dolomite) and high-Fe (ankerite) varieties. (B) Randomly disseminated pyrite and pyrite replacing the groundmass of a BM. (C) A pyrite – quartz – carbonate – roscoelite vein cutting a QBM sill and its associated contact aureole. This clearly indicates that P-stage 3.1 pyrite \pm quartz \pm carbonate \pm roscoelite veins post-date the development of P-stage 2.2 contact aureoles. Note the cm-scale.



P-stage 3.1 veins are younger than the contact metamorphism associated with TPS emplacement. This is evidenced by hornfels from drill core from under the Fosters Pit that contains abundant andalusite porphyroblasts that are crosscut by a pyrite –quartz–carbonate vein (Figure 4.6 C).

P-stage 3.2 - Brecciation.

Areally restricted clast-supported hydrothermal (?) breccias with fragments of Earn Group sedimentary rock and monzonite containing pyrite were observed in the Kokanee and Golden pits (Figure 4.7 A). The orientation and original shapes of stage 3.2 breccia bodies are unknown, as later faulting has disrupted the breccias, however, their margins appear to be reasonably planar. These breccias are characterised by the presence of abundant open space between many of the clasts and an infill of carbonate. P-stage 3.2 breccias contain clasts that are angular to sub angular and average between 1 and 3 cm in diameter. Pyrite ± quartz ± carbonate ± roscoelite veins were not observed to crosscut these breccias, however, clasts of monzonite within the breccia commonly contain disseminated pyrite and roscoelite (an alteration mineral that occurs within 2cm of the vein) and therefore this breccia is interpreted to be later than the pyrite ± quartz ± carbonate ± roscoelite veins.

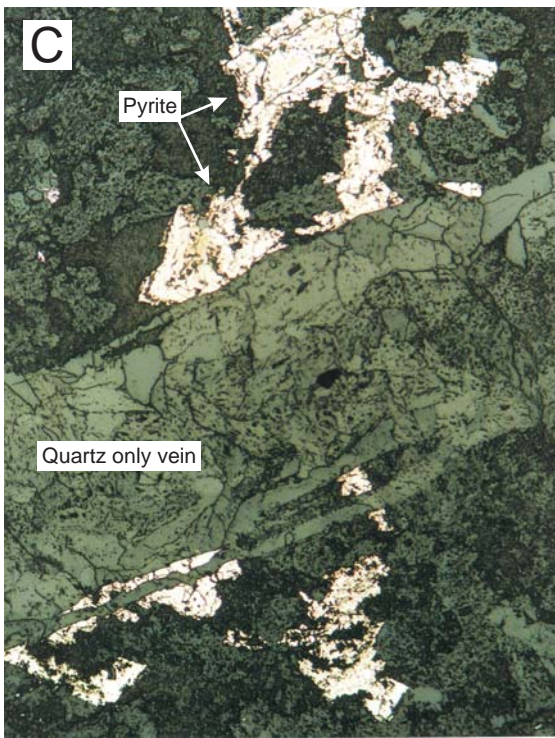
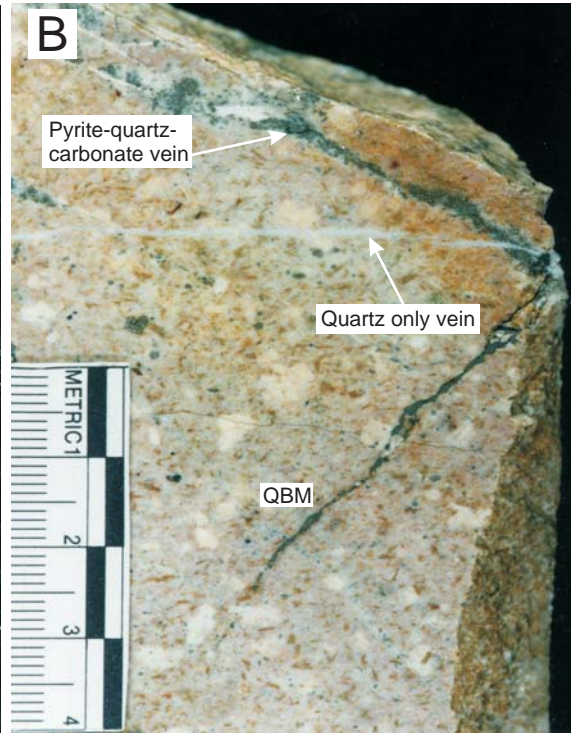
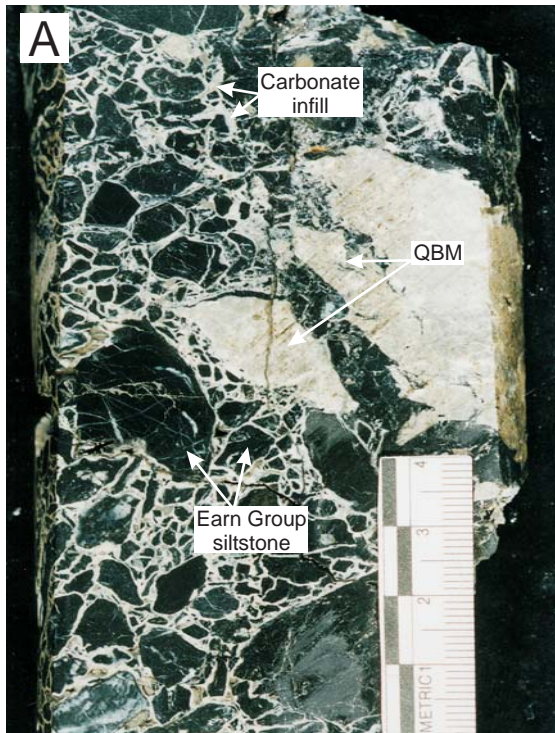
P-stage 3.3 - Quartz veins.

Quartz only veins cross-cut pyrite ± quartz ± carbonate ± roscoelite veins. This relationship is common and was observed throughout the Reserve Trend. The quartz veins are typically less than 1 mm in width, have sharp margins and show no evidence of wall rock alteration in hand specimen (Figure 4.7 B and C). These veins were differentiated from P-stage 3.1 veins primarily by the lack of pyrite and carbonate. It is possible that P-stage 3.3 represents a quartz only phase of stage 3.1. If this is the case then P-stage 3.3 veins must be the last phase of P-stage 3.1 as the quartz-only veins are not cut by other pyrite-bearing veins as is typical of P-stage 3.1 veins. The relationship between the P-stage 3.3 quartz veins, P-stage 3.2 breccia and P-stage 3.4 below is uncertain. P-stage 3.3 quartz veins can be distinguished from P-stage 1.3 quartz veins by their oxygen isotope signature (see chapter 6) and the fact that these P-stage 3.3 veins are hosted by intrusions while P-stage 1.3 veins are crosscut by intrusions.

P-stage 3.4 - Arsenopyrite ± carbonate ± quartz ± gold veins.

P-stage 3.4 veins occur within TPS intrusions and less commonly in Earn Group sedimentary rocks along the length of the Reserve Trend. These veins typically

Figure 4.7 Photographs of P-stages 3.2 and 3.3. (A) P-stage 3.2 breccia containing clasts of monzonite and siltstone. Infill between clasts is carbonate. (B) P-stage 3.3 quartz vein cutting a P-stage 3.1 pyrite – quartz – carbonate vein. (C) A photomicrograph of the sample shown in B above. Note that the quartz vein clearly cuts the pyrite. The scale bars in (A) and (B) are in cm intervals. The vein in the photomicrograph is approximately 1 mm wide.



comprise microcrystalline quartz and carbonate with lesser euhedral arsenopyrite (0.2 – 1 mm long). Vein abundance ranges from randomly spaced singular veins up to sheeted arrays (Figure 4.8 A) with vein densities on the order of 10 - 12 per metre. Vein orientations measured along the Reserve Trend suggest that arsenopyrite \pm quartz \pm carbonate \pm gold veins dominantly trend E and dip steeply to the north and south (Figure 4.8 B and C). Arsenopyrite \pm carbonate \pm quartz \pm gold veins are generally less than 3 mm in width and display sharp margins (Figure 4.8 D).

Alteration associated with P-stage 3.4 veins consists of carbonate, clay and arsenopyrite alteration of the wall rocks (Figure 4.8 E) with rare silicification. In monzonite sills carbonate has replaced phenocrysts of mafic minerals (hornblende, biotite and pyroxene) and with increasing alteration intensity both feldspar phenocrysts and the groundmass were replaced. Microprobe analysis indicates that two types of carbonate are present in P-stage 3.4 veins, dolomite and ankerite (Figure 4.9 A and Appendix 4). Roth (1994) reported the presence of kaolinite and illite in samples of alteration from Brewery Creek. The presence of these clays in zones of P-stage 3.4 alteration was confirmed using GADDS. All arsenopyrite is As deficient with a range of atomic As/S from 0.63 to 0.89 but typically 0.67 to 0.68 and atomic % As ranging from 25.99 to 31.58 (see chapter 5.4). In monzonite sills, arsenopyrite generally occurs as euhedral crystals that preferentially overgrow, or are seeded on, P-stage 3.1 pyrite (Figure 4.9 B) proximal to P-stage 3.4 veins but was also observed as individual euhedral grains. Both arsenopyrite overgrowths and individual crystals commonly replace carbonate altered relict mafic phenocrysts, typically along mineral cleavage (Figure 4.9 C). Arsenopyrite has also overgrown pyrite in sedimentary rocks, however, in the sedimentary rocks there is no clear relationship between arsenopyrite and veins. The relationship between P-stage 3.4 and P-stages 3.2 (brecciation) and 3.3 (quartz veins) are uncertain. Despite thin section and microprobe investigation gold was not observed. However, geochemical data shows a strong correlation between gold and arsenic (see chapter 5) suggesting that gold mineralisation occurred during this stage.

P-stage 3.5 - Breccia with halloysite infill.

Monzonite sills that lie along the Reserve Trend commonly display micro-fractured or breccia textures that contain an infill of halloysite, a hydrated form of kaolinite (Figure 4.10 A and Appendix 2). P-stage 3.5 breccias occur as discrete, linear, clast supported (clasts typically 1 – 5 cm across) breccias that regularly contain clasts of sheared rock, suggesting a fault breccia origin. The breccias are predominantly composed of sub-angular to sub-rounded fragments of monzonite with lesser fragments of sedimentary

Figure 4.8 Stereonets, photographs and a photomicrograph illustrating P-stage 3.4 arsenopyrite \pm quartz \pm carbonate \pm gold veins. (A) Sheeted arsenopyrite-quartz-carbonate-gold veins hosted by QBM. (B) Rose diagram indicating and overall E strike. (C) Poles to the plane of the vein, note the steep dip. (D) A photograph of an arsenopyrite-quartz-carbonate-gold vein illustrating the alteration halos around the vein, this is comprised of strong carbonate and lesser arsenopyrite. Scale bar has cm intervals. (E) A photomicrograph of an arsenopyrite-quartz-carbonate-gold vein illustrating strong carbonate alteration and euhedral arsenopyrite that occurs proximal to P-stage 3.4 veins. The vein in the photomicrograph is approximately 2 mm wide.

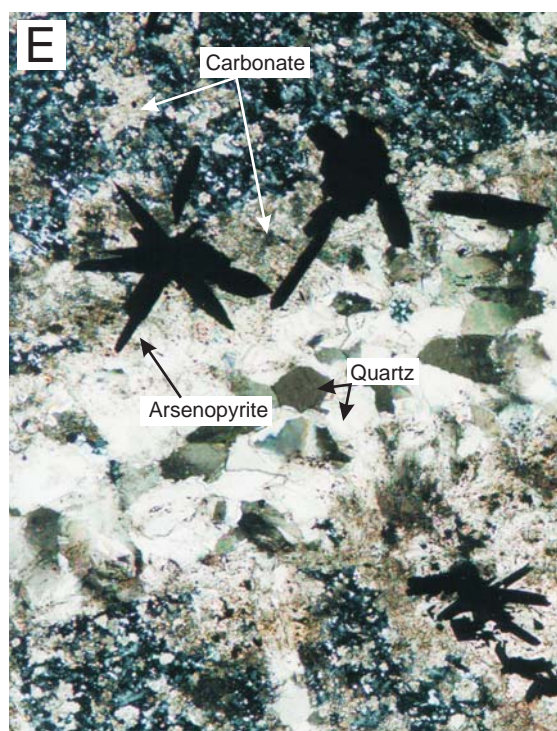
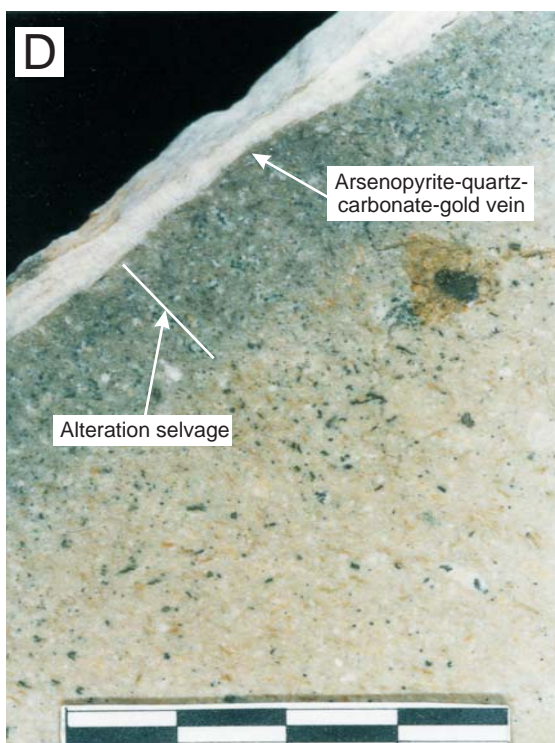
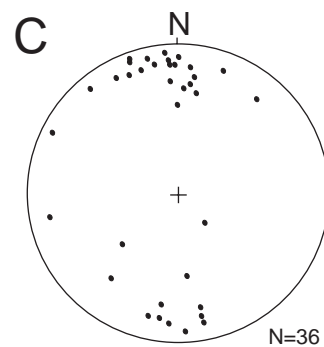
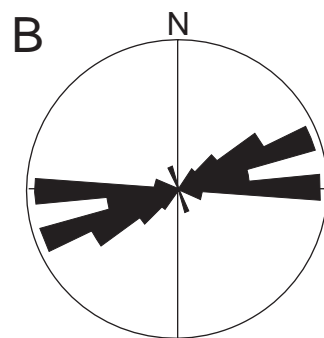
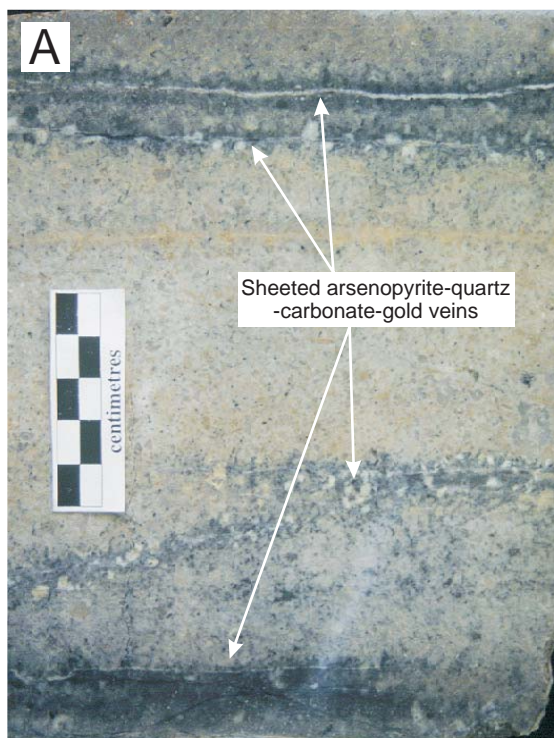


Figure 4.9 A ternary diagram and two photomicrographs illustrating P-stage 3.4 arsenopyrite \pm quartz \pm carbonate \pm gold. (A) Data plotted on the ternary diagram indicates that there are high-Mg (dolomite) and high-Fe (ankerite) carbonates associated with P-stage 3.4. (B) A photomicrograph illustrating P-stage 3.4 arsenopyrite that has overgrown P-stage 3.1 pyrite. The pyrite in the centre of the photo is approximately 2 mm long. (C) Arsenopyrite overgrowing pyrite along the cleavage seams of a carbonate altered, relict biotite phenocryst. The biotite phenocryst is approximately 3 mm wide.

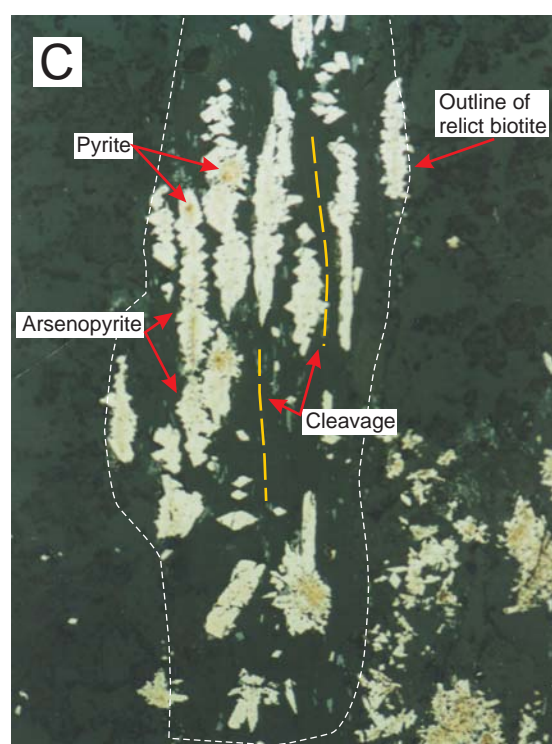
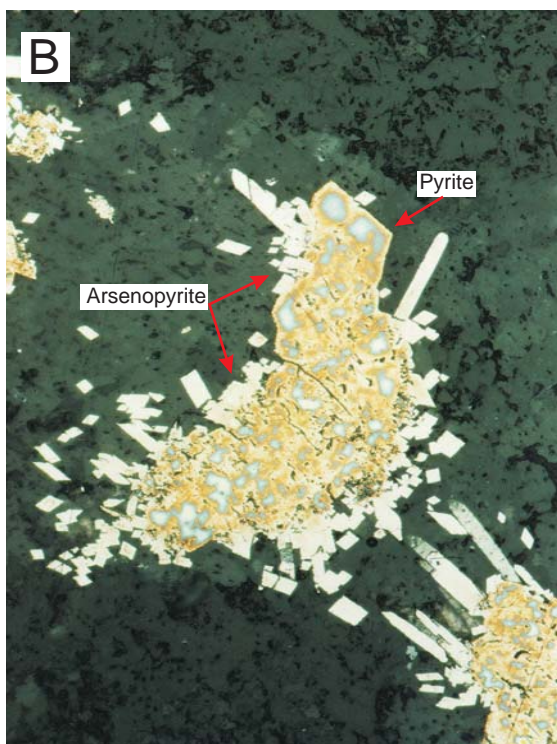
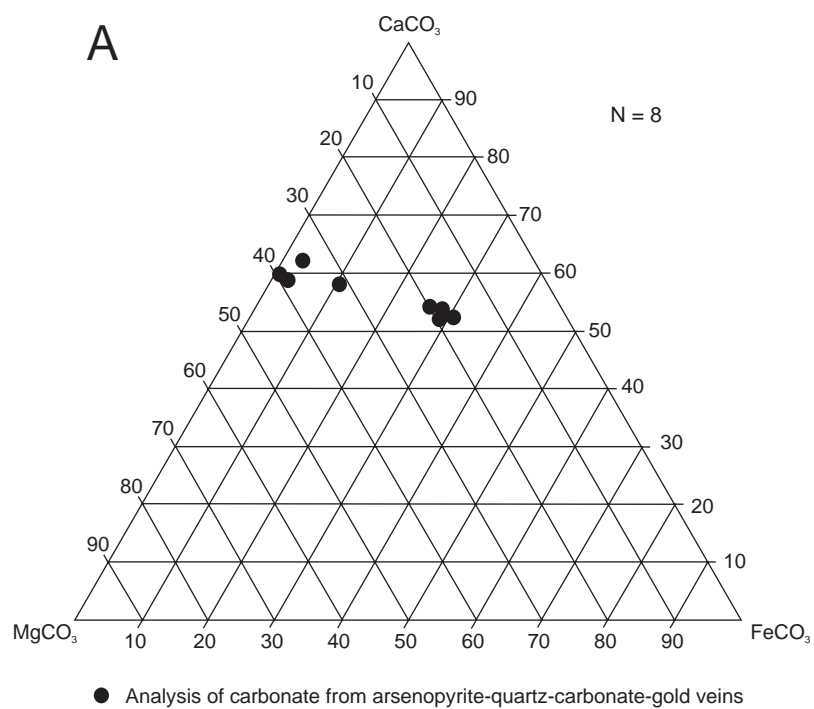
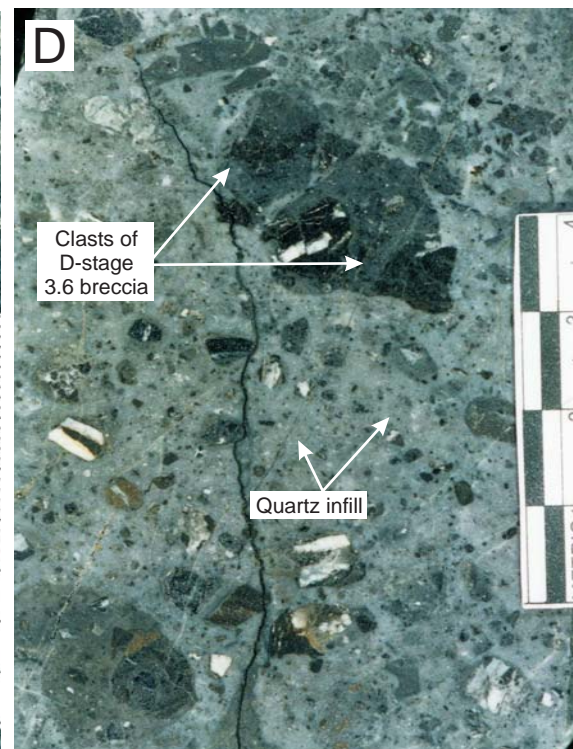
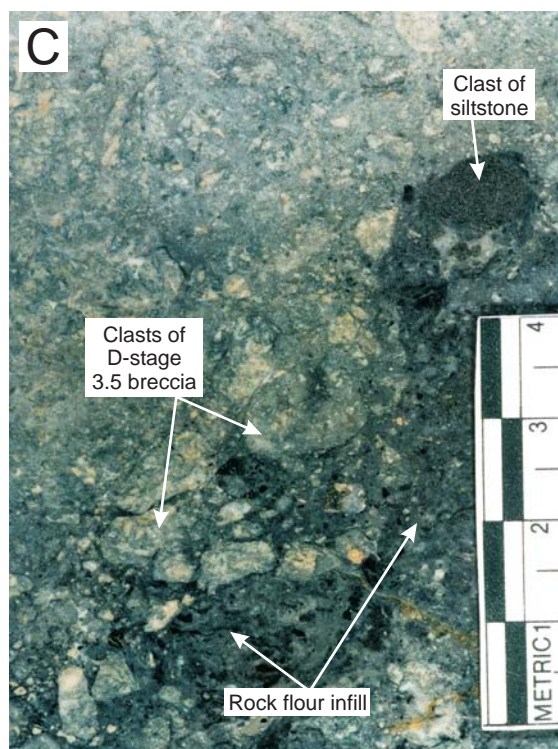
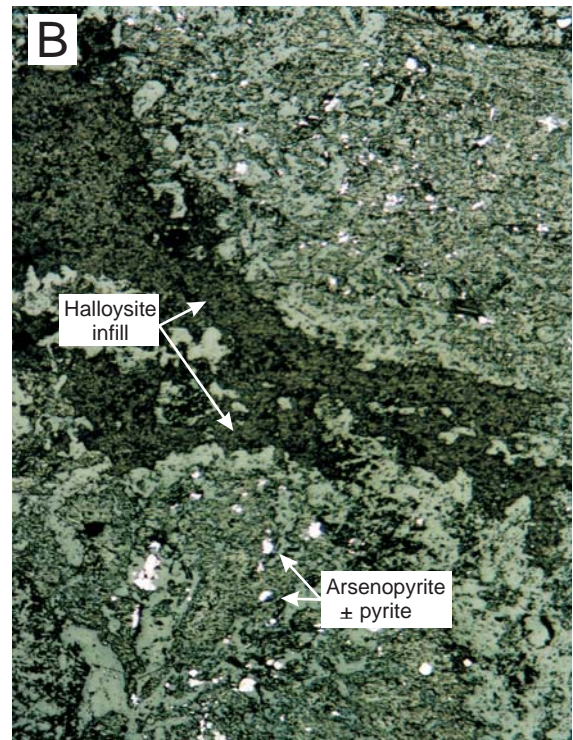
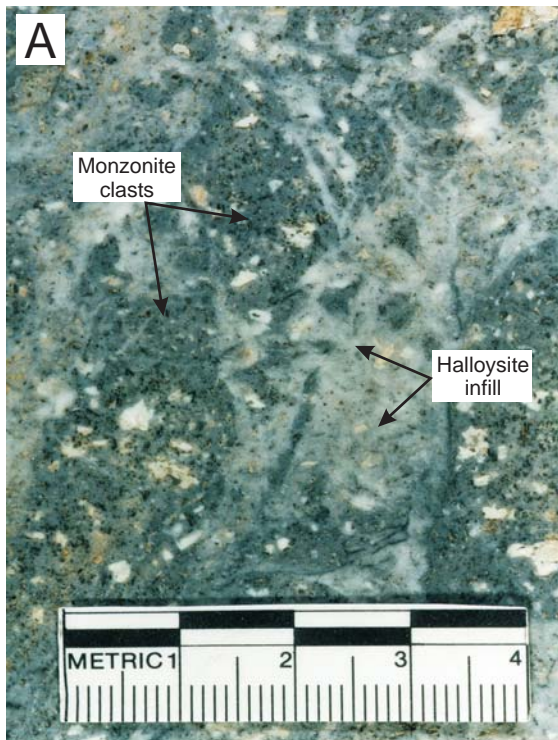


Figure 4.10 Photographs and a photomicrograph of P-stages 3.5, 3.6, and 3.7.

(A) P-stage 3.5 breccia with clasts of monzonite and an infill of halloysite. (B) A photomicrograph of a polished section of the rock in A above. Note the P-stage 3.4 arsenopyrite in the clasts, however, no veins are evident indicating the breccia post-dates P-stage 3.4. (C) P-stage 3.6 breccia with a dark grey coloured rock flour infill and clasts of P-stage 3.5 breccia. (D) P-stage 3.7 breccia with infill of quartz and clasts of P-stage 3.6 breccia. The scale bars in (A), (C), and (D) have cm intervals. Figure 4.10 B covers an area approximately 10 mm long.



rock. The halloysite infill is fine-grained and individual crystals have highly irregular boundaries. Microscopic investigation indicates that the halloysite infill does not alter the breccia clasts. The monzonite clasts within these breccias have been pervasively carbonate altered and commonly contain pyrite, roscoelite, and arsenopyrite (Figure 4.10 B). However, pyrite \pm quartz \pm carbonate \pm roscoelite (P-stage 3.1) and arsenopyrite \pm carbonate \pm quartz \pm gold (P-stage 3.4) veins do not cut these breccias, suggesting that this brecciation event post dated P-stage 3.1 and 3.4 veins.

P-stage 3.6 – Breccia with rock flour matrix.

A clast-supported breccia comprised of P-stage 3.5 breccia and sedimentary rock with a fine-grained dark infill of rock flour (Figure 4.10 C) lies under the Pacific Pit. The clasts of P-stage 3.6 breccia are rounded to sub-rounded and generally less than 1 cm in diameter. Several zones of P-stage 3.6 breccia up to 2 m wide were intersected in drill core, however, the overall morphology of the breccia is unknown.

P-stage 3.7 – Breccia with quartz infill.

P-stage 3.7 breccia comprises rounded to sub-rounded clasts of P-stage 3.6 breccia and sedimentary rock that are surrounded by a light grey quartz infill (Figure 4.10 D). Drilling under the Pacific Pit intersected this breccia, which occurs as several discrete zones up to 2 m wide, however, the overall morphology of P-stage 3.7 breccia is unknown. The breccia displays both clast- and matrix-supported morphologies with clast sizes that vary from 2 mm to 2 cm in diameter. The quartz infill is fine grained and individual crystals have highly irregular boundaries. Interestingly, the long axes of many of the crystals in the infill are aligned, however, the reason for this is uncertain. Microscopic investigation suggests that the quartz infill locally silicified clast margins.

P-stage 3.8 - Stibnite \pm quartz \pm carbonate \pm kaolinite veins and breccia infill.

The stibnite \pm quartz \pm carbonate \pm kaolinite mineral assemblage occurs throughout the Reserve Trend within veins (Figure 4.11 A), breccia veins and as fault breccia infill (Figure 4.11 B) that are hosted by TPS intrusions and Earn Group sedimentary rocks. P-stage 3.8 veins trend E and dip to the north and south (Figure 4.11 C and D). Fault breccias containing stibnite display a similar E trend but were also noted to trend NE (e.g. the main fault in Blue Pit contains significant stibnite infill). Stibnite \pm quartz \pm carbonate \pm kaolinite veins were observed up to 5 cm thick but are generally less than 1 cm in width. These veins comprise microcrystalline quartz, carbonate and kaolinite with subhedral to anhedral stibnite (0.5 to 5 cm long). The veins have sharp margins and vary in abundance from randomly spaced singular veins up to sheeted arrays with

vein densities on the order of 10 per metre. Breccia veins containing the stibnite \pm quartz \pm carbonate \pm kaolinite mineral assemblage are typically manifested as narrow ($< 10\text{cm}$ thick), elongate zones that are clast supported and contain sub-angular to angular clasts. However, massive stibnite was also observed as infill in a 2 m thick fault zone in the Blue Pit. Kaolinite occurs as a massive, white clay infill of veins and breccia zones and is common in the Golden and Lucky pits.

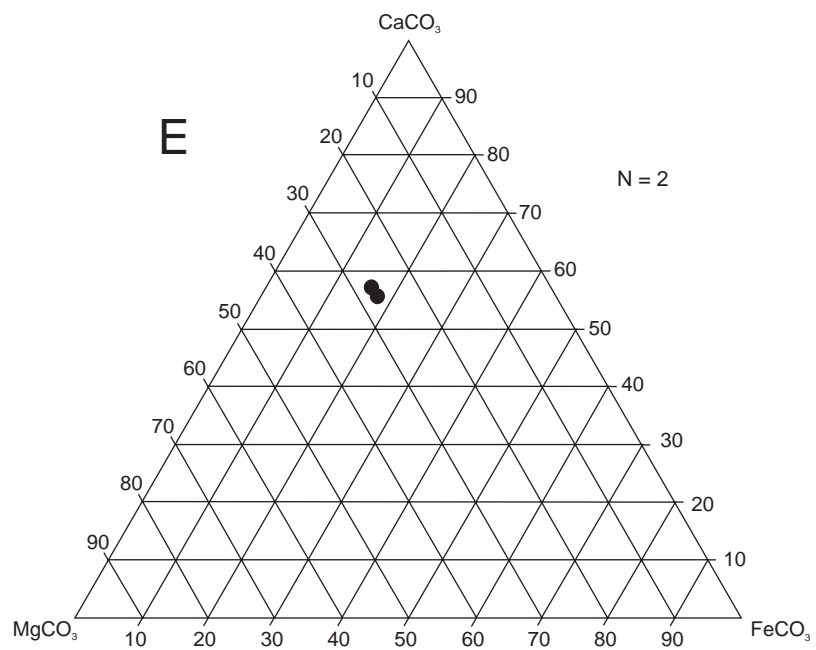
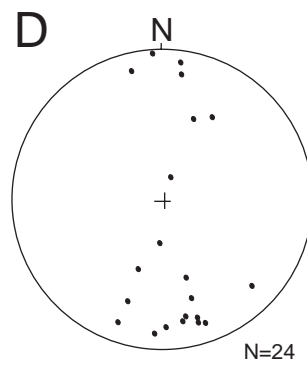
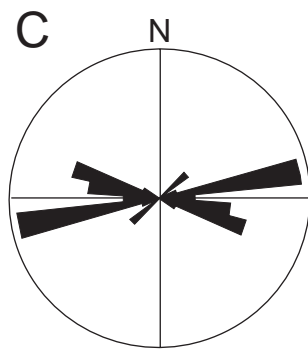
Alteration associated with stage 3.8 veins and infill is restricted to carbonate and kaolinite alteration of the wall rocks, with microprobe investigation identifying the carbonate as dolomite (Figure 4.11 E and Appendix 4). Stibnite (generally of massive form), and quartz were only observed as vein and breccia infill. This stage is younger than the P-stage 3.7 breccia as stibnite \pm quartz \pm carbonate \pm kaolinite infill was observed to overprint a breccia with P-stage 3.7 infill. P-stage 3.8 also clearly overprints P-stage 3.4 arsenopyrite \pm quartz \pm carbonate \pm gold. This is shown in figures 4.12 A where a P-stage 3.8 vein has cut P-stage 3.4 alteration and by figure 4.12 B that shows a breccia with clasts altered by P-stage 3.4 and an infill of stibnite. Though P-stage 3.8 veins and infill are widespread, they were not observed to be crosscut by any later hydrothermal events.

P-stage 4 - Weathering

The final stage in the paragenetic history of Brewery Creek is weathering. The Brewery Creek area was not affected by Quaternary glaciation that was common elsewhere in the Yukon (Clauge, 1992), and thus the upper parts of the ore zones are oxidised. The oxidised portions of the ore bodies are the only ore that has been mined at Brewery Creek to date.

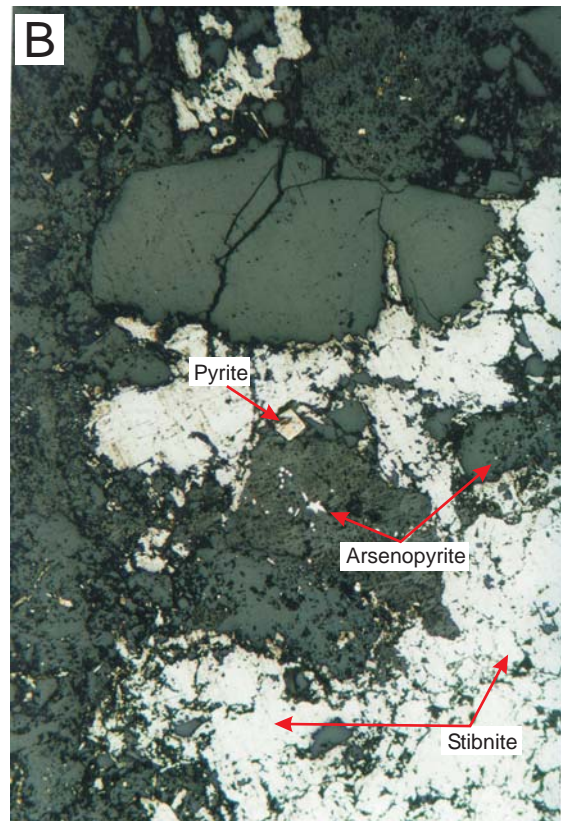
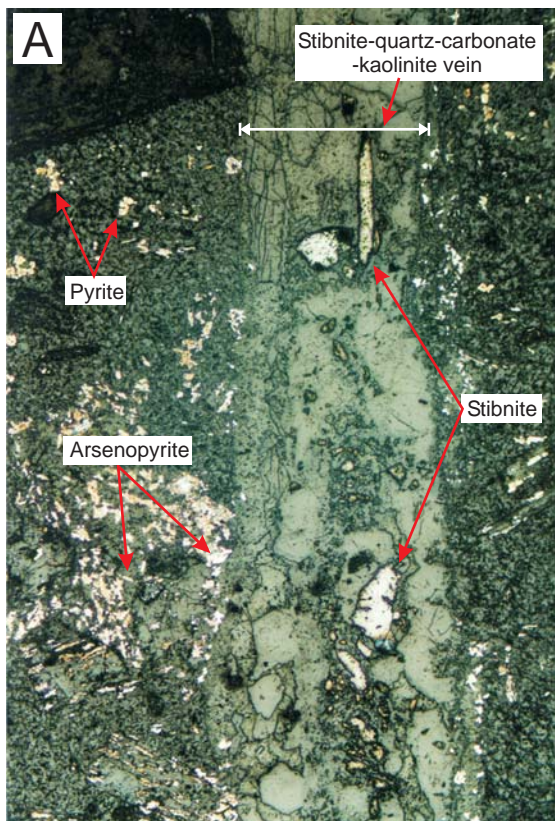
Extensive weathering persists to an average depth of 50 m below surface in intrusive rocks and 25 m below surface in sedimentary rocks. Oxidation minerals are goethite, limonite and jarosite after pyrite, scorodite after arsenopyrite, antimony ochre and kermesite after stibnite. Kaolinite and illite alteration of feldspars relates to P-stage 3.1 and 3.4 but kaolinite may have also resulted from weathering. Interestingly, samples logged as overburden and colluvium returned maximum values of 9.13 ppm Au and 7.92 ppm Au respectively (Chapter 5) indicating remobilisation (chemical or physical) of Au during weathering.

Figure 4.11 Photographs, stereonet and a ternary diagram illustrating P-stage 3.8 stibnite \pm quartz \pm carbonate \pm kaolinite. (A) A stibnite vein with minor quartz and carbonate in outcrop. Note the hammer for scale. (B) Stibnite – quartz – carbonate – kaolinite veins and breccia infill hosted by QBM. (C) Rose diagram displaying overall E strike of P-stage 3.8 veins. (D) Poles to the plane of P-stage 3.8 veins, note the dominantly steep dip. (E) Data plotted on the ternary diagram indicates that the carbonate in P-stage 3.8 veins is high in Mg (dolomite).



● Analysis of carbonate from stibnite-quartz-carbonate-feldspar veins

Figure 4.12 Photomicrographs illustrating the timing of P-stage 3.8 with respect to stages 3.1 and 3.4. (A) A photomicrograph of a P-stage 3.8 vein containing stibnite has cut P-stage 3.1 pyrite and 3.4 arsenopyrite alteration. The vein in the photomicrograph is approximately 4 mm wide (B) A photomicrograph of a breccia with P-stage 3.8 stibnite infill and clasts containing P-stage 3.1 pyrite and P-stage 3.4 arsenopyrite. The photomicrograph records and area approximately 4 mm wide.



4.4 Orientation and structural controls on the distribution of gold mineralisation

The bulk of the gold mineralisation across the Brewery Creek property has been localised along the broadly E oriented Reserve Trend. This suggests that a structure or structures along this trend acted as a fluid pathway and focussed gold-bearing fluids into suitable depositional sites. The Reserve Trend is oriented parallel to D-stage 4 thrust faults (section 3.5) which created much of the present structural architecture at Brewery Creek. The D-stage 4 faults are thought to have partly controlled the emplacement of TPS monzonite sills and reactivation of these faults post-TPS intrusion may have localised gold bearing fluids at property-scale.

In the open pits along the Reserve Trend gold assay results from exploration and blast-hole drilling have defined two distinct orientations of gold mineralisation, E and NE (Figure 4.13). These trends may be linked as in the Kokanee Pit (Figure 4.13 E) or they may show no apparent connection between one another as in the Golden Pit (Figure 4.13 C). Both E and NE mineralisation trends occur in pits dominated by intrusion-hosted gold mineralisation (eg. Kokanee, Golden, and Lucky), whereas only one of the two trends (either E or NE) is evident in pits dominated by sediment-hosted gold mineralisation (eg. Blue and Pacific). The E and NE gold mineralisation trends are apparent in the open pits for more than 5 km along the strike of the Reserve Trend. These constant orientations suggest that there are distinct structural controls on the distribution of gold mineralisation at mine-scale.

The E and NE gold mineralised zones dip steeply to the north and south (Figure 4.14) and are bound at depth by a moderately south dipping E trending fault termed the Basal Fault (section 3.5). Mineralisation trends along structure but not down dip, and no mineralisation has been found below this fault. The Basal Fault has been exposed in the Fosters Pit (Figure 4.14 and 4.15) where it juxtaposes a gold bearing monzonite sill in the hanging wall against barren monzonite sills and sedimentary rock in the footwall. This structural relationship has also been recognised in drill core throughout the Reserve Trend. Three distinct post-TPS sulphide-bearing vein events have been recognised at Brewery Creek and described in section 4.3. Measurements of P-stage 3.1, 3.4 and 3.8 vein types taken from the open pits along the Reserve Trend indicate that all 3 vein sets strike E (similar to the strike of the Reserve Trend) and dip steeply to the north and south (Figures 4.5 A and B, 4.8 B and C, and 4.11 C and D).

Figure 4.13 Gold Assay trends in the open pits. The diagram illustrates pit outlines of (A) Pacific Pit, (B) Blue Pit, (C) Golden Pit, (D) Lucky Pit and (E) Kokanee Pit overlain by gold assay trends. Note the strong E and NE mineralised trends. The gold assay trends are generated from maximum downhole gold in blasthole assay data projected to a single surface.

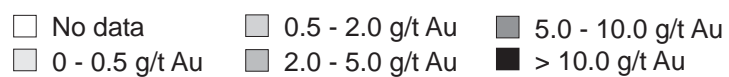
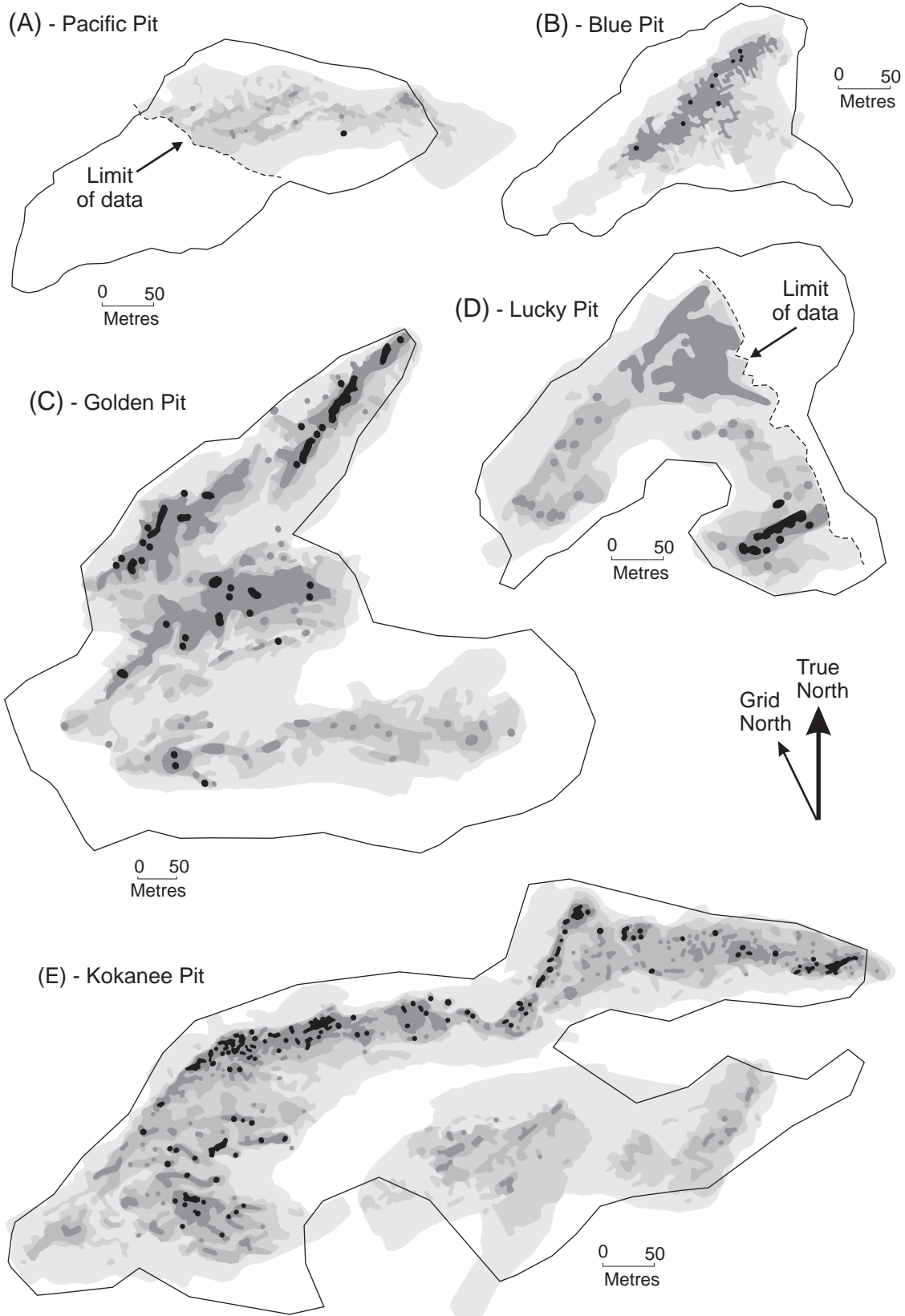


Figure 4.14 Cross sections through (A) the eastern and (B) western ends of Kokanee Pit looking west-southwest (mine grid west). Note that mineralisation dips moderately to steeply to the south and is bound at depth by a moderately dipping fault. Note also that intrusion in the footwall of the fault is not mineralised.

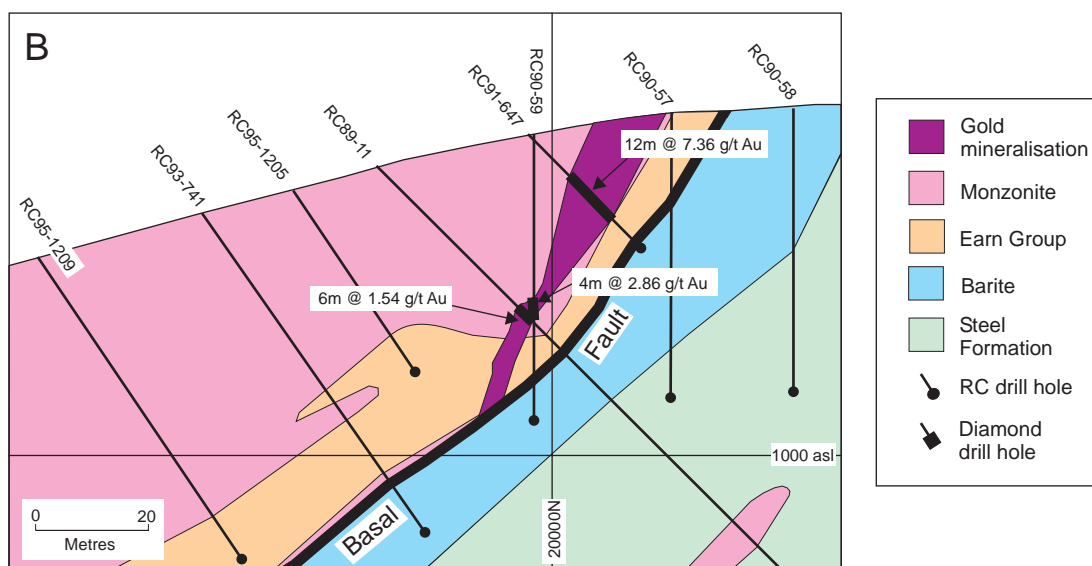
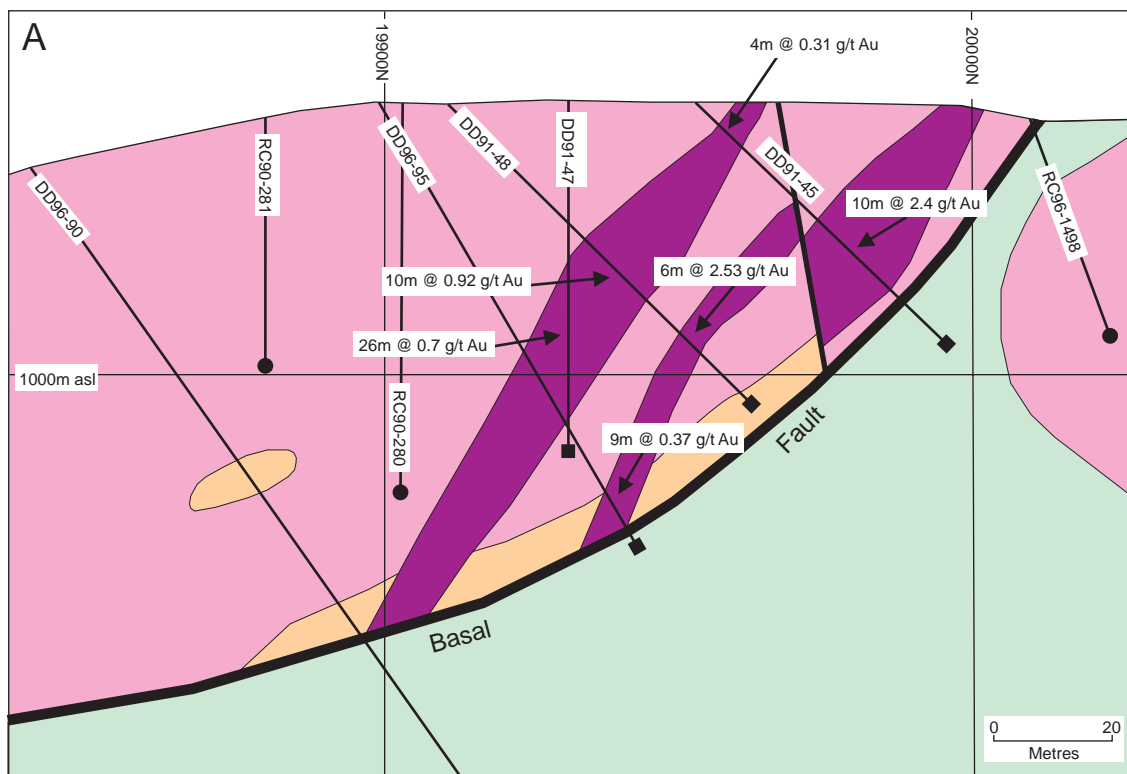
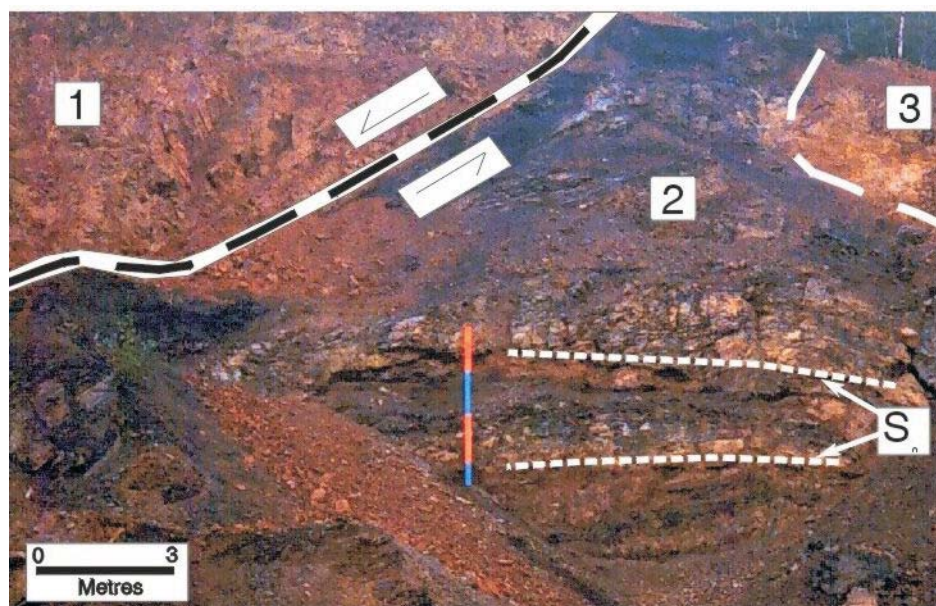


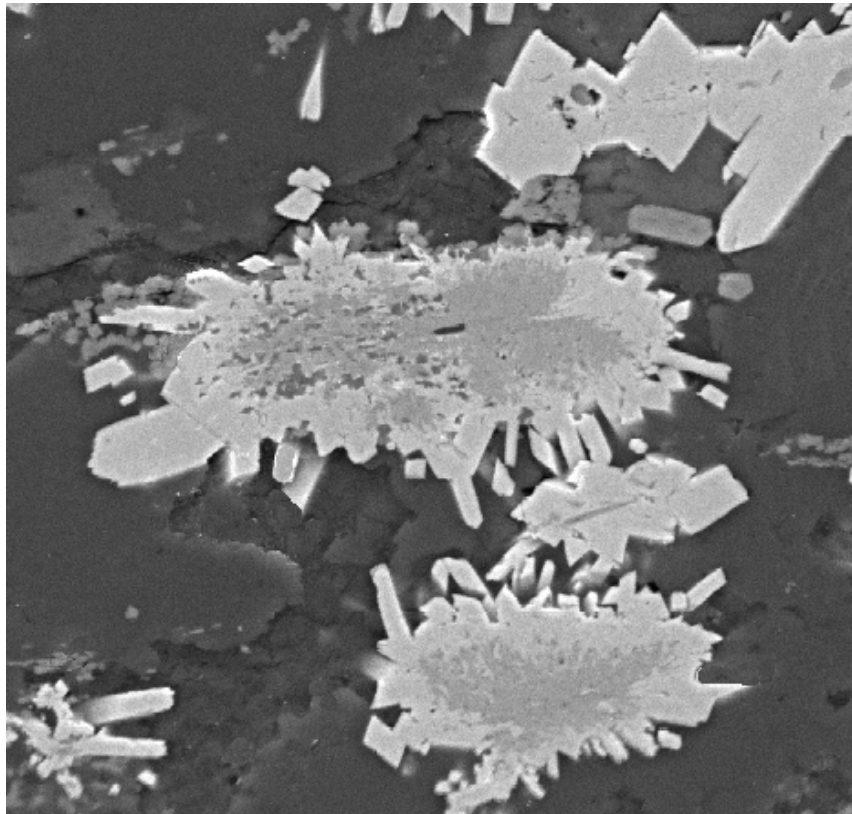
Figure 4.15 **A photograph of a wall in the Fosters Pit.** (1) is gold-bearing monzonite, (2) is unmineralised Earn Group, and (3) is unmineralised monzonite. Shear asymmetries along the fault at the base of monzonite (1) indicate normal movement. This fault is interpreted to be the Basal Fault and to bound mineralisation at depth.



Post-TPS fault sets also trend parallel to the gold assay trends. Four main orientations of post-TPS faulting (D-stage 7) have been described (section 3.5) with two of the post-TPS fault sets oriented E and NE. These E and NE post-TPS faults are commonly mineralised; in the western wall of the Blue Pit a gold-bearing NE trending fault juxtaposes chert-pebble conglomerate and siltstone against sandstone (Figure 3.19). This fault is the main structural feature in the Blue Pit and has a minimum normal movement of 70 m based on lithological offset. Disseminated gold mineralisation in the Blue Pit trends NE, parallel to this fault. A comprehensive structural model for mineralisation is presented in chapter 7.

CHAPTER FIVE

The geochemical signature of mineralisation and alteration at Brewery Creek



A scanning electron microprobe backscatter image of arsenopyrite (light grey) that has overgrown pyrite (grey) in biotite monzonite from the Kokanee pit. Image field of view is approximately 1 mm.

5.1 Chapter overview

Gold mineralisation at Brewery Creek is characterised by an Au-As-Sb \pm Ag-Pb geochemical signature. Elevated As (> 1000 ppm) is the best indicator of Au > 1 ppm and high concentrations of Sb in intrusive rocks and elevated levels of Ag and Sb in sedimentary rocks provide further indication of Au. Whole rock XRF major element analysis of alteration is characterised by enrichment of CO₂, K₂O, MnO, and SO₃ and depletion of Na₂O compared to unaltered rocks. This element mobility can be directly correlated to pervasive carbonate, sericite, pyrite, and arsenopyrite alteration of feldspar and biotite in the monzonite sills. CaO and Fe₂O₃ are comparatively immobile, which suggests that the Ca and Fe required to form calcite and pyrite respectively were sourced from destruction of feldspars and biotite.

LA-ICP-MS analysis of sulphide phases indicate that the highest Au concentrations are hosted by individual arsenopyrite crystals with lower but significant levels of Au also found in arsenopyrite overgrowths on pyrite and pyrite overgrown by arsenopyrite. Higher Au grades were found in wall rock arsenopyrite and arsenian pyrite than in vein hosted As-bearing sulphides.

Four separate geochemical datasets were used for this study, (1) an ICP-AES and ICP-OES dataset comprising 23,243 samples with 34 elements per sample, (2) a fire assay dataset with 78,658 gold analyses, (3) ICP-MS, ICP-OES, fire assay and XRF data describing 12 majors and 55 other elements from seven geologically well constrained samples, and (4) 75 LA-ICP-MS analyses with 19 elements per analysis collected from various sulphide phases.

This chapter addresses the following points:

- (1) Element distribution, zonation and correlations
- (2) The geochemical signature of gold mineralisation and alteration
- (3) The mineralogical location of gold
- (4) Variations in the geochemistry of the main sulphide phases

5.2 Element distribution and correlations

Between 1987 and 1998 Viceroy Resources Ltd established three geochemical databases, two comprising fire assay data and one with ICP-OES / -AES data. The fire assay data was partitioned into exploration drill and trench data and mine blasthole data.

The exploration fire assay database consists of 78,656 gold assays (Appendix 5). Samples were collected from diamond (122 holes for 8,895 m of core) and reverse circulation (RC; 2,310 holes for 126,108 m of RC drilling) drill holes and from trenching programs (318 trenches for 42,298 m) across the Brewery Creek property (drill holes and trench location are recorded in Appendix 6). The samples variably consisted of (1) approximately 2 m long sections of drill core that were halved, with half of the core sent for assay and the other half retained; (2) 2 m composite RC samples split with 30 % of the composite sample analysed for gold; and (3) systematic rock chip and grab samples from 2 m or 3 m sections of trenches. Where significant gold mineralisation was intersected the drill core was infrequently re-sampled and re-analysed across smaller, irregular, intervals. The geological constraints on these intervals were not recorded.

The mine blasthole fire assay database comprises 81,360 gold assays (Appendix 7). Samples were collected from 4 or 6 m deep percussion drill holes (80,760 holes for 333,055 m of percussion drilling) with each sample representing a composite over the entire hole. It should be noted that the mine blasthole data is presented for the Blue, Golden, Kokanee, Pacific and Lucky pits only. Assays for the Fosters and Canadian pits were inaccessible due to database problems.

The ICP database comprises 23,243 assays with 34 elements per assay including Ag, Al, As, B, Ba, Be, Bi, Ca, Cd, Co, Cr, Cu, Fe, Ga, Hg, K, La, Mg, Mn, Mo, Na, Ni, P, Pb, Sb, Sc, Sr, Ti, Th, Tl, U, V, W, and Zn. Geochemical samples used for these analyses were obtained from drill core, drill chips, and trenches subsequent to sampling for fire assay. The samples variably consisted of (1) approximately 2 m long sections of halved or quartered drill core; (2) re-split RC sample; and (3) systematic rock chip and grab samples from trenches.

For the purposes of this study the multi-element and exploration fire assay databases were combined with basic lithology data (Appendix 8) collected in Viceroy Exploration drill logs. Unfortunately the sampling for both fire assay and ICP-AES / -OES was not conducted with reference to geological parameters (e.g. lithological boundaries, alteration, veining, or structure) and little information describing geological features was recorded in digital format. The volume of data precluded re-logging all drill core, however, spot checks were carried out and the lithological classification is assumed to be consistent and broadly correct. Samples containing more than one recorded lithology, overburden or without a recorded lithology were removed from the dataset. Elements with assays mostly below detection were also removed (Be, Ga, Sc, and Ti). The final combined database contains 19,509 samples with 31 elements per sample and the corresponding lithology (Appendix 9).

It should be noted that several of the lithologies recorded by Viceroy Exploration do not correspond directly to the lithologies described in Chapter 3. Quartz monzonite described by Viceroy is not quartz monzonite as defined by IUGS standards. The quartz monzonite logged by Viceroy correlates to quartz-biotite monzonite described in Chapter 3 but also includes numerous samples that I would have classified as biotite monzonite. Viceroy geologists also frequently classified lithologies as limonitically altered. Most of this alteration is Fe-oxide staining that resulted from weathering and thus I did not classify anything as limonitically altered. Limestone logged by Viceroy likely corresponds to the limestone that comprises the Brewery Unit, however no other Brewery Unit-like lithologies were recorded by Viceroy. Hornfels and or calc silicate rocks are also absent from Viceroy's records.

The Viceroy lithology descriptions include classifications of overburden, no sample, road, unknown, mineralisation, stibnite, and quartz vein. These are, of course, not rock types but were used when the entire metre of trench or drilling comprised one of the above. Viceroy also used one stratigraphic marker in their logging; Steel Formation siltstone. The Steel Formation siltstone is typically wispy laminated and calcareous which is similar to the Brewery Unit siltstone but different from the carbonaceous and finely laminated Earn Group siltstones.

Descriptive statistics

Gold

To analyse the relationship between Au and various lithologies descriptive statistics were applied to the exploration fire assay database. In order to do this the fire assay

database was combined with the lithology database. However, the lithology data was collected by recording lithological boundaries whilst assay data was recorded in 2 m intervals. To combine the data Microsoft Excel 2000 was used to round assay intervals to a whole number. The 2 m assay intervals were then partitioned into 1 m intervals with the assay from the 2 m interval applied to each 1 m interval. Lithology boundaries were also rounded to a whole number. The data was then merged in Micromine (Version 8) and the corresponding lithology was attached to each assay interval. The resulting database contains 157,316 records, each with hole-ID, assay interval, assay and lithology. The data was subsequently exported to SPSS 11 (Statistical Package for the Social Sciences version 11), which was used to generate descriptive statistics. These are summarised in Table 5.1.

The results highlight the overall low grade of the Brewery Creek mine as only 9 % of the samples returned Au assays > 1 ppm, 4.1 % > 2 ppm, 1 % > 5 ppm, 0.2 % > 10 ppm and 0.03 % > 20 ppm. Poorly mineralised lithologies include brecciated chert and altered syenite (maximum assay values of 0.5 to 1 ppm Au), tuffaceous chert, tuffaceous shale, diorite, limonitic syenite, and unaltered syenite (maximum values < 0.5 ppm Au), and silicified sandstone (all assays below detection). The highest Au assay recorded at Brewery Creek was 105 ppm in limonitically altered quartz monzonite (RC drill hole 97-2019, 12 to 14 m). Assay values > 10 ppm Au were recorded in argillite, barite, chert, greywacke, shale, siltstone, Steel Formation siltstone, quartz monzonite, syenite, tuff and massive stibnite. Samples with Au grades > 10 ppm are also enriched in As (generally > 3000 ppm As). The percentage of Au assays > 1ppm was also calculated for each 'lithology' and shows that massive stibnite, massive quartz veins, quartz monzonite and biotite monzonite most commonly host higher grades. Thus while 'high grade' Au is not restricted to a specific lithology at Brewery Creek, monzonite is most commonly mineralised at > 1 ppm Au levels. Interestingly, samples logged as overburden and colluvium returned maximum values of 9.13 ppm Au and 7.92 ppm Au respectively, indicating that either the samples were mis-logged or that Au was remobilised during weathering.

Other elements

Descriptive statistics were also generated for the Viceroy multi-element data set. To refine the results the data was initially partitioned by rock type. Lithologies with < 20 assays were deemed statistically insignificant and were removed from the data set (e.g. altered quartz monzonite, greywacke, siltstone, sandstone, and Steel Formation siltstone that contain graphite and limestone). Elements with a large number of assays

Table 5.1 Summary of descriptive statistics applied to the Viceroy exploration fire assay data base. Economic gold grades were recorded in all but six lithologies. The highest gold grade recorded was 105 ppm in limonitically altered quartz monzonite. Note the high percentage of gold grades > 1 ppm in igneous rocks. The heading 'count' refers variably to the total number of samples analysed and the number of samples with > 1 ppm Au.

Rock Type	Viceroy Code	Count	Max gold (ppm)	> 1ppm Au	
				Count	%
Sedimentary rocks					
Argillite	ARG	16578	24.90	998	6
Argillite, graphitic	ARGG	21078	21.00	697	3
Barite	BAR	282	15.46	2	1
Chert	CH	1295	13.75	58	4
Chert, brecciated	CHBX	137	0.70	0	0
Chert, tuffaceous	CHT	167	0.17	0	0
Chert pebble conglomerate	CPC	1656	6.90	61	4
Greywacke	GW	1546	22.06	130	8
Limestone	LST	199	9.00	4	2
Shale	SH	6340	24.20	372	6
Shale, graphitic	SHG	3313	15.82	165	5
Shale, tuffaceous	TSH	14	0.05	0	0
Siltstone	SLT	3620	15.62	203	6
Siltstone, graphitic	SLTG	1063	3.54	26	2
Sandstone	SS	3377	8.96	301	9
Sandstone, graphitic	SSG	184	5.86	11	6
Sandstone, silicified	SSS	13	BD	0	0
Steel Formation siltstone	SST	8363	25.71	413	5
Steel Formation siltstone, cherty	SSTC	576	1.76	2	0
Steel Formation siltstone, graphitic	SSTG	138	1.75	2	1
Steel Formation siltstone, silicified	SSTS	118	2.72	4	3
Steel Formation siltstone, limonitic	LSST	207	3.24	6	3
Igneous rocks					
Monzonite, limonite altered	LAM	44	1.00	1	2
Biotite monzonite	BM	1047	2.28	28	3
Biotite monzonite, altered	ABM	502	2.43	8	2
Biotite monzonite, limonite altered	LABM	658	9.40	72	11
Biotite monzonite, limonitic	LBM	590	6.74	17	3
Quartz monzonite	QM	9472	17.20	331	3
Quartz monzonite, altered	AQM	15106	24.11	2287	15
Quartz monzonite, altered, graphitic	AQMG	38	8.09	11	29
Quartz monzonite, limonitic	LQM	2673	11.28	30	1
Quartz monzonite, limonite altered	LAQM	47408	105.00	7518	16
Diorite	DI	31	0.40	0	0
Syenite	SY	111	0.27	0	0
Syenite, altered	ASY	72	0.60	0	0
Syenite, limonite altered	LASY	524	100.00	13	2
Syenite, limonitic	LSY	67	0.33	0	0
Other					
Tuff	TUFF	2123	48.50	30	1
Dolerite	DR	421	3.19	10	2
Dolerite, limonite altered	LADR	430	3.40	14	3
Colluvium	CV	572	7.92	42	7
Fault	FT	588	6.64	38	6
Overburden	OB	3561	9.13	119	3
Quartz vein	QTZ	56	6.54	15	27
Massive stibnite	SB	88	12.00	31	35

below detection were also removed (e.g. Be, Ga, Sc, and Ti). Descriptive statistics were then generated for each lithology using Microsoft Excel 2000 (results summarised in Appendix 10).

The descriptive statistics show that maximum values of some elements vary dramatically between lithologies. Silver values of 450 ppm were recorded in quartz monzonite, and values > 100 ppm were encountered in altered quartz monzonite, argillite and shale. In most other lithologies maximum Ag contents were typically < 30 ppm. 104 Ag assays out of 19,509 were > 10 ppm and only 23% of the data was > 1 ppm Ag. The highest Cu value (12,974 ppm) was recorded in argillite with values > 1000 ppm found in altered quartz monzonite and shale. Typical maximum Cu values for lithologies were 250 to 400 ppm but were as low as 78 ppm in barite. Lead values > 16,000 ppm were assayed in argillite and quartz monzonite contrasting with a maximum of 34 ppm in Steel Formation siltstone. All Pb assays were above the detection limit, however, only 4% of the assays were > 100 ppm. Zinc levels were also all above the detection limits with 85% of the assays > 100 ppm Zn and 3.5% > 1,000 ppm Zn.

Maximum Sb values varied according to rock type with assays > 20,000 ppm in half of the lithologies and < 550 ppm in most of the remainder. More than 80% of the Sb assays were > 10 ppm, 25% were > 100 ppm and approximately 5% of the assays were > 1,000 ppm. Molybdenum assays were generally above detection with 90% of the assays > 2 ppm and 20 % > 10 ppm. A maximum Mo assay of 106 ppm was recorded in limonitically altered quartz monzonite. Bismuth and W were typically below detection with less than 20% of assays registering greater than 2 ppm Bi or W and only 130 Bi assays and 46 W assays out of 19,509 results were > 10 ppm. Maximum Bi values were generally < 40 ppm but values of 638 ppm and 198 ppm were recorded in tuff and limonitically altered quartz monzonite.

Barium values ranged from 56,096 ppm in argillite and > 10,000 ppm in graphitic argillite, chert pebble conglomerate, limonitically altered quartz monzonite, quartz monzonite and shale, to 660 ppm in dolerite. Barite samples with more than 10000 ppm Ba typically contained < 0.1 ppm Au and of the samples that contained > 1 ppm Au, < 3 % contained more than 2,000 ppm Ba. Mercury levels ranged from 219,000 ppm in argillite to below detection in dolerite and limonitically altered dolerite. The Hg assays are strongly polarised with almost 40% > 1,000 ppm Hg and another 45% below detection. This is highly anomalous and likely reflects an error in the data.

Arsenic concentrations were > 100 ppm in 67% of the analysis and > 1,000 ppm in 20%. Every lithology analysed, apart from barite, contained As at > 2,000 ppm levels (Table 5.2). The highest As assay was 30,260 ppm in tuff, and the same interval also recorded the highest Au assay for the multi-element data set. Arsenic assays above 10,000 ppm were recorded in unaltered, altered and limonitically altered quartz monzonite, siltstone, and shale. Average As values were highest in greywacke (1,203 ppm), limonitically altered quartz monzonite (999 ppm), and dolerite (972 ppm) with tuff recording an average of only 345 ppm As. The percentage of assays with As values > the mean plus two standard deviations was also calculated for each lithology. The results indicate that while quartz monzonite samples typically record higher As values than other lithologies, the percentage of highly As enriched samples for each lithology is comparable.

Element correlations

To understand element relationships the combined multi element and exploration fire assay database was analysed through correlation matrices generated in Microsoft Excel 2000. Correlation matrices were produced for the entire dataset and for rock types with enough assays to provide meaningful data. The resulting matrices are presented in Appendix 11. The matrices identify several suites of elements that display consistent correlations between rock types. All correlations with $r^2 > 0.5$ were deemed to be significant, and these are summarised in Table 5.3.

The most common correlation is Au-As \pm Ag that was evident in all lithologies except barite and limonitically altered dolerite. A Au-As correlation coefficient of 0.68 was calculated for the entire data set, however, correlation coefficients ranged from 0.51 in dolerite to 0.93 in tuff. Gold-Ag and As-Ag correlation coefficients for the entire dataset are 0.10 and 0.09 respectively, but were as high as 0.94 (Au-Ag) and 0.91 (As-Ag) in tuff. In felsic intrusive rocks Au correlated with As only ($r^2 = 0.54$, 0.64 in quartz monzonite and limonitically altered quartz monzonite respectively), but in other lithologies Au also correlated with Bi ($r^2 = 0.87$ in dolerite and limonitically altered dolerite, and 0.99 in tuff), Pb ($r^2 = 0.70$ in Steel Formation siltstone, 0.83 in tuff), and Sb ($r^2 = 0.50$ in Steel Formation siltstone, 0.52 in limonitically altered dolerite, 0.75 in chert) and less commonly Ba ($r^2 = 0.76$ in Steel Formation siltstone), Cd ($r^2 = 0.53$ in tuff, 0.59 in Steel Formation siltstone), Cr ($r^2 = 0.53$ in Steel Formation siltstone), Mo ($r^2 = 0.71$ in Steel Formation siltstone), Ni ($r^2 = 0.53$ in Steel Formation siltstone), V ($r^2 =$

Table 5.2 A summary of maximum As values and relative As enrichments in various lithologies. Arsenic concentrations > 10000 ppm were recorded in quartz monzonite, tuff, siltstone and shale. However, the percentage of As enrichment relative to the mean plus two standard deviations is similar in all lithologies suggesting that there is no lithological control on As distribution.

Rock Type	Viceroy code	Count	Max Arsenic (ppm)	Assays > mean + 2 standard deviations	
				Count	%
Sedimentary rocks					
Argillite	ARG	3056	7834	52	2
Argillite - graphitic	ARGG	1651	7805	55	3
Barite	BAR	80	339	6	8
Chert	CH	220	4307	12	5
Chert pebble conglomerate	CPC	161	6370	8	5
Greywacke	GW	125	5133	5	4
Shale	SH	899	10753	31	3
Shale - graphitic	SHG	112	4836	5	4
Siltstone	SLT	216	10000	11	5
Sandstone	SS	337	4421	13	4
Steel formation siltstone	SST	33	2910	3	9
Igneous rocks					
Quartz monzonite	QM	2327	10025	96	4
Quartz monzonite - altered	AQM	2189	14100	113	5
Quartz monzonite - limonitically altered	LAQM	7547	14032	365	5
Volanic rocks					
Dolerite	DR	125	6001	7	6
Dolerite - limonitically altered	LADR	80	2150	3	4
Tuff	TUFF	316	30260	4	1

Table 5.3 **A summary of element correlations versus rock type. Note that the most common correlation is Au-As \pm Ag.** Numerous elements consistently showed no correlation, in particular Bi, Hg, Sb, U and W.

	All Data	AQM	ARG	ARGG	BAR	CH	CPC	DR	GW	LADR	LAQM	QM	SH	SHG	SLT	SS	SST	TUFF
Correlations																		
Au-As +/- Ag																		
Ag-Pb +/- Sb																		
Al-K-Na +/- Ti																		
Ca-Mg +/- Sr																		
Cd-Zn +/- Cu, Mo, Ni, V																		
Co-Fe +/- Ni, Mn, Zn																		
La-Th																		
No correlation any other element																		
B																		
Ba																		
Bi																		
Cr																		
Hg																		
Mn																		
Pb																		
Sb																		
U																		
W																		



Correlation of $r^2 > 0.5$ for main elements listed (e.g. for Au-As +/- Ag only the Au-As correlation is considered)

No correlation for various elements in the respective rock types.

Correlation of $r^2 < 0.5$ with other elements not shown

0.69 in Steel Formation siltstone), and Zn ($r^2 = 0.56$ in Steel Formation siltstone). The strength of Au correlation and the lithologies that host the correlation is summarised in Table 5.4.

Silver also correlated with Pb \pm Sb in 10 lithologies, although Pb had no correlation in 7 out of 17 lithologies and Sb showed no correlation in 10 lithologies. The Ag-Pb and Ag-Sb correlation coefficients for the entire dataset were 0.68 and 0.19 respectively. The strongest and weakest correlations for Ag-Pb were 0.95 in tuff and -0.05 in greywacke and were 0.69 in shale and 0.01 in dolerite for Ag-Sb correlations.

Cadmium-Zn \pm Cu, Mo, Ni, V was also a common correlation with the Ni-Zn, Cu-V and Mo-Ni subsets consistently identified across lithologies. The average Cd-Zn, Ni-Zn, Cu-V and Mo-Ni correlation coefficients were 0.72, 0.55, 0.2, and 0.5 respectively. The strongest correlations were 0.95 for Cd-Zn in altered quartz monzonite, 0.95 for Ni-Zn in chert pebble conglomerate, 0.64 for Cu-V in chert, and 0.73 for Mo-Ni in greywacke. In felsic intrusive rocks Cd-Zn most commonly correlated, however, Cd-Zn-V and Cd-Zn-Pb correlations were identified in quartz monzonite and altered quartz monzonite respectively. In sedimentary rocks Cd also variably correlated with Cr ($r^2 = 0.69$), Fe ($r^2 = 0.56$), Mn ($r^2 = 0.51$), Mo ($r^2 = 0.55$), P ($r^2 = 0.64$), Pb ($r^2 = 0.55$), Sb ($r^2 = 0.50$), Sr ($r^2 = 0.56$), Ti ($r^2 = 0.53$), U ($r^2 = 0.63$), and W ($r^2 = 0.53$).

Cobalt correlated with Fe \pm Ni-Mn-Zn in 12 of the lithologies analysed and correlations of Co-Fe-Mn and Co-Fe-Ni were also repeatedly identified. The average correlation coefficient for Co-Fe was 0.68 with the strongest correlation (0.86) in graphitic argillite. The strongest correlation coefficients for Co-Mn, Co-Ni, and Co-Zn were 0.80 in siltstone, 0.92 in siltstone, and 0.77 in barite respectively. The Co-Fe \pm Ni-Mn-Zn correlations were evident in both sedimentary and intrusive lithologies. Cobalt also locally correlated with Hg ($r^2 = 0.52$), Mg ($r^2 = 0.53$), Na ($r^2 = -0.58$), P ($r^2 = 0.64$), Sr ($r^2 = 0.54$), Ti ($r^2 = 0.64$), V ($r^2 = 0.60$) and W ($r^2 = 0.76$).

A Ca-Mg \pm Sr correlation was identified in all lithologies except chert pebble conglomerate, dolerite and tuff and likely relates to the widespread distribution of carbonate (dolomite) veining and alteration (see Chapter 4). The Ca-Mg correlation coefficient averaged 0.63 across all of the data but ranged from 0.98 in Steel Formation siltstone to 0.53 in quartz monzonite. Calcium-Sr correlation coefficients varied from -0.58 in limonitically altered dolerite to 0.90 in barite and averaged 0.45 for the entire

Table 5.4 A summary of elements that show a significant correlation to gold.

The numbers represent the degree of correlation between gold and the elements listed with one representing a perfect positive correlation, zero representing no correlation and -1 representing a perfect negative correlation. The table shows that the major correlation is gold to arsenic. Other significant correlations are gold with silver, bismuth, lead and antimony, however, these are typically related to specific lithologies suggesting multiple controls on element relationships. In samples of Steel Formation siltstone Au correlated with Ag, As, Cd, Cr, Mo, Ni, Pb, Sb and Zn. Most of these correlations are unlikely to be significant and can be attributed to the small sample population. Note that there is no correlation between Au and Hg, and that Au does not correlate with As in barite.

Rock type	Viceroy code	Count	Ag	As	Bi	Cd	Cr	Hg	Mo	Ni	Pb	Sb	Zn
	All data	19509	0.10	0.68	0.22	0.01	-0.08	0.10	-0.06	-0.08	0.05	0.18	-0.01
Altered quartz monzonite	AQM	2189	0.11	0.64	-0.01	0.02	0.00	0.16	-0.04	-0.06	0.07	0.28	0.02
Argillite	ARG	3056	0.09	0.72	0.00	-0.01	-0.06	0.01	-0.10	-0.09	0.01	0.23	-0.07
Argillite, graphitic	ARGG	1651	0.11	0.73	0.02	-0.04	-0.06	0.04	-0.09	-0.11	0.04	0.23	-0.06
Barite	BAR	80	0.15	0.35	-0.10	0.01	0.17	0.04	0.00	0.10	0.07	0.41	0.03
Chert	CH	220	0.18	0.65	0.15	-0.09	0.00	-0.04	0.05	-0.08	0.08	0.75	-0.12
Chert pebble conglomerate	CPC	161	0.46	0.58	0.20	0.03	-0.12	0.25	-0.05	0.04	0.00	0.17	0.02
Dolerite	DR	135	0.18	0.51	0.87	0.06	-0.06	.	0.03	-0.10	0.40	0.07	-0.01
Greywacke	GW	125	0.39	0.72	0.19	-0.21	-0.01	0.15	-0.17	-0.19	0.02	0.41	-0.20
Limonitically altered dolerite	LADR	80	0.53	0.20	0.87	-0.13	0.20	.	0.06	-0.23	0.48	0.52	-0.20
Limonitically altered quartz monzonite	LAQM	7547	0.33	0.64	0.00	0.07	-0.06	0.14	0.00	-0.05	0.03	0.16	-0.02
Quartz monzonite	QM	2327	0.00	0.54	-0.03	0.09	-0.16	0.09	0.02	-0.02	0.00	0.13	0.02
Shale	SH	899	0.21	0.80	-0.05	0.10	0.02	0.13	-0.06	-0.08	0.08	0.27	-0.01
Shale, graphitic	SHG	112	0.62	0.91	-0.09	-0.07	0.07	-0.04	-0.18	-0.12	0.00	0.30	-0.14
Siltstone	SLT	216	0.65	0.69	0.14	0.04	-0.01	-0.12	-0.04	-0.13	-0.04	0.39	-0.18
Sandstone	SS	337	0.34	0.82	-0.05	-0.10	0.08	-0.07	0.03	-0.16	-0.02	0.08	-0.12
Steel Formation siltstone	SST	33	0.67	0.81	-0.05	0.59	0.53	0.50	0.71	0.53	0.70	0.50	0.56
Tuff	TUFF	316	0.94	0.93	0.99	0.53	-0.01	-0.03	0.43	0.01	0.83	0.21	0.23

dataset. The Ca-Mg \pm Sr relationship was consistent in the felsic intrusive rocks, however, Ca also correlated with Cd ($r^2 = 0.60$), Cu ($r^2 = 0.53$), La ($r^2 = 0.64$), Mn ($r^2 = 0.54$), Mo ($r^2 = 0.55$), Na ($r^2 = 0.59$), P ($r^2 = 0.59$), U ($r^2 = 0.84$), V ($r^2 = 0.54$), and Zn ($r^2 = 0.54$) in sedimentary rocks.

Other correlations identified include La-Th in 13 lithologies (the strongest and average r^2 values are 0.88 and 0.73 respectively), and Al-K-Na \pm Ti in 9 lithologies (the strongest and average r^2 values for Al-K are 0.93 and 0.86 respectively). Elements that rarely correlated with any other elements were B, Ba, Bi, Cr, Hg, Mn, Pb, Sb, U, and W. It is interesting to note the lack of correlation between Hg and other elements and specifically no correlation between Hg and Au. The Brewery Creek gold deposit was discovered during the investigation of Hg anomalies (R. Diment pers. comm. 1999).

Factor analysis

Factor analysis using Varimax rotation of data with Kaiser normalisation and principal component analysis extraction (Harman, 1976; Kaiser, 1958) was applied to further investigate elemental associations within the Viceroy multi-element data set and to characterise the metallogenic signature of gold mineralisation. Factor analysis identifies the inter-relationships between elements and detects clusters of elements in multi-dimensional data. This method allows a large geochemical dataset to be explained by a small number of factors; these factors describe the dominant associations between elements. The factors can be interpreted similarly to correlation coefficients so that the highest absolute values within each factor define a group of variables that are strongly inter-correlated. The factors are numerically ranked according to the percentage of variance that they describe with element associations in factor 1 accounting for the most variance. Factor scores (i.e., the relative correlation of each sample for a specific factor association) were also generated in order to investigate the relationship of factors to each lithology (Appendix 12). To carry out the factor analysis the data was initially log transformed, as geochemical data distributions are typically log normal, and 0.0001 was added to all data to remove the effects of zero values. The factor analysis was performed using the computer program SPSS (version 11), and the results are presented in Table 5.5a.

A nine-factor model explains approximately 73 % of the variation in the Viceroy multi-element database. Additional factors were deemed statistically insignificant as they are characterised by Eigen values less than 1.0 (Table 5.5b) and thus explained less of the

Table 5.5 **Factor analysis of the multi-element data set.** (A) A table documenting the calculated factors. Each column represents a factor with the elements that display the highest absolute values in that column defining the factor. Note that factor three correlates Au with As-Sb \pm Ag, Pb and that Hg does not correlate with Au. (B) Eigen values for the multi-element factor analysis. Eigen values less than one indicate that the factors are statistically insignificant. Note the percentage of variance that each factor describes.

A

Element	Component								
	1	2	3	4	5	6	7	8	9
Ag	-0.46	0.45	0.55	-0.04	0.15	0.03	0.00	0.11	0.02
Al	0.32	0.10	-0.11	0.69	0.08	0.35	0.21	0.04	0.00
As	0.17	-0.06	0.85	-0.17	-0.09	0.00	0.01	0.07	0.06
Au	0.05	-0.14	0.85	-0.11	-0.04	-0.11	-0.02	0.02	0.11
B	-0.39	0.38	-0.06	-0.24	0.05	0.02	0.34	0.24	-0.32
Ba	-0.03	0.06	0.04	0.05	-0.36	0.69	-0.05	-0.01	0.10
Bi	0.04	0.01	0.05	0.11	0.00	-0.01	-0.18	0.76	-0.02
Ca	0.12	-0.07	-0.17	0.09	0.91	-0.06	-0.04	0.00	0.00
Cd	-0.04	0.78	0.11	-0.10	0.10	0.13	-0.16	0.01	-0.01
Co	0.87	0.20	-0.05	0.07	-0.04	-0.16	0.06	0.00	0.04
Cr	-0.16	0.23	-0.02	0.33	0.31	0.18	0.27	-0.08	0.44
Cu	-0.28	0.73	-0.04	0.10	0.01	-0.07	0.02	0.20	0.05
Fe	0.88	0.02	0.13	0.10	-0.07	-0.06	0.06	0.05	-0.06
Hg	-0.08	0.13	0.02	-0.12	-0.10	0.07	-0.84	0.09	-0.09
K	-0.05	0.11	-0.16	0.60	0.02	-0.10	0.46	0.17	-0.41
La	0.57	-0.18	0.17	0.17	-0.02	0.62	-0.01	0.11	-0.13
Mg	0.22	-0.13	-0.25	0.36	0.73	-0.29	0.04	-0.05	-0.02
Mn	0.82	-0.08	0.12	-0.02	0.30	0.04	-0.11	-0.06	0.06
Mo	-0.29	0.63	0.01	-0.17	-0.15	0.18	0.24	0.02	0.17
Na	0.05	-0.14	-0.15	0.84	0.01	0.00	0.04	0.05	0.03
Ni	0.21	0.88	-0.13	-0.04	-0.13	-0.03	0.00	-0.02	0.12
P	-0.05	0.35	-0.13	0.17	0.33	0.69	-0.05	0.11	0.01
Pb	0.34	-0.03	0.55	-0.03	-0.02	0.22	0.00	0.07	-0.19
Sb	-0.01	0.17	0.77	-0.07	-0.15	-0.01	-0.06	-0.08	0.03
Sr	-0.19	0.12	0.05	-0.17	0.76	0.15	0.17	0.09	0.02
Ti	0.07	-0.13	-0.09	0.87	0.04	0.14	-0.09	-0.02	0.09
Th	0.67	-0.37	0.19	0.17	-0.08	0.38	0.07	0.09	-0.11
U	0.00	0.11	0.00	-0.05	0.06	0.14	0.17	0.63	0.31
V	-0.31	0.48	-0.10	0.19	0.16	0.55	-0.07	0.03	0.35
W	0.01	0.16	0.08	-0.01	-0.06	0.01	0.03	0.26	0.59
Zn	0.41	0.77	0.10	-0.09	0.03	0.13	-0.10	-0.03	0.03

B

Component	Initial Eigenvalues		
	Total	% of variance	Cumulative %
1	5.29	17.07	17.07
2	4.19	13.50	30.57
3	3.99	12.89	43.46
4	2.36	7.62	51.07
5	2.11	6.81	57.88
6	1.61	5.18	63.06
7	1.19	3.82	66.88
8	1.13	3.65	70.53
9	1.01	3.25	73.78
10	0.92	2.98	76.76
11	0.84	2.71	79.47
12	0.76	2.46	81.93

data variance than the single elements themselves. Factors 1, 2 and 3 each describe more than 10% variance in the data set. Factor 1 contains high loadings for Co, Fe, and Mn and smaller but significant values for La and Th. Samples that score highly into factor 1 were mostly felsic intrusive rocks, comprising 87% of the samples with factor scores greater than one. Factor 2 includes Cd, Cu, Mo, Ni, and Zn, a typical transition metal association. Samples of sedimentary rocks score highly on factor 2 and account for 72% of assays that have factor scores greater than one despite comprising only 26% of the multi-element data base. Out of the samples that scored within the top 100, 89 were sedimentary rocks and of those 73 were argillite or graphitic argillite.

Factor 3 describes Au predominantly associated with As and Sb but also with Ag and Pb and is the only factor to have a significant loading for Au. This factor suggests that As and Sb are consistently associated with Au, a correlation that reflects the presence of abundant arsenopyrite and stibnite in mineralised zones at Brewery Creek (Chapter 4 and section 5.4). Silver and / or Pb bearing minerals were not identified during this study but their association with gold likely reflects the presence of trace amounts of tetrahedrite ($(\text{Cu, Fe, Zn, Ag})_{12}\text{Sb}_4\text{S}_{13}$) and boulangerite ($\text{Pb}_5\text{Sb}_4\text{S}_{11}$) as documented by Honea (1997). The relationship between Au, As, Ag, Pb, and Sb is discussed further in section 5.4. Samples of intrusive rocks account for 68% of the top 100 scores for factor 3. This is higher than the percentage of intrusive rock in the multi-element database (i.e. felsic intrusive rocks - 63%, sedimentary rocks - 26%, and volcanic rocks - 13%) and likely reflects the fact that monzonite sills host the majority of ore at Brewery Creek. However, sedimentary rocks comprise 31% of the top 100 scores, suggesting that distribution of elements included in factor 3 is unlikely to be solely controlled by rock type. Interestingly 50% of the samples with a negative correlation > -2 are tuff even though tuff samples account for $< 13\%$ of the data and tuff hosts the highest Au and As values for this dataset. The reasons for this are unclear but might be related to how a tuff was identified (i.e. was it really a tuff or was it an altered rock that looked like tuff).

Factors 4 and 5 describe 7% and 6% of the data variance respectively. Factor 4 links Na with Ti, Al, and K. These elements form a variety of common silicate minerals and in particular feldspars and clays. Samples of felsic intrusive rocks comprise 85% of the top 1000 factor 4 scores with samples of sedimentary rock accounting for 10% and volcanic rock 5%. Thus this factor most likely reflects primary variance in unaltered sample composition, in particular in felsic intrusive rock, and secondary variance related to alteration and weathering. Factor 5 clusters Ca and Mg with Sr, and can be

attributed to the widespread distribution of carbonate (and / or dolomite) veining and alteration (Chapter 4). The top 100 scores for factor 5 included 54 samples of argillite and 18 of other sedimentary rocks.

Factors 6, 7, and 9 record the element associations Ba-La-P-V, -Hg-K and to a lesser extent -Hg-K-B-Cr, and -K-W-Cr respectively. Investigation of samples that record factor scores within the top 100 for each factor show that at least 70% of the samples were sedimentary rocks and more than half of those are argillite. Thus, these factors most probably reflect variations in the sedimentary protolith and more specifically the argillite or black shale component. Finally factor 8 documents a Bi-U relationship. The top 100 scores for factor 8 comprised 28% felsic intrusive rock, 32% sedimentary rock and 42% volcanic rock. However, for factor scores > 1, 53% of the samples were felsic intrusive rock and 39% were sedimentary rock. Bismuth and U assays are typically below detection (Bi 80% and U 90% below detection), thus factor 8 is interpreted to reflect minor litho-geochemical variations among a few samples.

Factor analysis was also performed on data partitioned into (1) major rock type (felsic intrusive rocks, carbonaceous sedimentary rock, and other sedimentary rock) to look for lithological controls on factors, and (2) mineralised zones (West Big Rock, Moosehead, Blue, Pacific, Canadian, Fosters, Kokanee, Golden, Lucky, and Bohemian) to potentially identify element zonation along the Reserve Trend. Factor analysis of data partitioned into three major rock types provides similar results (Appendix 13) to the factor analysis of the entire dataset. The element relationships Co-Fe-Mn, Au-As-Sb \pm Ag-Pb, Al-Na \pm K-Ti, Ca-Mg \pm Sr, and La-Th were identified in all lithologies though the amount of variance that each factor describes shows minor changes between lithology. Thus, the element correlations described in these factors are unlikely to be controlled by lithology. Other element associations are less consistent. Nickel and Zn correlate with Co-Fe-Mn in sedimentary rocks and Cd-Cu-Mo in felsic igneous rocks. Mercury variably correlates with Cd-Ba-P-V, and negatively with K and Cr. Tungsten correlates with U, Bi and Pb, but Bi shows no correlation to any other elements in sedimentary rocks. As these element relationships vary between lithology they are likely to be at least partly controlled by lithology.

Factors describing Co-Fe \pm Mn-Ni, Au-As-Sb \pm Ag-Pb, Na-Ti \pm Al-K, Ca-Mg \pm Sr, La-Th, and Cd-Cu \pm Ni-W-Mo element relationships were evident in all mineralised zones (Appendix 14), though La-Th was variably correlated with Co-Fe-Mn, Al, and Ba. Minor element variability was noted in all of the Co-Fe \pm Mn-Ni, Au-As-Sb \pm Ag-Pb, Na-Ti \pm

Al-K, Ca-Mg \pm Sr, La-Th, and Cd-Cu \pm Ni-W-Mo factors, however, this variation is simply interpreted to reflect litho-geochemical variations among a few samples. The repeatedly identified factors suggest that the controls on these elements associations are consistent along the Reserve Trend. The consistent Au-As-Sb \pm Ag-Pb correlations suggest that only one geochemical style of mineralisation is present.

Factor analysis and gold exploration

The Au-As-Sb \pm Ag-Pb relationship identified in factor 3 and in the correlation matrices suggests that As-Sb, and to a lesser extent Ag-Pb, may be used in exploration to target potential Au mineralisation and to highlight areas where drilling might not have intersected Au mineralisation but where Au mineralisation is likely to be present nearby. To quantify these results two sets of cross-sections were generated that display lithology, Ag, As, Pb, and Sb concentration data overlain by Au mineralisation > 1 ppm. The sections cut known Au mineralisation in felsic intrusive rocks in the Golden pit (Section 21760 E – Figures 5.1 a - g) and in sedimentary rocks in the Blue pit (Section 18470 E – Figures 5.2 a - g). The southerly dip of the lithologies and Ag, As, Au, Pb and Sb grades interpreted on the sections is consistent with the orientation of bedding, veins and faults measured on the surface (Chapters 3.5 and 4.4). The geological and geochemical interpretation of sections presented is assumed to be broadly correct but is limited by the lack of down-hole information (i.e. structures, mineralogy, and orientation of drill-holes) and uncertainty of grade continuity between drill holes.

The sections show that lithology is not the primary control on the distribution of Au, Ag, As, Pb and Sb. Element enrichments occur in both sedimentary and intrusive rocks and trend across lithology boundaries. In intrusive rocks Au grades > 1 ppm best correlate with As, generally occurring in zones of > 1000 ppm As (Figure 5.1 c). Antimony > 250 ppm correlates with Au > 5 ppm, however, a zone of 2-5 ppm Au mineralisation occurs in an area of < 50 ppm Sb suggesting similar but not identical controls on the distribution of Au and Sb (Figure 5.1 d). Moderate to low grades of Ag and Pb accompany >1 ppm Au grades (Figure 5.1 e and f), however, the correlation between Au and Ag-Pb is less clear than between Au and As-Sb.

The distribution of Au > 1 ppm is also most comparable to As in sedimentary rocks with zones of > 1 ppm Au mineralisation typically recording As values > 2000 ppm (Figure 5.2 c). Similar trends are evident in the entire Viceroy multi element data set with 89% of the Au grades > 1 ppm corresponding to As grades > 1000 ppm. Elevated Sb occurs

Figure 5.1 Cross-sections through the Golden pit (21760E) illustrating the distribution of elements that comprise factor three (A, C, D, E, F), lithology (B), and the factor 3 scores (G). Values of each element and the factor scores have been contoured. Gold contours are overlain on As, Sb, Ag, Pb, lithology, and factor scores for comparison. Note that Au and As concentrations are similar but that factor 3 scores best describe the distribution of Au. Cross-sections are drawn looking west.

Figure 5.1 A

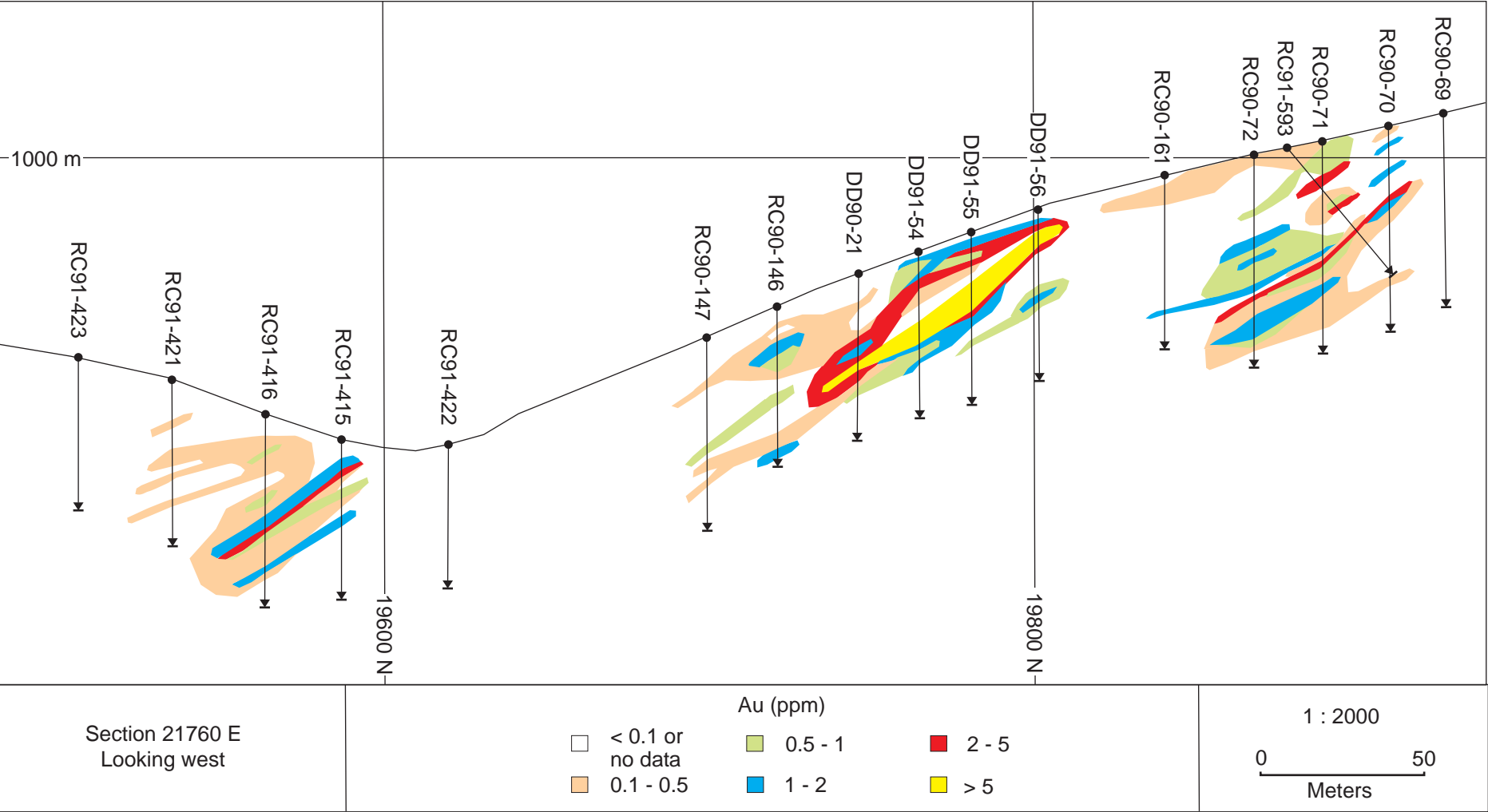


Figure 5.1 B

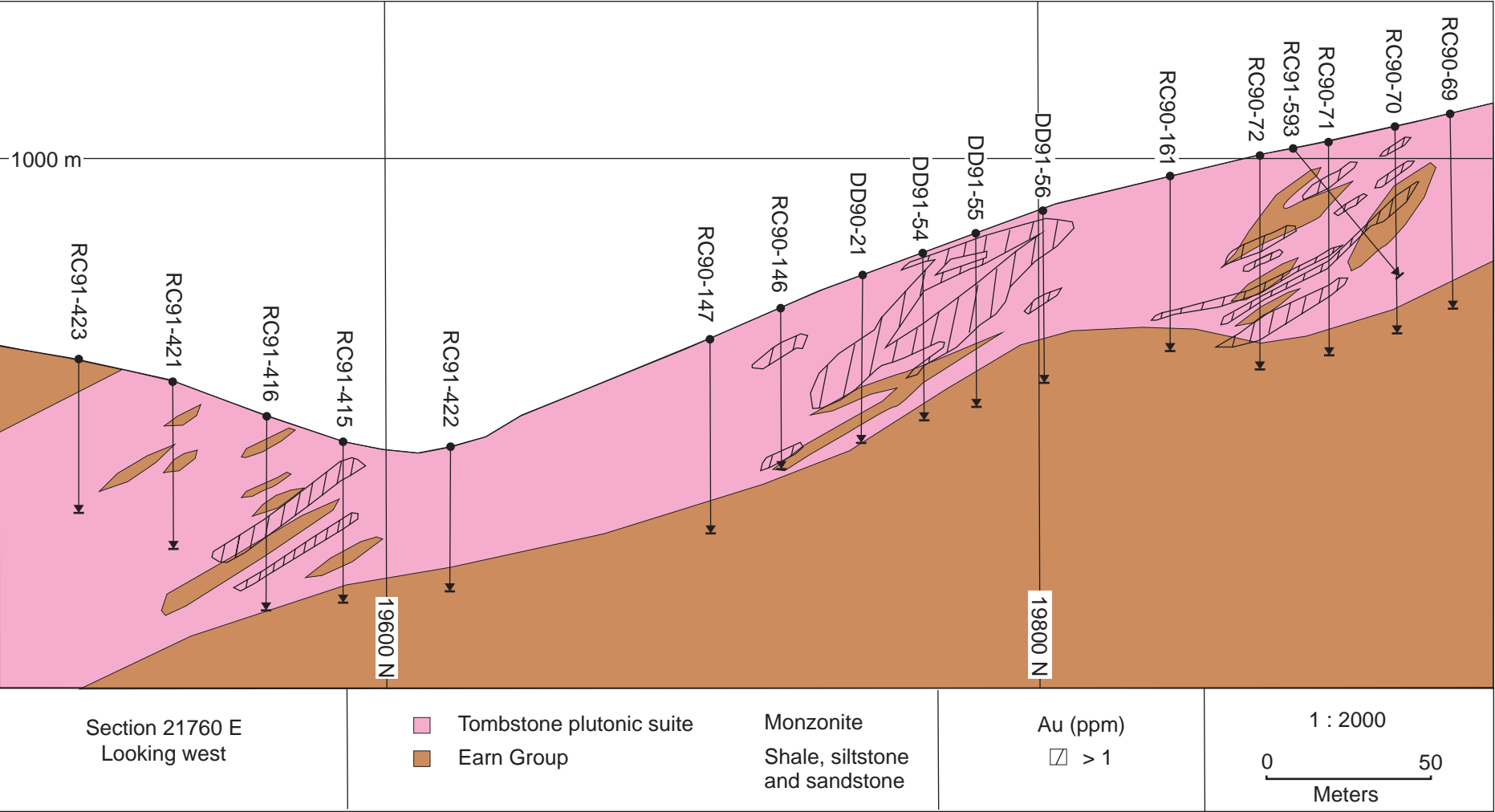


Figure 5.1 C

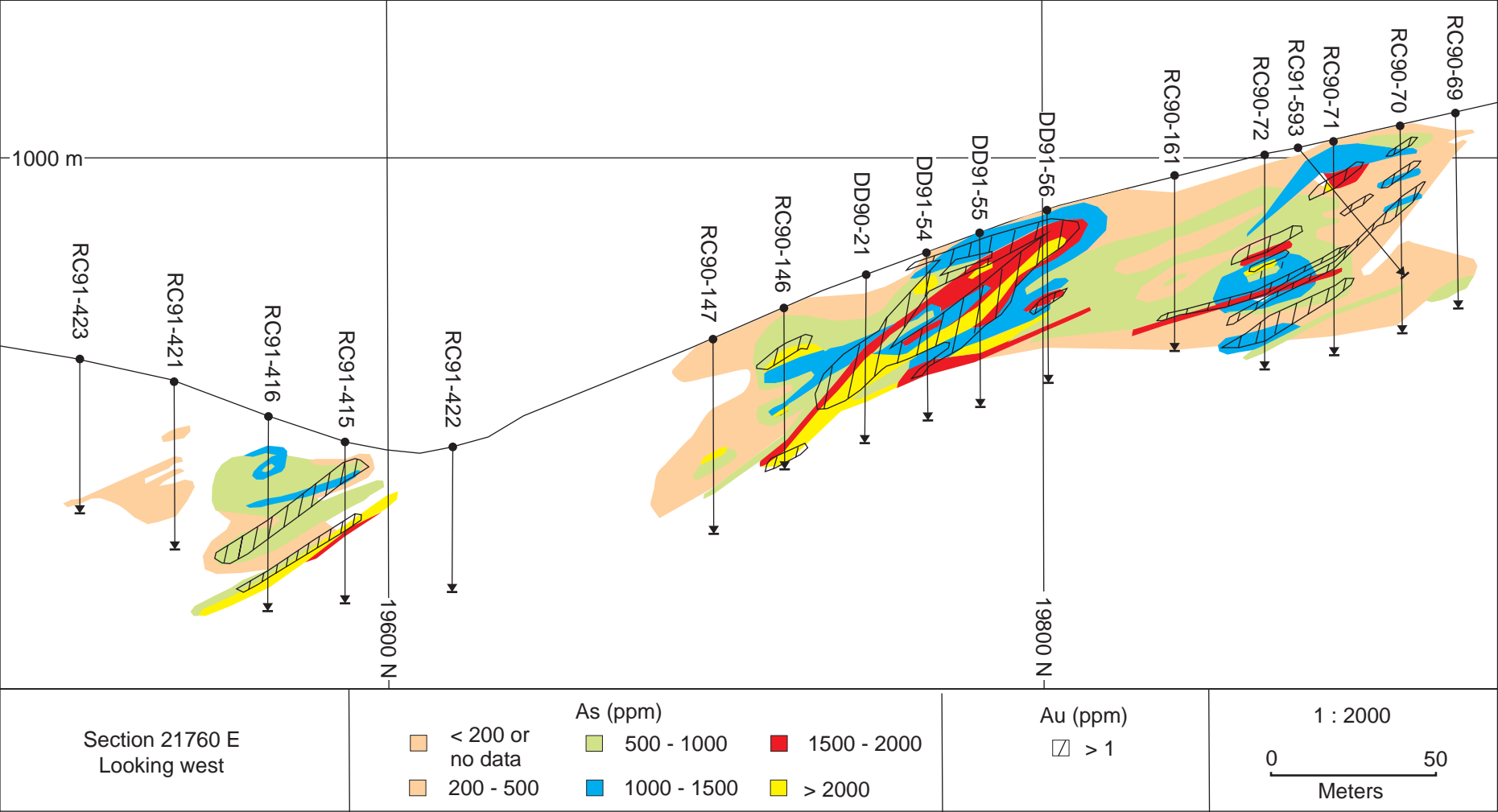


Figure 5.1 D

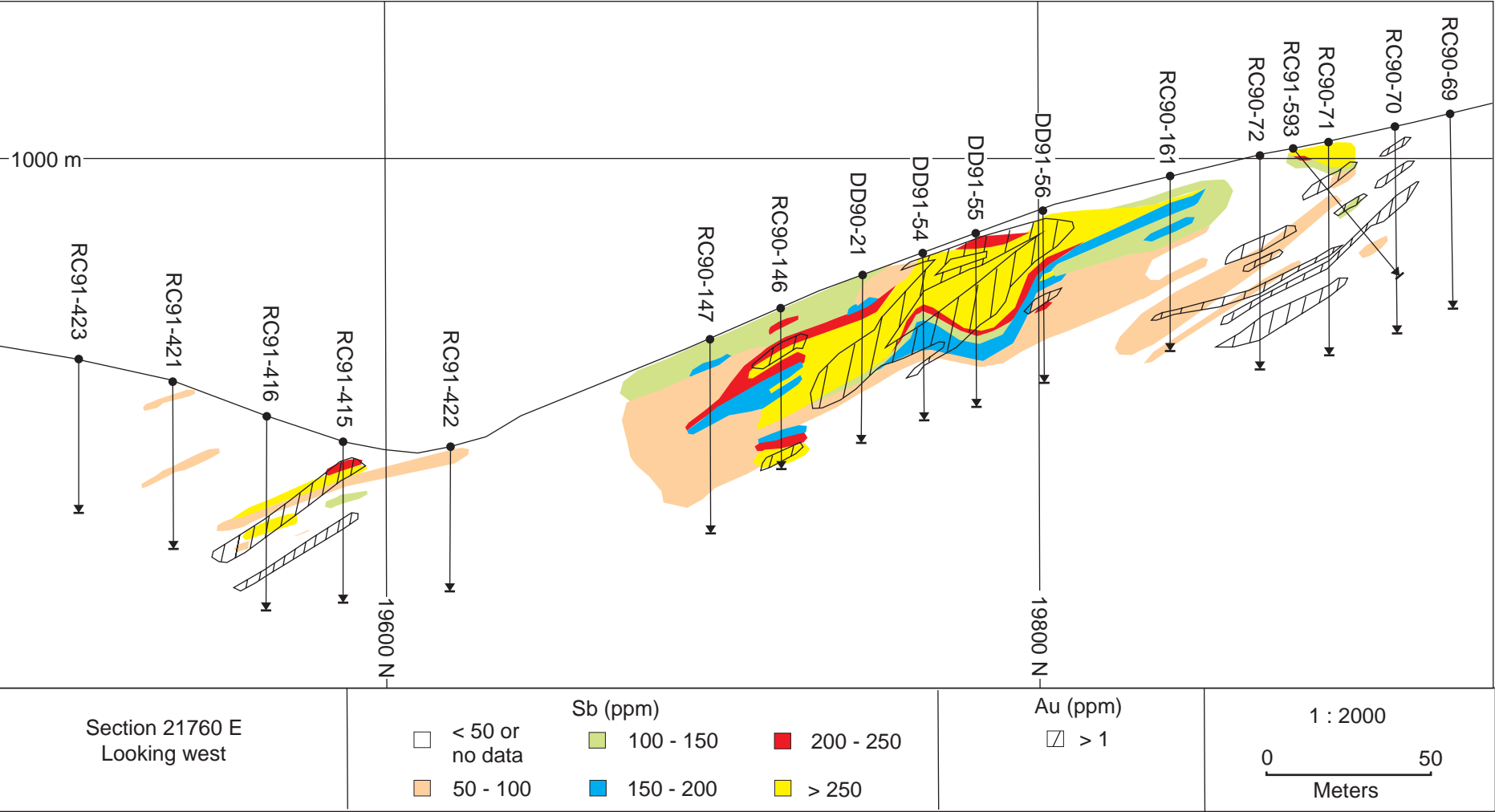


Figure 5.1 E

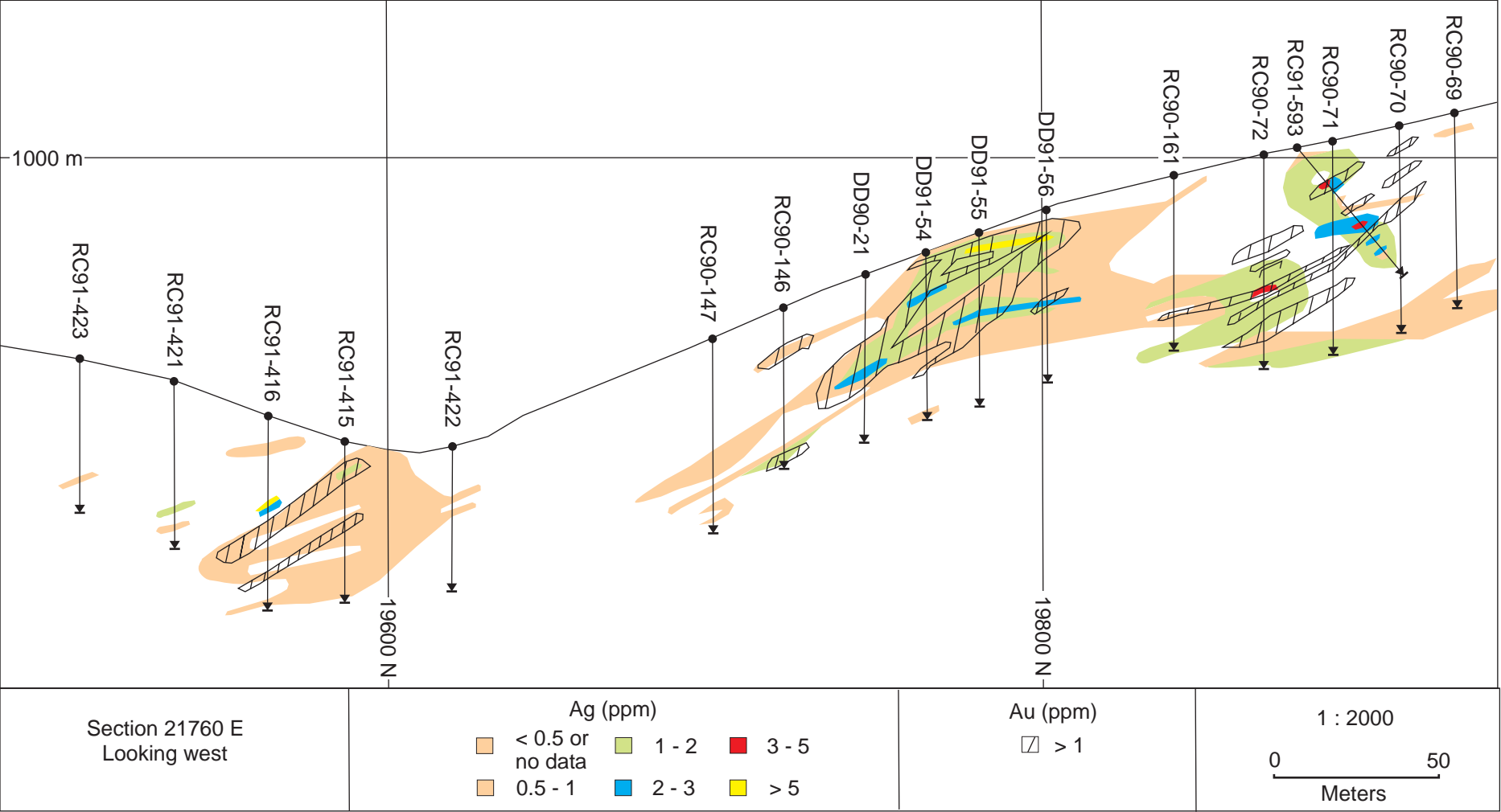


Figure 5.1 F

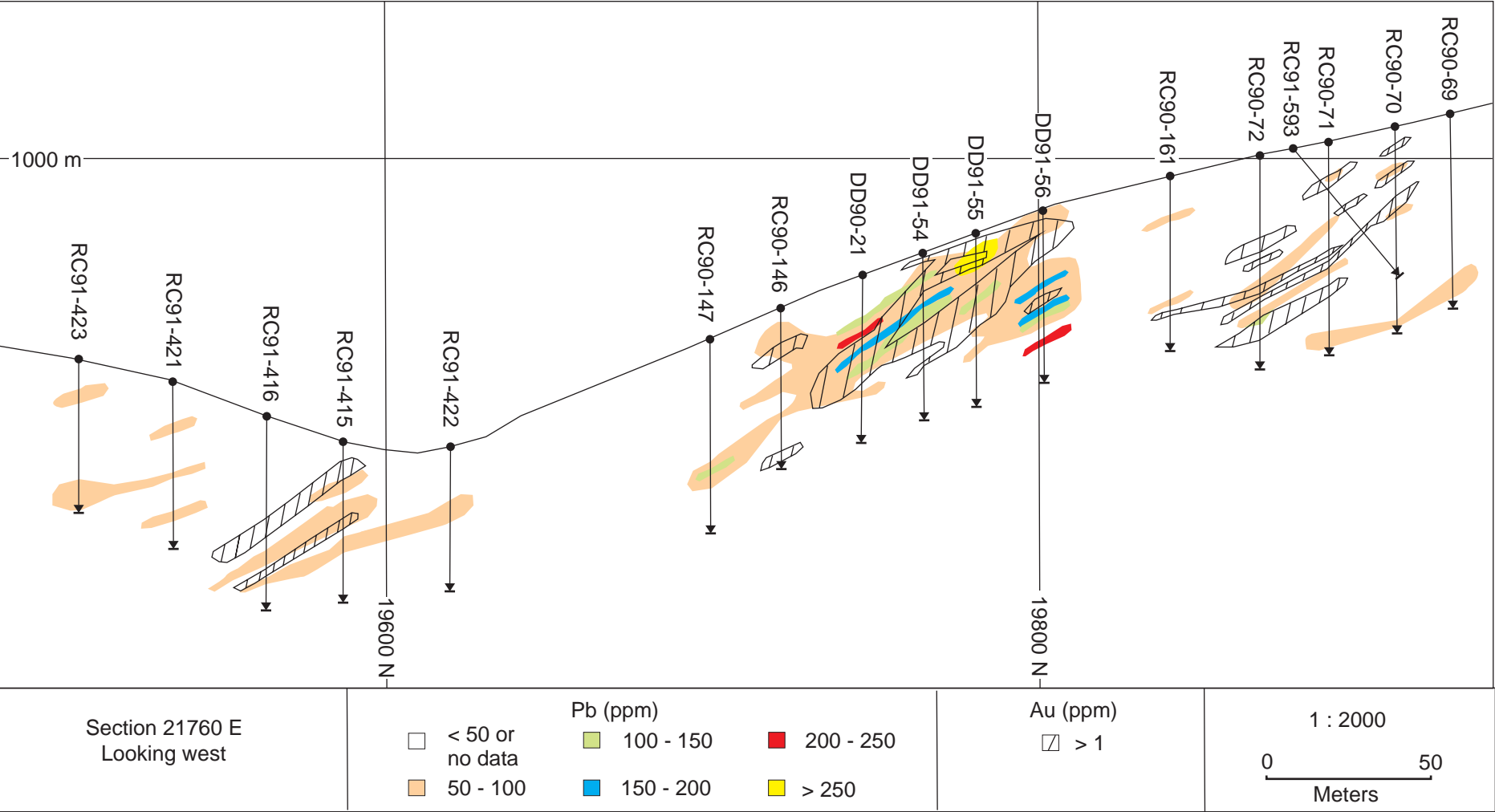
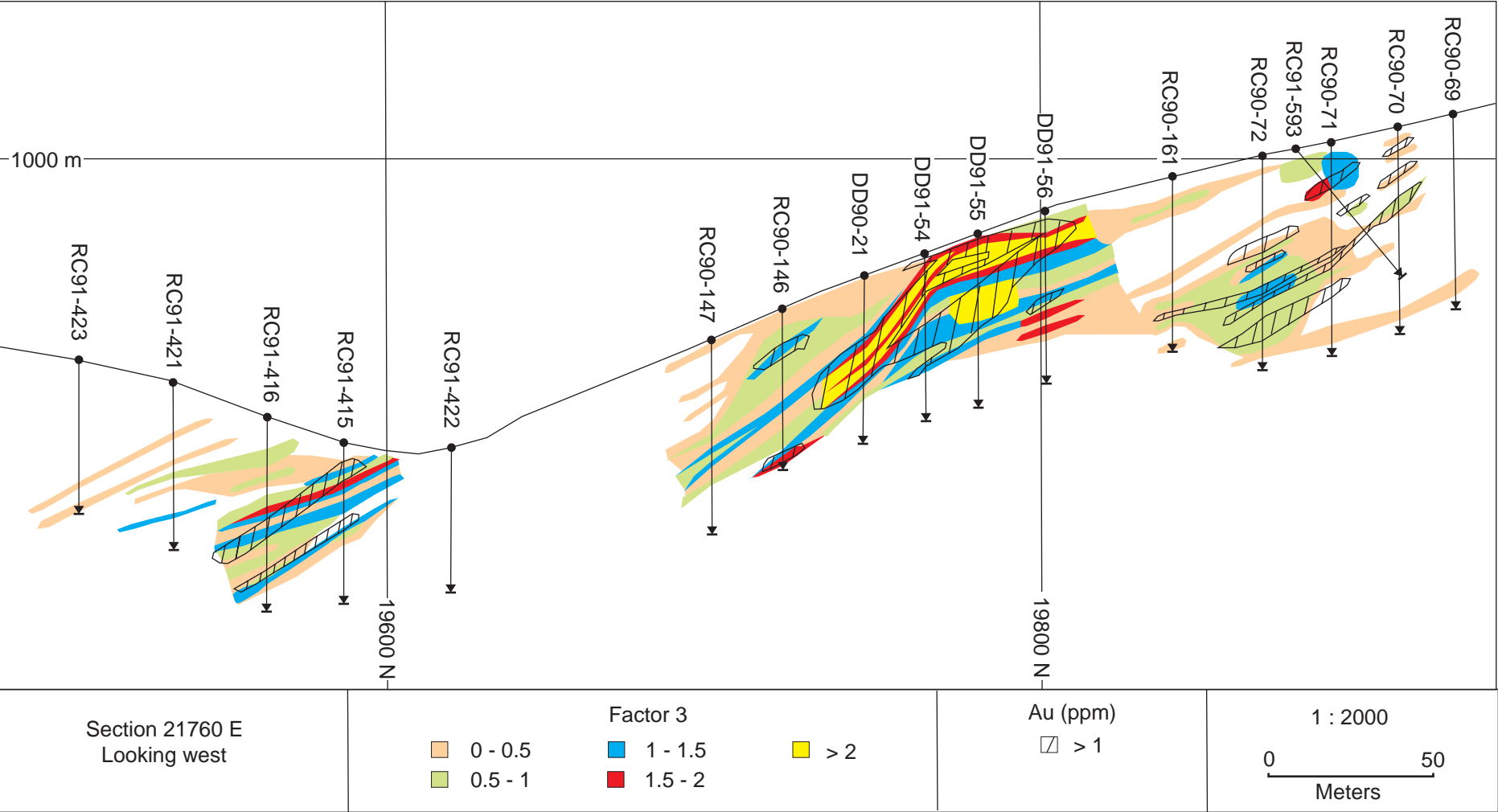


Figure 5.1 G



in broadly the same area as elevated Au but the zones do not correspond in detail. Approximately half of the Au grades > 1 ppm occur in zones of < 100 ppm Sb and the majority of Sb grades > 150 ppm lie outside zones of > 1ppm Au (Figure 5.2 d). Silver better describes Au in sedimentary rocks than in intrusive rocks with most Ag mineralisation > 2 ppm corresponding to > 1 ppm Au grades (Figure 5.2 e). The distribution of Pb shows no correlation to zones of > 1 ppm Au (Figure 5.2 f).

Overall, elevated As (> 1000 ppm) is the best indicator of Au > 1 ppm with high concentrations of Sb in intrusive rocks and elevated levels of Ag and Sb in sedimentary rocks providing further indication of Au. The close relationship between Au and As also suggests similar, if not identical, controls on the distribution of these elements (see sections 4.3 and 5.4). Lead and Au do not correlate well on these sections, however, factor 3 was generated from factor analysis for a much larger dataset. The sections do indicate that individual elements are not accurate indicators of Au grades because high grades of Sb and less commonly Ag, As, and Pb are evident in areas with less than 1ppm Au and high Au grades were recorded in zones of low grade Pb, Sb, Ag and to a lesser extent As.

Plots of factor 3 scores were generated to combine factor 3 element concentrations into a single number. The scores describe the relative correlation of the factor association to each sample, thereby weighting each sample according to its content of Ag, As, Au, Pb, and Sb. In sedimentary rocks zones of > 1 ppm Au are consistently associated with factor scores greater than 1, almost all of the factor scores > 1 are associated with > 1 ppm Au, and the highest Au grades correlate to the highest factor scores (Figure 5.2 g). In intrusive rocks the relationship is less consistent. The highest Au grades correspond to the strongest factor 3 scores, however, in the northern part of the section Au grades > 1 ppm occur in areas of factor scores > 0.5; this zone also contains low levels of As, Pb and Sb (Figure 5.1 g).

The sections show that the elements described in factor 3 correlate to Au in varying degrees. Comparison of factor 3 scores to Au concentration indicates that factor scores in sedimentary, and to a lesser extent intrusive rocks highlight more tightly constrained zones and better reflect Au grades. Thus, the factor scores provide a better method of predicting the location and grade of gold mineralisation than individual elements. Plotting scores from factor 3 may also highlight areas of mineralisation that were not recorded in drill data.

Figure 5.2 Cross-sections through the Blue pit (18470E) illustrating the distribution of elements that comprise factor 3 (A, C, D, E, F), lithology (B), and the factor 3 scores (G). Values of each element and the factor scores have been contoured. Gold contours are overlain on As, Sb, Ag, Pb, lithology, and factor scores for comparison. Note that Au and As concentrations are similar but that factor 3 scores best describe the distribution of Au. Cross-sections are drawn looking west.

Figure 5.2 A

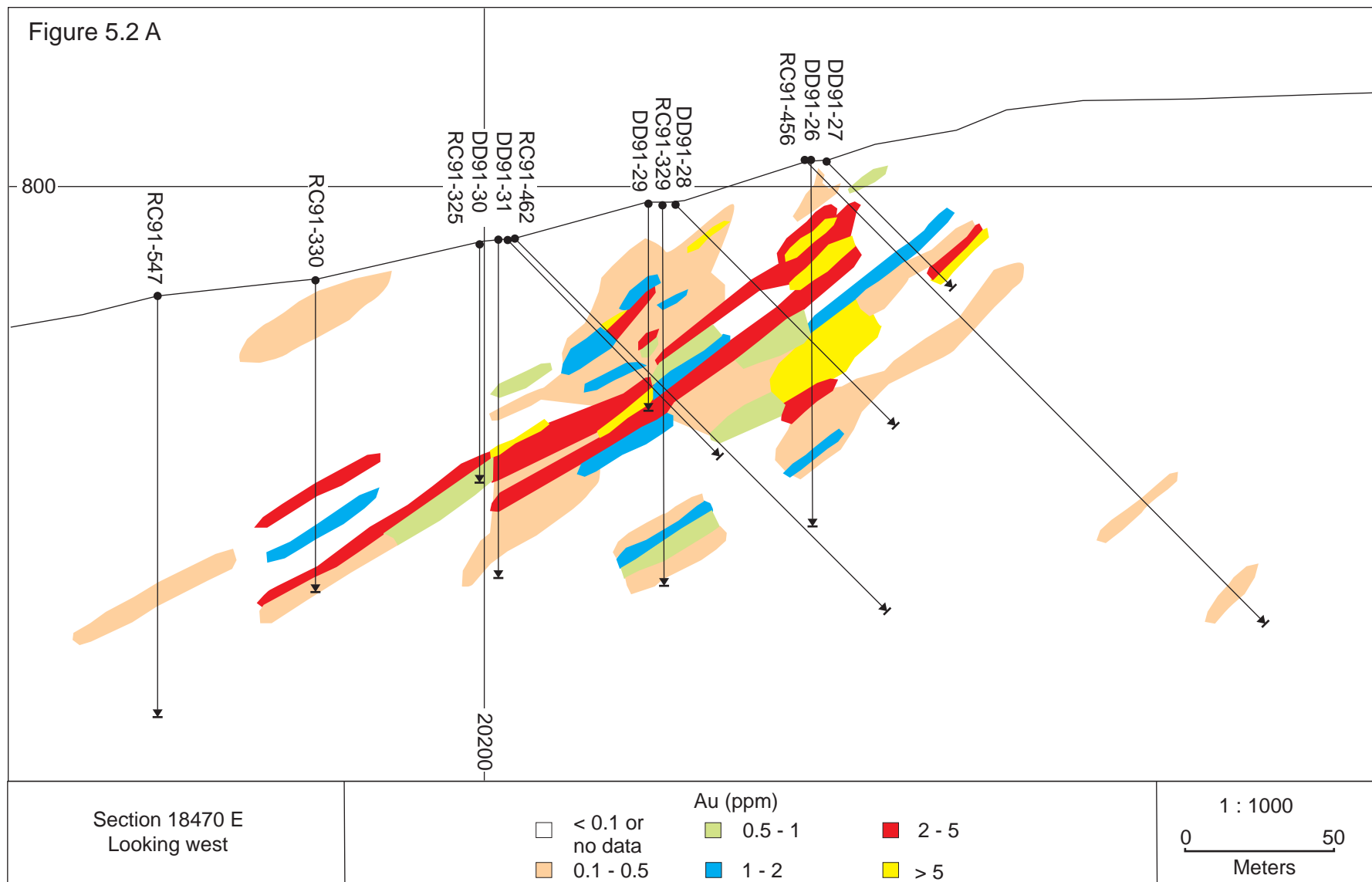


Figure 5.2 B

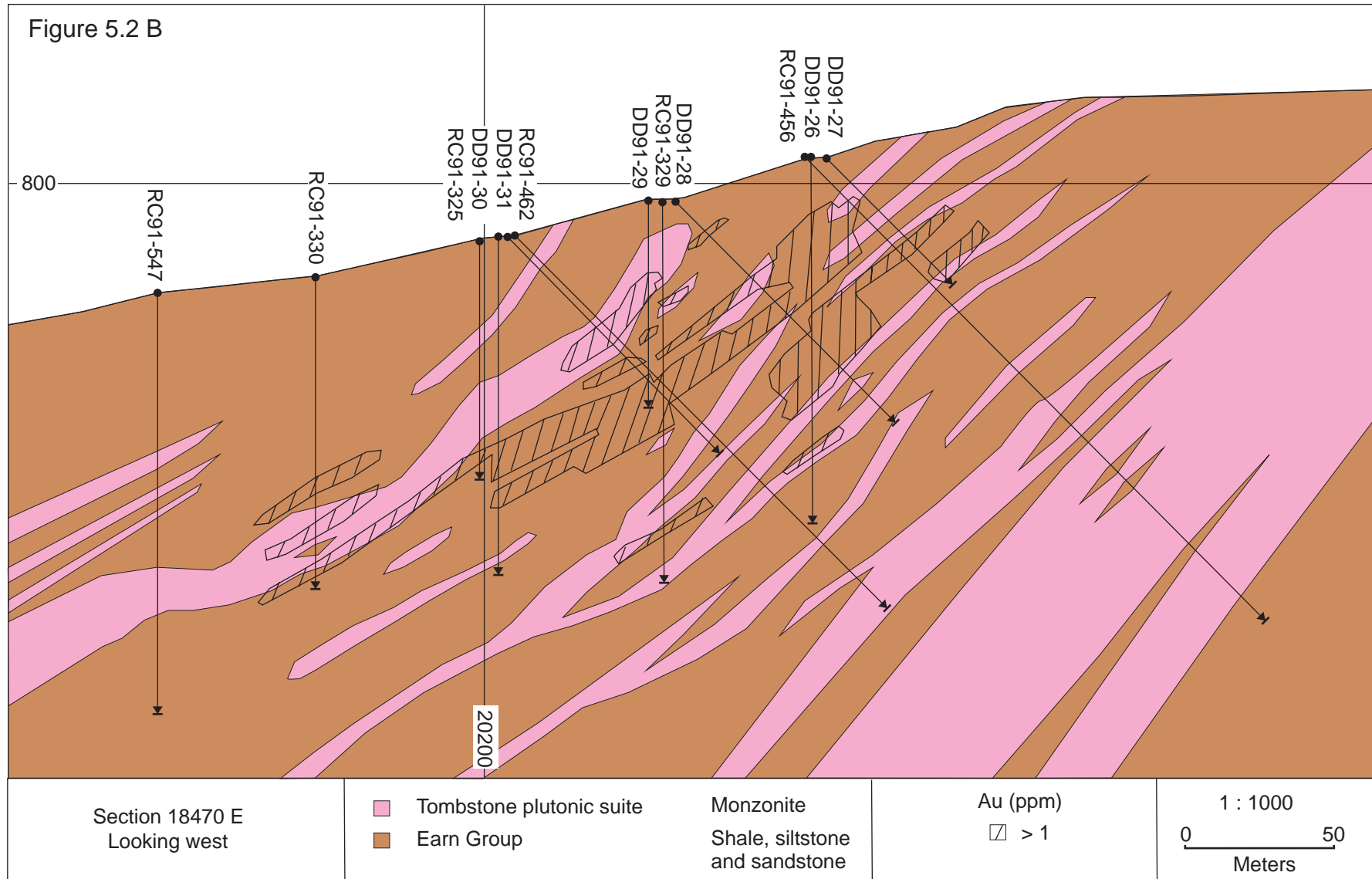


Figure 5.2 C

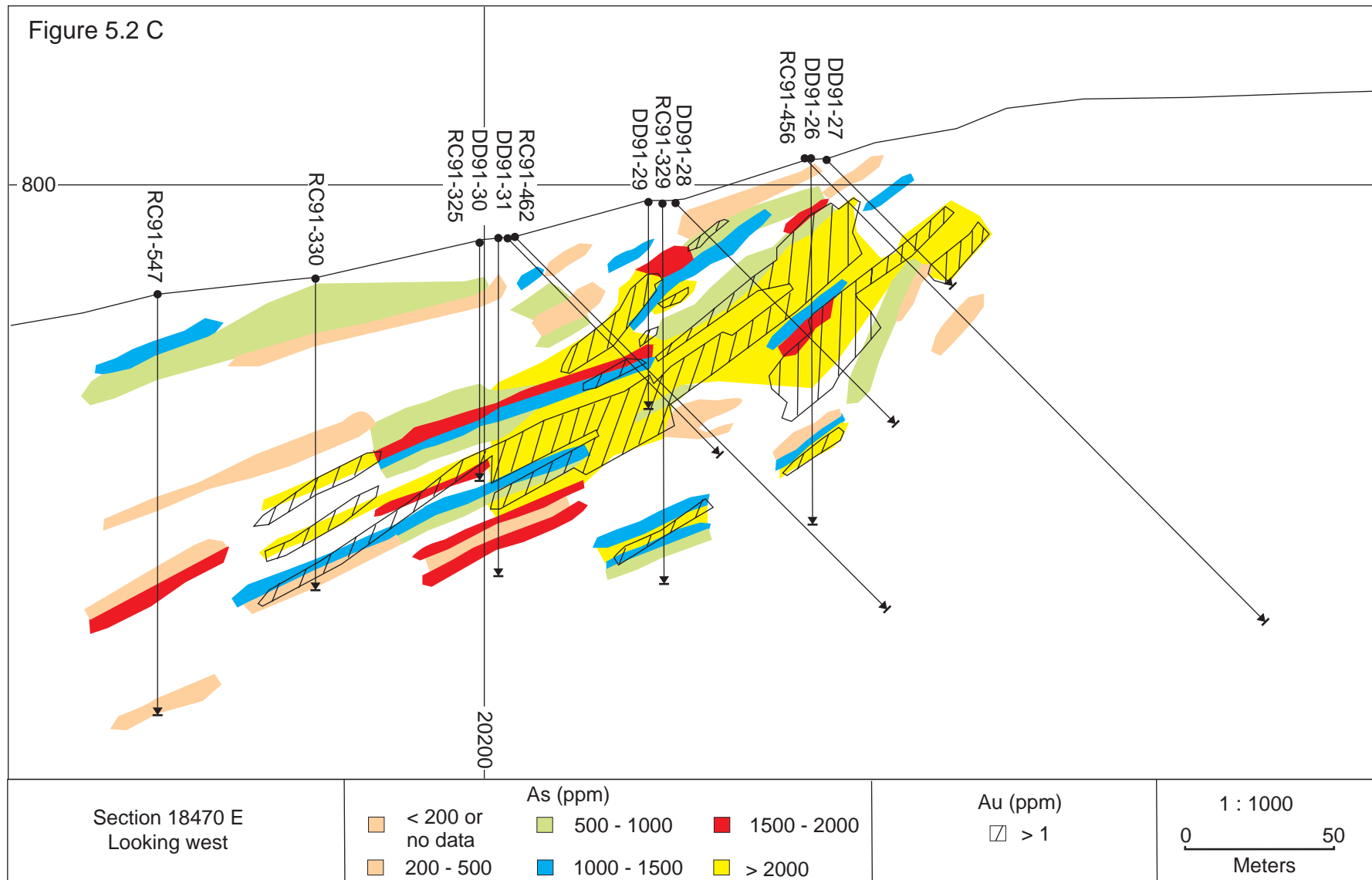


Figure 5.2 D

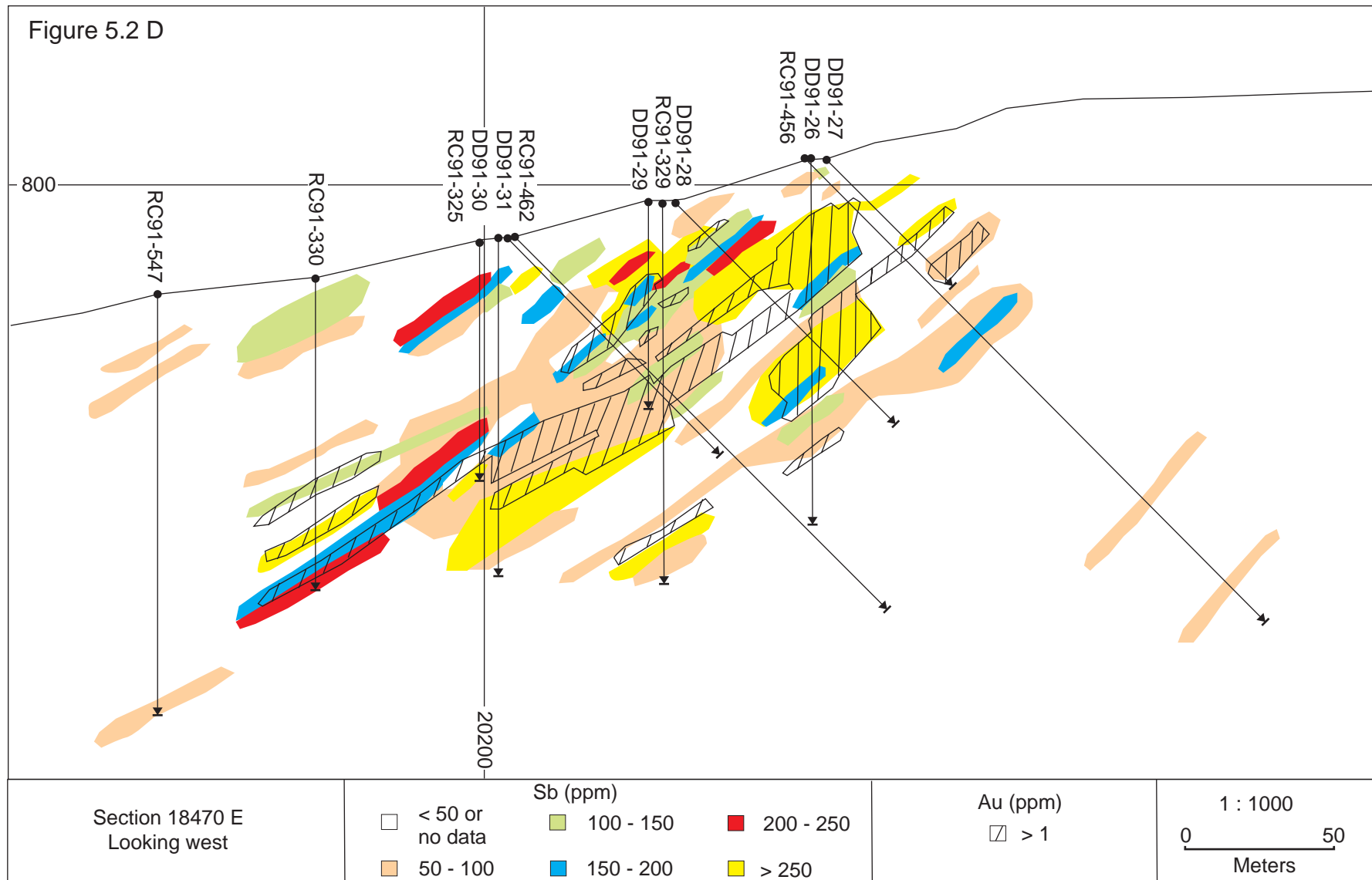


Figure 5.2 E

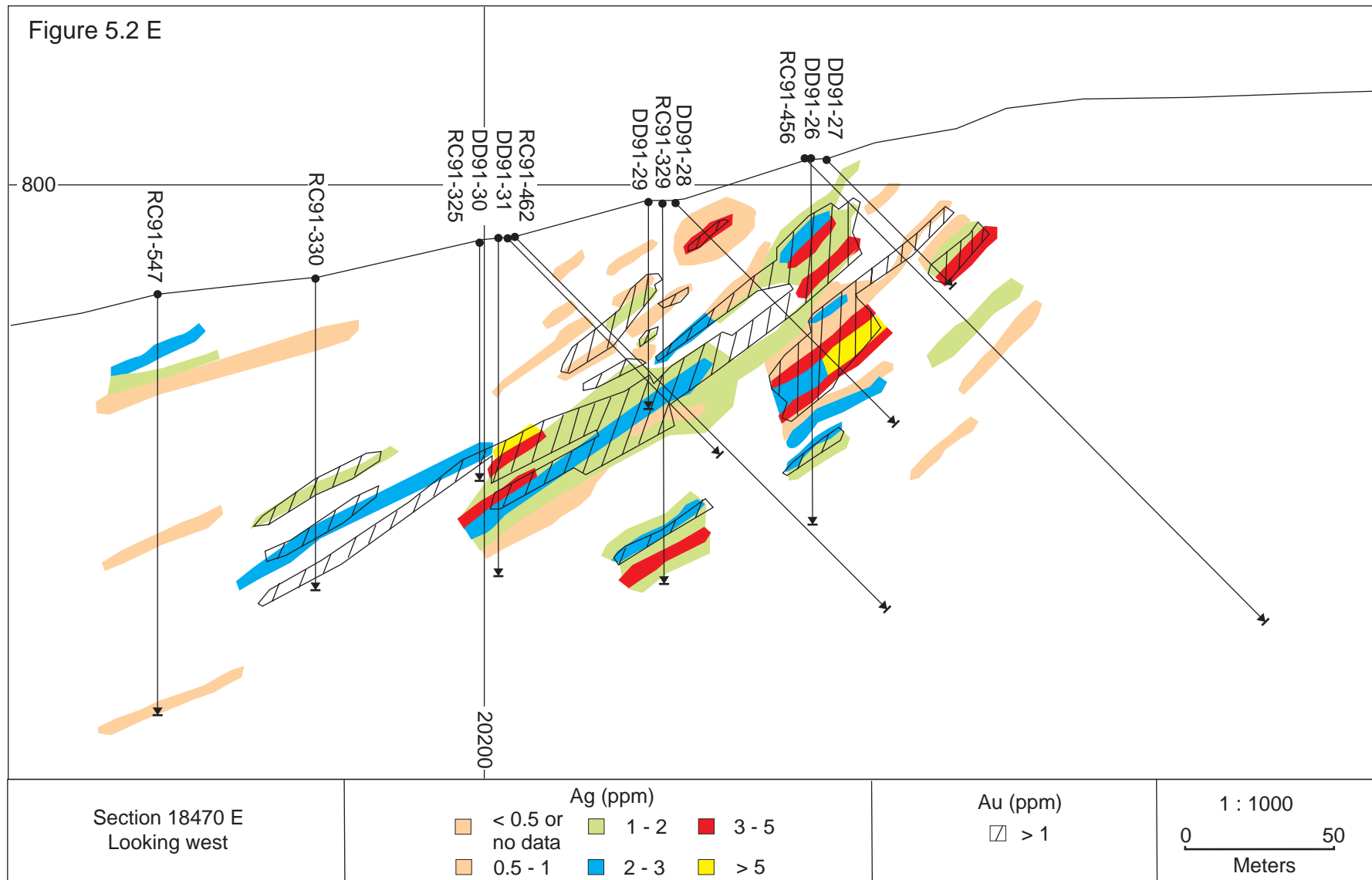


Figure 5.2 F

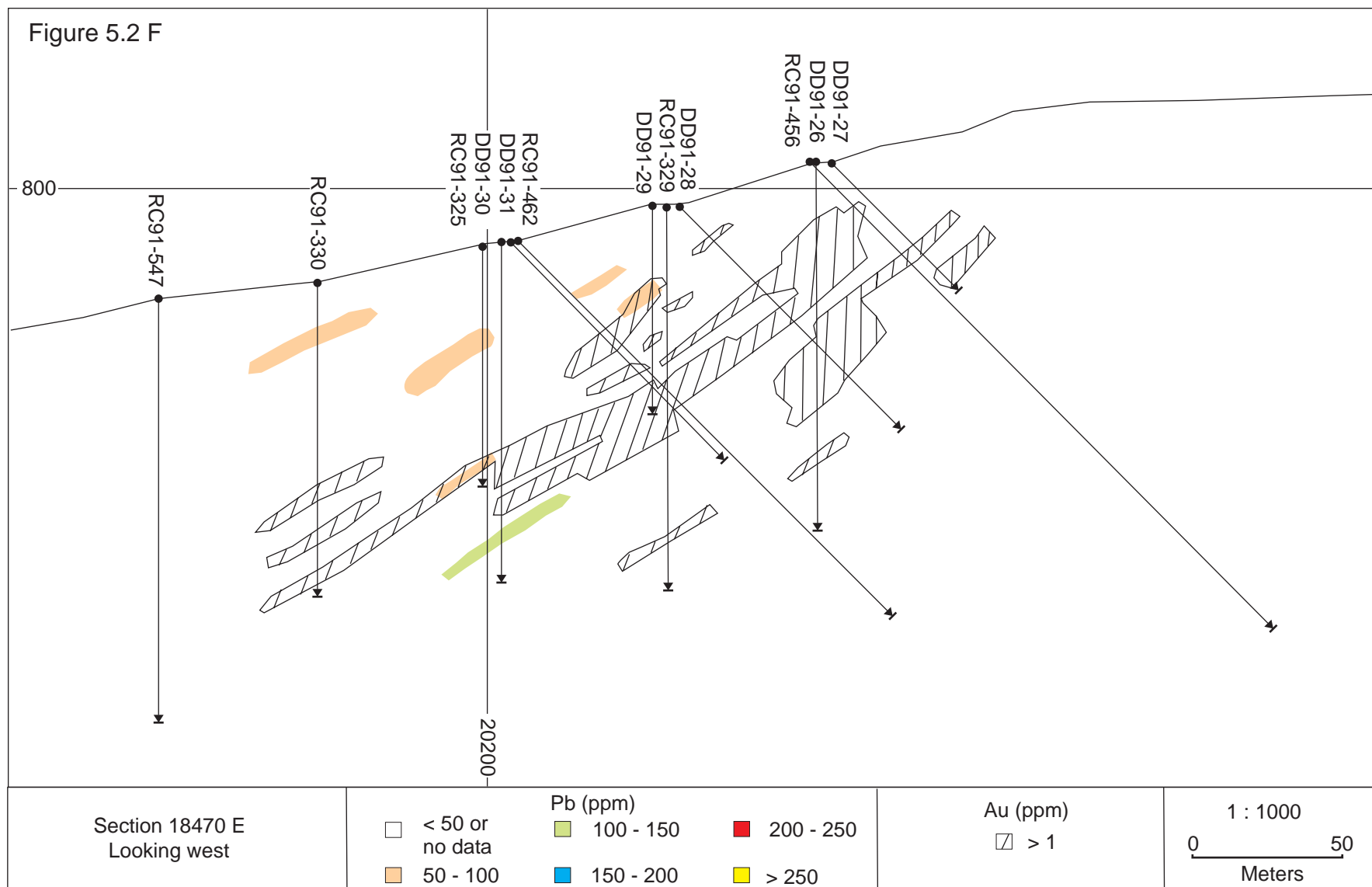
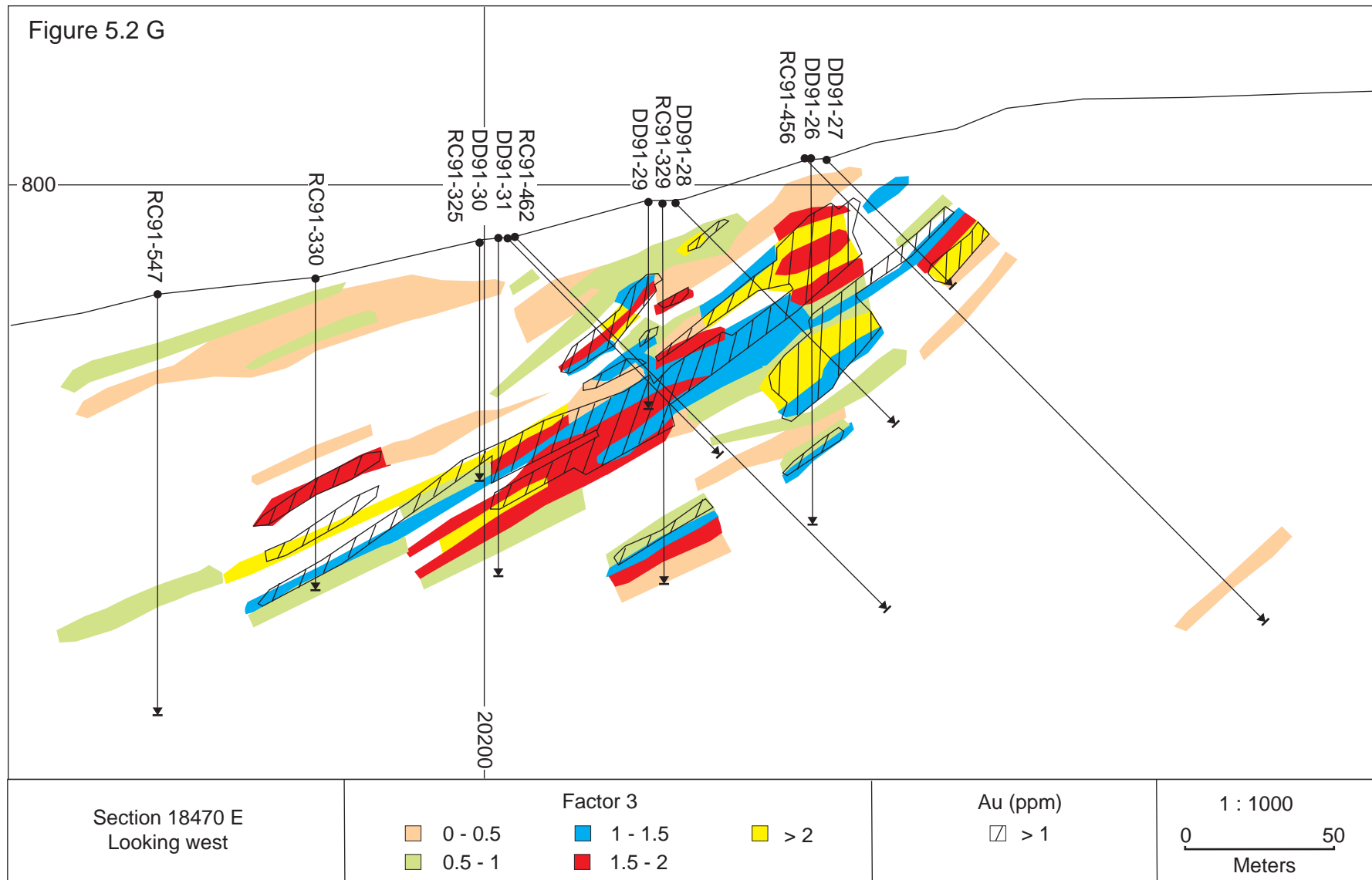


Figure 5.2 G



5.3 The geochemistry of mineralisation and alteration.

The datasets collected by Viceroy provide an extensive overview of element distribution and document element relationships. However, geological criteria (i.e. mineralisation, alteration, veining, etc) were not applied to the selection of 2 m bulk analysis samples and therefore this data alone cannot be used to accurately constrain the geochemistry of mineralisation. To document the geochemical signature of mineralisation and alteration seven variably altered samples were analysed for gold, major oxides and a suite of 22 other trace elements using fire assay, XRF, and ICP-MS/OES methods.

Samples of monzonite were chosen for analysis, as monzonite hosts 70% of the gold mineralisation at Brewery Creek. The samples analysed included un-mineralised monzonite and mineralised monzonite containing proximal and distal P-stage 3.1 pyrite-quartz-carbonate-roscoelite and P-stage 3.4 arsenopyrite-quartz-carbonate-gold alteration. Proximal alteration was classified as alteration immediately adjacent to, but not including, the vein. For the purposes of this research, proximal alteration is defined by a dark grey halo, typically < 1 cm wide, surrounding the vein that comprises > 15 % sulphide minerals (Figure 5.3). Samples of distal alteration were typically collected 2-5 cm from the vein and contain ≤ 10 % sulphide. Though the samples were selected with care, gold mineralisation at Brewery Creek is a process that involves the interrelationship of several stages of the paragenesis (see chapter 4). Thus while it was possible to collect samples containing only P-stage 3.1 alteration, it was impossible to collect samples of P-stage 3.4 without at least minor earlier alteration. Table 5.6 briefly describes each sample.

Element mobility plots

The isocon technique of Grant (1986) has been used to investigate element mobility during hydrothermal alteration. Grant (1986) modified the equations of Gresens (1967) to produce a simple graphical means of assessing element mobility. The technique quantifies mass/volume changes and hence gains and losses of individual elements. Isocon diagrams were generated to compare un-mineralised, distal and proximal mineralisation in monzonite for P-stages 3.1 and 3.4. Prior to plotting the data each element was multiplied by a variable so as to scale all values between zero and ten. The multiplication factors were arbitrarily chosen in order to distribute the elements

Figure 5.3 **Photograph illustrating proximal and distal alteration around an arsenopyrite-quartz-carbonate-gold vein as defined for geochemical sampling.** The well-defined dark grey vein halo defines increased sulphide content (generally > 15%) and strong carbonate alteration and is classified as proximal alteration. Distal alteration is the zone generally 2-5 cm from the vein with < 10% sulphide minerals. Scale bar is in centimetres.

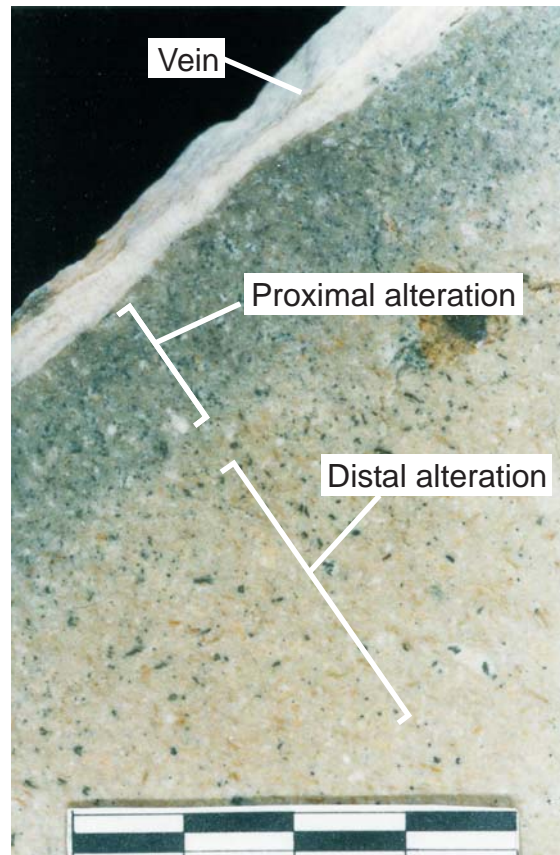


Table 5.6 **Descriptions of samples selected for major element oxide and trace element geochemistry.** Samples MGC 03 and 04 are only altered by P-stage 3.1 while samples MGC 06 – 09 are altered by P-stages 3.1 and 3.4. The nature of gold mineralisation made it impossible to select samples altered solely by P-stage 3.4.

Sample	Sample location	Rock Type	Paragenetic stage	Description
MGC 01	Southern wall of Golden pit	Monzonite		Unaltered, medium grained biotite monzonite
MGC 03	Southern wall of Golden pit	Monzonite	3.1	Biotite monzonite with strong to moderate pyrite and carbonate alteration. Sample taken adjacent to a 0.5 cm thick pyrite-carbonate-quartz vein (proximal).
MGC 04	Southern wall of Golden pit	Monzonite	3.1	Biotite monzonite with weak pyrite and moderate carbonate alteration. Sample taken 3-6 cm from pyrite-carbonate-quartz vein described above (distal).
MGC 06	Southern wall of Golden pit	Monzonite	3.4 (minor 3.1)	Biotite monzonite with strong arsenopyrite and carbonate alteration. Minor pyrite also present. Sample taken adjacent to a 2 mm thick arsenopyrite-quartz-carbonate-gold vein (proximal).
MGC 07	Southern wall of Golden pit	Monzonite	3.4 and 3.1	Biotite monzonite with weak pyrite and arsenopyrite (?) and moderate carbonate alteration. Sample taken 2-5 cm from arsenopyrite-bearing vein described above (distal).
MGC 08	Southern wall of Golden pit	Monzonite	3.4 (minor 3.1)	Biotite monzonite with moderate arsenopyrite and carbonate alteration. Some pyrite also present. Sample taken adjacent to a 1 mm thick arsenopyrite-quartz-carbonate-gold vein (proximal). Includes vein material.
MGC 09	Southern wall of Golden pit	Monzonite	3.4 and 3.1	Biotite monzonite with weak pyrite and arsenopyrite (?) and moderate carbonate alteration. Sample taken 4 cm from arsenopyrite-bearing vein described above (distal).

across the diagram and to allow for easier discrimination of mobile and immobile elements. The initial and scaled data are presented in tables 5.7 and 5.8 respectively.

The scaled data was plotted on scatter graphs and isocon lines were calculated manually using a visual line of best fit (statistically determined lines of best fit are invalid for these graphs as the graphs are ratio plots calculated using arbitrarily chosen multiplication factors) for commonly immobile elements (i.e. Al_2O_3 , TiO_2 , Y, and Zr; Rollinson, 1996). For the purposes of this discussion immobile elements are defined as elements not affected by hydrothermal processes. However, it is important to recognise that there can be significant primary variance in 'immobile' element concentrations, especially with small sample sizes. For example, Zr and Ti can vary through processes such as fractional crystallisation (Bowen, 1928) and partial melting in igneous rocks and mixing lines in sedimentary rocks (Bhatia, 1983; Argast and Donnelly, 1987). Therefore, it is important to distinguish element mobility trends associated with alteration from apparent element mobility that results from primary variations in element concentration in the host rock.

The isocon diagrams are interpreted by comparing the plotted location of elements to the isocon lines. Elements that plot co-linearly with the zero intercept can be classified as immobile. Correlation with commonly immobile elements thus allows the detection of a broader suite of immobile elements. Elements that plot below the line are those that are added with respect to the unaltered sample. Elements that plot above the line are those that are lost with respect to the unaltered sample. For further ease of interpretation the actual gain or loss of each element has been plotted in a bar chart expressed as a percentage relationship. The isocon line also indicates relative mass gain or loss. Isocon line slopes greater than one correspond to mass gain and slopes less than one correspond to mass loss. The percentage of gain or loss can be measured directly from the graph. It should be noted that density was not calculated prior to sample analysis. Given that the host rocks were identical for each sample set (i.e. all biotite monzonite) and that alteration is only moderately developed, it can be assumed that density will be close to constant. Thus, despite the lack of density information isocons can be constructed for mass changes. Volume changes could not be quantified, as this would require density information.

Table 5.7 Major element oxide and trace element geochemical data of selected samples from Brewery Creek. The samples include unaltered monzonite (MGC 01) and proximal and distal examples of P-stage 3.1 and 3.4 alteration in monzonite (MGC 06-09). See Table 5.6 for sample descriptions.

Method	Element	Units	MGC01	MGC03	MGC04	MGC06	MGC07	MGC08	MGC09
XRF	SiO2	%	62.70	58.19	59.22	62.27	66.44	57.43	65.06
XRF	TiO2	%	0.62	0.55	0.61	0.68	0.70	0.59	0.64
XRF	Al2O3	%	14.99	13.63	14.72	14.99	14.97	13.86	15.87
XRF	Fe2O3T	%	4.69	3.73	4.20	5.01	5.27	4.39	4.71
XRF	MnO	%	0.08	0.10	0.07	0.14	0.11	0.11	0.08
XRF	MgO	%	2.50	2.43	2.49	2.53	2.69	2.46	2.76
XRF	CaO	%	4.49	3.92	4.40	4.58	4.85	4.60	4.23
XRF	Na2O	%	2.42	0.41	0.45	0.10	0.28	0.39	0.37
XRF	K2O	%	4.59	5.61	4.30	5.90	5.27	5.68	4.49
XRF	P2O5	%	0.29	0.26	0.30	0.23	0.29	0.24	0.32
XRF	SO3	%	0.45	1.00	0.48	0.68	0.55	0.63	0.52
XRF	CO2	%	3.03	8.41	10.22	11.08	10.93	9.55	7.89
MS	Ag	ppm	0.02	0.03	0.01	0.23	0.18	0.16	0.11
MS	As	ppm	1.59	1259.00	44.12	11390.00	267.90	3079.00	31.86
fire	Au	ppm	0.02	0.29	0.02	6.87	0.02	0.95	0.04
MS	Ba	ppm	2846.80	1108.80	2750.00	676.50	1281.80	1157.80	3154.80
MS	Bi	ppm	0.08	0.10	0.08	0.07	0.06	0.17	0.21
MS	Cd	ppm	0.11	0.48	0.28	0.55	0.47	0.60	0.40
XRF	Co	ppm	14.00	17.00	14.00	38.00	14.00	49.00	15.00
OES	Cr	ppm	44.65	49.36	44.83	52.94	47.06	54.45	48.23
XRF	Cu	ppm	17.01	18.80	15.00	16.00	14.77	19.14	17.00
XRF	Ga	ppm	20.00	17.30	18.03	24.00	20.00	21.00	20.00
MS	La	ppm	47.73	26.59	43.32	27.26	32.61	35.45	33.34
MS	Mo	ppm	1.69	1.68	1.83	1.54	1.58	2.01	2.11
XRF	Ni	ppm	10.00	10.00	9.00	15.00	10.00	13.00	11.00
MS	Pb	ppm	27.90	28.31	26.06	35.83	38.12	50.84	53.42
MS	Sb	ppm	1.47	22.03	11.30	102.90	28.84	53.57	31.10
XRF	Sc	ppm	14.00	12.40	13.40	13.64	16.00	14.76	15.00
MS	Sn	ppm	1.01	1.53	1.01	1.59	1.06	2.17	1.89
MS	U	ppm	5.29	4.96	5.22	6.46	5.85	5.72	4.80
XRF	V	ppm	165.00	156.00	170.00	162.00	185.00	158.00	165.80
MS	W	ppm	86.40	117.50	79.53	247.60	83.33	586.60	156.80
XRF	Y	ppm	22.00	20.00	22.00	22.00	20.00	21.00	23.00
XRF	Zn	ppm	75.00	41.00	61.00	58.44	83.56	70.00	81.00
XRF	Zr	ppm	156.00	182.00	176.00	177.00	187.00	165.00	173.00

XRF X-ray fluorescence
MS ICP mass spectrometry
OES ICP optical emission spectrometry

Table 5.8 **Converted data for isocon diagrams.** For ease of plotting the data has been multiplied by a variable factor so that all analyses fall between 0 and 10.

Element	Conversion	MGC01	MGC03	MGC04	MGC06	MGC07	MGC08	MGC09
Al2O3	0.4	6.00	5.45	5.89	6.00	5.99	5.54	6.35
CaO	2	8.98	7.83	8.80	9.15	9.69	9.20	8.45
CO2	0.8	2.42	6.73	8.18	8.86	8.74	7.64	6.31
Fe2O3T	1	4.69	3.73	4.20	5.01	5.27	4.39	4.71
K2O	1.5	6.89	8.42	6.45	8.85	7.90	8.52	6.73
MgO	3.42	8.55	8.31	8.52	8.66	9.21	8.41	9.43
MnO	50	4.00	4.90	3.40	7.00	5.50	5.50	3.92
Na2O	4	9.68	1.64	1.80	0.40	1.12	1.56	1.48
P2O5	17	4.93	4.42	5.10	3.91	4.93	4.08	5.44
SiO2	0.132	8.28	7.68	7.82	8.22	8.77	7.58	8.59
SO3	9.5	4.28	9.50	4.56	6.50	5.23	6.01	4.92
TiO2	12	7.44	6.60	7.32	8.16	8.40	7.08	7.68
Ag	40	0.80	1.20	0.48	9.20	7.32	6.44	4.40
As	0.0008	0.00	1.01	0.04	9.11	0.21	2.46	0.03
Au	1.3	0.03	0.38	0.03	8.93	0.03	1.24	0.05
Ba	0.002	5.69	2.22	5.50	1.35	2.56	2.32	6.31
Bi	45	3.81	4.60	3.51	3.16	2.73	7.50	9.47
Cd	9	1.02	4.31	2.51	4.95	4.27	5.38	3.59
Co	0.2	2.80	3.40	2.80	7.60	2.80	9.80	3.00
Cr	0.17	7.59	8.39	7.62	9.00	8.00	9.26	8.20
Cu	0.415	7.06	7.80	6.23	6.64	6.13	7.94	7.06
Ga	0.4	8.00	6.92	7.21	9.60	8.00	8.40	8.00
La	0.2	9.55	5.32	8.66	5.45	6.52	7.09	6.67
Mo	4	6.78	6.72	7.32	6.15	6.32	8.02	8.43
Ni	0.56	5.60	5.60	5.04	8.40	5.60	7.28	6.16
Pb	0.18	5.02	5.10	4.69	6.45	6.86	9.15	9.62
Sb	0.09	0.13	1.98	1.02	9.26	2.60	4.82	2.80
Sc	0.5	7.00	6.20	6.70	6.82	8.00	7.38	7.50
Sn	4	4.05	6.13	4.05	6.36	4.25	8.68	7.58
U	1	5.29	4.96	5.22	6.46	5.85	5.72	4.80
V	0.05	8.25	7.80	8.50	8.10	9.25	7.90	8.29
W	0.015	1.30	1.76	1.19	3.71	1.25	8.80	2.35
Y	0.3	6.60	6.00	6.60	6.60	6.00	6.30	6.90
Zn	0.09	6.75	3.69	5.49	5.26	7.52	6.30	7.29
Zr	0.04	6.24	7.28	7.04	7.08	7.48	6.60	6.92

P-stage 3.1

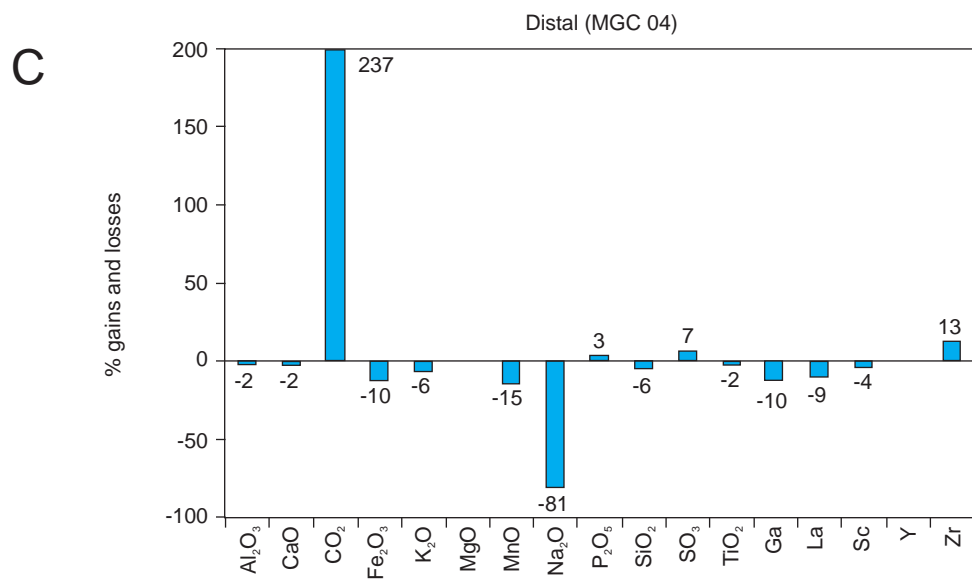
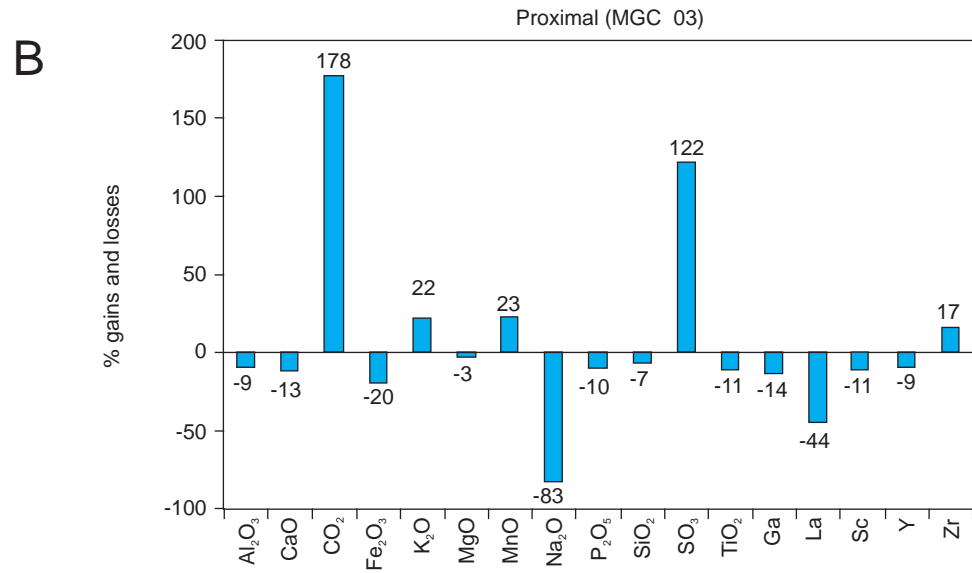
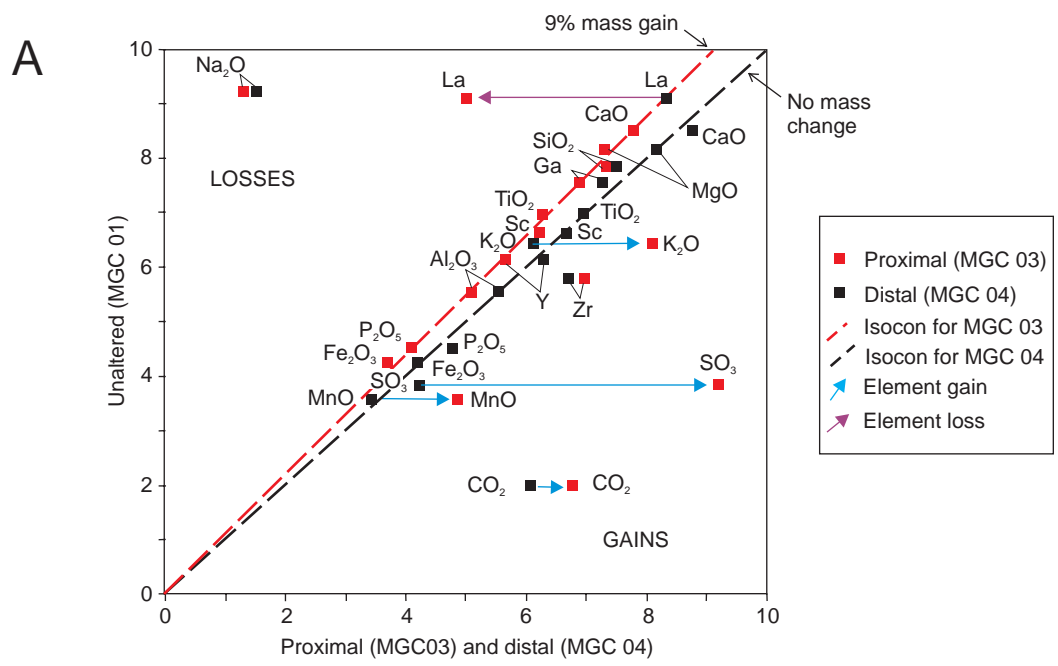
Scaled geochemical data from samples of P-stage 3.1 proximal (MGC 03) and distal (MGC 04) alteration of monzonite has been plotted against scaled data from unaltered monzonite (MGC 01) as shown on Figure 5.4. The isocon line plotted for proximal versus unaltered data has a slope of 1.09 indicating an overall mass gain of 9 %. Major components gained in proximal alteration zones during stage 3.1 include CO₂, SO₃, MnO and K₂O with Na₂O lost. Arsenic, Au, Cd, and Sb are markedly enriched, with comparatively minor enrichment of Ag, Bi, Co, Sn, and W. Depleted metals include Ba, and Zn. The isocon line plotted for distal versus unaltered data has a slope of one indicating no overall mass change, however, several elements have been variously enriched and depleted. The only major element significantly enriched is CO₂ with Na₂O depleted. Other enrichments include As, Cd, and Sb. Silver and Zn are the most depleted elements. Of note is that Zr and La consistently plot away from the isocon as shown on Figures 5.4 to 5.6. This consistent variation likely reflects changes in the primary igneous geochemistry (i.e. through processes such as fractional crystallisation) or problems with sample size (i.e. nugget effects created by irregular zircon, monazite and apatite grain distribution) rather than hydrothermal alteration processes.

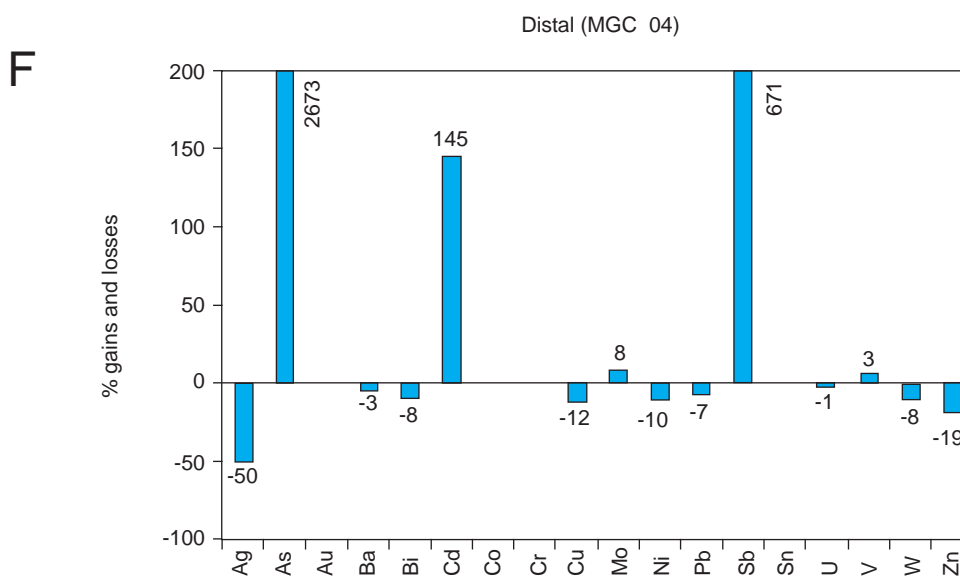
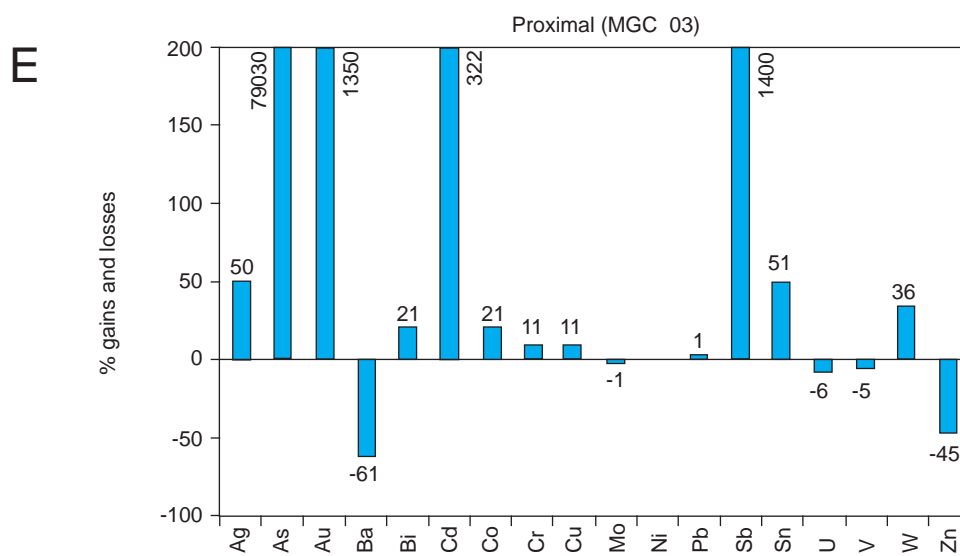
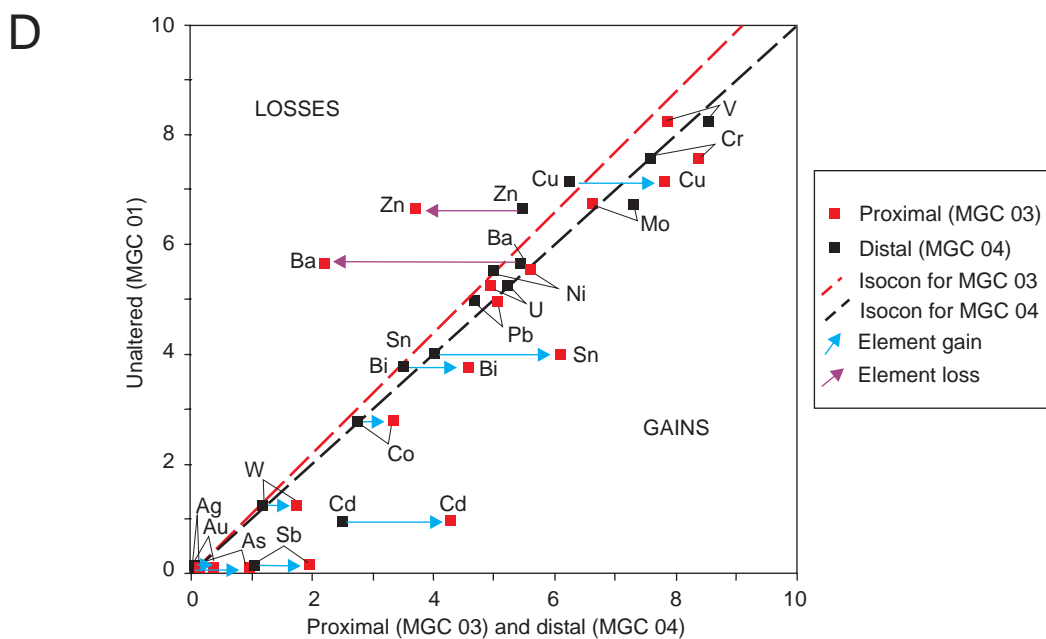
Variations between proximal-unaltered and distal-unaltered element ratios are also documented on Figure 5.4. Proximal alteration zones recorded higher levels of the major element oxides SO₃, MnO, K₂O, and CO₂ than distal zones. Metal concentrations similarly vary between alteration zones with As, Au, Cd, Sb, and to a lesser extent Ag, Bi, Co, Sn and W enriched in the proximal alteration sample compared to the distal alteration sample. Metals that were comparatively depleted in the proximal alteration zone are Ba and Zn.

P-stage 3.4

Scaled geochemical data from P-stage 3.4 proximal-distal sample pairs MGC06-07 and MGC 08-09 has been plotted against scaled data from unaltered monzonite (MGC 01) as shown on Figures 5.5 and 5.6 respectively. The isocon line plotted for proximal alteration sample MGC 06 versus unaltered data has a slope of 0.96, indicating an overall mass loss of 4%. Major components lost from monzonite in the proximal alteration zone are Na₂O and to a lesser extent P₂O₅, while major elements gained include CO₂, MnO, SO₃, and K₂O. Lanthanum was also lost and Ga was gained. Metals that were enriched are Ag, As, Au, Cd, Co, Sb, W, and to a lesser extent Cr, Ni, Pb, Sn, and U. Metals that are depleted include Ba, Bi, and Zn. The isocon line plotted for the corresponding sample of distal alteration (MGC 07) versus unaltered data has a

Figure 5.4 **Element enrichment and depletion associated with P-stage 3.1 pyrite-carbonate-quartz proximal and distal alteration of monzonite.** The isocon diagrams (A – major elements and D - metals) were plotted using the technique of Grant (1986). Isocon lines were calculated manually with reference to Al_2O_3 , TiO_2 , Y, and Zr, elements that are typically immobile. The diagrams are interpreted such that any elements that plot along or immediately adjacent to the isocon are considered to be immobile. Those that plot above the line are depleted and elements that plot below the line are enriched. The arrows on the diagrams indicate relative element gain and loss from distal to proximal zones. The slope of the isocon line for distal alteration is one indicating no mass change. The isocon line for proximal alteration records a 9% mass gain. Note the depletion of Na_2O and addition of K_2O , SO_3 , MnO , and CO_2 . Elevated Au, As, and Sb are also present however these elements and their associated minerals had not been previously associated with this paragenetic stage. Graphs of percentage loss or gain for major elements (B and C) and metals (E and F) have also been plotted for ease of interpretation.





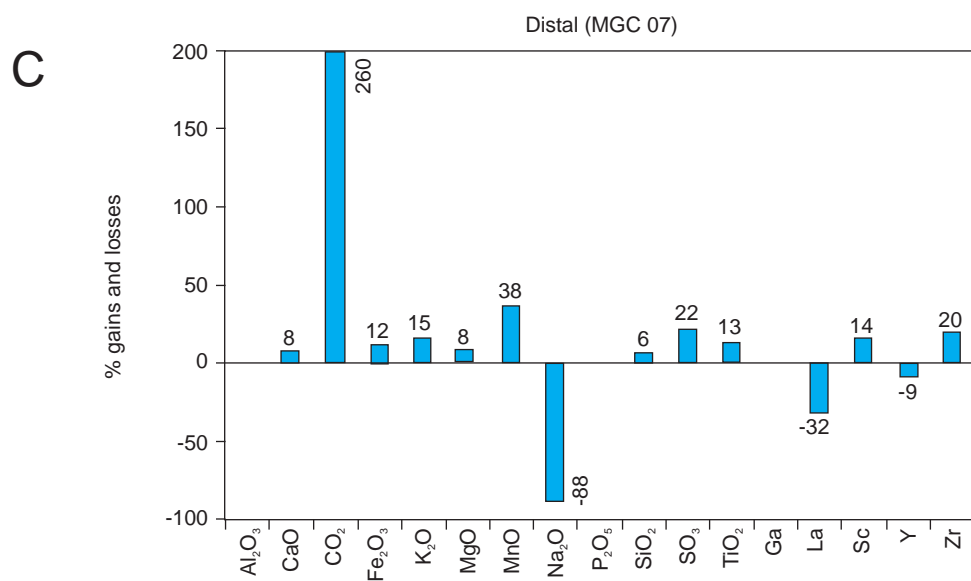
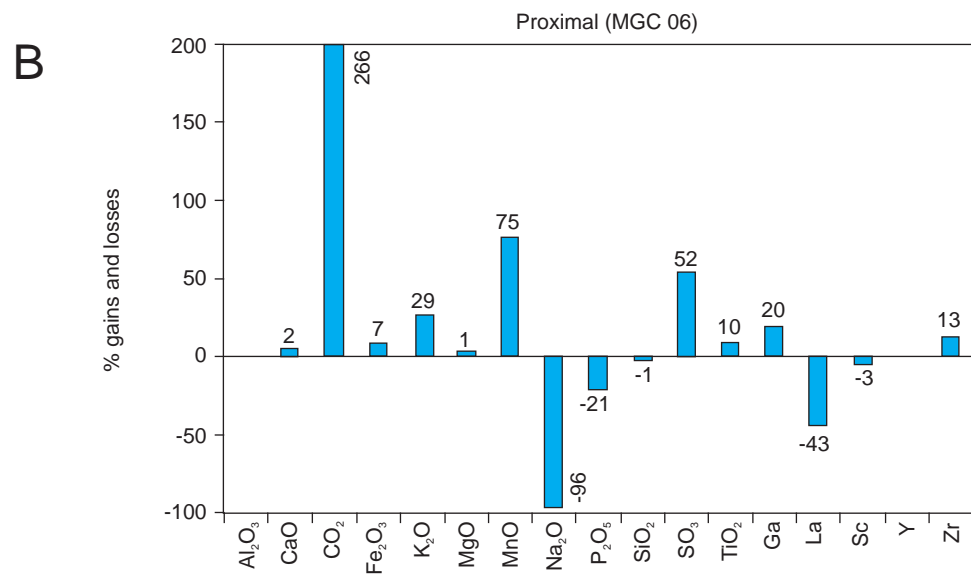
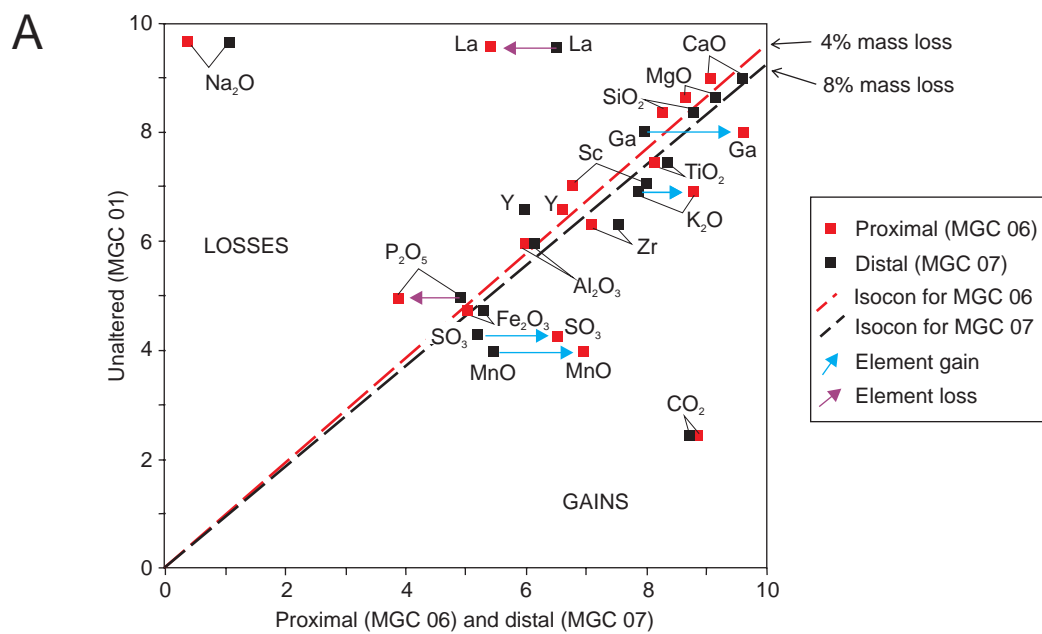
slope of 0.92, indicating a mass loss of 8%. Major elements enriched in the distal alteration zone are CO₂, MnO, and SO₃, while Na₂O is depleted. Metals that show enriched concentrations are Ag, As, Cd, Pb, and Sb, while Ba and Bi are depleted.

A small mass gain of 3% was calculated for MGC 08 from an isocon line plotted with a slope of 1.03. Major components gained in the proximal alteration zone include CO₂, K₂O, MnO, and SO₃, and major elements lost are Na₂O and P₂O₅. Most of the metals analysed were elevated by > 80% including Ag, As, Au, Bi, Cd, Co, Pb, Sb, Sn, and W with Cr and Ni also elevated but at lower levels. Barium was the only depleted metal. The isocon line plotted for the corresponding sample of distal alteration (MGC 09) versus unaltered data has a slope of 0.96, indicating a mass loss of 4%. Na₂O was the only major elements lost from monzonite in the distal alteration zone and CO₂ showed the largest enrichment. Most metals were recorded as enriched including Ag, As, Au, Bi, Cd, Pb, Sb, Sn, W, and to a lesser extent Mo.

Several differences in element concentration and mobility are evident between the MGC06-07 and MGC 08-09 sample pairs. For elements that show the same overall enrichment or depletion trends but a variation in concentration (i.e. Au which is enriched in all samples but more so in MGC06) the differences can be attributed to changes in alteration intensity. The major element oxides show the same enrichment or depletion trends for both sample pairs; however, there are some differences for metals. Barium is depleted in all samples except for MGC09, which recorded 11% enrichment. Bismuth, Cu and Mo are depleted in MGC06 and MGC07 but enriched in MGC08 and MGC09. Uranium is enriched in all samples except for MGC09, which was slightly depleted (-9%) and W showed enrichment levels >80% in all samples except for MGC07, which recorded a small depletion (-4%). The differences in Bi, Cu, and Mo concentration between MGC06/07 and MGC08/09 suggest that the concentration of these elements is not controlled by stage 3.4 alteration. The reasons for differences in Bi, Ba, Cu, Mo, U, and W concentrations are unclear but may include the effects of overprinting alteration, sample size and element distribution, an impure sample (i.e. a barite vein in the sample), and analytical error such as incorrect measurement.

Variations between proximal-unaltered and distal-unaltered element ratios are also documented on Figures 5.5 and 5.6. Proximal alteration zones consistently recorded higher concentrations of CO₂, MnO, SO₃, K₂O, Ag, As, Au, Cd, Co, Cr, Ni, Sb, Sn, and W, and lower concentrations of P₂O₅, Ba and Zn than distal zones.

Figure 5.5 **Element enrichment and depletion associated with P-stage 3.4 arsenopyrite-carbonate-quartz-gold proximal and distal alteration of monzonite.** The isocon diagrams (A – major elements and D - metals) were plotted using the technique of Grant (1986). Isocon lines were calculated manually with reference to Al_2O_3 , TiO_2 , Y, and Zr, elements that are typically immobile. The diagrams are interpreted such that any elements that plot along or immediately adjacent to the isocon are considered to be immobile. Those that plot above the line are depleted and elements that plot below the line are enriched. The arrows on the diagrams indicate relative element gain and loss from distal to proximal zones. The slope of the isocon line for distal alteration is 0.92 indicating a mass loss of 8%. The isocon line for proximal alteration records a 4% mass loss. Note the depletion of Na_2O and Ba and addition of MnO, CO_2 , K_2O , SO_3 , Ag, Au, As, Sb, Cd, Co and W. For ease of interpretation, graphs of percentage loss or gain for major elements (B and C) and metals (E and F) have also been plotted.



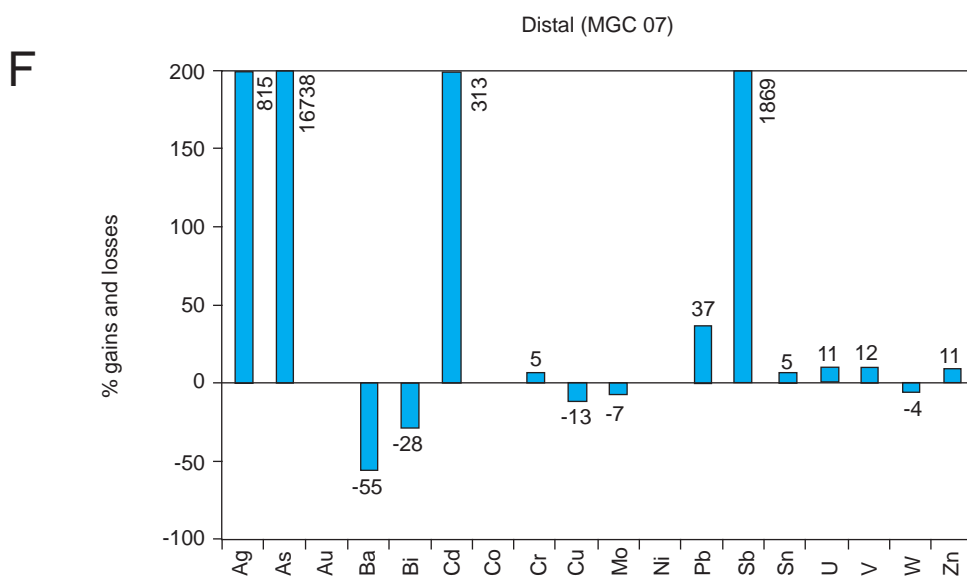
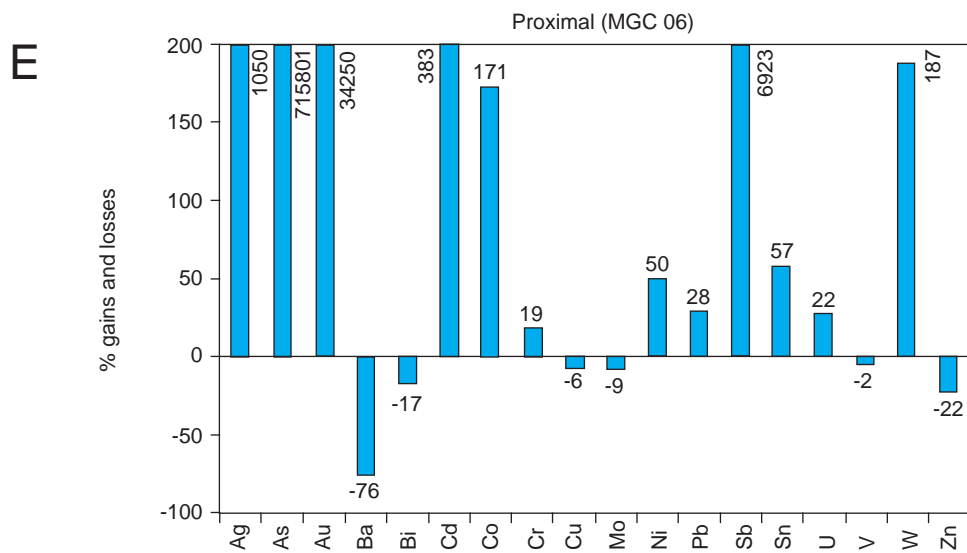
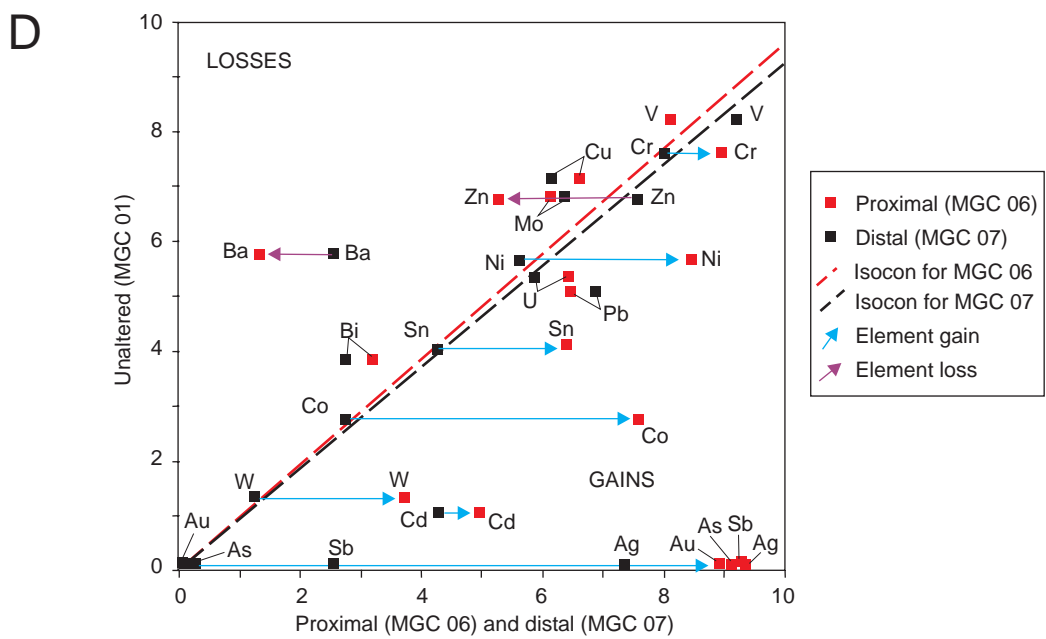
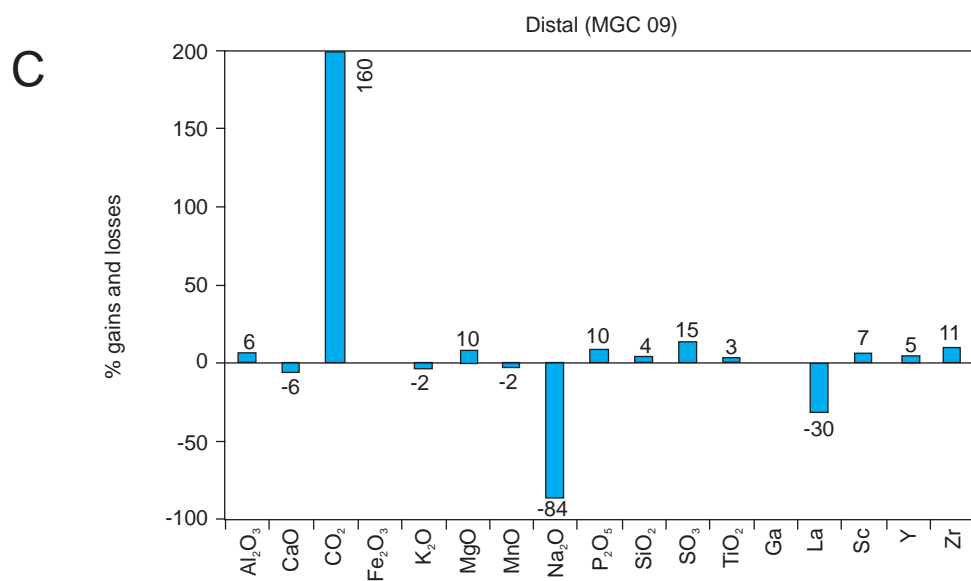
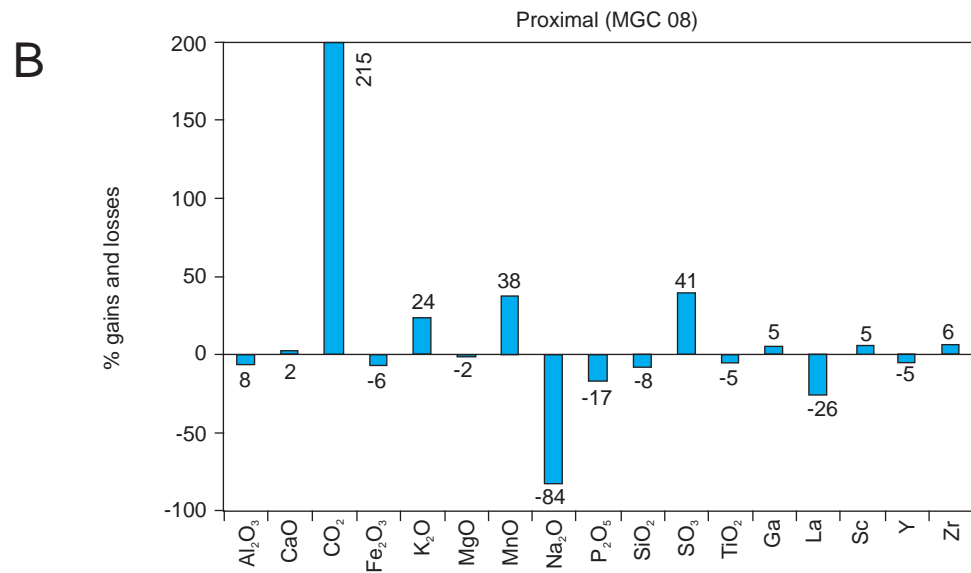
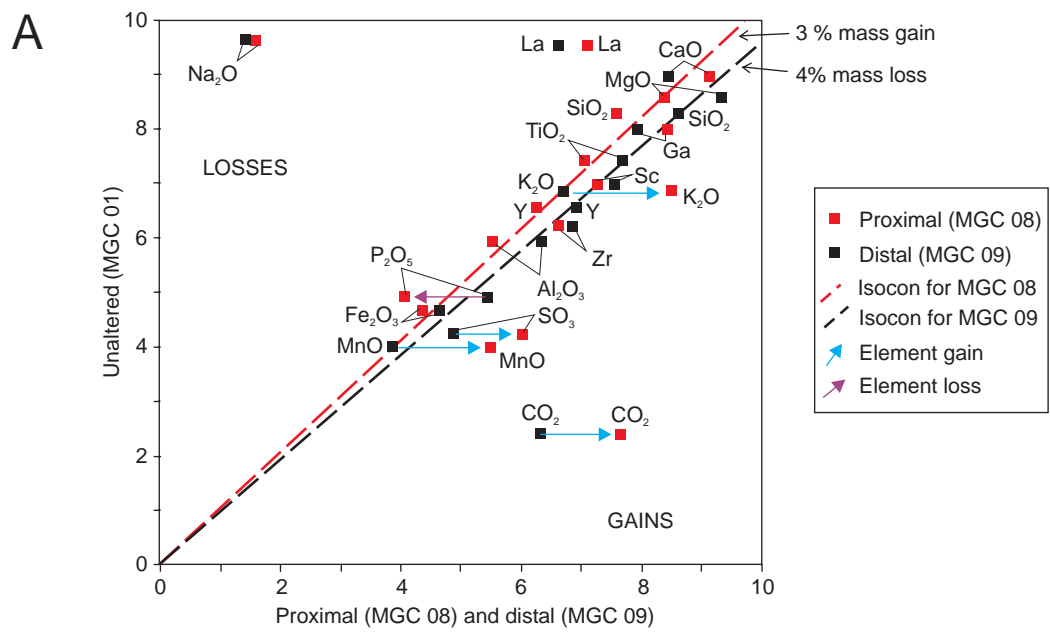
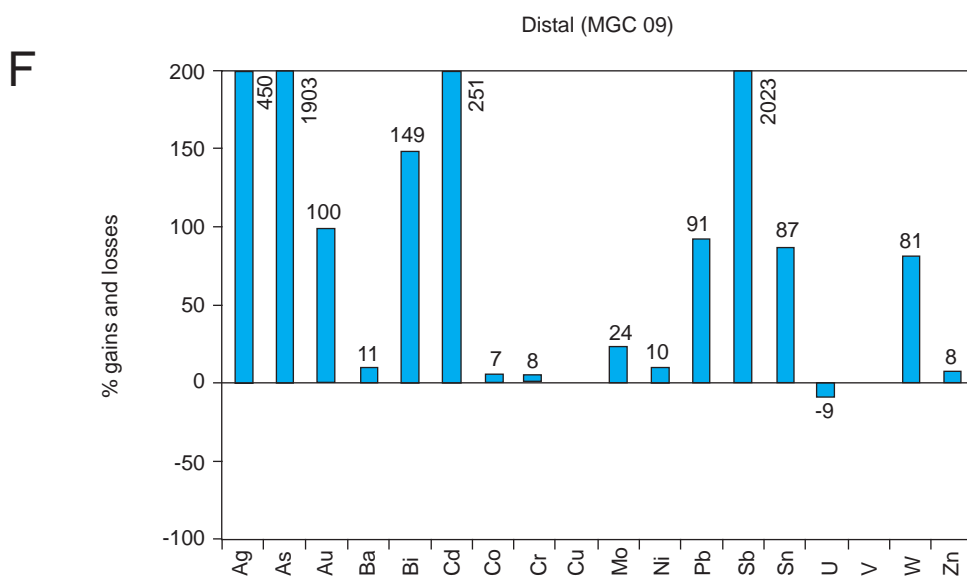
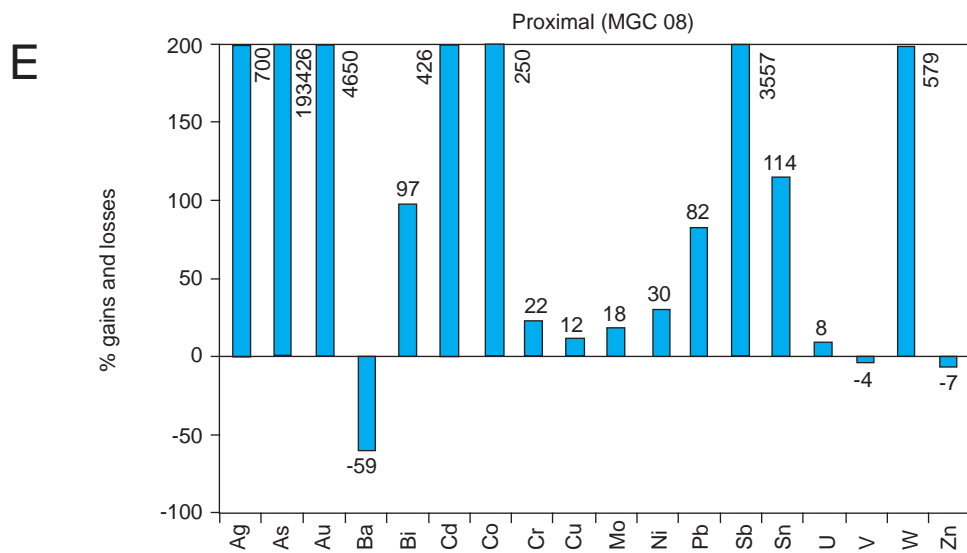
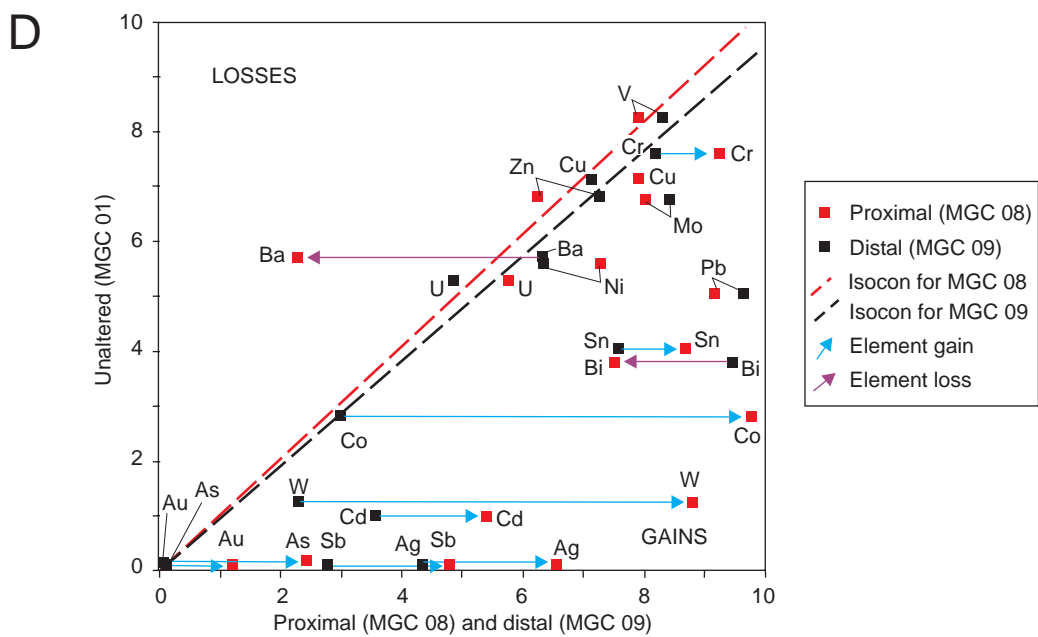


Figure 5.6 **Element enrichment and depletion associated with P-stage 3.4 arsenopyrite-carbonate-quartz-gold proximal and distal alteration of monzonite.** The isocon diagrams (A – major elements and D - metals) were plotted using the technique of Grant (1986). Isocon lines were calculated manually with reference to Al_2O_3 , TiO_2 , Y, and Zr, elements that are typically immobile. The diagrams are interpreted such that any elements that plot along or immediately adjacent to the isocon are considered to be immobile. Those that plot above the line are depleted and elements that plot below the line are enriched. The arrows on the diagrams indicate relative element gain and loss from distal to proximal zones. The slope of the isocon line for distal alteration is 0.96 indicating a mass loss of 4%. The isocon line for proximal alteration records a 3% mass gain. Note the depletion of Na_2O and Ba and addition of MnO, CO_2 , K_2O , SO_3 , Ag, Au, As, Sb, Cd, Co and W. Graphs of percentage loss or gain for major elements (B and C) and metals (E and F) have also been plotted for ease of interpretation.





A discussion of element enrichment and depletion

Analysing a small number of tightly constrained samples is a powerful way of resolving the geochemical signature of several stages of alteration. However, the limited number of samples analysed can produce results that do not represent alteration on a larger scale. Element enrichment and depletion trends identified in this chapter can be related to previously described alteration mineral assemblages and element correlations. Elevated levels of CO_2 and SO_3 and depleted Na_2O recorded by MGC03, MGC06 and MGC08 likely correspond to pervasive carbonate and pyrite or carbonate and arsenopyrite alteration of feldspars associated with stage 3.1 and stage 3.4 respectively (chapter 4). Enriched MnO may be associated with carbonate alteration as small amounts of Mn were detected in ankerite and dolomite present in stage 3.1 and 3.4 veins. Elevated MnO may also correspond to pyrite alteration in stage 3.1. Elevated levels of K_2O can be correlated with illite (possibly after sericite) alteration around stage 3.1 and stage 3.4 veins (chapter 4). Despite the pervasive carbonate and pyrite alteration, CaO and Fe_2O_3 are not enriched. Thus, the Ca and Fe required to form calcite and pyrite respectively was likely sourced from destruction of feldspars and biotite.

Metal enrichments recorded by samples of stage 3.1 and 3.4 altered monzonite are grouped similarly to the element suites recorded by correlation matrices and factor analysis. For example, Au-As-Sb-Ag-Pb addition recorded by MGC 06 and 08 is consistent with the $\text{Au-As-Sb} \pm \text{Ag-Pb}$ element relationships identified using factor analysis and correlation matrices in chapter 5.2. Enrichment of Co-Mn in samples of stage 3.4 alteration is similar to the Co-Fe-Mn correlation also established by factor analysis and perhaps further indicates that Mn enrichment is associated with sulphide alteration. Tin and W are consistently enriched in the proximal alteration zones and elevated levels of Sn and W are a common feature of IRGS. Observed Ba depletion may relate to alteration of feldspars as Ba commonly substitutes into igneous feldspars.

5.4 Geochemistry of the main sulphide phases at Brewery Creek.

The incorporation of gold into iron sulphide and sulpharsenide minerals has been inferred for many years (Boyle, 1979). Arsenopyrite, arsenian pyrite and pyrite are the most common hosts of gold, however, gold also occurs in lesser concentrations in marcasite, pyrrhotite, chalcopyrite, galena, tetrahedrite, bornite, sphalerite, and stibnite

(e.g. Cabri et al., 1989; Cook and Chrysosoulis, 1990; Cabri, 1992; Fleet et al., 1993; Fleet and Mumin, 1997; Oberthur et al., 1997; Genkin et al. 1998; Simon et al., 1999; Ashley et al., 2000). The term 'invisible gold' (synonyms include 'hidden', 'sub-microscopic' and 'refractory') was introduced by Bürg (1930) to denote gold in solid solution and of colloidal size within sulphide grains and evolved to the current definition of gold undetectable with optical microscopy or scanning electron microscopy (Cook and Chrysosoulis, 1990). The most famous examples of deposits containing invisible gold in sulphide minerals are those of the Carlin Trend (sediment-hosted gold) but this style of mineralisation has also been noted in mesothermal (Iode or orogenic), epithermal, and volcanic-hosted massive sulphide deposit styles (e.g. Cabri et al., 1989; Cathelineau et al., 1989; Seabrook, 1989; Cook and Chrysosoulis, 1990; cabri, 1992; Arehart et al, 1993; Fleet et al., 1993, Mumin et al., 1994; Huston et al., 1995; Oberthür et al., 1997; Fleet and Mumin, 1997; Genkin et al., 1998; Simon et al., 1999; Ashley et al., 2000).

At Brewery Creek, paragenetic studies (chapter 4) using optical microscopy and EDS (energy dispersive spectrometer) microprobe data resolved several distinct pyrite and arsenopyrite morphologies but failed to document gold. Metallurgical testing (Laprenune, 1997) commissioned by Viceroy, indicated that the bulk of the gold mineralisation along the Reserve Trend occurs in association with arsenopyrite as invisible gold, with free gold amounting to less than 10% of the ore. However, these findings were not correlated to specific arsenopyrite morphologies nor did they investigate the possibility of gold in arsenic-rich pyrite. To resolve the relationship between gold, arsenopyrite and pyrite, and to investigate the composition of individual sulphide grains, laser ablation - inductively coupled plasma - mass spectrometry (LA-ICP-MS) was performed on 13 paragenetically well-constrained samples. The analysis recorded a suite of 16 trace elements including Ag, As, Au, Bi, Cd, Co, Cu, Mn, Mo, Ni, Pb, Sb, Se, Sn, W, and Zn. Similar studies have been carried out on samples from other deposits (Watling et al., 1995; Chenery et al., 1995; Baker et al., 2005).

Samples for the LA-ICP-MS study were collected from the Blue (MJL 49, 54), Golden (MJL 50, 58, 61), Kokanee (MJL 55, 62, 63), Fosters (MJL 52), and Canadian (MJL 53) open pits and from the North Slope (MJL 57) and Schooner (MJL 51 and 56) zones so as to provide examples of all variations in sulphide morphology. Pyrite grains analysed by LA-ICP-MS were sampled from carbonaceous shale, monzonite, at the shale-monzonite margin, a monzonite-shale breccia, paragenetic stage 3.1 veins, and in proximal and distal alteration zones around stage 3.1 veins. Samples with pyrrhotite

were taken from monzonite and contact metamorphosed siltstone adjacent to a monzonite sill. All arsenopyrite grains analysed were in samples of monzonite, but were located within stage 3.4 veins or in proximal or distal alteration sites. Sulphide grains > 80-100 µm in diameter were preferentially ablated so as to reduce the possibility of ablating more than one sulphide morphology. Samples of arsenopyrite from sedimentary rocks were not evaluated, as arsenopyrite grains were too small (< 50 µm) to obtain a successful arsenopyrite-only ablation. Samples of stibnite analysed in this study were hosted by monzonite. Sulphide grains classified as proximal were located within 0.5 cm of a vein, distal samples are grains of sulphide that are between 0.5 and 2 cm from a vein and disseminated sulphides are those that show no clear spatial relationship to a vein. The relative location of each sulphide grain analysed is shown on Figures 5.7 and 5.8. Table 5.9 provides descriptions of the samples used in the LA-ICP-MS study, and Table 5.10 summarises the variation in concentration of various trace elements within different sulphide morphologies. LA-ICP-MS analytical methodology and full geochemical results are presented in Appendices 2 and 15 respectively.

Resolution of the gold-arsenopyrite-pyrite relationship

Sulphide phases investigated by this study include (1) arsenopyrite, (2) arsenopyrite overgrowths on pyrite, (3) pyrite, (4) pyrite in a rock also containing arsenopyrite, (5) pyrite with an overgrowth of arsenopyrite, (6) cores and (7) rims of pyrite overgrown by pyrite, (8) cores and (9) rims of pyrite overgrown by pyrite in a rock also containing arsenopyrite, (10) pyrrhotite, and (11) stibnite. Pyrite overgrowths on pyrite crystals and rare micro-scale zoning within pyrite were noted in chapter 4. Zoned arsenopyrite crystals, a common feature of invisible gold systems, were only rarely identified at Brewery Creek (Figure 5.9). Previous investigations of zoned arsenopyrite show that zoning corresponds to variations predominantly in As but also in Fe and S (Wu and Delbove, 1989; Hammond and Tabata, 1997; Yang et al., 1998; Savage et al., 2000). Microprobe investigation of arsenopyrite zonation at Brewery Creek indicates that As and S are variable and Fe is consistently stoichiometric. All arsenopyrite analysed were As-deficient but show a restricted compositional range with atomic % As values of 25.99 to 28.21. The zoning within arsenopyrite was too fine to analyse individual zones (< 50 µm) and it is possible that some of the analyses were of pyrite rather than arsenopyrite as reflected by the low As and high Mn values. Microprobe analysis indicates that pyrite, pyrrhotite and stibnite are near-stoichiometric (Table 5.11).

Figure 5.7 **A schematic diagram illustrating the distribution of pyrite and pyrrhotite grains analysed by LA-ICP-MS.** Note the spatial relationship between sulphide grains, veins and alteration halos. The pyrrhotite corresponds to P-stages 2.1 (MJL50) and 2.2 (MJL51) and all pyrite overgrowing monzonite can be attributed to P-stage 3.1 alteration. The sample numbers are annotated on the diagram. Descriptions of each sample can be found in Table 5.9 and the corresponding data is presented in Appendix 15.

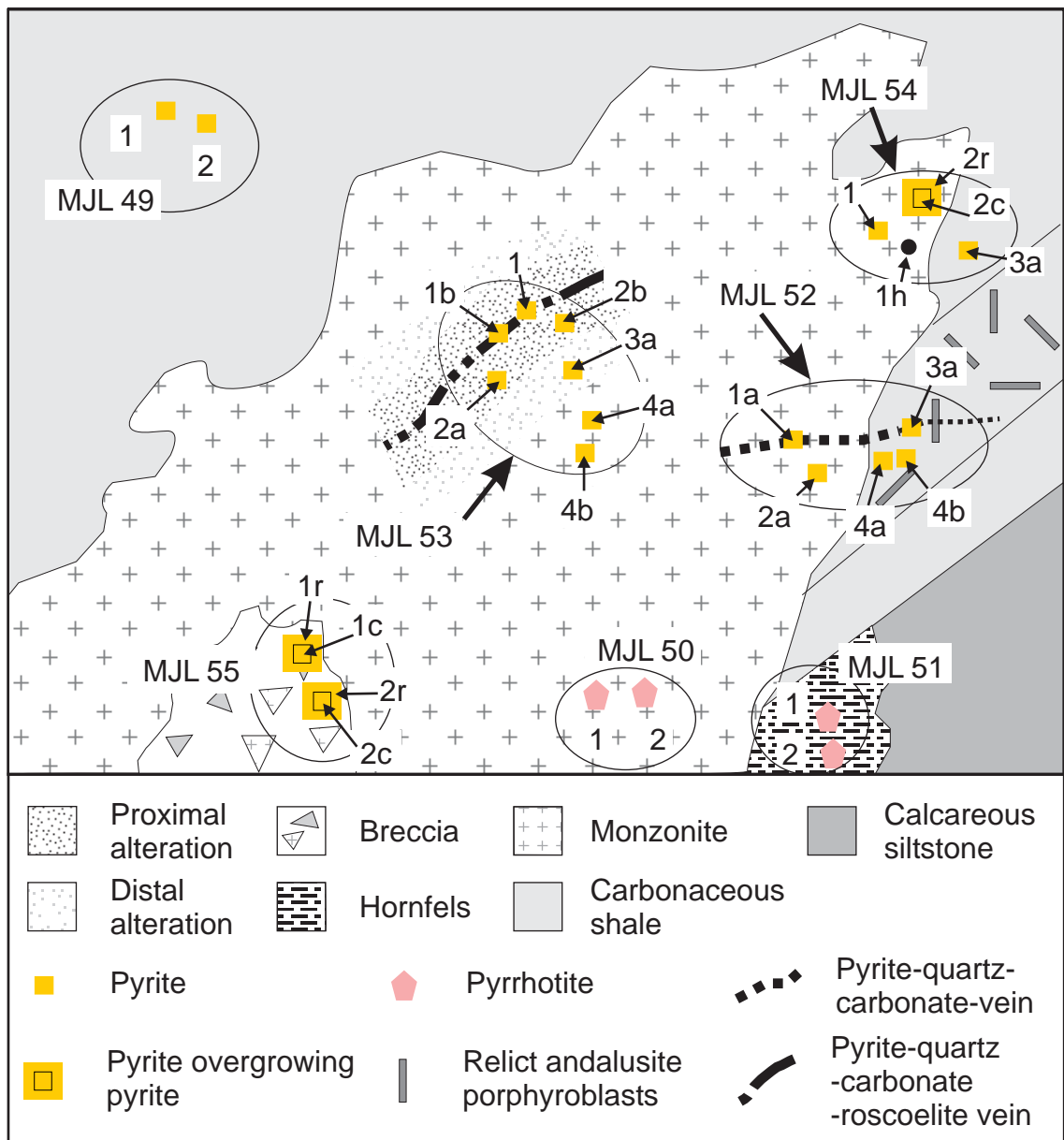
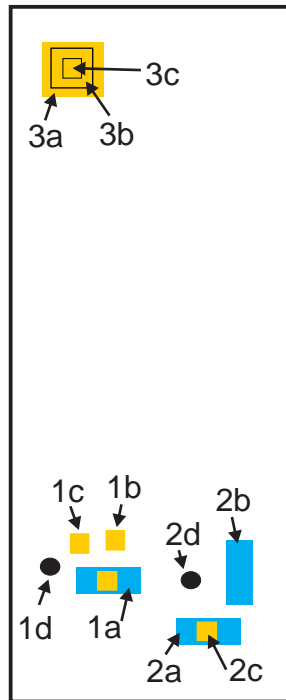
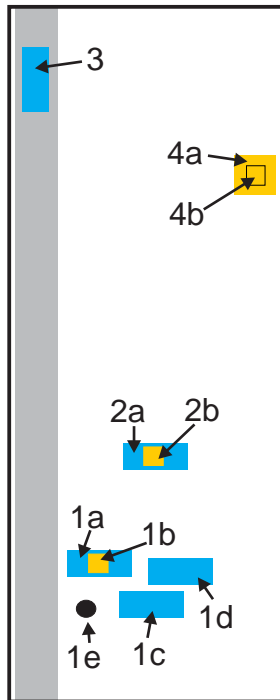


Figure 5.8 **A schematic diagram illustrating the distribution of sulphides analysed by LA-ICP-MS in samples MJL 56-63.** Note the location of sulphide grains with respect to veins and alteration halos. All pyrite can be correlated to P-stage 3.1, arsenopyrite to P-stage 3.4 and stibnite to P-stage 3.8. The sample numbers are annotated on the diagram. Descriptions of each sample can be found in Table 5.9 and the corresponding data is presented in appendix 15.

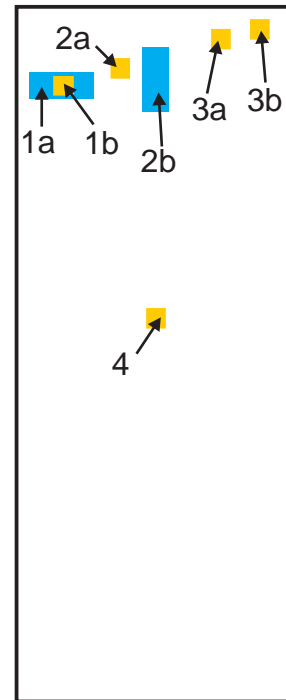
MJL 56



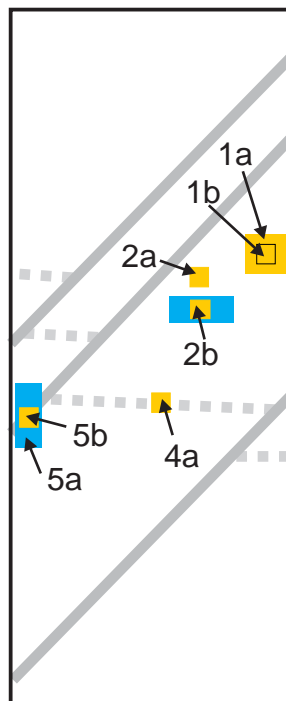
MJL 57



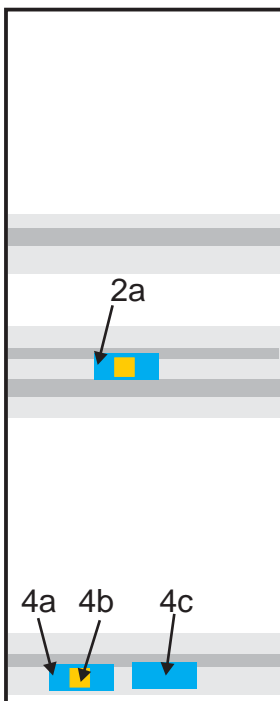
MJL 58



MJL 61



MJL62



MJL63

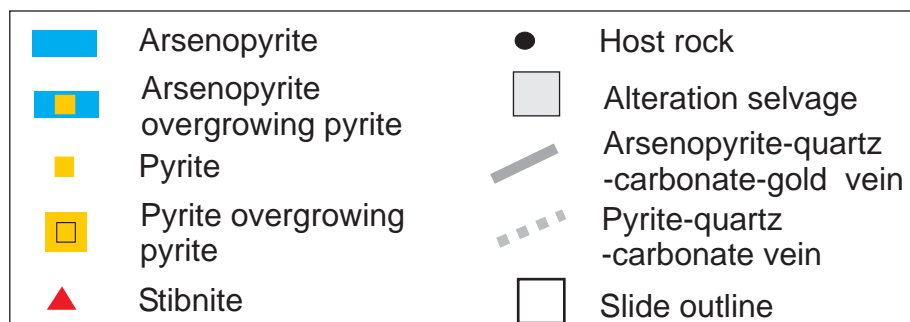
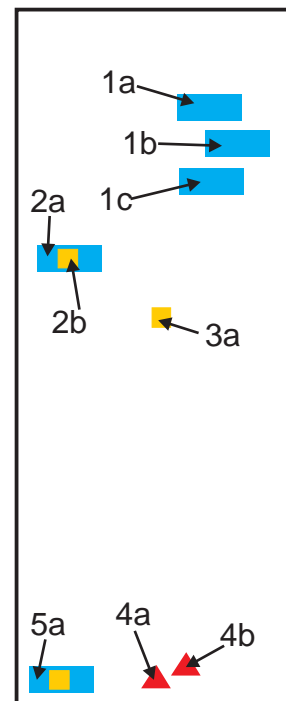


Table 5.9 **Description of samples used for LA-ICP-MS analysis.** Note that the samples incorporate P-stages 1.1, 2.1, 2.2, 3.1, 3.4, and 3.8 and that the samples were sourced from several different mineralised zones.

Sample	Sample location	Rock Type	P-stage	Description
MJL 49	Lucky pit	Carbonaceous shale	1.1	Massive bedded pyrite in Earn Group carbonaceous shale with pyrite grains 1-2 mm in diameter
MJL 50	Schooner zone	Biotite monzonite	2.1	Unaltered monzonite with pyrrhotite grains up to 2 mm in diameter
MJL 51	Schooner zone	Tremolite skarn	2.2	Tremolite-bearing skarn in Steel Formation adjacent to biotite monzonite sill. Pyrrhotite present throughout as grains < 5mm in diameter
MJL 52	Drill hole under Fosters pit (DD89-3, 50m)	Quartz biotite monzonite and carbonaceous shale	3.1	An andalusite-rich contact aureole and quartz-biotite monzonite cut by a pyrite-quartz-carbonate vein. Pyrite crystals typically < 1mm in diameter.
MJL 53	Drill hole into the West Big Rock zone (DD96-105, 98m).	Quartz biotite monzonite	3.1	Quartz biotite monzonite cut by a pyrite-quartz-carbonate-roscoelite vein. Pyrite crystals < 2 mm in diameter.
MJL 54	Golden pit	Biotite monzonite and carbonaceous shale	3.1	Contact between monzonite and Earn Group shale. Pyrite hosted by both intrusive and sedimentary rocks analysed. Sulphide grains typically < 2mm in diameter.
MJL 55	Kokanee pit	Breccia in quartz biotite monzonite	3.1	Pyrite hosted within a breccia comprised of monzonite and shale. Pyrite grains < 3mm in diameter.
MJL 56	Schooner zone	Biotite monzonite	3.1 and 3.4	Arsenopyrite-quartz-carbonate-gold veins within biotite monzonite. Arsenopyrite crystals < 2mm in length, some grains overgrow pyrite. Sample also contains a pyrite grain with three stages of growth.
MJL 57	North Slope zone	Quartz biotite monzonite	3.1 and 3.4	Arsenopyrite-quartz-carbonate-gold veins within quartz biotite monzonite. Arsenopyrite crystals < 1 mm in length, some grains overgrow pyrite. Zoned pyrite grain also present approximately 3 mm in diameter.
MJL 58	Golden pit	Biotite monzonite	3.1 and 3.4	Biotite monzonite with arsenopyrite, pyrite, carbonate, clay, gold alteration. No veins within thin section however original sample contained arsenopyrite-quartz-carbonate-gold vein.

Sample	Sample location	Rock Type	P-stage	Description
MJL 61	Golden pit	Biotite monzonite	3.1 and 3.4	Arsenopyrite-quartz-carbonate-gold and pyrite-quartz-carbonate veins within biotite monzonite. The arsenopyrite-bearing veins clearly cross-cut the pyrite-bearing veins. Arsenopyrite crystals < 1 mm in length, some grains overgrow pyrite. Zoned pyrite grains present up to 2 mm in diameter.
MJL 62	Kokanee pit	Biotite monzonite	3.1 and 3.4	Several arsenopyrite-quartz-carbonate-gold veins within biotite monzonite. Arsenopyrite crystals < 1 mm in length, some grains overgrow pyrite.
MJL 63	Kokanee pit	Quartz biotite monzonite	3.1, 3.4, and 3.8	Arsenopyrite, pyrite, carbonate, clay, gold alteration of quartz biotite monzonite. No veins in thin section or hand sample. Monzonite has been brecciated with massive stibnite infill.

Table 5.10 **Mean, median, minimum and maximum values of various trace elements in arsenopyrite, pyrite, pyrrhotite and stibnite at Brewery Creek.** Note the high levels of Au and Ag in arsenopyrite compared with other sulphides.

Mineral		Ag (ppm)	As (ppm)	Au (ppm)	Bi (ppm)	Cd (ppm)	Co (ppm)	Cu (ppm)	Fe (ppm)	Mn (ppm)	Mo (ppm)
Arsenopyrite (8)	Mean	45.43	104972.08	787.37	1.33	2.68	97.31	234.57	411539.61	17434.21	3.89
	Median	19.29	112415.46	323.87	0.59	1.28	28.38	140.78	411539.57	11031.98	3.94
	Minimum	0.26	2014.02	13.94	0.26	0.53	3.65	71.82	411539.47	50.34	0.32
	Maximum	119.46	163325.93	1880.83	4.49	9.53	393.23	508.16	411539.77	65347.32	6.96
Arsenopyrite on pyrite (11)	Mean	34.64	113886.66	293.65	5.49	1.51	113.68	100.59	411539.57	1422.12	3.20
	Median	27.30	75979.60	262.66	0.88	0.92	63.98	70.22	411539.59	1112.08	1.06
	Minimum	1.00	10230.32	18.32	0.24	0.23	11.88	35.48	411539.40	11.78	0.33
	Maximum	121.19	294398.77	1169.47	49.15	7.45	318.01	295.54	411539.74	4916.26	12.32
Pyrite overgrown by arsenopyrite (8)	Mean	25.62	94853.14	101.61	18.47	1.17	175.81	136.56	465531.61	1686.20	10.32
	Median	20.79	50251.38	52.39	3.27	0.58	127.89	123.75	465531.60	102.39	2.43
	Minimum	1.70	6299.70	6.94	0.18	0.18	15.64	41.71	465531.41	6.45	0.33
	Maximum	53.54	439595.44	304.24	123.56	5.40	387.76	348.11	465531.88	10311.03	57.54
Pyrite in a rock with arsenopyrite (16)	Mean	11.68	24741.05	9.51	11.41	0.76	1285.26	132.95	465531.58	911.23	161.51
	Median	8.32	2489.32	2.58	3.12	0.48	134.77	54.48	465531.56	58.21	0.90
	Minimum	2.72	25.84	0.04	1.22	0.20	1.87	8.35	465531.41	1.22	0.02
	Maximum	37.78	247943.22	69.09	61.80	2.15	11419.01	1250.37	465531.94	7565.05	1629.87
Pyrite (22)	Mean	7.47	1986.18	0.36	7.80	2.63	206.56	183.27	465531.58	155.80	19.99
	Median	5.96	785.80	0.18	2.90	0.78	111.90	74.46	465531.56	5.23	2.65
	Minimum	0.76	31.93	0.03	0.07	0.31	0.43	10.29	465531.53	1.64	0.10
	Maximum	23.56	7254.63	1.17	50.86	32.70	1475.87	1299.97	465531.69	1489.59	158.46
Pyrrhotite (4)	Mean	3.28	69.66	0.12	5.03	2.49	273.23	3.24	600006.42	5.29	9.46
	Median	2.51	5.97	0.10	1.48	2.07	270.27	3.66	600006.41	5.74	11.39
	Minimum	0.81	3.61	0.05	1.13	1.48	120.54	1.60	600006.31	1.24	0.36
	Maximum	7.29	263.08	0.21	16.02	4.32	431.83	4.06	600006.56	8.44	14.70
Stibnite (2)	Mean	4.58	242.52	0.02	0.06	0.45	0.01	25.75	37.31	1.34	0.02
	Median	4.58	242.52	0.02	0.06	0.45	0.01	25.75	37.31	1.34	0.02
	Minimum	3.60	230.52	0.02	0.05	0.37	0.01	16.05	26.33	0.37	0.02
	Maximum	5.56	254.51	0.02	0.06	0.53	0.02	35.44	48.29	2.32	0.03

Mineral		Ni (60) (ppm)	Ni (62) (ppm)	Pb (ppm)	S (ppm)	Sb (ppm)	Se (ppm)	Sn (ppm)	W (ppm)	Zn (ppm)
Arsenopyrite (8)	Mean	37.53	110.77	140.45	236320.18	1207.03	208.46	1.89	41.28	665.82
	Median	21.89	33.82	147.73	236320.17	1353.63	192.54	1.67	20.57	238.51
	Minimum	11.71	14.62	12.04	236320.09	11.08	24.91	0.58	1.25	12.97
	Maximum	116.98	457.22	228.94	236320.22	1825.24	718.58	4.66	96.98	2479.42
Arsenopyrite on pyrite (11)	Mean	1786.49	129.36	255.58	236320.15	1062.30	101.82	3.83	57.80	297.48
	Median	78.74	85.37	211.46	236320.16	996.55	103.92	2.75	3.58	12.55
	Minimum	1.19	6.58	106.96	236320.07	344.83	17.53	0.46	0.09	4.03
	Maximum	18550.10	438.50	448.42	236320.22	1701.23	173.09	11.18	266.42	2742.31
Pyrite overgrown by arsenopyrite	Mean	188.45	238.33	408.16	534428.86	1114.83	75.49	3.31	34.13	2668.75
	Median	97.08	118.34	276.75	534428.88	751.75	43.90	1.31	4.96	356.42
	Minimum	4.42	8.04	86.80	534428.69	137.72	17.89	0.22	0.08	9.39
	Maximum	550.65	732.08	1001.04	534429.00	3113.28	194.16	14.07	180.05	17770.62
Pyrite in a rock with arsenopyrite (24)	Mean	447.53	530.72	923.24	534428.80	696.26	59.64	2.60	7.55	311.84
	Median	63.16	76.44	571.44	534428.81	215.02	55.12	2.30	1.23	80.51
	Minimum	0.79	3.14	147.59	534428.63	38.17	14.63	0.12	0.09	1.64
	Maximum	3698.71	4287.90	5595.18	534429.00	4767.20	135.46	7.32	83.57	1567.95
Pyrite (22)	Mean	873.00	1029.07	494.56	534428.89	216.23	231.09	3.57	1.42	507.19
	Median	228.15	271.14	162.00	534428.88	64.58	140.67	0.90	0.53	20.75
	Minimum	7.84	8.86	22.68	534428.81	6.02	13.36	0.13	0.01	0.89
	Maximum	4870.15	5632.38	3955.78	534429.00	2339.71	883.32	19.73	5.44	7031.10
Pyrrhotite (4)	Mean	3408.04	4032.44	52.17	400271.30	22.51	259.31	5.16	1.23	20.68
	Median	3391.33	4028.33	8.03	400271.30	28.21	239.57	4.49	0.15	22.76
	Minimum	297.94	354.56	3.62	400271.28	0.79	86.01	0.26	0.07	7.12
	Maximum	6551.56	7718.52	189.00	400271.31	32.83	472.08	11.39	4.53	30.09
Stibnite (2)	Mean	0.35	0.88	81.91	283125.31	716888.53	1158.92	15.66	0.02	18.32
	Median	0.35	0.88	81.91	283125.31	716888.53	1158.92	15.66	0.02	18.32
	Minimum	0.12	0.55	69.94	283125.31	716888.50	1145.37	3.27	0.02	11.99
	Maximum	0.58	1.21	93.88	283125.31	716888.56	1172.47	28.04	0.02	24.64

Figure 5.9 Scanning electron microprobe backscatter images of pyrite overgrown by arsenopyrite. The samples are from the Golden (A) and Kokanee (B, D) pits and the Schooner zone (C). The arsenopyrite crystals are typically un-zoned (A-C), but rare zoned arsenopyrite was noted (D). The highly irregular pyrite – arsenopyrite margin in (B) indicates that pyrite is resorbed by arsenopyrite. Images (A) and (B) are of an area approximately approximately 300 microns wide and (C) and (D) are of an area approximately 200 microns wide.

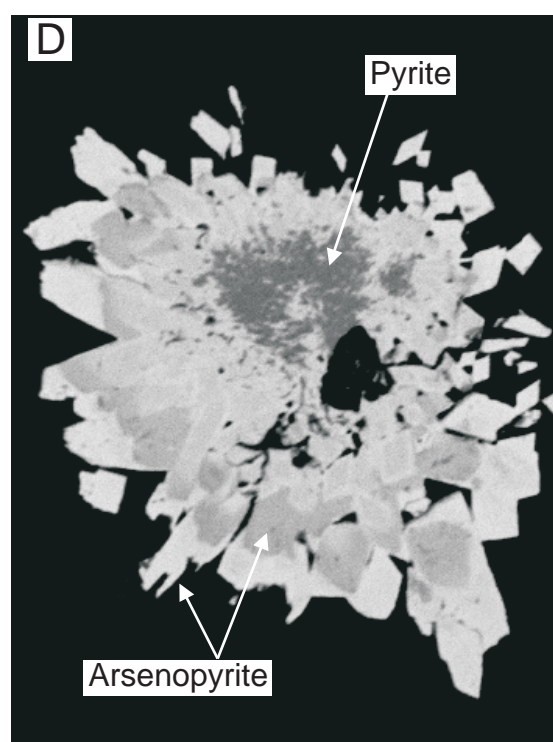
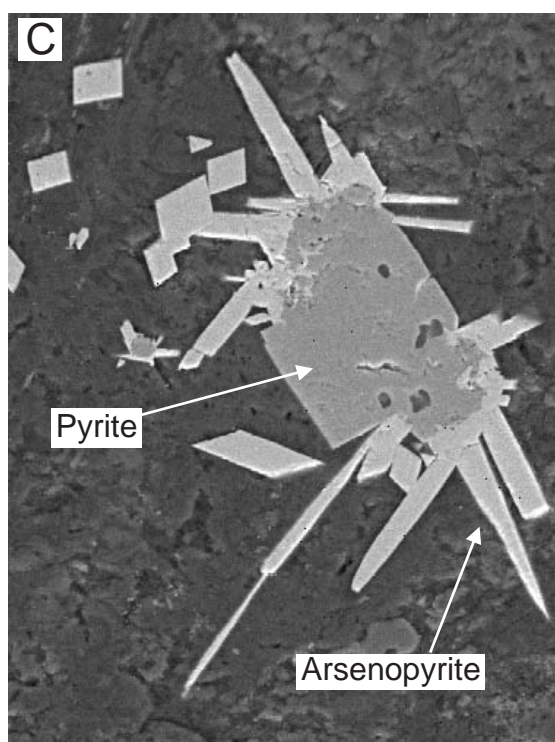
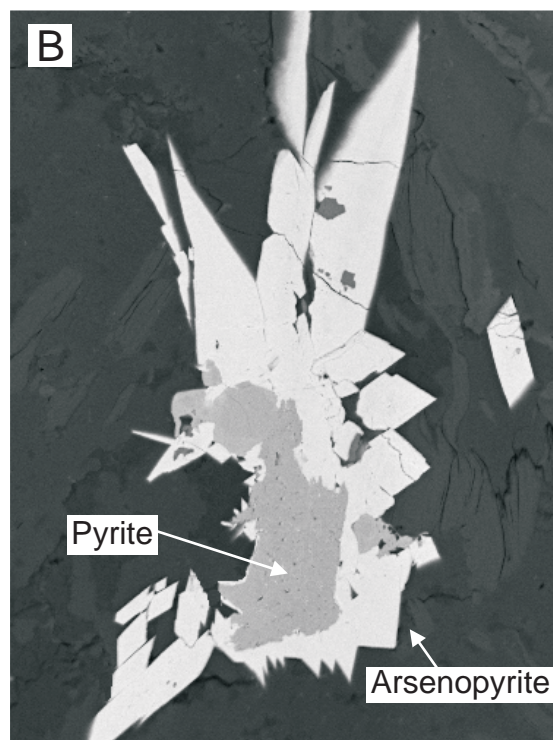
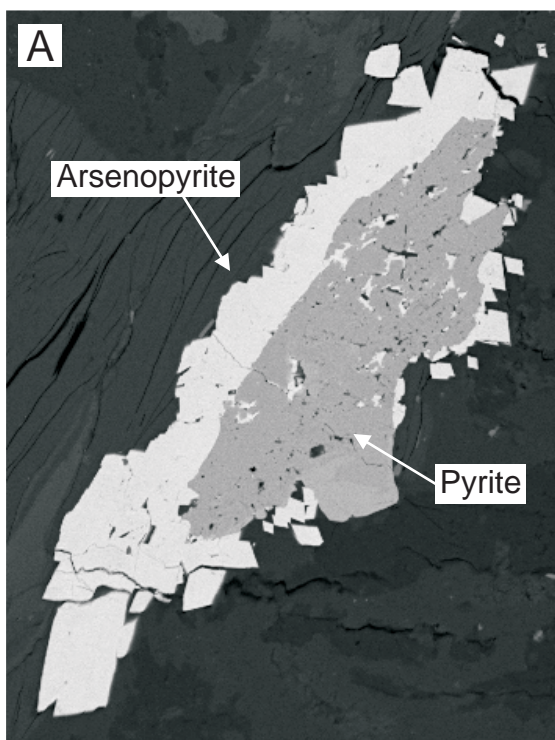


Table 5.11 Atomic % of the major components in arsenopyrite, pyrite, pyrrhotite, and stibnite. Note that arsenopyrite is As-deficient and S-enriched but that the variation between samples is minor.

Mineral	Atomic %			
	Fe	S	As	Sb
Arsenopyrite	33.20	38.59	28.21	
	33.54	39.56	26.90	
	33.15	39.74	27.10	
	33.27	40.74	25.99	
	33.29	39.86	26.85	
	33.52	39.70	26.78	
Pyrite	35.09	64.91		
	34.33	65.67		
	34.17	65.83		
	35.05	64.95		
	33.86	66.14		
	33.87	66.13		
	33.87	66.13		
	34.96	65.04		
	35.35	64.65		
	36.05	63.95		
Pyrrhotite	49.85	50.33		
	49.93	50.15		
	49.62	51.01		
Stibnite		58.68		41.32
		59.16		40.84
		58.65		41.35
		59.00		41.00
		58.66		41.34
		58.59		41.41

LA-ICP-MS data shows that gold contents range from below detection in stibnite to greater than 1000 ppm in arsenopyrite (Figure 5.10). Arsenopyrite grains recorded the highest gold content of 1881 ppm (sample MJL 63) but also recorded values as low as 14 ppm Au. Arsenopyrite overgrowths on pyrite displayed similar levels with a maximum of 1169 ppm Au and a minimum of 18 ppm Au. An average concentration of 501 ppm Au and a median of 262 ppm was calculated for all arsenopyrite analyses. Zones of distal alteration contain the highest gold grades with maximum gold values of vein hosted and proximal arsenopyrite grains an order of magnitude less (Figure 5.11). The maximum gold concentrations for both arsenopyrite and arsenopyrite overgrown on pyrite were from arsenopyrite grains located within stage 3.4 distal alteration zones. The minimum Au concentration from arsenopyrite in distal alteration zones was 60 ppm. Samples from stage 3.4 proximal alteration range from 14 to 403 ppm Au and vein hosted arsenopyrite show Au concentrations between 196 and 341 ppm. The lowest concentration of Au in both arsenopyrite and arsenopyrite overgrown on pyrite (18 ppm) was from sample MJL 57 that contained a prominent arsenopyrite-carbonate-quartz-gold vein.

Analysis of pyrite grains shows that gold concentrations vary according to the presence or absence of arsenopyrite in the same sample. Pyrite in samples devoid of arsenopyrite recorded Au concentrations of 0.03 (i.e. just above the lower detection limit for Au) to 1.08 ppm and had an average of 0.25 ppm. Considering that sulphides comprise a maximum of 10% of the ore at Brewery Creek and that sulphides host the bulk of gold mineralisation, an economically significant Au assay in pyrite would be 5, or more likely 10 ppm. The rim and core of pyrite grains with overgrowths of pyrite also recorded low gold concentrations with a range of 0.24 to 1.17 ppm Au and an average of 0.64 ppm Au. Disseminated pyrite and pyrite in zones of stage 3.1 distal and proximal alteration recorded higher individual gold grades (0.48 to 1.08 ppm) than pyrite hosted by stage 3.1 veins (maximum of 0.25 ppm Au).

The highest gold concentrations recorded in pyrite were for pyrite grains overgrown by arsenopyrite with values of 6.94 to 304.24 ppm Au and an average of 101.61 ppm Au. Individual analyses of disseminated pyrite overgrown by arsenopyrite, and pyrite overgrown by arsenopyrite in a sample of proximal stage 3.4 alteration, recorded higher gold concentrations (304.24 ppm Au and 281.43 ppm Au respectively) than pyrite overgrown by arsenopyrite in a stage 3.4 vein (ppm 84.60 ppm Au). Once again the highest gold concentration for this morphology was from sample MJL 63 and the

Figure 5.10 Histograms of gold grades in various sulphide morphologies at Brewery Creek. The graphs show gold grades in (A) arsenopyrite – aspy, (B) arsenopyrite overgrowths on pyrite – aspy/py, (C) pyrite – py, (D) pyrite in a sample containing arsenopyrite – py(aspy), (E) pyrite overgrown by arsenopyrite – py/aspy, (F) cores and rims of pyrite overgrown by pyrite – pyc and pyr respectively, and (G) cores and rims of pyrite overgrown by pyrite in a sample also containing arsenopyrite – pyc(aspy) and pyr(aspy) respectively. Note that arsenopyrite and arsenopyrite overgrowths on pyrite recorded gold grades more than an order of magnitude greater than analysis of pyrite.

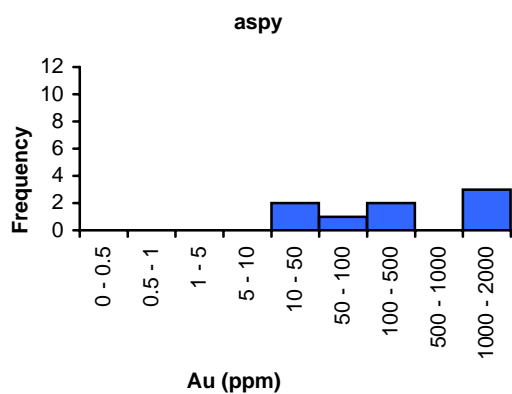
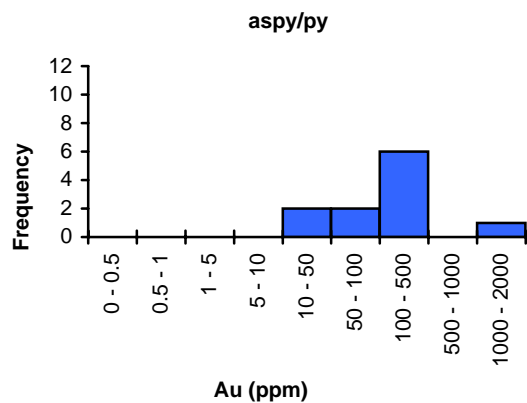
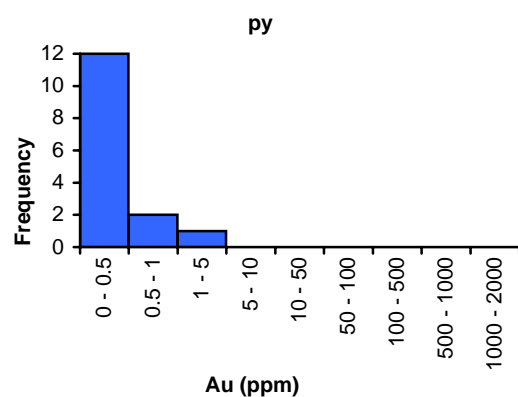
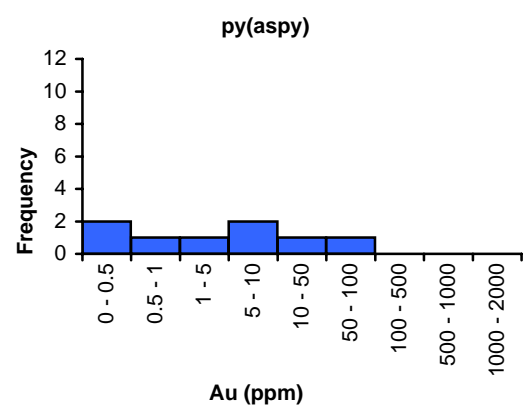
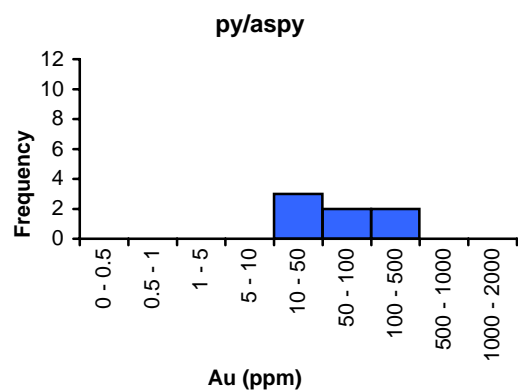
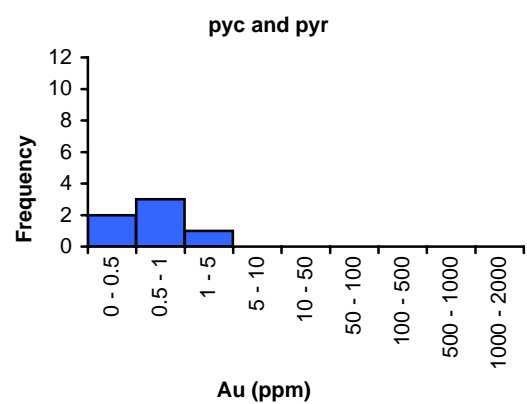
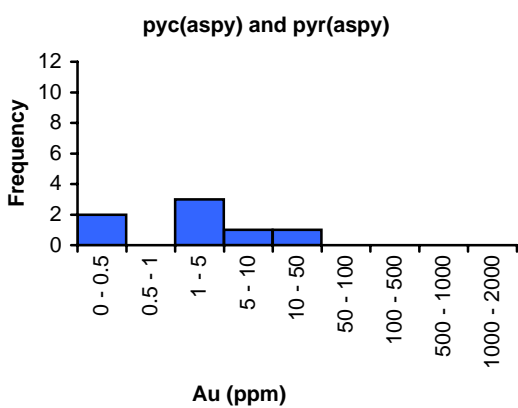
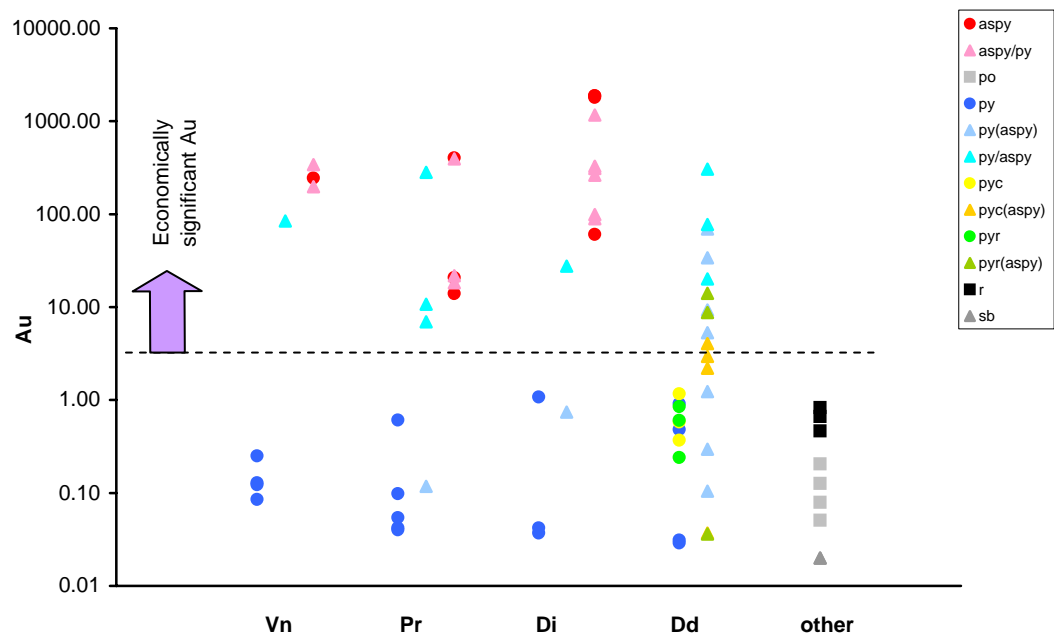
A**B****C****D****E****F****G**

Figure 5.11 A graph illustrating the variation in Au concentration with respect to alteration zones and sulphide morphology. Note that arsenopyrite in distal alteration zones hosts the highest gold grades. Abbreviations on the X-axis refer to sample location with respect to veins; Vn - vein, Pr – proximal alteration, Di – distal alteration, Dd – disseminated sulphide. Abbreviations in the legend translate as aspy – arsenopyrite, aspy/py – arsenopyrite overgrowths on pyrite, po - pyrrhotite, py - pyrite, py(aspy) pyrite in a sample containing arsenopyrite, py/aspy - pyrite overgrown by arsenopyrite, pyc and pyr - cores and rims (respectively) of pyrite overgrown by pyrite, pyc(aspy) and pyr(aspy) - cores and rims (respectively) of pyrite overgrown by pyrite in a sample also containing arsenopyrite, r – host rock, and sb – stibnite.



lowest from MJL 57 indicating that there is a high degree of variation in Au concentration within sulphide morphologies across the Brewery Creek deposit.

Pyrite in samples that also contain arsenopyrite vary in Au concentration from 0.11 to 69.05 ppm with an average of 13.35 ppm Au. No samples of pyrite in stage 3.1 veins were analysed for this morphology, however, gold concentrations were higher in disseminated pyrite than pyrite proximal to stage 3.4 veins. The concentration of Au in the rim and core of pyrite grains with overgrowths of pyrite in samples also containing arsenopyrite varied from 0.04 to 14.05 ppm Au with an average of 4.58 ppm Au. Samples of the rim of pyrite (14.05 and 8.71 ppm Au) overgrowths or zoned pyrite contained higher gold concentrations than the core (4.05 and 2.95 ppm Au). Pyrrhotite and stibnite recorded no significant Au concentrations with values of 0.05 to 0.21 ppm Au and 0.02 ppm Au respectively.

The relationship between gold and various elements in sulphide minerals

Geochemical investigations described in sections 5.2 and 5.3 documented distinct correlations between Au and/or stage 3.4 alteration and several trace elements, in particular As, Sb, Ag, and Pb. To further constrain these relationships the concentration of Au was plotted against other trace element concentrations recorded during the LA-ICP-MS study (Figures 5.12 and 5.13). A Au versus As graph was initially generated for all LA-ICP-MS data as strong Au-As relationships were evident in previously documented geochemical research. The graph displays a weak positive correlation between Au and As ($r^2=0.27$), however, overall high Au is associated with high As (Figure 5.12 A) but the relative concentrations are variable. Inspection of data from different samples indicates that As contents vary significantly between samples and between individual arsenopyrite grains within samples (e.g As contents of arsenopyrite in sample MJL 63 vary between 28365 and 109518 ppm). Plots of individual samples were generated to remove some of the effects of this variation and confirm the strong Au-As relationship with r^2 values of 0.97 and 0.99 (Figure 5.12 B and C).

Gold also variably correlates with Ag, Cd, Cu, Mn, Sb, and Se. A good correlation ($r^2=0.6$) exists between Au-Ag for all data and individual sulphide morphologies record r^2 values as strong as 0.96 and 0.84 for arsenopyrite and arsenopyrite overgrowths on pyrite respectively (Figure 5.13 A). Gold correlated moderately with Cd ($r^2=0.53$) and weakly with Pb ($r^2=0.37$) in analyses of pyrite but showed no correlation in arsenopyrite and other sulphide morphologies at elevated Au contents (Figure 5.13 B and C). There is no correlation between Au and Cu in pyrite (Figure 5.13 D) but a strong correlation

Figure 5.12 **Graphs illustrating the relationship between Au and As.** (A) For all LA-ICP-MS data and for arsenopyrite from individual samples (B and C). A weak positive correlation can be seen in (A) and elevated Au clearly correlates with elevated As. A strong positive correlation between Au and As can be demonstrated for analysis of arsenopyrite across a single sample (B and C). See Figure 5.11 for an explanation of the legend in (A).

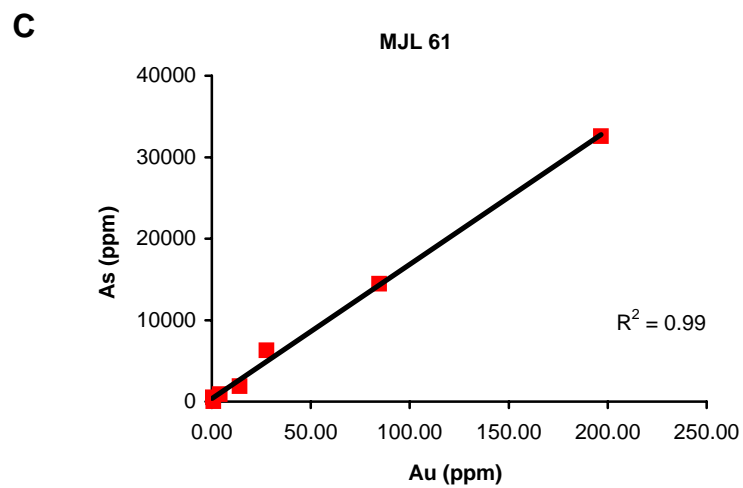
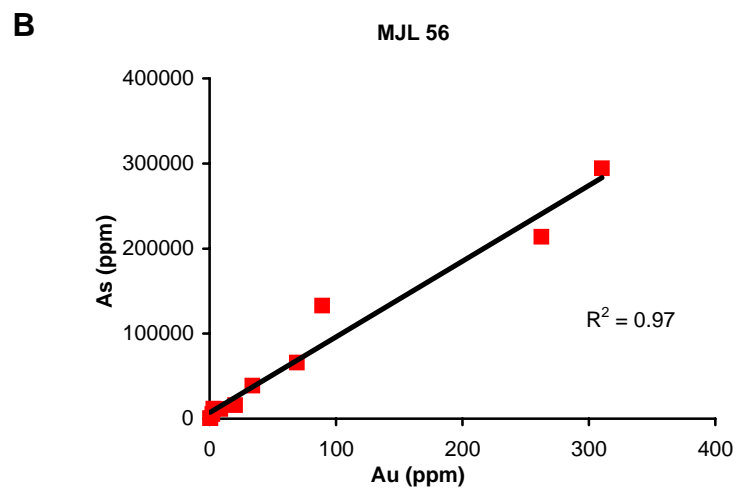
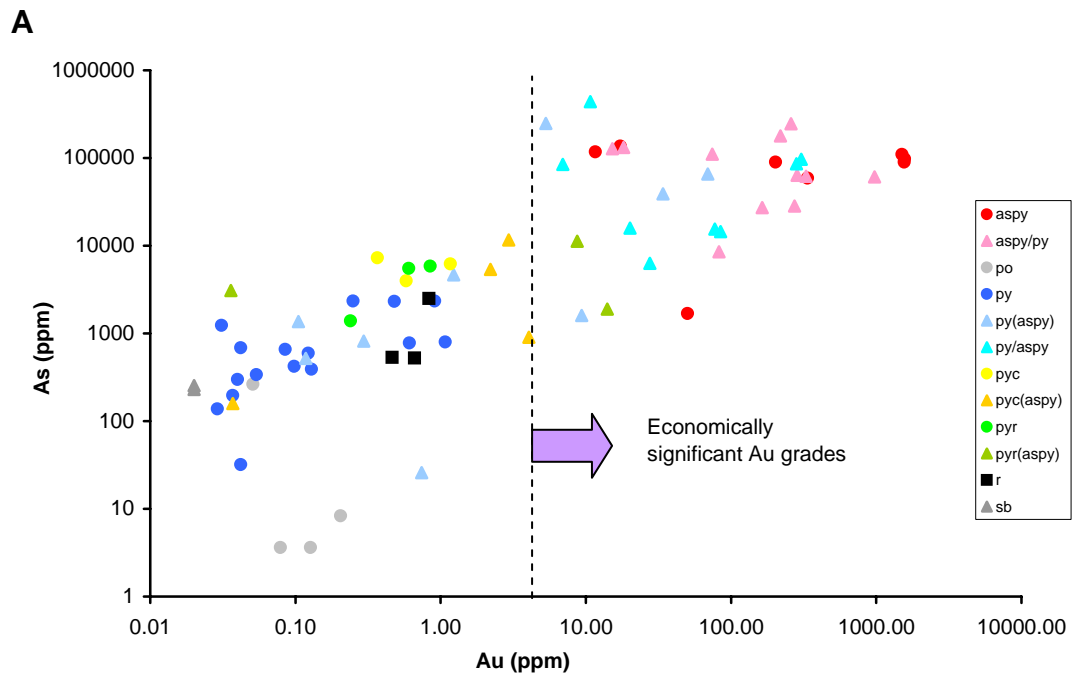
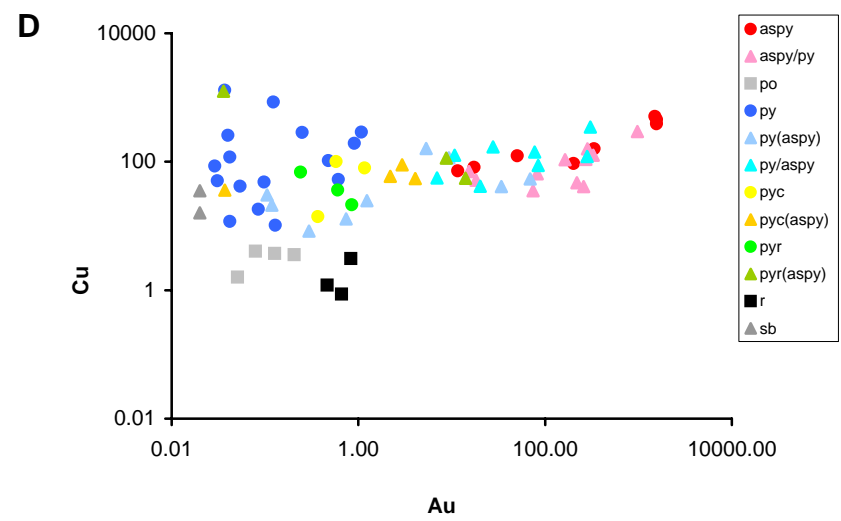
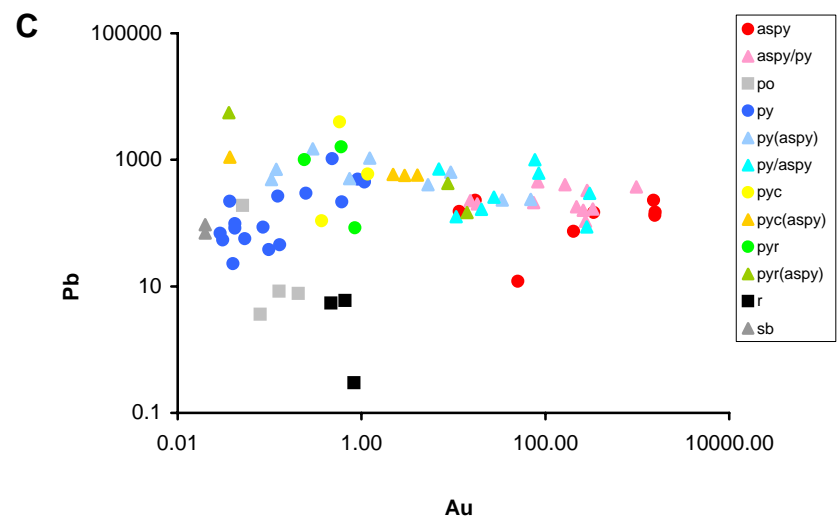
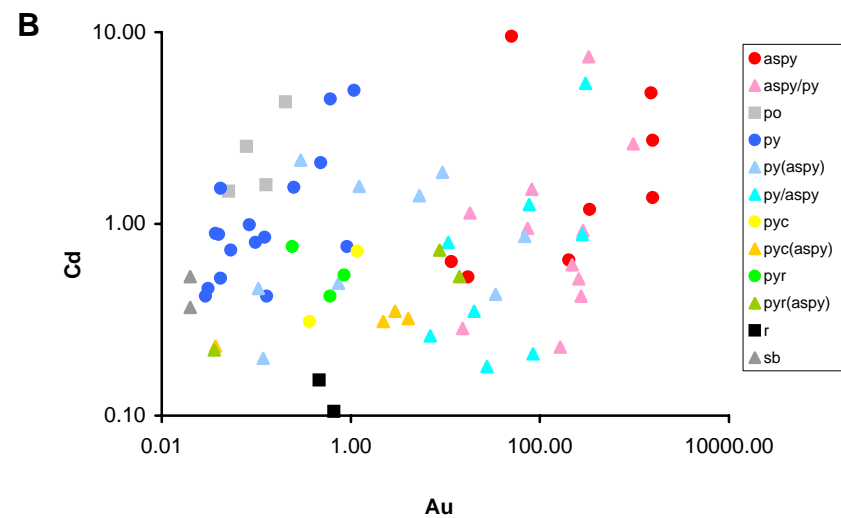
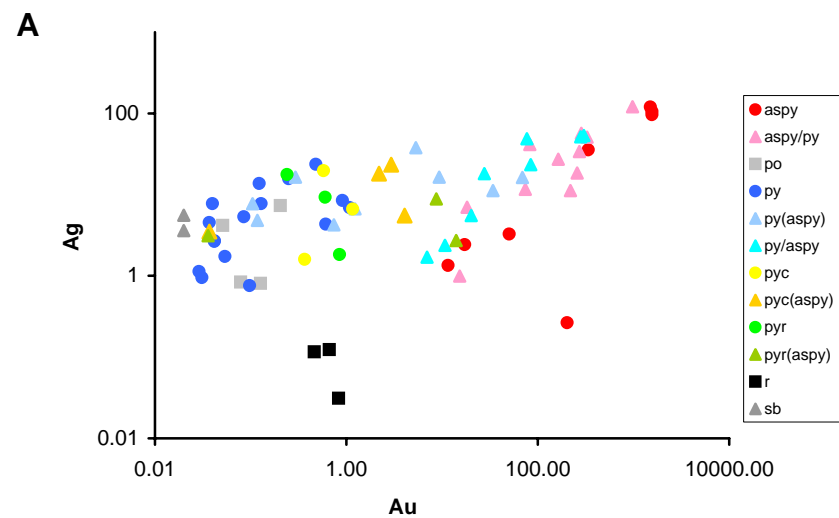
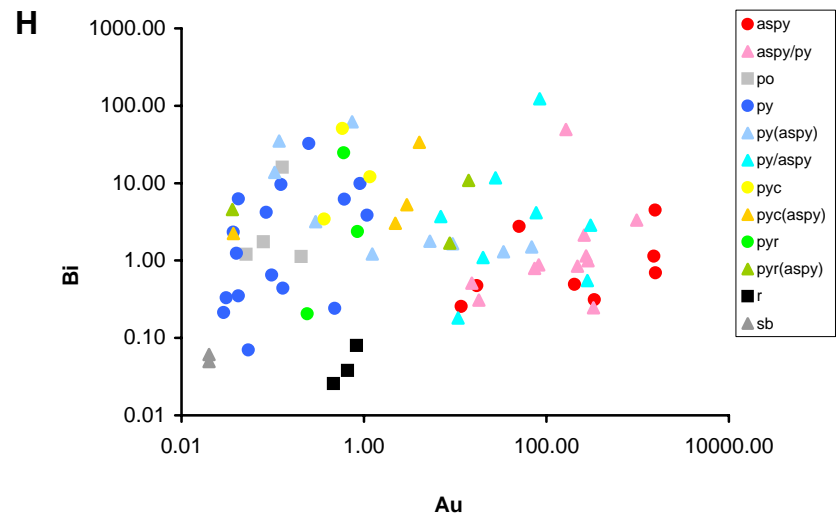
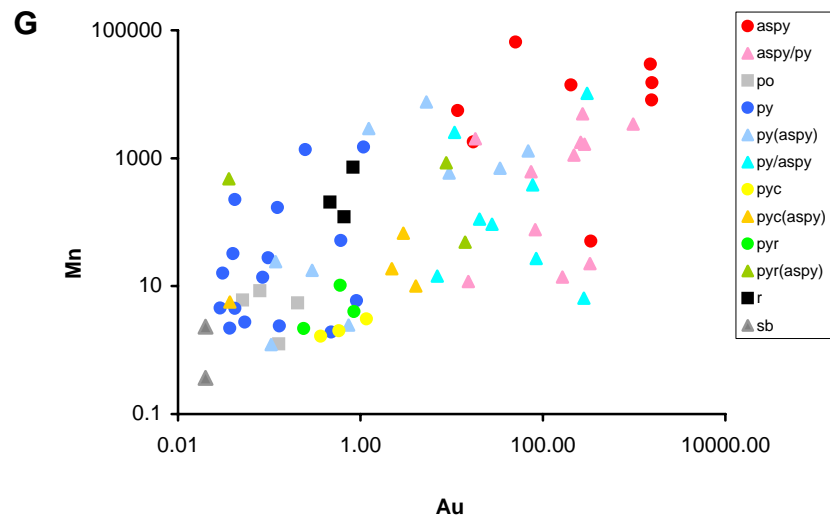
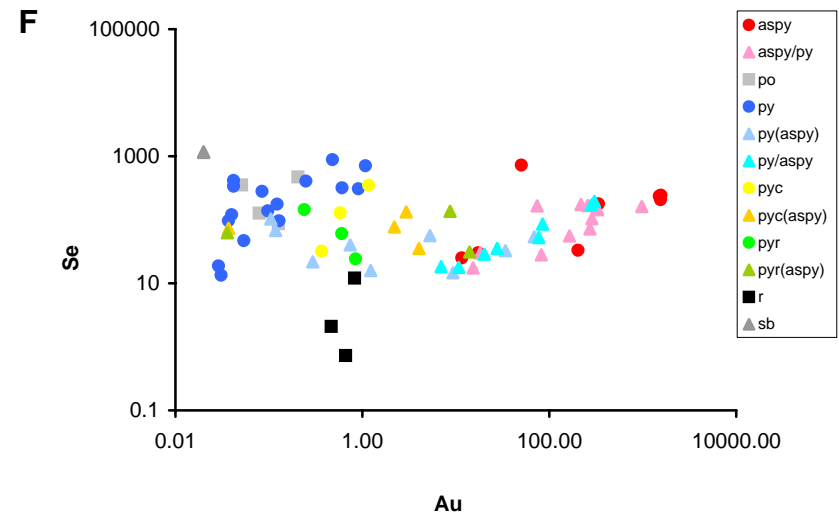
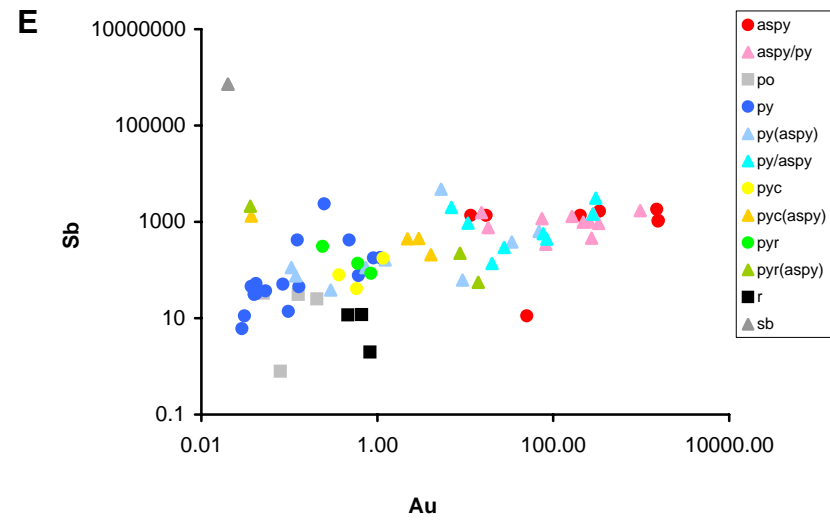
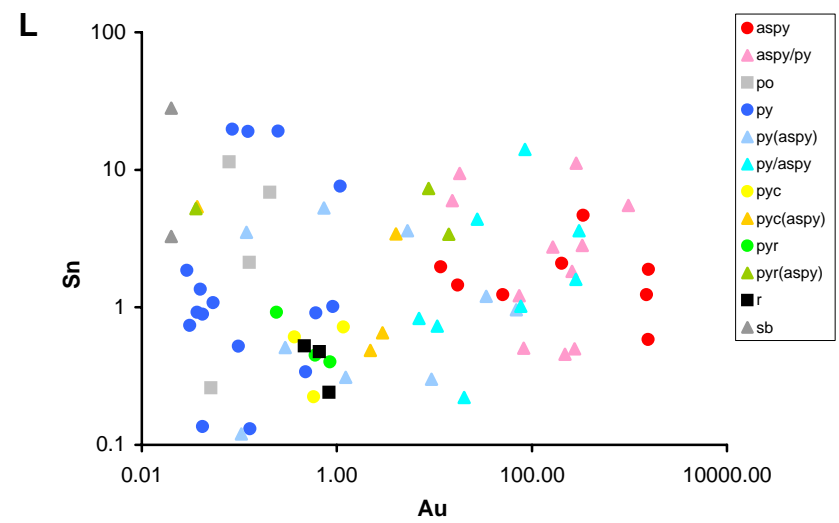
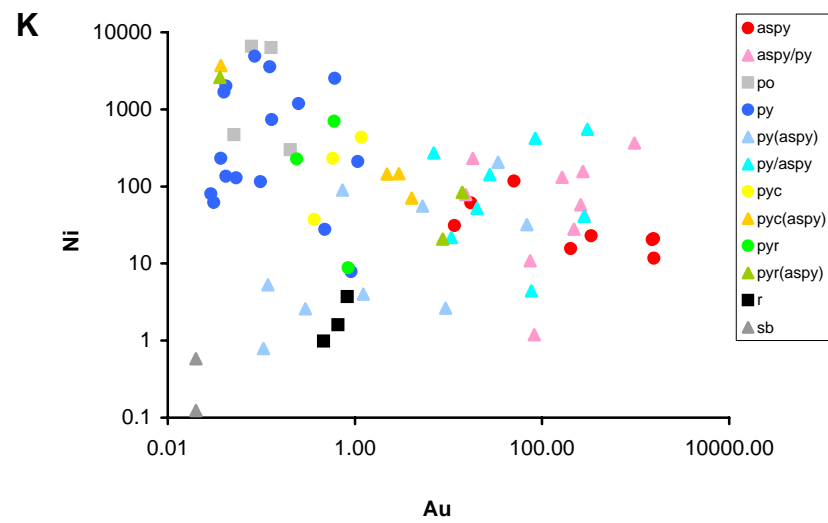
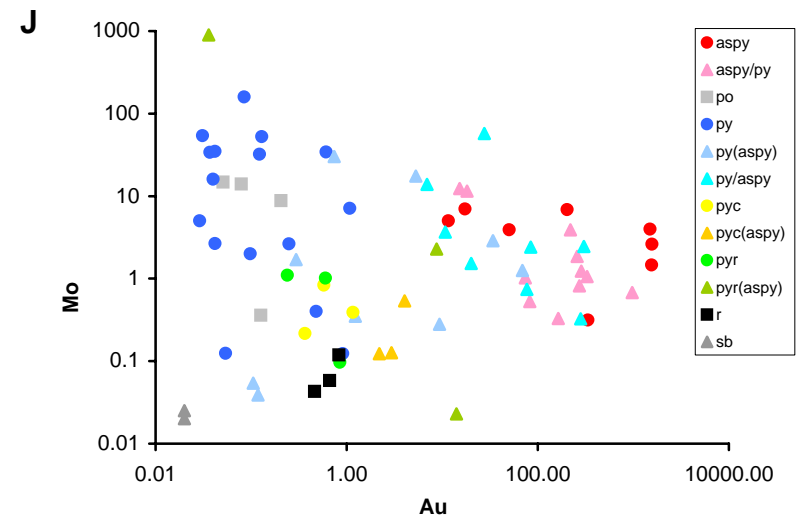
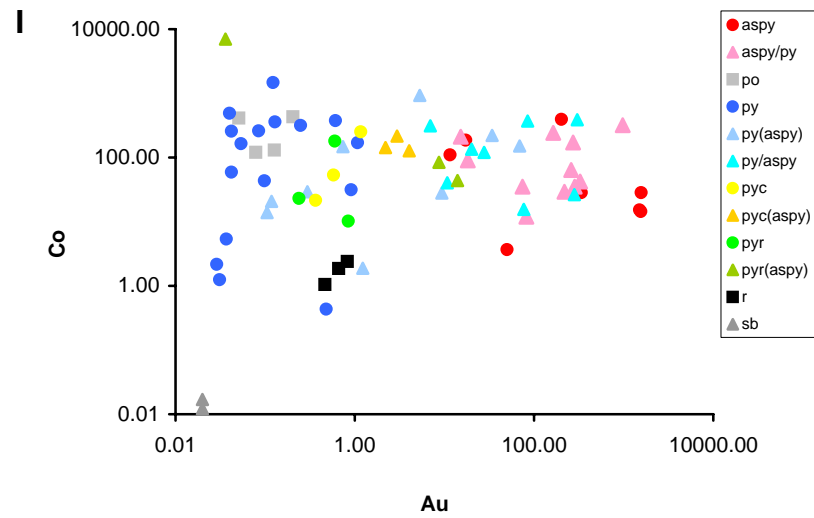
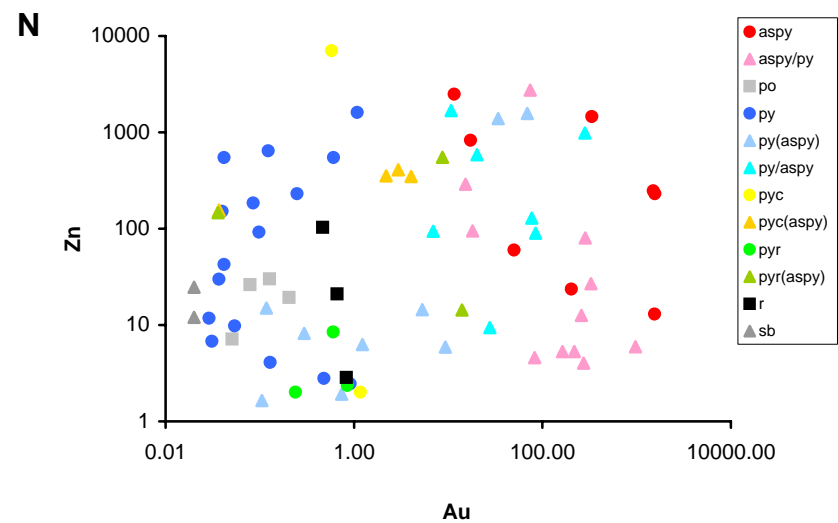
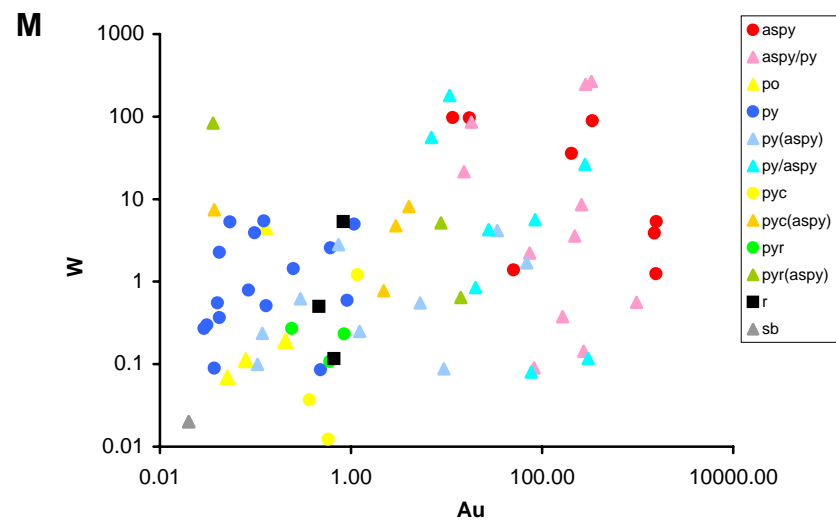


Figure 5.13 **Graphs illustrating the relationship between Au and various trace elements.** Graphs of Au versus Ag (A) and Se (F) show an overall weak to moderate correlation however analysis of arsenopyrite show a strong correlation. Of note, in samples of arsenopyrite Au also correlates with Cu (D) and Sb (E) but not Pb (C). See Figure 5.11 for an explanation of the legend.





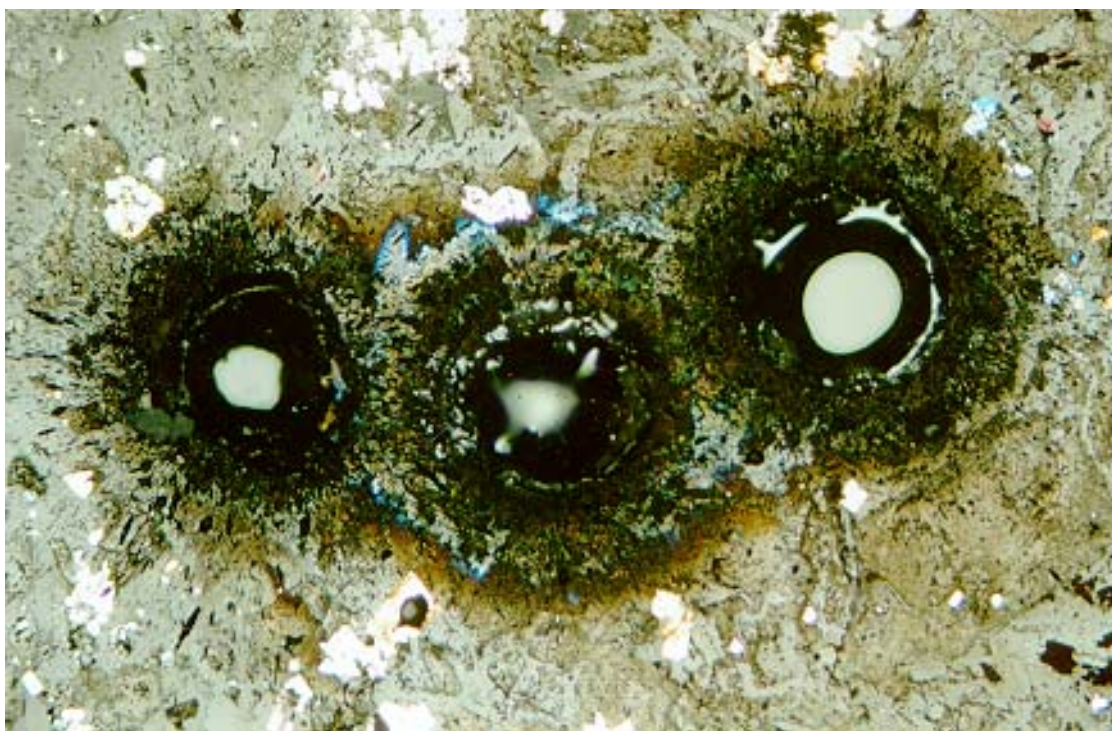




between Au and Cu in arsenopyrite ($r^2=0.84$) and arsenopyrite overgrowths on pyrite ($r^2=0.67$). A weak correlation ($r^2=0.3$) was noted between Au-Sb for all data but also for individual sulphide morphologies including pyrite overgrown by arsenopyrite and arsenopyrite overgrowths on pyrite (Figure 5.13 E). Plots of Au versus Se (Figure 5.13 F) show an overall moderate negative correlation ($r^2= -0.59$), however, positive Au-Se correlations are recorded by pyrite overgrown by arsenopyrite (0.98), pyrite (0.39), and arsenopyrite overgrowths on pyrite (0.26). This suggests that sulphide type controls the overall Se concentration (i.e. pyrite contains higher levels of Se than arsenopyrite) but that this concentration also varies with respect to Au. The graph of Au versus Mn shows a broad positive correlation (Figure 5.13 G), however, the r^2 value is only 0.15 and no correlations are evident for individual morphologies. Other elements analysed (Bi, Co, Mo, Ni, Sn, Zn, and W) show no clear relationship to Au concentration (Figure 5.13 H – N).

CHAPTER SIX

Stable isotopes



The photomicrograph shows the destructive effects of laser ablation on a polished section of monzonite altered by carbonate and pyrite. The large holes result from laser ablation for sulphur isotopes while the small hole in the pyrite crystal below and to the left of the central large hole is a result of LA-ICP-MS. The field of view of the photomicrograph is approximately 6 millimetres.

6.1 Chapter overview

Light stable isotope (C, O, and S) analyses of rocks and minerals have been used in many studies to constrain the source of water, sulphur and carbon (and by extrapolation metals), to indicate the origin of ore-bearing fluids, and to document the fluid temperature during mineral formation (e.g. Ohmoto, 1986). Seventy-eight oxygen, carbon and sulphur isotope analyses were performed on samples from Brewery Creek to investigate the source of fluids and the evolution of fluid isotope composition over time. The resulting data includes 34 oxygen, 13 carbon and 31 sulphur isotope analyses from samples of pre-, syn-, and post-intrusion quartz, carbonate and sulphide minerals and intrusion-hosted biotite and roscoelite (Table 6.1).

Temperatures estimated from fluid inclusions, alteration assemblages and isotope pairs range from 680°C in monzonite sills, to ~ 440 and 470 °C for P-stage 3.1 and 3.4 respectively and 150°C for P-stage 3.8. $\delta^{18}\text{O}_{\text{fluid}}$ calculated from quartz mineral separates range from -5.5 to 13.6 ‰, with $\delta^{18}\text{O}_{\text{fluid}}$ and $\delta^{13}\text{C}_{\text{fluid}}$ from carbonate minerals estimated to be -4.4 to 14.3 ‰ and -8.7 to -2.3 ‰ respectively. $\delta^{34}\text{S}_{\text{fluid}}$ calculated from pyrrhotite, pyrite, arsenopyrite and stibnite varied from -2.0 to 19.6 ‰.

This chapter addresses the following points:

1. Silicate oxygen, carbonate carbon and oxygen and sulphide sulphur isotope analysis
2. Temperature estimates from fluid inclusions, alteration assemblages, and isotope pairs
3. $\delta^{18}\text{O}_{\text{fluid}}$, $\delta^{34}\text{S}_{\text{fluid}}$, and $\delta^{13}\text{C}_{\text{fluid}}$ estimates

Table 6.1 ^{18}O , ^{13}C , and ^{34}S isotope data tabulated according to paragenetic stage. Abbreviations in the 'Mineral' column are as follows - Aspy = arsenopyrite, Bi = biotite, Cb = carbonate, Po = pyrrhotite, Py = pyrite, Qz = quartz, Ro = roscoelite, Sb = stibnite. Abbreviations in the 'Lab' column are as follows – CSIRO = Commonwealth Science and Industrial Research Organisation, USGS = United States Geological Survey, U-Tas = University of Tasmania, VIEPS = Victorian Institute of Earth and Planetary Sciences.

Paragenetic stage	Sample #	Isotope	Mineral	Geological location of sample	Lab	Result		
						$\delta^{18}\text{O}$	$\delta^{13}\text{C}$	$\delta^{34}\text{S}$
P-stage 1: Pre-TPS								
1.1 Early pyrite	M24 PY	S	Py	Pyrite from pyrite veins hosted by Earn Gp. siltstone	USGS			54.0
	M37 PY	S	Py	Disseminated pyrite in Steel Fm. siltstone	USGS			28.0
1.2 Early carbonate	M61	O,C	Cb	Menzie creek volcanics breccia infill	VIEPS	22.0	-7.6	
	M60	O,C	Cb	Carbonate vein in Steel Fm. siltstone	VIEPS	4.7	-5.8	
1.3 Early quartz	M51qz	O	Qz	Quartz vein from Steel Fm. siltstone	USGS	23.1		
	M52qz	O	Qz	Quartz vein from Earn Gp. siltstone	USGS	21.5		
P-stage 2: Syn-TPS								
2.1 Intrusion	M62 - B	O	Bi	Biotite from unaltered biotite monzonite	CSIRO	8.9		
	M63 - B	O	Bi	Biotite from unaltered biotite monzonite	CSIRO	8.5		
	M62 - Q	O	Qz	Quartz phenocrysts from unaltered biotite monzonite	CSIRO	12.4		
	M63 - Q	O	Qz	Quartz phenocrysts from unaltered biotite monzonite	CSIRO	13.0		
	M1qz	O	Qz	Quartz phenocrysts from unaltered biotite monzonite	USGS	12.7		
	M53qz	O	Qz	Quartz phenocrysts from unaltered biotite monzonite	USGS	13.1		
	M25 PO	S	Po	Pyrrhotite from unaltered biotite monzonite	USGS			9.1
	MJL 50	S	Po	Pyrrhotite from unaltered biotite monzonite	U-Tas			11.1
2.2 Contact metamorphism	M26 PO	S	Po	Pyrrhotite from tremolite skarn adjacent to biotite monzonite	USGS			0.4
P-stage 3: Post-TPS								
3.1 Pyrite-quartz-carbonate-roscoelite	M69	O	Qz	Pyrite-quartz-carbonate vein in monzonite	CSIRO	11.6		
	M55qz	O	Qz	Pyrite-quartz-carbonate vein in monzonite	USGS	11.2		
	M56qz	O	Qz	Pyrite-quartz-carbonate vein in monzonite	USGS	11.6		
	M5qz	O	Qz	Pyrite-quartz-carbonate vein in monzonite	USGS	8.5		
	M65	O	Qz	Pyrite-quartz-carbonate-roscoelite vein in monzonite	CSIRO	16.6		

Paragenetic stage	Sample #	Isotope	Mineral	Geological location of sample	Lab	Result		
						$\delta^{18}\text{O}$	$\delta^{13}\text{C}$	$\delta^{34}\text{S}$
3.1 Pyrite-quartz-carbonate-roscoelite	M3qz	O	Qz	Pyrite-quartz-carbonate-roscoelite vein in monzonite	USGS	16.6		
	M19qz	O	Ro	Pyrite-quartz-carbonate-roscoelite vein in monzonite	USGS	8.4		
	M4ro	O	Ro	Pyrite-quartz-carbonate-roscoelite vein in monzonite	USGS	10.2		
	M64	O,C	Cb	Pyrite-quartz-carbonate-roscoelite vein in monzonite	VIEPS	14.9	-4.8	
	M66	O,C	Cb	Pyrite-quartz-carbonate vein in monzonite that cuts andalusite contact aureole	VIEPS	3.0	-4.6	
	M67	O,C	Cb	Pyrite-carbonate vein in monzonite	VIEPS	15.2	-6.4	
	M68	O,C	Cb	Pyrite-quartz-carbonate vein in monzonite	VIEPS	4.3	-7.1	
	M70	O,C	Cb	Pyrite-quartz-carbonate vein in monzonite	VIEPS	7.0	-6.6	
	M38 PY	S	Py	Disseminated pyrite from Earn Gp. siltstone	USGS			14.5
	M27 PY	S	Py	Disseminated pyrite in monzonite close to sill margin	USGS			20.3
	M28 PY	S	Py	Pyrite only veins in monzonite	USGS			2.2
	M29 PY	S	Py	Pyrite-quartz-carbonate vein in monzonite	USGS			1.1
	M31 PY	S	Py	Disseminated pyrite in a breccia with clasts of monzonite	USGS			7.2
	M32 PY	S	Py	Disseminated pyrite in a breccia with clasts of monzonite	USGS			13.5
	M39 PY	S	Py	Disseminated pyrite in monzonite	USGS			3.8
	MJL 52 - py1	S	Py	Pyrite adjacent to pyrite-quartz-carbonate vein in monzonite close to sill margin	U-Tas			7.1
	MJL 52 - py2	S	Py	Pyrite adjacent to pyrite-quartz-carbonate vein that cuts andalusite rich contact aureole	U-Tas			-0.5
	mjl 52 py 3	S	Py	Pyrite adjacent to pyrite-quartz-carbonate vein that cuts andalusite rich contact aureole	U-Tas			1.5
	mjl 52 py 4	S	Py	Pyrite adjacent to pyrite-quartz-carbonate vein in monzonite close to sill margin	U-Tas			18.7
	MJL 53 - py1	S	Py	Pyrite from pyrite-quartz-carbonate-roscoelite vein hosted by monzonite	U-Tas			7.0
	MJL 53 py 2	S	Py	Pyrite from pyrite-quartz-carbonate-roscoelite vein hosted by monzonite	U-Tas			14.3
	MJL 54 - py1	S	Py	Disseminated pyrite hosted by sheared carbonaceous shale immediately adjacent to a monzonite sill	U-Tas			17.0

Paragenetic stage	Sample #	Isotope	Mineral	Geological location of sample	Lab	Result		
						$\delta^{18}\text{O}$	$\delta^{13}\text{C}$	$\delta^{34}\text{S}$
3.1 Pyrite-quartz-carbonate-roscoelite	MJL 54 - py2	S	Py	Disseminated pyrite in monzonite at sill margin and immediately adjacent to sheared carbonaceous shale	U-Tas			14.8
	MJL 55 py core	S	Py	Core of zoned pyrite hosted in a monzonite breccia	U-Tas			14.3
	MJL 55 py rim	S	Py	Rim of zoned pyrite hosted in a monzonite breccia	U-Tas			13.8
	MJL 60 py2	S	Py	Disseminated pyrite in monzonite	U-Tas			6.3
	mjl 61 py 1	S	Py	Pyrite next to pyrite-quartz-carbonate vein in monzonite	U-Tas			13.8
3.2 Breccia	M71	O,C	Cb	Carbonate vein cutting brecciated monzonite	VIEPS	4.7	-5.8	
3.3 Quartz veins	M57qz	O	Qz	Quartz vein in monzonite	USGS	11.1		
3.4 Arsenopyrite-carbonate-quartz-gold	M73	O	Qz	Arsenopyrite-quartz-carbonate vein in monzonite	CSIRO	6.4		
	M79	O,C	Cb	Arsenopyrite-quartz-carbonate vein in monzonite	VIEPS	8.7	-6.8	
	M76	O,C	Cb	Arsenopyrite-quartz-carbonate vein in monzonite	VIEPS	12.0	-8.5	
	M75	O,C	Cb	Arsenopyrite-quartz-carbonate vein in monzonite	VIEPS	3.4	-5.8	
	M74	O,C	Cb	Arsenopyrite-quartz-carbonate vein in monzonite	VIEPS	4.8	-5.0	
	MJL 60 aspy 1	S	Aspy	Arsenopyrite from arsenopyrite-quartz-carbonate vein selvage in monzonite	U-Tas			5.8
	MJL 60 aspy 2	S	Aspy	Arsenopyrite from arsenopyrite-quartz-carbonate vein selvage in monzonite	U-Tas			6.0
	MJL 59 aspy 1	S	Aspy	Disseminated arsenopyrite within monzonite	U-Tas			6.5
	MJL 57 aspy 2	S	Aspy	Disseminated arsenopyrite within monzonite	U-Tas			9.0
3.8 Stibnite-quartz-carbonate-feldspar	M81	O	Qz	Stibnite-quartz-carbonate-feldspar vein in monzonite	CSIRO	10.0		
	M58qz	O	Qz	Stibnite-quartz-carbonate-feldspar vein in monzonite	USGS	13.3		
	M59qz	O	Qz	Stibnite-quartz-carbonate-feldspar vein in monzonite	USGS	12.8		
	M80	O,C	Cb	Stibnite-quartz-carbonate-feldspar vein in monzonite	VIEPS	5.1	-6.0	
	M30 STIB	S	Sb	Stibnite-quartz-carbonate-feldspar vein in monzonite	USGS			-2.1
	M33 STIB	S	Sb	Stibnite infill of breccia with clasts of Steel Fm. siltstone	USGS			-4.1
	M35 STIB	S	Sb	Stibnite infill of breccia with clasts of Earn Gp. siltstone	USGS			-2.0

6.2 Quartz, biotite and roscoelite oxygen isotope analyses

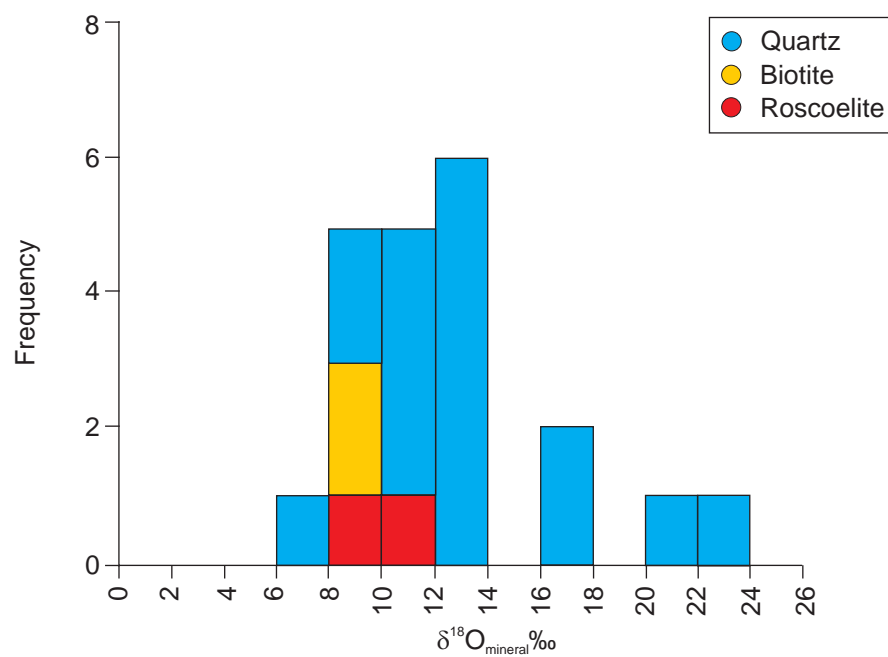
Oxygen isotope analysis on hand picked quartz, biotite and roscoelite mineral separates was performed at the United States Geological Survey (USGS) stable isotope facilities in Denver, Colorado and at the Commonwealth Science and Industrial Research Organisation (CSIRO) - Centre for Isotopic Studies (CIS) in Sydney, New South Wales. The analytical methods used at the USGS and at CSIRO closely follow the procedures described by Clayton and Mayeda (1963). The CO₂ gases produced during analysis were measured using a Finnegan MAT 252 mass spectrometer in dual inlet mode and have a reproducibility of 0.2 ‰ at both laboratories. Oxygen results from the USGS and CSIRO laboratories are expressed in 'δ' notation relative to Vienna Standard Mean Ocean Water (VSMOW).

The δ¹⁸O values determined for 17 quartz, 2 biotite and 2 roscoelite separates vary from 6.3 to 23.1 ‰ with the bulk of the samples returning results between 8.0 and 14.0 ‰ (Figure 6.1). Quartz sampled from pre-TPS quartz veins hosted in Steel Formation and Earn Group siltstone returned the highest isotope values of 23.1 ‰ and 21.5 ‰. δ¹⁸O values for quartz phenocrysts separated from biotite monzonite intrusions were tightly grouped between 12.4 to 13.1 ‰. Samples of quartz from P-stage 3.1 pyrite-quartz-carbonate ± roscoelite veins range between 8.5 and 16.6 ‰. Two veins that contained roscoelite returned identical values of 16.6 ‰ while veins without roscoelite have δ¹⁸O values between 11.2 and 11.6 ‰. A δ¹⁸O value of 8.5 ‰ was also recorded for quartz from a pyrite-quartz-carbonate vein.

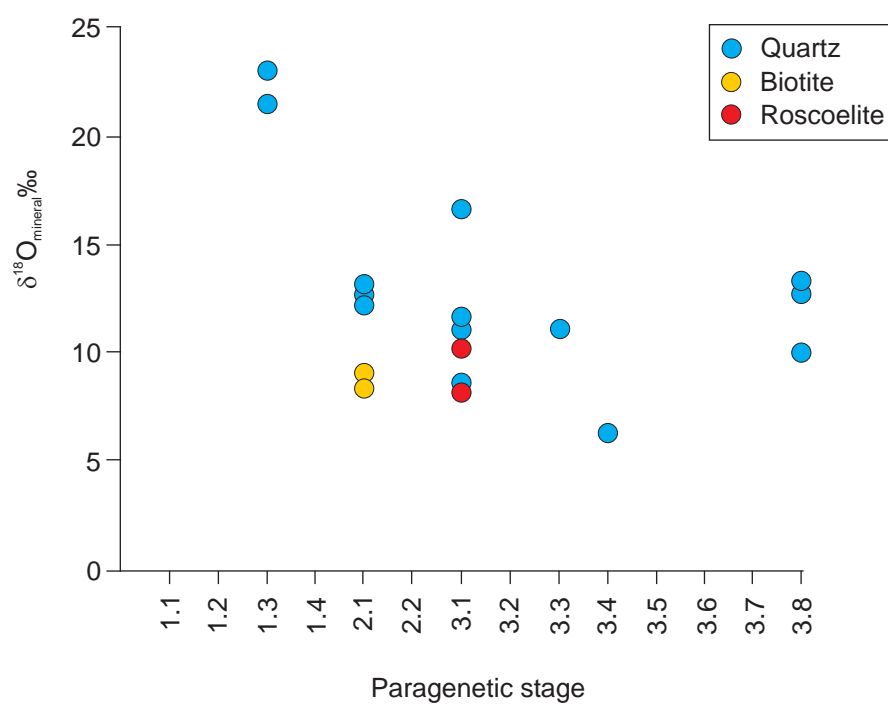
Quartz separated from a P-stage 3.4 arsenopyrite-carbonate-quartz-gold vein recorded the lowest δ¹⁸O of 6.4 ‰. Unfortunately only one quartz separate could be obtained from P-stage 3.4 veins as these veins are typically less than 3 mm wide and contain little quartz. δ¹⁸O values measured for quartz from stibnite-quartz-carbonate-feldspar veins were 9.9 ‰, 12.8 ‰, and 13.3 ‰ while analysis of biotite and roscoelite returned δ¹⁸O values of 8.5 to 8.9 ‰ and 8.4 to 10.2 ‰ respectively.

Figure 6.1 $\delta^{18}\text{O}_{\text{mineral}}$ values from quartz, biotite and roscoelite mineral separates. (A) A stacked histogram of $\delta^{18}\text{O}$ values. Note that most of the data falls between 8 ‰ and 14 ‰. (B) $\delta^{18}\text{O}$ values plotted with respect to paragenetic stage. Note that all samples were hosted in monzonite except for P-stage 3.1 veins that were hosted by sedimentary rocks.

A



B



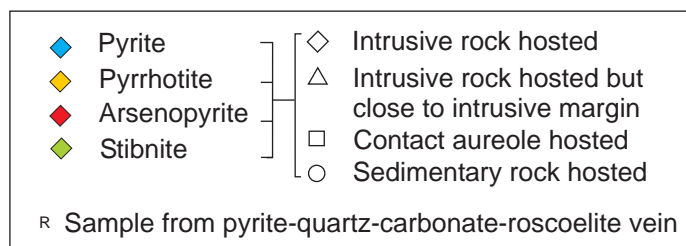
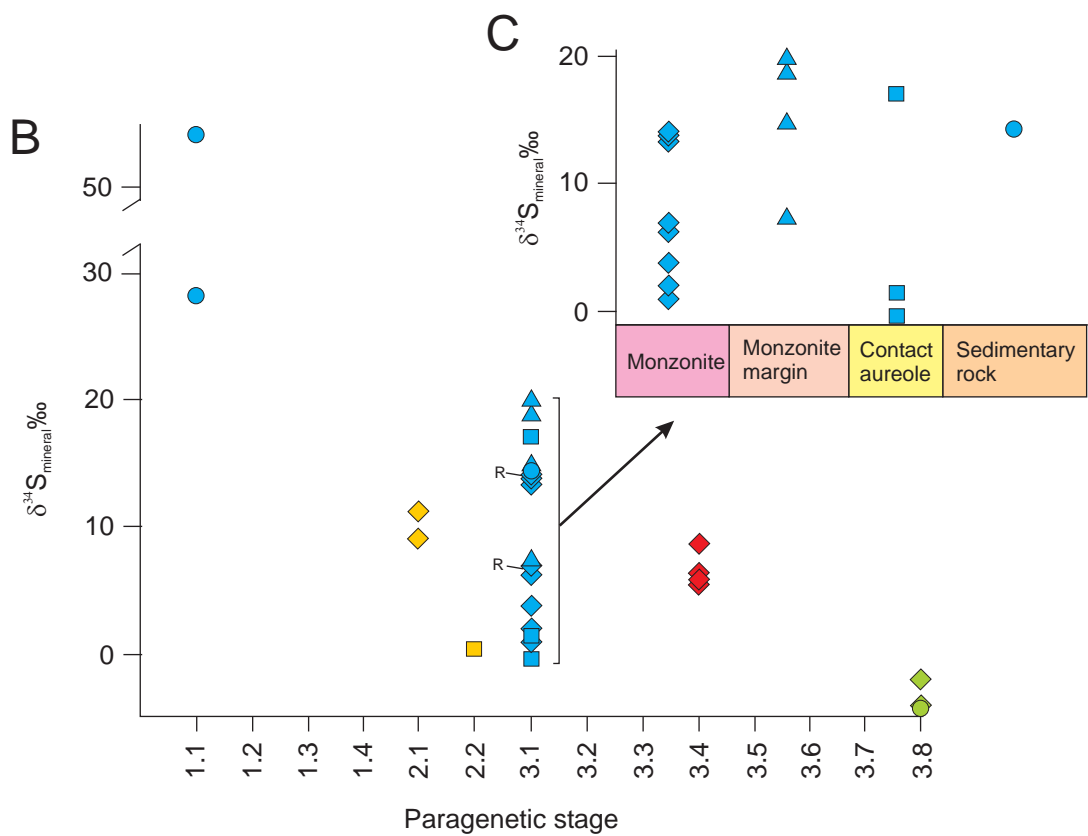
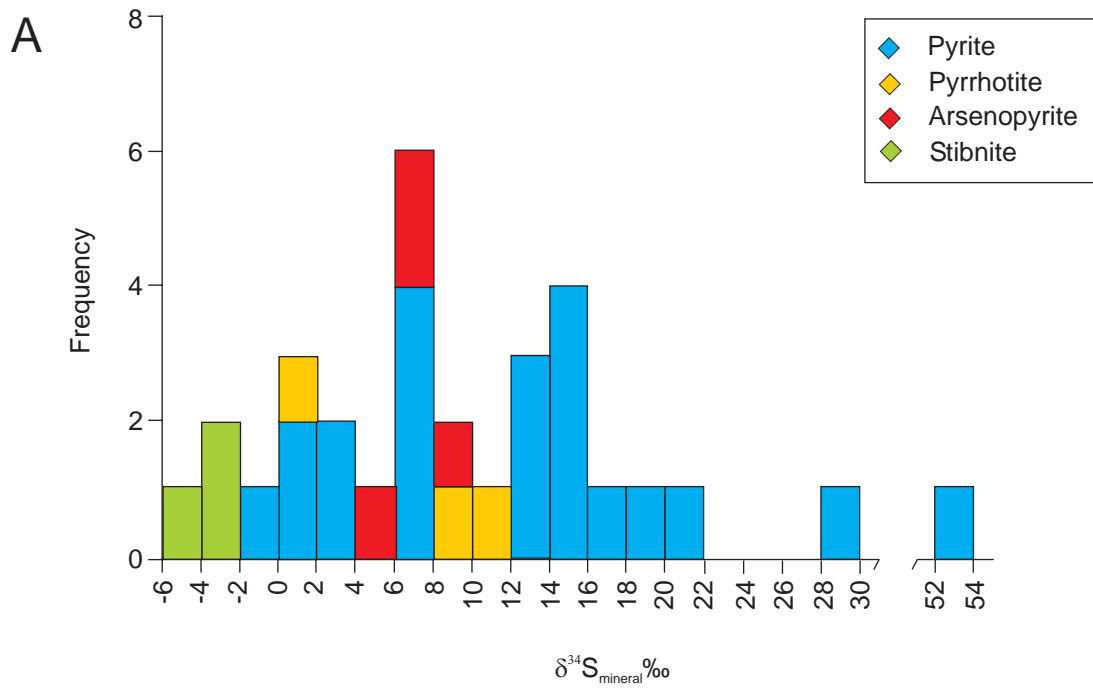
6.3 Pyrrhotite, pyrite, arsenopyrite and stibnite sulphur isotope analyses

Sulphur isotope analysis on hand picked mineral separates were also performed at the USGS laboratories and in-situ laser ablation sulphur isotope analysis was performed at the University of Tasmania - Central Science Laboratory (CSL), Hobart, Tasmania. At the USGS laboratories the SO_2 produced during analysis is measured by the continuous flow technique of Giesemann et al. (1994) in a Micromass Optima mass spectrometer and the results have a reproducibility of 0.2 ‰. At the CSL a Quantronix Nd:YAG laser, with an ablation spot resolution of 100 - 300 μm , was used to ablate sulphide grains and produce SO_2 . Isotopic analysis of the extracted SO_2 was performed with a VG SIRA Series 2 triple-collector mass spectrometer. The SO_2 gas was calibrated against NBS 123 sphalerite (17.1 ‰ $\delta^{34}\text{S}$) using Broken Hill (3.4 ‰ $\delta^{34}\text{S}$) and Rosebery (12.4 ‰ $\delta^{34}\text{S}$) galena as working standards to establish a calibration curve. Analytical uncertainties of ± 0.7 ‰ apply to these results. A detailed description of the apparatus and method for sulphur isotope analysis by in-situ laser ablation of sulphide grains can be found in Huston et al. (1995b). Sulphur isotope results from the USGS and CSL are expressed in 'δ' notation relative to Cañon Diablo Troilite (CDT). Note that care was taken to analyse a specific paragenetic phase and or a specific mineral. However, given the complex zoning of some of the sulphide minerals, especially arsenopyrite, some of the results may reflect homogenisation of two or more stages.

The $\delta^{34}\text{S}$ values determined for 3 pyrrhotite, 21 pyrite, 4 arsenopyrite, and 3 stibnite mineral separates vary from -4.1 to 54.0 ‰ with the majority of samples recording $\delta^{34}\text{S}$ values of 6.0 to 20.0 ‰ (Figure 6.2). Pyrite, interpreted to be pre-TPS and hosted by Earn Group and Steel Formation siltstone, records the highest $\delta^{34}\text{S}$ values of 54.0 ‰ and 28.0 ‰. Syn-intrusion pyrrhotite has values of 11.1 and 9.1 ‰ from samples of monzonite and 0.4 ‰ from a sample of contact metamorphosed Steel Formation. Post-TPS, P-stage 3.1 pyrite recorded a wide distribution in $\delta^{34}\text{S}$ values from -0.5 to 20.3 ‰. The majority of values ranged between 13.5 ‰ and 14.8 ‰ with 7 analyses of disseminated pyrite, variably hosted by monzonite, a breccia of monzonite and Earn Group siltstone, recording results within this range.

The variation in S isotope values occurs from cm- to deposit-scale. Sample MJL 52 (a thin section 2.5 cm wide by 5 cm long) encompasses the margin of a biotite monzonite

Figure 6.2 $\delta^{34}\text{S}_{\text{mineral}}$ values of pyrite, pyrrhotite, arsenopyrite and stibnite mineral separates and in-situ laser ablation of sulphide grains. (A) A stacked histogram of $\delta^{34}\text{S}$ values. (B) $\delta^{34}\text{S}$ values plotted with respect to paragenetic stage. Note the variation in $\delta^{34}\text{S}$ of pyrite and that there appear to be two populations of $\delta^{34}\text{S}$ values for P-stage 3.1. In contrast, limited arsenopyrite and stibnite analyses form tight clusters.



sill and an adjacent andalusite-rich contact aureole, both of which are cut by a P-stage 3.1 vein. Pyrite from the contact aureole returned $\delta^{34}\text{S}$ values of -0.5 ‰ and 1.5 ‰, while pyrite hosted by monzonite recorded values of 7.1 ‰ and 18.1 ‰. Similar values for P-stage 3.1 pyrite were documented elsewhere in the deposit with disseminated pyrite in monzonite and Earn Group siltstone having results of 20.3 ‰ and 17.0 ‰ respectively. Values of 3.8 ‰, 2.2 ‰, and 1.1 ‰ and 7.2 ‰, 7.0 ‰, and 6.3 ‰ were also noted in disseminated and vein-hosted pyrite in monzonite respectively. Thus the variation in isotope values for this stage appears to be at least partly related to host rocks and their location with respect to monzonite sill margins (Figure 6.2). This is further discussed in chapter 7.

Four arsenopyrite grains returned $\delta^{34}\text{S}$ values of 5.8 ‰, 6.0 ‰, 6.5 ‰ and 9.0 ‰. The sample that assayed at 9.0 ‰ was obtained from North Slope whilst all others were from the Reserve Trend, thus location may also play some role in isotopic composition. Sulphur isotope analysis of stibnite grains produced consistently negative values of -2.0 to -4.1 ‰.

6.4 Carbonate carbon and oxygen isotope analyses

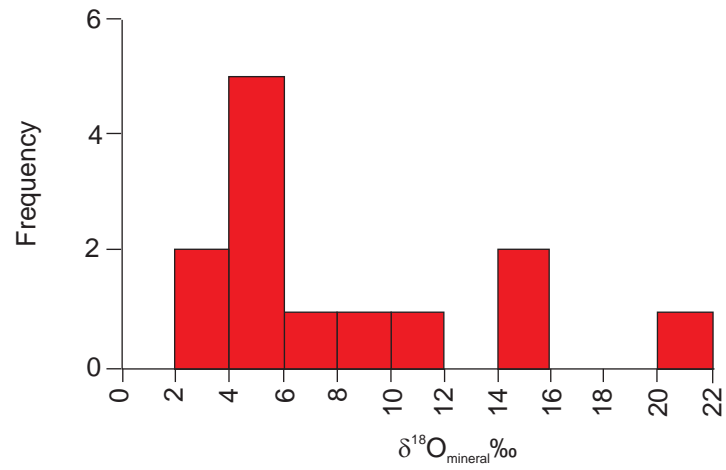
Hand picked carbonate mineral separates were analysed at the Victorian Institute of Earth and Planetary Sciences (VIEPS) isotope facilities at Monash University in Melbourne, Victoria. Stable isotope ratios were measured using a Finnigan MAT 252 mass spectrometer. CO_2 was extracted from carbonate by reaction of mixed carbonate-silicate powders with 100% H_3PO_4 at 25 °C for 12-18 hours in sealed vessels using the method of McCrea (1950). Calibration was measured against an internal calcite standard ISACC that has been calibrated using IAEA-CO-1. Precision based on replicate analyses is 0.1‰ ($\delta^{13}\text{C}$) and 0.2‰ ($\delta^{18}\text{O}$). Carbon isotope results from VIEPS are expressed in 'δ' notation relative to the Vienna Pee Dee Belemnite (VPDB). Oxygen isotope values were determined with reference to VPDB but have been recalculated using the equation below and are presented in 'δ' notation relative to VSMOW.

$$\delta^{18}\text{O}_{\text{VSMOW}} = 1.03091 \delta^{18}\text{O}_{\text{VPDB}} + 30.91\text{‰} \quad (\text{Coplen et al., 1983})$$

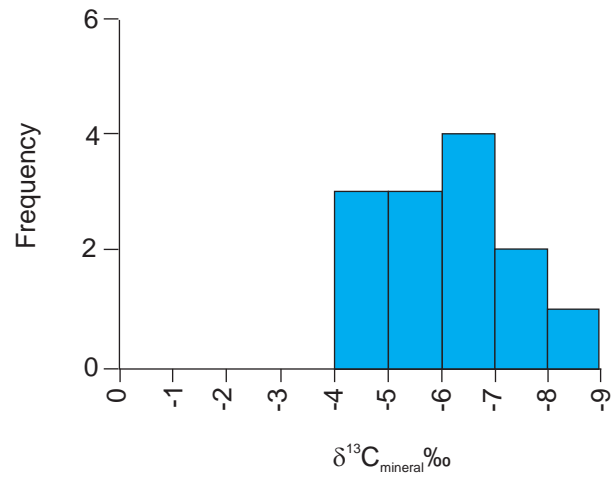
The $\delta^{18}\text{O}$ values determined for 13 carbonate mineral separates vary from 3.0 to 22.0 ‰. In contrast to the $\delta^{18}\text{O}$ values, $\delta^{13}\text{C}$ analyses record a relatively restricted range from -4.6 to -8.5 ‰ (Figure 6.3). No relationship is evident between relative changes in

Figure 6.3 $\delta^{18}\text{O}_{\text{mineral}}$ and $\delta^{13}\text{C}_{\text{mineral}}$ values of carbonate mineral separates. (A) A stacked histogram of $\delta^{18}\text{O}$ values, (B) A stacked histogram of $\delta^{13}\text{C}$ values, and (C) $\delta^{18}\text{O}$ plotted against $\delta^{13}\text{C}$ with symbols coloured according to paragenetic stage. Note that there is a large variation in $\delta^{18}\text{O}$ values but only a narrow range of $\delta^{13}\text{C}$.

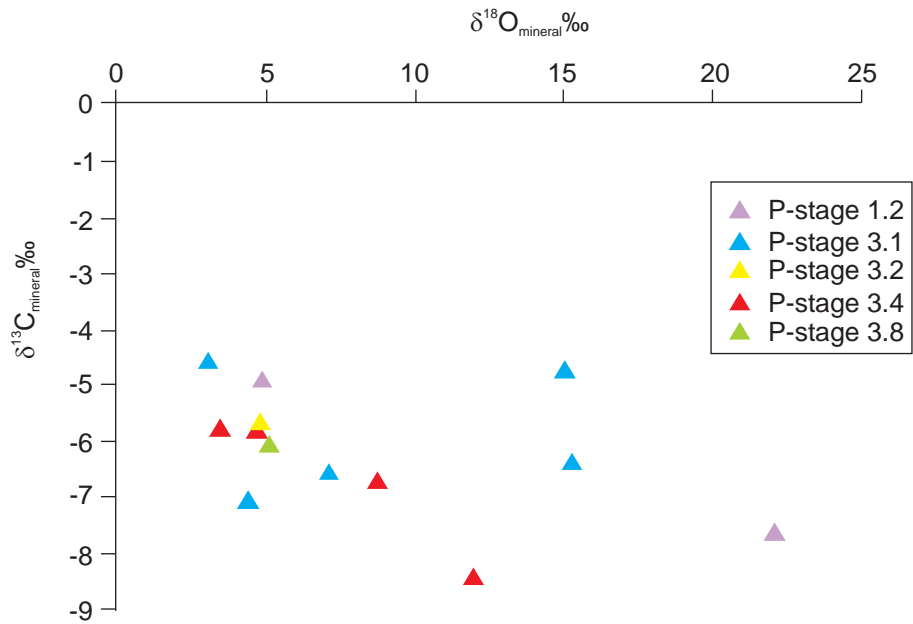
A



B



C



$\delta^{18}\text{O}$ and $\delta^{13}\text{C}$ values (Figure 6.3c). Samples of pre-TPS carbonate returned $\delta^{18}\text{O}$ and $\delta^{13}\text{C}$ values of 22.0 ‰ and -4.7 ‰ and 7.6 ‰ and -5.8 ‰ respectively. The higher $\delta^{18}\text{O}$ is similar to the O-isotope values obtained from quartz separates. However, the lower $\delta^{18}\text{O}$ value is similar to O-isotope values from post-TPS veins suggesting that this sample may relate to post-TPS fluids and that the identification of the corresponding vein as pre-TPS may have been incorrect.

$\delta^{18}\text{O}$ values recorded for carbonates from P-stage 3.1 veins vary from 3.0 to 15.2 ‰ and $\delta^{13}\text{C}$ values for the same samples vary between -4.6 and -7.1 ‰. Large variations in isotope values for both $\delta^{18}\text{O}$ from quartz and $\delta^{34}\text{S}$ from pyrite were also noted for this stage. O-isotopes from 4 samples of P-stage 3.4 carbonate are 3.4 ‰, 4.8 ‰, 8.7 ‰ and 12.0 ‰. The corresponding $\delta^{13}\text{C}$ values are -5.0 ‰, -5.8 ‰, -6.8 ‰, and -8.5 ‰. One sample of carbonate from a stage 3.8 stibnite bearing vein gave $\delta^{18}\text{O}$ and $\delta^{13}\text{C}$ values of 5.1 ‰ and -6.0 ‰ respectively.

6.5 Temperature estimates

Estimating the temperature of fluids during mineralisation can provide important information on deposit formation and in particular precipitation mechanisms. Most deposit case studies use fluid inclusion data to measure inclusion homogenisation temperatures and subsequently estimate the minimum and / or trapping temperature of vein formation. Various other methods can be used to estimate temperature including data from alteration assemblages, mineral solid solution series and isotopes.

Fluid inclusion temperature estimates

Optical microscopy investigation of the post-TPS sulphide bearing veins at Brewery Creek indicated that most of the fluid inclusions were below the size limit required for fluid inclusion studies. Limited fluid inclusion work has been completed previously on samples of quartz phenocrysts from monzonite sills (Baker, 2002) and veins (Dunne, 1995) from Brewery Creek, however, most of the veins were not constrained paragenetically. Dunne (1995) also noted that most fluid inclusions were beyond the working range for fluid inclusion studies (< 1 micron in maximum diameter).

Baker (2002) reported that quartz phenocrysts from monzonite sills (P-stage 2.1) contained coexisting halite-bearing brine and $\text{CO}_2 - \text{H}_2\text{O}$ inclusions and suggested that the inclusions were trapped at ~ 0.5 kbars in a two phase immiscible field. The halite-

bearing inclusions recorded homogenisation temperatures of 432 – 631 °C and salinities of 30-36 eq. wt.% NaCl. CO₂ – H₂O inclusions recorded homogenisation temperatures of 418 – 445 °C and salinities of < 10 eq. wt.% NaCl.

The study by Dunne (1995) evaluated fluid inclusions in (1) comb/cockade and vug-fill quartz with no indication of associated sulphide minerals and therefore no paragenetic constraints, and (2) quartz-stibnite veins which correspond to P-stage 3.8 of the paragenesis described in this thesis. Fluid inclusion studies on primary inclusions from vug-fill quartz crystals gave homogenisation temperatures of 134 – 300 °C and salinities of 1 - 7.5 eq. wt.% NaCl. Secondary inclusions from the same quartz types gave homogenisation temperatures of 122 – 365 °C and salinities of 1 – 5 eq. wt.% NaCl. Homogenisation temperatures measured for primary fluid from quartz-stibnite veins range from 140 °C - 295 °C and the salinities measured were 1-4 eq. Wt.% NaCl. Unfortunately, all fluid inclusions measured had necked and therefore homogenisation temperatures are unreliable but can be considered as minimum temperatures.

Temperature estimates from alteration assemblages

Andalusite phenocrysts contained within the contact aureole of monzonite sills at Brewery Creek constrain sill emplacement temperatures to > 500°C at 1 kbar and < 550°C at 2 kbar (Spear and Cheney, 1989; Spear, 1993). The alteration assemblage associated with mineralisation at Brewery Creek consists of carbonate-illite (sericite)-quartz-roscoelite-pyrite-arsenopyrite. Similar assemblages have been noted in epithermal and orogenic deposits and have been interpreted to form over a wide range of temperatures from 150-300°C in epithermal deposits (White and Hedenquist, 1995; Cooke and Simmons, 2000) to more than 400°C in orogenic deposits (Mueller et al., 2004).

Roscoelite ($K(V^{3+}, Al, Mg)_2AlSi_3O_{10}(OH)_2$; Gaines et al., 1997) has been previously documented in epithermal Au-Ag deposits (Ronacher et al., 2002, 2004), oxidised portions of sedimentary U-V ores (Breit, 1995), black shales (Peacor et al., 2000), and as reduction spots in red beds (Hofmann, 1991). At the Porgera gold mine quartz-roscoelite-pyrite-gold veins record homogenisation temperatures of 120 to 170 °C (Ronacher et al., 2004) while in the Placerville mining district roscoelite formed at temperatures of less than 100°C (Breit, 1995). However, no information has been published regarding temperature constraints on roscoelite formation.

Kretschmar and Scott (1976) investigated phase relations in the Fe-As-S system and described a geothermometer based on the atomic % As in arsenopyrite. Sharp et al. (1985) reviewed the arsenopyrite geothermometer of Kretschmar and Scott (1976) and suggested that it was only valid for ore deposits metamorphosed at low or intermediate grades. They further noted that the poor accuracy of the geothermometer. Temperatures calculated using the arsenopyrite geothermometer (Kretschmar and Scott, 1976) for arsenopyrite co-existing with pyrite at Brewery Creek range from 250°C for arsenopyrite with 28 atomic % As to ~ 70°C for arsenopyrite with As at 26 atomic %. Though mineralisation occurring at 250°C is reasonable, mineralisation at 70°C seems unlikely. If mineralisation spanned this temperature range there would be extensive evidence of boiling (e.g. lattice calcite or quartz, colloform and crustiform bands and comb quartz vein textures), which are absent at Brewery Creek. Furthermore, arsenopyrite crystals at Brewery Creek have lower levels of As in their core, this would therefore indicate an increase in temperature during crystal growth, which is the opposite of most other hydrothermal systems and highly unusual. Thus, application of the arsenopyrite geothermometer at Brewery Creek leads to dubious results best explained by significant deviation from arsenopyrite stoichiometry to highly As-deficient compositions. In addition, disequilibrium arsenopyrite crystallisation conditions were likely as suggested by fine-scale compositional zoning observed in some arsenopyrite crystals.

Temperatures from isotope pairs

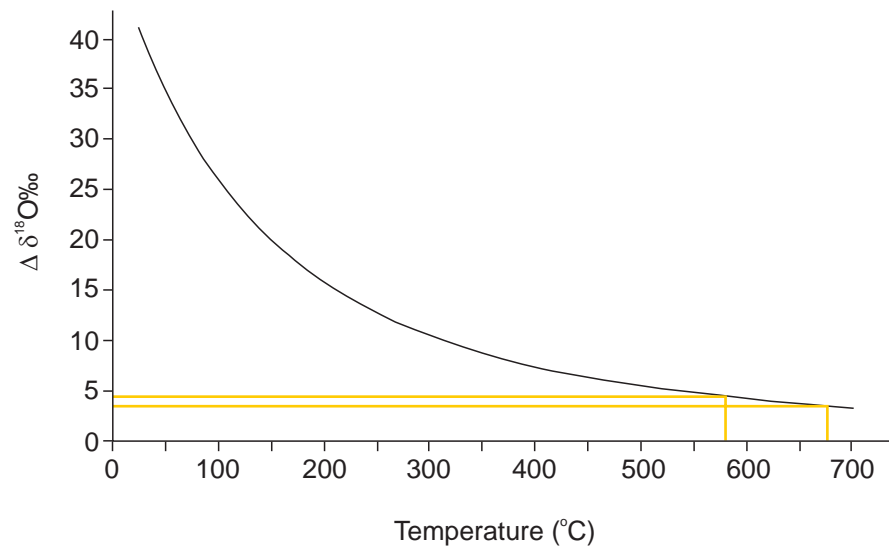
Temperatures can also be estimated by comparing the magnitude of isotope fractionation between minerals that precipitated in equilibrium (e.g. Friedman and O'Neil, 1977). Unlike fluid inclusion temperatures, isotope fractionation and therefore isotope geo-thermometry is not affected by pressure. However, to accurately calculate temperature, mineral pairs used for isotope geo-thermometry need to have formed at the same temperature, from the same fluid and to have remained unaffected by later isotopic re-equilibration through alteration, and/or weathering (Campbell and Larson, 1998).

Oxygen and sulphur isotopes are most commonly used for isotope geo-thermometry. The fluid temperature during precipitation of quartz and biotite phenocrysts in a TPS biotite monzonite sill was calculated using the quartz - biotite isotope fractionation curve of Bottinga and Javoy (1975; Figure 6.4 A). Quartz phenocrysts used for $\delta^{18}\text{O}$ measurements show evidence of resorption and thus the calculated temperature may not be accurate due to disequilibrium. The two quartz - biotite mineral pairs analysed

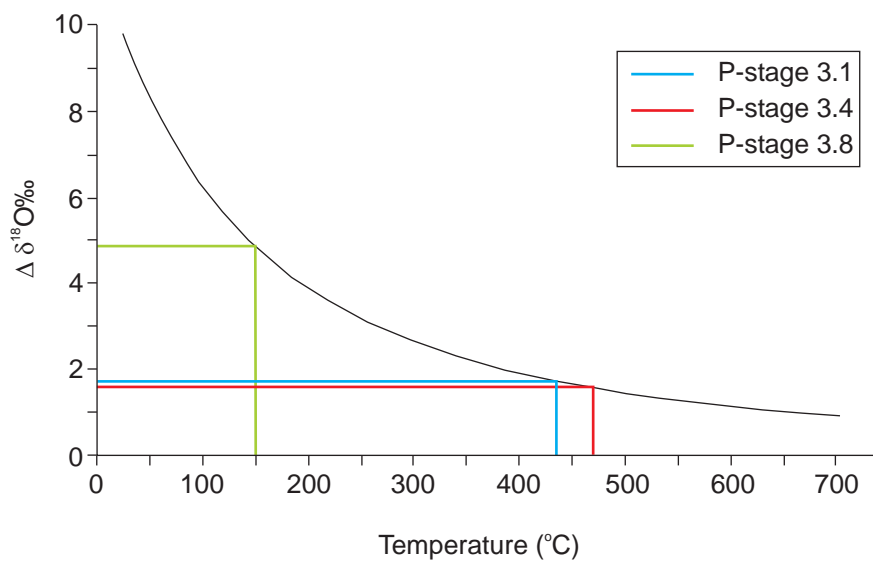
Figure 6.4 Oxygen isotope fractionation curves used to calculate temperature.

(A) A graph illustrating the quartz – biotite oxygen isotope fractionation curve of Bottinga and Javoy (1975). The difference in $\delta^{18}\text{O}$ values between quartz and biotite is plotted to give fluid temperatures for biotite monzonite sills. (B) A graph illustrating the quartz – carbonate oxygen isotope fractionation curve of Sharp and Krischner (1994). The method described in (A) above was used to calculate fluid temperatures for P-stages 3.1, 3.4 and 3.8.

A



B



gave temperatures of 580 °C and 680 °C. This is similar to the 430 - 630 °C fluid inclusion homogenisation temperature range calculated by Baker (2002) for quartz phenocrysts from the Schooner zone. The results are also consistent with >500°C temperatures indicated by the presence of andalusite porphyroblasts in monzonite contact aureoles. The variation between the calculated fluid inclusion and $\delta^{18}\text{O}$ mineral pair temperatures may result from local variations within the deposit, a combination of disequilibrium between quartz and biotite, and potential variations in cooling rates that affect isotopic fractionation (Campbell and Larson, 1998).

At Brewery Creek quartz and calcite are inter-grown and commonly share grain contacts in all post-TPS sulphide-bearing veins (P-stage 3.1, 3.4, and 3.8). Petrographic examination of P-stages 3.1, 3.4, and 3.8 veins found no evidence of disequilibrium between quartz and calcite (e.g. resorption/corrosion, replacement, mineral overgrowths). Isotopic re-equilibration with later fluids is, however, a possibility as indicated by necked and secondary fluid inclusions and multiple events of quartz and carbonate veining. Despite this uncertainty the difference between calculated $\delta^{18}\text{O}$ fractionation factors for quartz-carbonate mineral pairs were plotted against the quartz-carbonate isotope fractionation curve of Sharp and Kirschner (1994; Figure 6.4 B). The resulting calculated temperatures are ~ 440 °C for P-stage 3.1, ~ 470 °C for P-stage 3.4, and ~ 150 °C for P-stage 3.8.

The temperatures for P-stage 3.1 and 3.4 are higher than expected. Similar temperatures were noted by Stephens (2003) at Clear Creek and Dublin Gulch, however, both of these systems have a distinct skarn association. The veins analysed by Stephens (2003) also host minerals such as muscovite, tourmaline and hedenbergite which are not present in veins hosted along the Reserve Trend. However, the calculated temperatures for P-stage 3.1 and 3.4 cannot be discounted as skarn style mineralisation with tremolite, pyrrhotite and arsenopyrite was noted in the Schooner Zone. Furthermore, contact metamorphism between TPS monzonite sills and Earn Group sedimentary rocks is typically poorly developed along the Reserve Trend.

The final stages in the paragenetic history of most ore systems typically form from lower temperature fluids than the earlier stages. This should be expected from a cooling hydrothermal system, and in particular systems associated with the emplacement of magma. This is also the case at Brewery Creek with calculated temperatures for P-stages 3.1 and 3.4 ~ 200 °C higher than P-stage 3.8. The 150 °C temperature calculated for P-stage 3.8 is comparable to the homogenisation

temperatures (Dunne, 1995), considered to be minimum temperature estimates, of fluid inclusions from the same stage (140 °C to 295 °C). At temperatures below ~ 250 °C isotope exchange reactions require long periods of time to reach equilibrium (Matsuhisa et al., 1978). P-stage 3.8 veins are typically less than 2 cm wide and the fluids contained within are likely to have cooled quickly. Thus the calculated 150 °C temperature should also be considered as a minimum temperature.

No coeval sulphide phases have been documented at Brewery Creek and therefore sulphur isotope geothermometry cannot be used to estimate fluid temperatures.

6.6 Fluid $\delta^{18}\text{O}$ estimates from quartz

In addition to calculating temperatures of mineral deposition, stable isotopes can also be used to determine the source of hydrothermal fluids. Fluid $\delta^{18}\text{O}$ values can be estimated by using the $\delta^{18}\text{O}$ values obtained from minerals combined with known fractionation factors and temperature data. In this study the quartz - water fractionation equations of Zheng (1993) and Sharp and Kirschner (1994) were used to calculate fluid $\delta^{18}\text{O}$ values. Temperatures calculated from fluid inclusions, alteration assemblages and isotope pairs range from 680°C in monzonite sills to 150°C (considered to be a minimum temperature) in the final sulphide-bearing stage of the paragenesis and describe a cooling hydrothermal system. Given the significant range in temperature estimates, the $\delta^{18}\text{O}_{\text{fluid}}$ was calculated for selected temperature ranges from 150 - 700 °C (Table 6.2).

Phenocrysts from biotite monzonite sills yielded $\delta^{18}\text{O}$ values of 12.4 to 13.1 ‰. Using quartz-water fractionation equations of Sharp and Kirschner (1994) and Zheng (1993), the $\Delta^{18}\text{O}$ between quartz and H_2O at 500 to 700 °C varies from 3.1 to 1.0 ‰ respectively. The calculated fluid $\delta^{18}\text{O}$ values are therefore 9.6 to 11.8 ‰.

$\delta^{18}\text{O}$ values of quartz from P-stage 3.1 veins have values of 11.2 to 11.6 ‰ for pyrite-quartz-carbonate veins and 16.6 ‰ for pyrite-quartz-carbonate-roscoelite veins. The $\Delta^{18}\text{O}$ between quartz and H_2O at 250 to 500 °C varies from 10.4 to 3.0 ‰ respectively. This gives fluid $\delta^{18}\text{O}$ values of 1.1 to 8.5 ‰ for P-stage 3.1 veins without roscoelite and 6.2 to 13.6 ‰ for P-stage 3.1 veins with roscoelite.

Table 6.2 $\delta^{18}\text{O}_{\text{fluid}}$ **estimates from quartz mineral separates.** The data were calculated using the $\Delta^{18}\text{O}_{\text{mineral-fluid}}$ equations of Sharp and Krischner (1994) and Zheng (1993) at the temperatures shown. Note the variation in values through the paragenesis.

Paragenetic stage	Sample numbers	Notes	Mineral $\delta^{18}\text{O}$ ‰	Equation	Fluid $\delta^{18}\text{O}$ ‰ at the following temperatures (°C)											
					150	200	250	300	350	400	450	500	550	600	650	700
2.1	M62, M63, M1qz, M53qz	Quartz phenocrysts from monzonite	12.4-13.1. mean 12.8	Sharp and Krischner (1994) Zheng (1993)								9.6	10.3	10.9	11.4	11.8
												9.8	10.3	10.7	11.0	11.3
3.1	M65, M3qz	Quartz from pyrite-quartz-carbonate-roscoelite vein in monzonite	16.6	Sharp and Krischner (1994) Zheng (1993)			6.2	8.4	10.1	11.4	12.5	13.4				
							7.6	9.6	11	12.1	12.9	13.6				
	M55, M56, M69	Quartz from pyrite-quartz-carbonate vein in monzonite	11.2.-11.6. mean 11.5	Sharp and Krischner (1994) Zheng (1993)			1.1	3.3	5	6.3	7.4	8.3				
							2.5	4.5	5.9	7	7.8	8.5				
3.3	M57	Quartz only vein in monzonite	11.1	Sharp and Krischner (1994) Zheng (1993)			0.7	2.9	4.6	5.9	7	7.9				
							2.1	4.1	5.5	6.6	7.4	8.1				
3.4	M73	Quartz from arsenopyrite-quartz-carbonate-gold vein in monzonite	6.4	Sharp and Krischner (1994) Zheng (1993)			-4	-1.8	-0.1	1.2	2.3	3.2				
							-2.6	-0.6	0.8	1.9	2.7	3.4				
3.8	M58, M59, M81	Quartz from stibnite-quartz-carbonate-feldspar vein	10.0-13.3. mean 12.0	Sharp and Krischner (1994) Zheng (1993)	-5.5	-1.4	1.6	3.8								
					-3.5	0.4	3	5								

The only $\delta^{18}\text{O}$ value of quartz from a P-stage 3.4 vein was 6.4 ‰. At temperatures of 250 to 500 °C the $\Delta^{18}\text{O}$ values range between 10.4 to 3.0 ‰, and the calculated $\delta^{18}\text{O}$ value of the fluid is -4.0 to 3.4 ‰. The late stage stibnite-quartz-carbonate-feldspar veins ($\delta^{18}\text{O}$ of 10.0 to 13.3 ‰), are interpreted to have formed at temperatures of 150 to 300 °C. At these temperatures calculated $\Delta^{18}\text{O}$ values are 17.0 to 7.0 ‰, and corresponding fluid $\delta^{18}\text{O}$ values are -5.5 to 5 ‰. Given that 150 °C is the minimum temperature, the $\delta^{18}\text{O}$ fluid value of -5.5 ‰ must also be considered as a minimum value.

6.7 Fluid $\delta^{18}\text{O}$ and $\delta^{13}\text{C}$ estimates from carbonates

The dolomite- H_2O fractionation equation of Golyshev et al. (1981) and the dolomite- CO_2 fractionation equation of Ohmoto and Rye (1979) were used to calculate the $\delta^{18}\text{O}$ and $\delta^{13}\text{C}$ of the fluid respectively. No carbonate minerals were sampled from stage 2.1 monzonite sills, however, carbonate mineral separates were collected from P-stages 3.1, 3.2, 3.4 and 3.8. Given the significant range in temperature estimates for the sampled stages, the $\delta^{18}\text{O}$ and $\delta^{13}\text{C}$ of the fluid were calculated for temperatures ranging from 150 - 500 °C (Table 6.3 and 6.4).

Measured $\delta^{18}\text{O}$ of carbonate separates varies significantly within and across paragenetic stages. For temperatures from 250 to 500 °C the corresponding $\Delta^{18}\text{O}$ values range between 7.4 and 0.9 (Golyshev et al., 1981). Carbonate from P-stage 3.1 pyrite-quartz-carbonate-roscoelite and pyrite-carbonate veins returned $\delta^{18}\text{O}$ values of ~ 15 ‰ and correspond to $\delta^{18}\text{O}$ fluid values of 7.5 to 14.3 ‰. Carbonate separates from P-stage 3.1 pyrite-quartz-carbonate veins have $\delta^{18}\text{O}$ values of 3.0 to 7.0 ‰. Using the same $\Delta^{18}\text{O}$ values as above, fluid $\delta^{18}\text{O}$ values are -4.4 to 6.1 ‰.

Carbonate separates from P-stage 3.4 arsenopyrite-quartz-carbonate-gold veins have similar $\delta^{18}\text{O}$ values to P-stage 3.1. At temperatures of 250 to 500 °C the highest $\delta^{18}\text{O}$ value of 12 ‰ is consistent with fluid $\delta^{18}\text{O}$ values of 4.6 to 11.1 ‰ and the lower values of 3.4 ‰ and 4.8 ‰ are equivalent to fluid $\delta^{18}\text{O}$ values of -4.0 to 3.9 ‰. Only one P-stage 3.8 carbonate separate was analysed and has a $\delta^{18}\text{O}$ value of 5.1 ‰. At 150 to 300 °C, the $\Delta^{18}\text{O}$ between dolomite and water varies between 13.7 and 5.4 ‰ (Golyshev et al., 1981) and the calculated $\delta^{18}\text{O}$ value of the fluid is -8.7 to -0.4 ‰.

Table 6.3 $\delta^{18}\text{O}_{\text{fluid}}$ **estimates from carbonate mineral separates.** The data were calculated using the dolomite-H₂O fractionation equation of Golyshev et al. (1981) at the temperatures shown. Note that there is a wide range in $\delta^{18}\text{O}_{\text{fluid}}$ values at the same temperature suggesting that there were multiple sources of oxygen.

Paragenetic stage	Sample numbers	Notes	Mineral $\delta^{18}\text{O}$ ‰	Fluid $\delta^{18}\text{O}$ ‰ at the following temperatures (°C)							
				150	200	250	300	350	400	450	500
3.1	M64	Pyrite-quartz-carbonate-roscoelite vein in monzonite	14.9			7.5	9.5	11.0	12.2	13.2	14.0
	M66	Pyrite-quartz-carbonate vein in monzonite that cuts andalusite contact aureole	3.0			-4.4	-2.4	-0.9	0.3	1.3	2.1
	M67	Pyrite-carbonate vein in monzonite	15.2			7.8	9.8	11.3	12.5	13.5	14.3
	M68	Pyrite-quartz-carbonate vein in monzonite	4.3			-3.1	-1.1	0.4	1.6	2.6	3.4
	M70	Pyrite-quartz-carbonate vein in monzonite	7.0			-0.4	1.6	3.1	4.3	5.3	6.1
3.2	M71	Carbonate vein cutting brecciated monzonite	4.7			-2.7	-0.7	0.8	2.0	3.0	3.8
3.4	M79	Arsenopyrite-quartz-carbonate vein in monzonite	8.7			1.3	3.3	4.8	6.0	7.0	7.8
	M76	Arsenopyrite-quartz-carbonate vein in monzonite	12.0			4.6	6.6	8.1	9.3	10.3	11.1
	M75	Arsenopyrite-quartz-carbonate vein in monzonite	3.4			-4.0	-2.0	-0.5	0.7	1.7	2.5
	M74	Arsenopyrite-quartz-carbonate vein in monzonite	4.8			-2.6	-0.6	0.9	2.1	3.1	3.9
3.8	M80	Stibnite-quartz-carbonate-feldspar vein in monzonite	5.1	-8.7	-5.1	-2.4	-0.4				

Table 6.4 $\delta^{13}\text{O}_{\text{fluid}}$ **estimates from carbonate mineral separates.** The data were calculated using the dolomite- CO_2 fractionation equation of Ohmoto and Rye (1979) at the temperatures shown. Note that $\delta^{13}\text{C}_{\text{fluid}}$ is typically between -4 ‰ to -7 ‰.

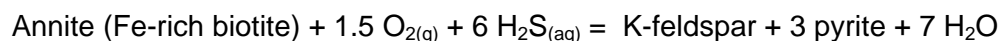
Paragenetic stage	Sample numbers	Notes	Mineral $\delta^{13}\text{C}$ ‰	Fluid $\delta^{13}\text{C}$ ‰ at the following temperatures (°C)							
				150	200	250	300	350	400	450	500
3.1	M64	Pyrite-quartz-carbonate-roscoelite vein in monzonite	-4.8			-4.3	-3.5	-3.0	-2.7	-2.5	-2.5
	M66	Pyrite-quartz-carbonate vein in monzonite that cuts andalusite contact aureole	-4.6			-4.1	-3.3	-2.8	-2.5	-2.3	-2.3
	M67	Pyrite-carbonate vein in monzonite	-6.4			-5.9	-5.1	-4.6	-4.3	-4.1	-4.1
	M68	Pyrite-quartz-carbonate vein in monzonite	-7.1			-6.6	-5.8	-5.3	-5.0	-4.8	-4.8
	M70	Pyrite-quartz-carbonate vein in monzonite	-6.6			-6.1	-5.3	-4.8	-4.5	-4.3	-4.3
3.2	M71	Carbonate vein cutting brecciated monzonite	-5.8			-5.3	-4.5	-4.0	-3.7	-3.5	-3.5
3.4	M79	Arsenopyrite-quartz-carbonate vein in monzonite	-6.8			-6.3	-5.5	-5.0	-4.7	-4.5	-4.5
	M76	Arsenopyrite-quartz-carbonate vein in monzonite	-8.5			-8.0	-7.2	-6.7	-6.4	-6.2	-6.2
	M75	Arsenopyrite-quartz-carbonate vein in monzonite	-5.8			-5.3	-4.5	-4.0	-3.7	-3.5	-3.5
	M74	Arsenopyrite-quartz-carbonate vein in monzonite	-5.0			-4.5	-3.7	-3.2	-2.9	-2.7	-2.7
3.8	M80	Stibnite-quartz-carbonate-feldspar vein in monzonite	-6.0	-8.7	-6.8	-5.5	-4.7				

The $\delta^{13}\text{C}$ values of carbonate separates were similar for all stages with values of -4.6 to -8.5 ‰. At temperatures of 250 to 500 °C, $\Delta^{13}\text{C}$ between carbonate and CO_2 varies from -2.3 to -0.5 ‰ (Ohmoto and Rye, 1979). Thus measured $\delta^{13}\text{C}$ values of -8.5 to -4.6 ‰ for P-stage 3.1 to 3.4 are equivalent to CO_2 $\delta^{13}\text{C}$ values of -8.0 to -2.5 ‰. Temperatures for P-stage 3.8 veins (150 to 300 °C) correspond to for carbonate- CO_2 $\Delta^{13}\text{C}$ values of -2.7 to -1.3 ‰ (Ohmoto and Rye, 1979). The measured $\delta^{13}\text{C}$ of -6.0 is therefore consistent with CO_2 $\delta^{13}\text{C}$ values of -8.7 to -4.7 ‰.

6.8 Fluid $\delta^{34}\text{S}$ estimates

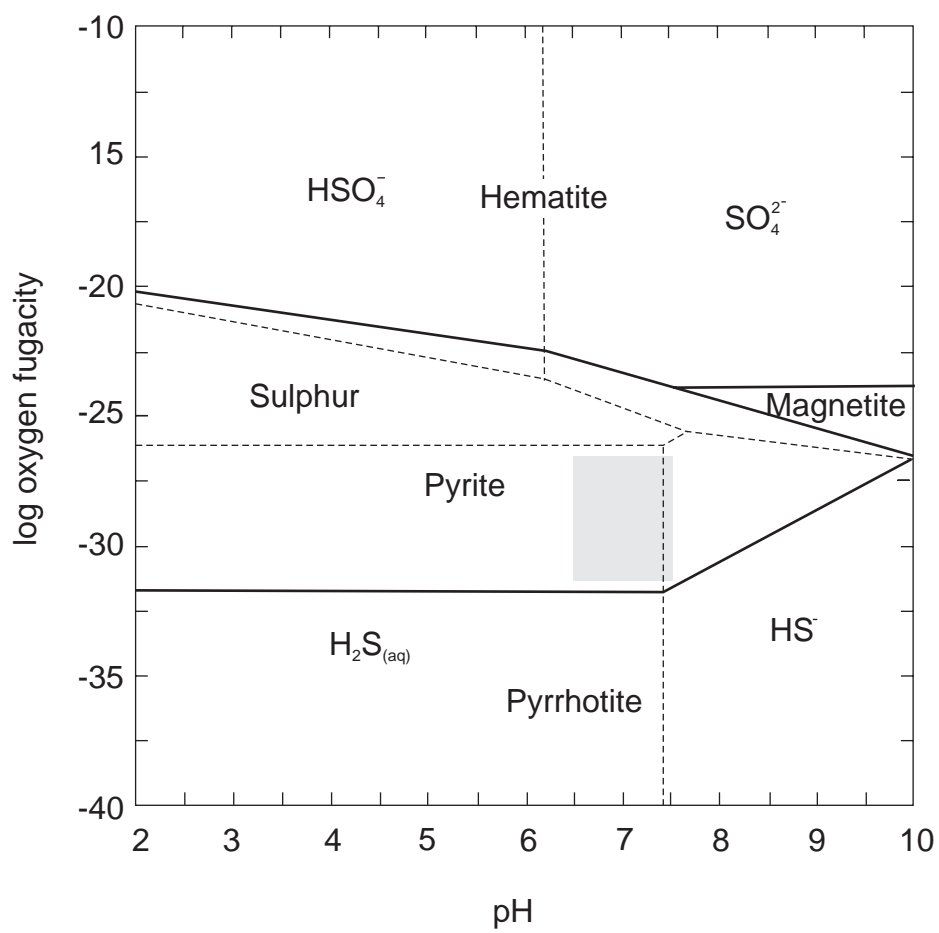
Gold-bearing arsenopyrite and significant S enrichment of altered wall rocks highlight the importance of S in mineralising processes at Brewery Creek. Calculation of $\delta^{34}\text{S}_{\text{fluid}}$ can be problematic as the relationship between mineral and fluid is not simply controlled by temperature, fluid source, and wall rock interactions as it is for $\delta^{18}\text{O}$, but is most strongly influenced by redox reactions, S speciation, and pH (Ohmoto and Rye, 1979). Accordingly, the $\delta^{34}\text{S}_{\text{fluid}}$ and the source of S cannot be directly estimated from the $\delta^{34}\text{S}_{\text{mineral}}$ unless the variables that control the mineral-fluid relationship are resolved.

It is possible to constrain the pH, redox state and sulphur speciation of fluids that were present during mineralisation at Brewery Creek by using known mineral relationships. Extensive carbonate and clay (illite and kaolinite) alteration possibly after feldspar at Brewery Creek indicates that the pH is most likely to be near neutral (Deer et al., 1992; Cooke and Simmons, 2000). Pyrite that has overgrown biotite suggests that the following reaction can be written:



Where the equivalent of K-feldspar at Brewery Creek are illite and kaolinite. The sulphur activity for this reaction was calculated using the computer program Geochemists Workbench at 400°C and 2.5 kb and which gave log a H_2S of 1.3 and log a SO_4^{2-} of -26.67. This suggests that H_2S is the dominant species and is ~ 30 times greater in concentration than SO_4^{2-} . Rye and Ohmoto (1979) and Ohmoto (1986) also report H_2S to be the dominant S species under conditions similar to those at Brewery Creek. A pH - log $f\text{O}_2$ was also constructed with Geochemists Workbench at 400°C and 2.5 kb and indicates $f\text{O}_2$ of ~ -26 to -32 (Figure 6.5). Unfortunately no data were

Figure 6.5 **A pH - log fO_2 diagram for stage 3.1 mineralisation.** The diagram was calculated using the computer program Geochemists Workbench for the reaction annite (Fe-rich biotite) + 1.5 $O_{2(g)}$ + 6 $H_2S_{(aq)}$ = K-feldspar + 3 pyrite + 7 H_2O at 400°C, 2.5 Kb and a log H_2S activity of 1.3 to replicate the P-stage 3.1 alteration. K-feldspar was not observed with P-stage 3.1 but is used in place of illite and kaolinite. The dashed lines are the calculated boundaries between S species and the solid lines are the boundaries between mineral phases. The shaded rectangle represents the likely pH and fO_2 conditions of the mineralising system during P-stage 3.1. The proposed conditions are constrained by the presence of pyrite and absence of pyrrhotite, hematite, magnetite and native sulphur.



available in Geochemists Workbench for pressures < 2.5 kb, however, similar plots by Hofstra and Cline (2000) at 225°C and 500 bars also show that the mineralising fluid would be reduced and that H₂S is the dominant species. Thus the hydrothermal fluid present during mineralisation at Brewery Creek was reduced and near neutral and S speciation was dominated by H₂S.

The pyrrhotite-H₂S, pyrite-H₂S, arsenopyrite-H₂S and stibnite-H₂S fractionation equations of Ohmoto and Rye (1979) were used to calculate the $\delta^{34}\text{S}_{\text{fluid}}$. Given the significant range in temperature estimates for paragenetic stages 2.1 to 3.8, the $\delta^{34}\text{S}_{\text{fluid}}$ was calculated for temperatures ranging from 150 - 700 °C (Table 6.5). Two samples of pyrrhotite from monzonite have $\delta^{34}\text{S}_{\text{mineral}}$ values of 9.1 ‰ and 11.1 ‰ and average 10.1 ‰. At temperatures of 500 to 700 °C the $\Delta^{34}\text{S}_{\text{mineral-fluid}}$ values are limited to 0.2 to 0.1, thus the corresponding $\delta^{34}\text{S}_{\text{fluid}}$ is 8.9 to 11.0 ‰. Pyrrhotite from tremolite skarn adjacent to a monzonite sill has a $\delta^{34}\text{S}_{\text{mineral}}$ value of 0.4 ‰. Using temperatures and therefore $\Delta^{34}\text{S}_{\text{mineral-fluid}}$ values calculated for monzonite sills, the $\delta^{34}\text{S}_{\text{fluid}}$ is 0.2 to 0.1 ‰.

P-stage 3.1 $\delta^{34}\text{S}_{\text{mineral}}$ values for pyrite vary by ~ 20 ‰ and can be partitioned into two groups with $\delta^{34}\text{S}_{\text{mineral}}$ values of -0.5 to 7.2 ‰ and 13.5 to 20.3 ‰. At temperatures of 200 to 500 °C the $\Delta^{34}\text{S}_{\text{mineral-fluid}}$ values vary between 1.5 and 0.7 and calculated $\delta^{34}\text{S}_{\text{fluid}}$ are -2.0 to 6.5 ‰ and 12.0 to 19.6 ‰ respectively. Analyses of arsenopyrite gave $\delta^{34}\text{S}_{\text{mineral}}$ values of 5.8 to 9.0 ‰. At the same temperatures as P-stage 3.1 and using similar $\Delta^{34}\text{S}_{\text{mineral-fluid}}$ values the $\delta^{34}\text{S}_{\text{fluid}}$ is calculated to be 4.3 to 8.3 ‰. $\delta^{34}\text{S}_{\text{mineral}}$ for stage 3.8 stibnite varies from -2.0 to -4.1 ‰. At temperatures of 150 to 300 °C the $\Delta^{34}\text{S}_{\text{mineral-fluid}}$ values are -4.2 to -2.3 and the estimated $\delta^{34}\text{S}_{\text{fluid}}$ are -1.8 to 2.2 ‰.

The results and implications of the O, C, and S isotope research further discussed in Chapter 7.

Table 6.5 **$\delta^{34}\text{S}_{\text{fluid}}$ estimated from sulphur mineral separates and laser ablation.** The data were calculated using the sulphide- H_2S fractionation equations of Ohmoto and Rye (1979) at the temperatures shown. Note the wide range in $\delta^{34}\text{S}_{\text{fluid}}$ for sulphides from P-stage 3.1. Note also the change in $\delta^{34}\text{S}_{\text{fluid}}$ through the paragenesis.

Alteration stage	Sample numbers	Notes	Mineral $\delta^{34}\text{S} \text{‰}$	Fluid $\delta^{34}\text{S} \text{‰}$ at the following temperatures (°C)											
				150	200	250	300	350	400	450	500	550	600	650	700
2.1	M25 PO, M50	Pyrrhotite (primary?) from monzonite sill	9.1, 11.1. mean 10.1								9.9	9.9	10.0	10.0	10.0
2.2	M26 PO	Pyrrhotite from tremolite skarn adjacent to monzonite sill	0.4								0.2	0.2	0.1	0.1	0.1
3.1	M38 PY	Disseminated pyrite from Earn Gp. siltstone	14.5			13.0	13.3	13.5	13.6	13.7	13.8				
	M27 PY	Disseminated pyrite in monzonite close to sill margin	20.3			18.8	19.1	19.3	19.4	19.5	19.6				
	M28 PY	Pyrite only veins in monzonite	2.2			0.7	1.0	1.2	1.3	1.4	1.5				
	M29 PY	Pyrite-quartz-carbonate vein in monzonite	1.1			-0.4	-0.1	0.1	0.2	0.3	0.4				
	M31 PY	Disseminated pyrite in a breccia with clasts of monzonite	7.2			5.7	6.0	6.2	6.3	6.4	6.5				
	M32 PY	Disseminated pyrite in a breccia with clasts of monzonite	13.5			12.0	12.3	12.5	12.6	12.7	12.8				
	M39 PY	Disseminated pyrite in monzonite	3.8			2.3	2.6	2.8	2.9	3.0	3.1				
	mjl52py1	Pyrite adjacent to pyrite-quartz-carbonate vein in monzonite close to sill margin	7.1			5.6	5.9	6.1	6.2	6.3	6.4				
	mjl52py2	Pyrite adjacent to pyrite-quartz-carbonate vein that cuts andalusite rich contact aureole	-0.5			-2.0	-1.7	-1.5	-1.4	-1.3	-1.2				
	mjl52py3	Pyrite adjacent to pyrite-quartz-carbonate vein that cuts andalusite rich contact aureole	1.5			0.0	0.3	0.5	0.6	0.7	0.8				
	mjl52py4	Pyrite adjacent to pyrite-quartz-carbonate vein in monzonite close to sill margin	18.7			17.2	17.5	17.7	17.8	17.9	18.0				

Alteration stage	Sample numbers	Notes	Mineral $\delta^{34}\text{S}$ ‰	Fluid $\delta^{34}\text{S}$ ‰ at the following temperatures (°C)											
				150	200	250	300	350	400	450	500	550	600	650	700
	mjl53py1	Pyrite from pyrite-quartz-carbonate-rocsoelite vein hosted by monzonite	7.0			5.5	5.8	6.0	6.1	6.2	6.3				
	mjl53py2	Pyrite from pyrite-quartz-carbonate-rocsoelite vein hosted by monzonite	14.3			12.8	13.1	13.3	13.4	13.5	13.6				
	mjl54py1	Disseminated pyrite hosted by sheared carbonaceous shale immediately adjacent to a monzonite sill	17.0			15.5	15.8	16.0	16.1	16.2	16.3				
	mjl54py2	Disseminated pyrite in monzonite at sill margin and immediately adjacent to sheared carbonaceous shale	14.8			13.3	13.6	13.8	13.9	14.0	14.1				
	mjl55py core	Core of zoned pyrite hosted in a monzonite breccia	14.3			12.8	13.1	13.3	13.4	13.5	13.6				
	mjl55 py rim	Rim of zoned pyrite hosted in a monzonite breccia	13.8			12.3	12.6	12.8	12.9	13.0	13.1				
	mjl60py2	Disseminated pyrite in monzonite	6.3			4.8	5.1	5.3	5.4	5.5	5.6				
	mjl61py1	Pyrite next to pyrite-quartz-carbonate vein in monzonite	13.8			12.3	12.6	12.8	12.9	13.0	13.1				
3.4	mjl60 aspy 1	Arsenopyrite from arsenopyrite-quartz-carbonate vein selvage in monzonite	5.8			4.3	4.6	4.8	4.9	5.0	5.1				
	mjl60 aspy 2	Arsenopyrite from arsenopyrite-quartz-carbonate vein selvage in monzonite	6.0			4.5	4.8	5.0	5.1	5.2	5.3				
	mjl59 aspy 1	Disseminated arsenopyrite within monzonite	6.5			5.0	5.3	5.5	5.6	5.7	5.8				
	mjl57 aspy 2	Disseminated arsenopyrite within monzonite	9.0			7.5	7.8	8.0	8.1	8.2	8.3				
3.8	M30 STIB	Stibnite-quartz-carbonate-feldspar vein in monzonite	-2.1	2.1	1.2	0.6	0.2								
	M33 STIB	Stibnite infill of breccia with clasts of Steel Fm. siltstone	-4.1	0.1	-0.8	-1.4	-1.8								
	M35 STIB	Stibnite infill of breccia with clasts of Earn Gp. siltstone	-2.0	2.2	1.3	0.7	0.3								

CHAPTER SEVEN

The evolution of the Brewery Creek gold deposit – discussion and conclusions



A couple of buildings built during the gold boom of the late 1800's and still surviving, somewhat precariously, in down town Dawson City. The centre of Dawson is heritage listed and all new buildings are built in the style of the gold rush days.

7.1 Chapter overview

The Brewery Creek gold deposit is an example of a structurally controlled intrusion-related gold system. Zones of gold mineralisation along the Reserve Trend consistently strike E and NE and dip steeply to the south. Similarly oriented veins and faults were observed in all of the open pits. The 3 dimensional orientation of mineralisation, veins, and faults are best explained by mineralisation occurring during extension.

Hydrothermal fluids associated with mineralisation were reduced, CO₂ rich and near neutral in pH. Gold was likely to have been transported as a bisulphide complex and the predominance of Au-bearing wall rock arsenopyrite and arsenian pyrite emphasise the importance of sulphidation reactions as a Au precipitation mechanism.

Isotope data provide evidence for significant input of magmatic fluids into the mineralising system at Brewery Creek. The calculated fluid compositions are consistent with an initial mixed magmatic and crustal (sedimentary) source that is replaced over time by a mixed magmatic and evolved meteoric fluid source. Thus a genetic model for mineralisation is described and is based on emplacement of felsic magma and subsequent cooling of the associated hydrothermal system.

This chapter addresses the following points:

- (1) A structural model for gold mineralisation at Brewery Creek
- (2) The chemistry and sources of mineralising fluids
- (3) Gold transport and deposition mechanisms
- (4) A genetic model for the development of the Brewery Creek deposit
- (5) Classification of the Brewery Creek deposit

7.2 Structural controls on mineralisation

Despite significant research on intrusion-related gold deposits in the Yukon and elsewhere in the world there is little published information that describes the structural controls on these deposits. Poulsen et al. (1997) were the first to surmise that mineralisation in the Yukon might have occurred during a relatively short-lived period of N-S extension, coinciding with TPS magmatism. Recently, Stephens (2003) and Stephens et al. (2004) presented comprehensive structural studies from the spatially separate Clear Creek and Scheelite Dome gold prospects and the Dublin Gulch gold deposit, all of which lie within the central Yukon. Here the gold mineralisation trends variably E, ENE, and NW and their interpretation is that these shared orientations reflect a regional extensional structural control on gold mineralisation. This interpretation is supported by similarly oriented mineralisation trends that have been described at Brewery Creek (Lindsay et al., 2000, 2002), Emerald Lake (Duncan et al., 1998), Mike Lake (Poulsen et al., 1997), and similarly oriented post-TPS faults recognised elsewhere in the Selwyn Basin (e.g. Gordey and Anderson, 1993).

A structural model for gold mineralisation at Brewery Creek

Distinct fault controls on the location of mineralisation at both property- and mine-scales have been documented in section 4.4. Mineralisation and faults trending E and NE and mineralised veins trending E suggest that a structural model may be developed to explain the regular distribution of mineralisation along the Reserve Trend. Thus, a three-step model incorporating structural and paragenetic data (sections 3.5 and 4.3 respectively) is described below.

Structural preparation of a site for later mineralisation

A critical feature of a structural model for mineralisation along the Reserve Trend is the early development of faults that structurally prepare the area and provide a mechanism to subsequently focus sill emplacement and mineralisation over a strike length of more than 12 km. D-stage 4 thrust faults are oriented broadly parallel to the Reserve Trend (Figure 3.1) and are thus interpreted to represent the first stage in its development. These faults display dip-slip offsets of up to 250 m and possibly extend down dip for several kilometres where-by the D-stage 4 faults have the potential to access significant fluid reservoirs. Multiple episodes of fluid flow along these structures is evident; for example Figure 4.4b shows a monzonite sill that has intruded a shear zone

containing several stages of pre-TPS quartz veining. A broad NNE trending fold (D-stage 5) deformed the D-stage 4 faults.

The D-stage 4 faults and D-stage 5 folds have been offset by property-scale NE trending faults (D-stage 6). The D-stage 6 faults are oriented parallel to the NE trending mineralised zones, however, their role during mineralisation is unclear. The emplacement of TPS sills annealed the D-stage 6 faults. Sill emplacement is likely to have been at least in part controlled by pre-existing D-stage 4 structures (chapter 3). The reactivation of D-stage 4 structures during a period of N-S oriented extension would facilitate sill emplacement.

TPS sills are crosscut by numerous, variably oriented normal faults (D-stage 7), which indicate that the extensional structural regime was sustained following sill emplacement. The D-stage 7 faults dominantly strike NW, NNE, NE, and E and have a steep to moderate dip. The 45° variation in strike and field relationships that show mutually crosscutting faults suggest that there were significant variations in the local stress field. The initial development of D-stage 7 faults is interpreted to have occurred prior to mineralisation as veins and mineralisation were observed to crosscut these faults. In the Blue Pit the major structure is a NE trending fault that juxtaposes monzonite sills, siltstone and sandstone against chert pebble conglomerate, siltstone and shale and indicates a minimum normal dip-slip movement of 70 metres. Gold mineralisation is evenly distributed around this fault and does not show any significant offset (pers. com. R. Diment). This suggests that the fault was active prior to mineralisation to offset the lithology, but was also active during mineralisation to allow fluid flow.

Mineralisation during extension

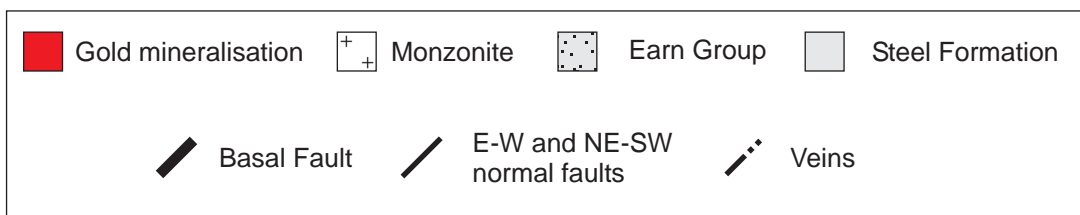
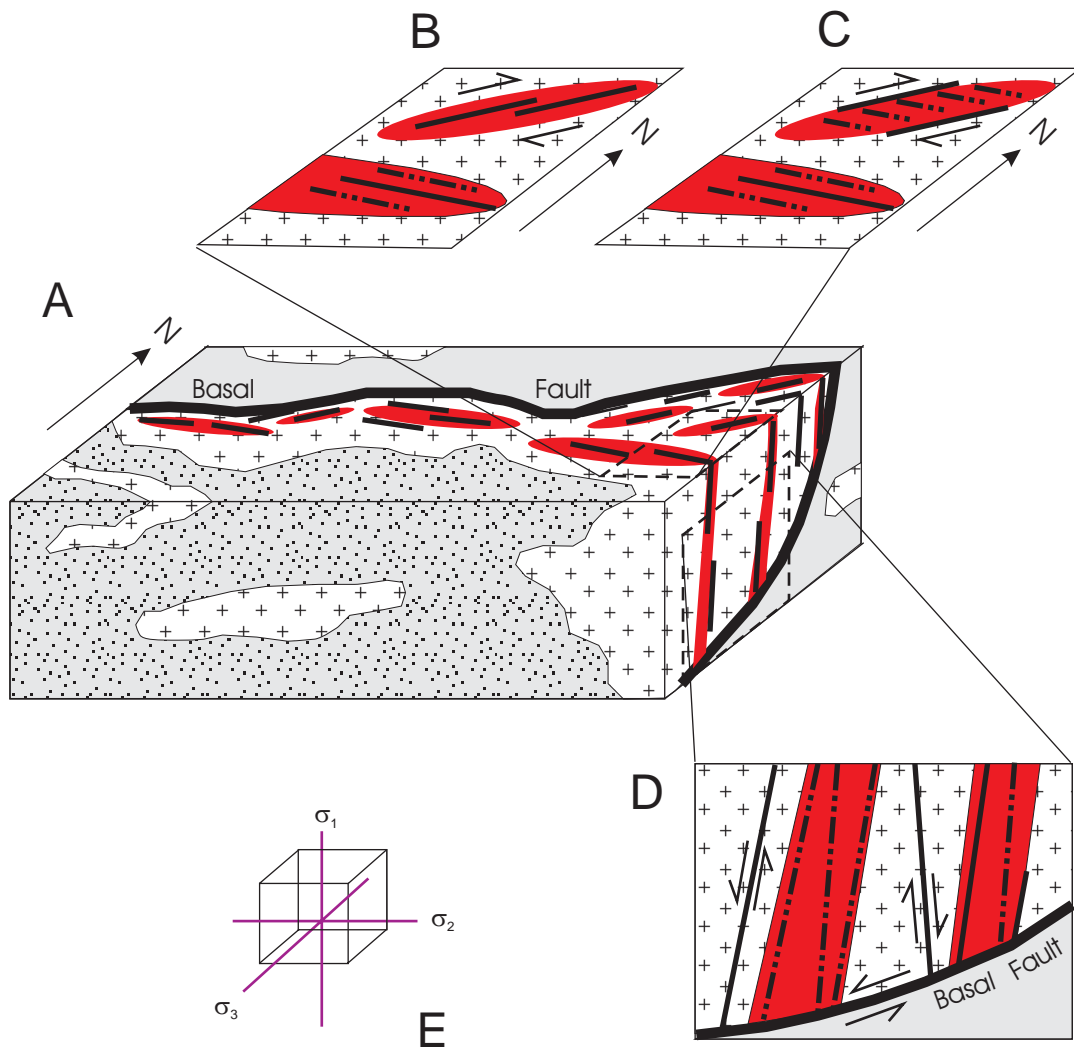
Discrete mineralised zones consistently striking E and NE combined with mineralised E and NE oriented faults, and an E trending fault that bounds mineralisation at depth, suggest that there were distinct mine-scale fault controls on the distribution of gold mineralisation along the Reserve Trend. For gold mineralisation to occur simultaneously on E and NE trending structures both fault sets must have been active during mineralisation. Furthermore an active property-scale structure or structures must have been present to focus the mineralising fluid along the Reserve Trend for more than 12 km and into the mine-scale E and NE faults.

Mineralisation likely occurred during a period of extension as suggested by (1) observed normal displacement evident on most of the post-TPS faults cropping out along the Reserve Trend (e.g. the Basal Fault and the steeply dipping E and NE trending structures), (2) steeply dipping E and NE trending mineralised zones, and (3) steeply dipping E trending gold bearing veins. Thus, the Basal Fault may be interpreted to represent a master fluid focussing structure developed in a site that was structurally prepared by earlier faulting (D-stage 4) and reactivated to produce normal dip-slip offset during extension. The smaller, variably oriented steeply dipping faults would represent secondary structures that developed and/or reactivated D-stage 6 (?) and D-stage 7 faults in response to movement along the Basal Fault and provided suitably oriented fluid pathways. In this case σ_1 would be broadly vertical to sub-vertical, with σ_2 trending E-W and σ_3 oriented N-S in a horizontal plane.

Alternatively, the relationship between the Basal Fault and mineralisation illustrated in Figures 4.14 and 4.15 can be interpreted such that the Basal Fault cross cuts mineralisation. The model proposed here does not preclude post-mineralisation reactivation of the Basal Fault but rather suggests that a property-scale structure must be active to focus mineralisation along the Reserve Trend. The Basal Fault potentially represents a reactivated D-stage 4 thrust fault, and exhibits a displacement that is consistent with movement on the mineralised E and NE trending normal faults. Furthermore, gold mineralisation appears to be related to the Basal Fault because gold grades are generally higher in areas proximal to the Basal Fault such as in the northern parts of the open pits and where the fault is steeply dipping (Figures 4.13 and 4.14).

The extensional structural model suggested above describes mineralisation trending E and NE but does not explain why most gold-bearing veins and the majority of post-TPS veins trend E. The lack of NE trending veins suggests that NE trending faults did not dilate as much as E trending faults and indicates that the NE oriented structures were in the most suitable orientation for slip during mineralisation. However, the presence of NE striking mineralisation requires gold-bearing fluid to have moved along the NE oriented faults. Thus, the paucity of NE striking veins may be explained by mineralisation occurring in an extensional structural environment that contained a component of strike-slip. If σ_1 was oriented sub-vertically and plunging steeply to the east, or if σ_1 was vertical and σ_2 was in an approximately horizontal E oriented direction, then dextral movement would occur on the NE trending faults. E trending veins and/or disseminated mineralisation could then be generated around or along these faults (Figure 7.1) in a trans-tensional structural regime that was dominated by extension.

Figure 7.1 **A schematic diagram illustrating the extensional model proposed for Reserve Trend mineralisation.** Extension is interpreted to reactivate the Basal Fault shown in (A) and the steeply dipping E-W and NE-SW trending faults (B, C, D). The Basal Fault may be interpreted to represent a master fluid focussing structure developed in a site that was structurally prepared by earlier faulting. The smaller, variably oriented steeply dipping faults would represent secondary structures that developed or reactivated in response to movement along the Basal Fault and provided suitably oriented fluid trapping zones. Minor strike-slip movement on the Basal Fault can explain the absence of NE striking veins. This would allow microfracture, microdilation and disseminated mineralisation around NE striking faults (B) and/or the development of E-W oriented veins in NE striking mineralised zones. The interpreted orientation of σ_1 , σ_2 , and σ_3 is shown in (E).



However, the strike-slip displacement on NE faults must be small. If there were substantial strike-slip movement then the angle between E and NE faults would result in mineralisation preferentially distributed along the E striking fault set. Furthermore, there is no appreciable offset on stage 6 faults that transect the Reserve Trend.

Despite the development of numerous normal faults, deformation during mineralisation is interpreted to be weak. Many of the faults in the open pits are poorly developed and offsets are typically < 5 m. Features such as horsetails and step-overs are only rarely developed at Brewery Creek. Furthermore there is no evidence for substantial fault movement during mineralisation, which contrasts with lode gold and some epithermal and intrusion-related gold systems (Bierlein and Crowe, 2000; Hedenquist et al., 2000, Thompson and Newberry, 2000).

Monzonite sills host > 70% of the known gold mineralisation at Brewery Creek and sedimentary rocks contain < 30%. Thus, it is tempting to infer that competency contrasts between the sedimentary and intrusive rocks preferentially partition mineralisation into the sills. Numerous authors have proposed competency contrasts as a mechanism for localising mineralisation (e.g. Oliver et al., 1990; Ridley, 1993). The role of competency contrast in localising mineralisation at Brewery Creek is uncertain. Cross sections through the pits (Figures 5.1 and 5.2) show that mineralisation cuts lithology boundaries and average Au grades in the sedimentary rock hosted Blue pit are the third highest on the property, higher than most of the pits in intrusive rock hosted mineralisation. However, veins are more common in intrusive rocks. This suggests that lithology competency may partly control the style of mineralisation present with vein-related mineralisation in competent units and disseminated mineralisation dominant in less competent lithologies.

The structural model of extension during mineralisation proposed for Brewery Creek is similar to the models of extension during mineralisation that were suggested by Poulsen et al. (1997), Stephens (2003), and Stephens et al. (2004). However, the model for Brewery Creek differs in detail from Stephens (2003) and Stephens et al. (2004) who implied that at Clear Creek, Scheelite Dome, and Dublin Gulch mineralisation is related to steep E-W veins linked with NNW trending strike slip faults. These differences may reflect local changes in the stress field and/or depth of deposit formation.

Post-ore deformation and Tintina age gold mineralisation / remobilisation

Although the structural model proposed here explains the E trending mineralisation along the Reserve Trend and at North Slope, the model does not explain NW trending mineralised zones and NW trending gold-bearing sheeted veins in the Classic Zone. The local stress regime that produced D-stage 7 faults may have continued to be active following mineralisation but was subsequently overridden by regional stresses that produced movement on the Tintina Fault. Movement on the Tintina Fault likely activated / reactivated the Classic Fault, which dextrally offset mineralisation along the Reserve Trend by approximately 1.5 kilometres.

In the Classic Zone Au-bearing veins and Au-mineralised zones lie immediately adjacent to, and trend parallel to, the Classic Fault. The Classic Fault does not offset mineralisation at the Classic Zone. The veins at the Classic Zone differ from those along the Reserve Trend in strike but also in mineralogy as there is no evidence of arsenopyrite and all of the Au is non-refractory (Park, 1999). These relationships suggest that two distinct mineralising events may have occurred at Brewery Creek during two distinct structural regimes.

It is possible that mineralisation at the Classic Zone represents Au remobilised from another site during deformation associated with movement on the Classic or Tintina Faults. If remobilisation occurred the original source of Au is unlikely to have been from the currently defined resources at Brewery Creek as the primary gold distribution patterns along the Reserve Trend (i.e. pyrite overgrown by arsenopyrite and zoned arsenopyrite crystals) are unlikely to have been preserved during remobilisation.

7.3 Lithological and mineralogical constraints on fluid oxidation state and pH

The chemical nature and composition of mineralising fluids will place constraints on fluid sources, metal precipitation mechanisms and potential sites of mineralisation. Most fluid composition studies rely heavily on fluid inclusion and stable isotope data. However, the attributes of known mineralisation (i.e. associated alteration, host rocks, mineral paragenesis, etc.) will also help to resolve the chemistry of the mineralising fluid.

The preferential distribution of Au in intrusive rocks and not black shales (see chapter 5) suggests that the oxidation state of the Au-bearing fluids was probably reduced. If the fluids were oxidised they would have reacted with the strongly reduced carbonaceous shale and mineralisation would have been preferentially distributed into Earn Group sedimentary rocks, assuming fluid pathways through the shale were available. Reduced mineralising fluids are also supported by the sulphide mineral paragenesis. Early pyrrhotite followed by pyrite indicates that either the sulphur and oxygen fugacity of the fluids increased, or that the pH decreased (if the initial fluids were highly alkaline), or that the temperature of the fluids decreased over time (Hofstra and Cline, 2000). However, at 400°C the boundary between pyrrhotite and pyrite is at $\log fO_2$ of -32 (Figure 6.5) indicating the fluids may be considered reduced.

The approximate pH (i.e. acid, neutral or alkaline) of the mineralising fluids can be estimated using alteration minerals. The mineralisation alteration assemblage at Brewery Creek comprises pyrite - arsenopyrite - stibnite - quartz - carbonate - illite - kaolinite (after feldspar) - roscoelite. Similar assemblages have been noted in low sulphidation epithermal (Cooke and Simmons, 2000) and orogenic (Hagemann and Cassidy, 2000) gold deposits and have been interpreted to reflect ore deposition from a near-neutral pH fluid. Extensive carbonate alteration at Brewery Creek similarly indicates that the pH of the fluid must have been near neutral or alkaline. Substantial CO_2 addition but Ca stability was documented on isocon diagrams in Chapter 5. This signifies that the hydrothermal fluids were rich in CO_2 and that carbonates formed through CO_2 rich fluids interacting with Ca bearing minerals (e.g. feldspars).

A neutral to alkaline pH is also supported by the absence of significant known mineralisation in limestone or calcareous siltstone at Brewery Creek. If the ore forming fluids were acid then it is reasonable to expect that mineralisation would be preferentially distributed into calcareous sedimentary rocks. Furthermore, Murrowchick and Barnes (1986) and Murrowchick (1992) state that at moderate to high temperatures the solubility of pyrite is 6 to 10 orders of magnitude less than pyrrhotite. At these temperatures and at a pH of < 5, marcasite will form rather than pyrite. Though pyrrhotite is present in monzonite sills, marcasite was not observed at Brewery Creek and therefore the pH must be > 5.

7.4 Hydrothermal transport and deposition of Au

Mechanisms of Au transport: Au speciation and complexes

In most hydrothermal systems gold in solution occurs in the +1 valence state due to the low oxidation potential of hydrothermal waters (Seward, 1991). Au^+ has a low solubility and is therefore unlikely to form significant mineralisation. Higher Au solubilities can be achieved by the formation of Au complexes with various ligands (e.g. Cl^- , HS^- , CN^- , OH^- , etc.) and are necessary to generate high aqueous Au concentrations in order to form significant ore deposits (Brown, 1986; Gammons and Williams-Jones, 1995; Seward and Barnes, 1997). Seward (1991) resolved the relative stabilities of Au halide complexes as $\text{AuI}_2^- > \text{AuBr}_2^- > \text{AuCl}_2^- \gg \text{AuF}_2^-$, however, given that Cl concentrations are much greater than other halides in hydrothermal systems AuCl_2^- is thought to be the most important Au halide complex. The stability of Cl complexes is strongly dependant on temperature and AuCl_2^- is unlikely to be a significant transporting agent below 300°C (Gammons and Williams-Jones, 1995).

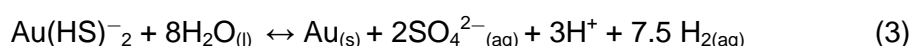
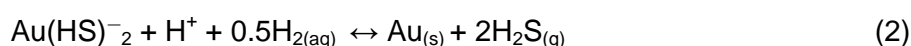
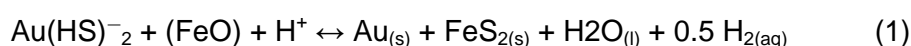
Antimony-rich systems, such as Brewery Creek, and low sulphide Au deposits are indicative of a hydrothermal ore system in which metal transport was dominated by bisulphide complexes (Goldfarb et al., 2004). Numerous studies have shown that Au, Ag, As, Sb, Hg and possibly other metals are commonly carried as bisulphide complexes in hydrothermal solutions (Barnes, 1979; Seward, 1989; Seward and Barnes, 1997). The bisulphide ligand (HS^-) is believed to be the principal transporting species when both chloride and bisulphide ligands are present in solution in significant quantities (Hayashi and Ohmoto, 1991).

Experimental studies have derived the thermodynamic properties for several hydrosulphide Au complexes at high temperature (>300°C) including $\text{Au}(\text{HS})_2^-$ (Seward, 1973; Gammons and Williams-Jones, 1995), $\text{HAu}(\text{HS})_{2(\text{aq})}$ (Hayashi and Ohmoto, 1991), and $\text{AuHS}_{(\text{aq})}$ (Benning and Seward, 1996). $\text{AuHS}_{(\text{aq})}$ was determined to be the dominant Au transporting species in low pH solutions over a wide range of total sulphur concentrations and temperatures (Benning and Seward, 1996). Hydrosulphide complexes are important for Au transport in reduced fluids with high sulphur concentrations. In moderately acidic and reduced conditions $\text{AuHS}_{(\text{aq})}$ dominates, whereas $\text{Au}(\text{HS})_2^-$ is more common in neutral pH and strongly reduced environments (Cooke and Simmons, 2000), such as those likely present during mineralisation at Brewery Creek. The maximum solubility for Au in bisulphide

complexes occurs in near-neutral pH conditions and the activity of reduced sulphur is the most important control on Au transport as a reduced sulphur complex (Moss and Scott, 2001).

Precipitation of Au from the hydrothermal fluid

Gold deposition results from the chemical reactions that take place within the fluid and adjacent wall rocks. If Au is transported as a bisulphide complex in reduced, near-neutral pH waters, then chemically effective reactions for Au deposition will include wall rock sulphidation (reaction 1), $\text{H}_2\text{S}_{(\text{aq})}$ loss via boiling (reaction 2) or destabilisation of reduced sulphur-bearing species through mixing with groundwater (reaction 3; Hyland and Bancroft, 1989; Cooke and Simmons, 2000):



Sulphidation of wall-rock monzonite was observed at Brewery Creek. This is evidenced by pyrite preferentially replacing carbonate altered mafic phenocrysts (typically biotite) along mineral cleavage seams. Arsenopyrite also occurs along mafic mineral cleavage seams, either as overgrowths on pyrite or less commonly as individual crystals. Phenocrysts cut by veins are the most strongly altered and most pyrite and arsenopyrite is hosted within the wall rock. Gold is included within arsenopyrite, and to a lesser extent pyrite, most likely within the crystal lattice but possibly also as inclusions (see below). In this situation Fe in the wall rock, and specifically in mafic phenocrysts, has reacted with reduced S, as well as As, sequestered from the hydrothermal fluid, to form arsenopyrite and pyrite, with arsenopyrite also acquiring Fe from pyrite. Sulphidation of monzonite is further supported by geochemical data (see isocon diagrams in chapter 5) that shows no significant increase in Fe concentration from unaltered to altered samples despite the obvious increase in Fe-sulphide content.

Mixing has also been suggested as a mechanism for depositing Au from bisulphide complexes (Corbett and Leach, 1998). Stable isotope studies on rocks from Brewery Creek (see section 7.5) indicate the presence of mixed magmatic and meteoric fluids during Au mineralisation. However, this does not indicate that fluid mixing caused Au

deposition. Cooke and Simmons (2000) point out that most models for mixing do not address chemical and mass balance considerations or the physical problems of mixing two waters that have different densities and temperatures. Cooke and McPhail (2000) and Simmons and Browne (2000) also note that in some instances mixing may increase, or have no effect, on the solubility of Au. For mixing to be a viable Au depositional mechanism from a reduced, near neutral pH fluid, the Au-bearing fluid would need to be oxidised (Reed and Spycher, 1985). However, this would require mixing with steam-heated acid sulphate water, which is largely restricted to the water table (Hedenquist, 1991).

Boiling is unlikely to have been a significant process in the mineralisation at Brewery Creek. The effectiveness of boiling for Au deposition in epithermal environments has been described by numerous authors (e.g. Drummond and Ohmoto, 1985; Seward, 1989) and boiling induced H₂S loss leading to the deposition of electrum has been documented in modern systems (Brown, 1986). However, the distinctive gangue mineral assemblages and textures that are typically associated with boiling fluids (e.g. bladed carbonate, lattice textured quartz, adularia; Cooke and Simmons, 2000) and zoned mineralisation styles common in boiling systems were not observed at Brewery Creek.

Invisible Au and mechanisms for incorporating Au into arsenopyrite

Numerous studies have investigated the incorporation of Au into sulphides and placed distinct geochemical parameters on this style of mineralisation. These investigations can be used to constrain likely mechanisms of incorporation of Au into arsenopyrite at Brewery Creek. The incorporation of Au into iron sulphide and sulf-arsenide minerals has been inferred for many years (Burg, 1930; Boyle, 1979). Where Au is in apparent solid solution with sulphides it is commonly termed invisible (synonyms include hidden, refractory and chemically bound). Invisible Au contained within pyrite and arsenopyrite has been documented in mesothermal and epithermal vein deposits, Carlin deposits and volcanic-hosted massive sulphide deposits (e.g. Cabri et al., 1989; Cathelineau et al., 1989; Wu and Delbove, 1989; Cook and Cryssoulis, 1990; Cabri, 1992; Arehart et al., 1993; Fleet et al., 1993; Mumin et al., 1994; Chenery et al., 1995; Huston et al., 1995; Oberthur et al., 1997; Moller et al., 1997; Genkin et al., 1998; Yang et al., 1998; Simon et al., 1999; Asadi et al., 2000; Ashley et al., 2000; Steele et al., 2000). Arsenopyrite is the most common host of invisible Au with Au concentrations of up to 1.5 wt% reported in natural arsenopyrite, although concentrations generally do not

exceed 1000 to 2000 ppm (Johan et al., 1989; Cabri et al., 1992), and up to 3 wt% in synthetic arsenopyrite (Fleet and Mumin, 1997). Within pyrite, arsenian zones preferentially incorporate Au (Fleet et al., 1993; Oberthur et al., 1997; Simon et al., 1999) and other metals including Cu, Ag, Sb (Griffin et al., 1991).

At Brewery Creek Au is present in arsenopyrite at > 1500 ppm levels and in pyrite at up to 300 ppm. The proportion of arsenopyrite in the ore will therefore strongly influence the amount of Au present. All arsenopyrite grains analysed are As-deficient but show a restricted compositional range with atomic wt% As values of 25.99 to 28.21. Arsenopyrite overgrowths on pyrite and the recorded As-deficiency imply that there may be considerable solid solution with a pyrite phase, however, unlike the results of Fleet and Mumin (1997) there is no evidence for a complete solid solution between FeAsS and FeS₂. Compositional zoning on a micron-scale was observed using back scatter electron-imaging techniques. Zoned and un-zoned crystals both have higher As and lower S on crystal rims compared to crystal cores and zoning is interpreted to result from variation in As/S ratios.

The formation of zoned arsenopyrite crystals has been interpreted to result from changing physiochemical conditions in ore forming fluids (Yang et al., 1998; Savage et al., 2000), including disequilibrium growth conditions (Wu and Delbove, 1989), episodic flow (Hammond and Tabata, 1997), pressure decreases, and wall rock reactions like sulphidation and carbonatisation (Huston et al., 1995; Yang et al., 1998; Ashley et al., 2000; Savage et al., 2000). Sulphidation and carbonatisation typify the alteration at Brewery Creek and Au preferentially distributed into wall rock arsenopyrite and arsenian pyrite emphasizes the importance of sulphidation reactions in the formation of the deposit. Changes in temperature are unlikely to play a major role in the incorporation of Au into arsenopyrite (Wu et al., 1990). Thus, changes in temperature are similarly unlikely to be important in Au-mineralisation at Brewery Creek even though there appears to have been a significant drop in temperature over time.

The morphology of Au within arsenopyrite and other Fe-sulphides is deposit-specific. Gold may exist within arsenopyrite as sub-microscopic, colloidal sized particles (Bakken et al., 1989; Chenery et al., 1995), or may be incorporated within the crystal structure through non-stoichiometric substitution (Cabri et al., 1989; Wu et al., 1990; Fleet et al 1993; Fleet and Mumin, 1997; Cabri et al., 2000). In some deposits both forms may occur (Yang, et al., 1998; Simon et al 1999). Metallurgical testing at Brewery Creek has indicated that up to 36% of the sediment hosted ore occurs as free

Au (Laprenune, 1997). Free Au was not observed in hypogene intrusion-hosted mineralisation at Brewery Creek and investigation of other deposits has also failed to demonstrate the presence of particulate Au despite measured Au values of > 1500 ppm (Genkin et al., 1998; Ashley et al., 2000). The reasons for the presence of both invisible and particulate Au at Brewery Creek were not investigated in this study but may be due to fluid evolution, Au-bearing Fe-sulphide dissolution and re-precipitation, multiple fluids and multiple mechanisms of precipitation such as chemisorption and electrochemical deposition (Cathelineau et al., 1991; Boiron et al., 1992; Arehart et al., 1993; Neumayr et al., 1993; Moller and Kersten, 1994; Fleet and Mumin, 1997; Oberthur et al., 1997; Genkin et al., 1998).

The composition of the arsenopyrite at Brewery Creek also provides insights into the composition of fluid that the arsenopyrite precipitated from. The stability field of arsenopyrite as a function of $f(S_2)$ and temperature is constrained by sulphidation reactions (Barton, 1969). At Brewery Creek pyrite overgrown by arsenopyrite suggests the following reaction occurred



The sulphidation reaction will buffer $f(S_2)$ at a given temperature and uniquely define the composition of any given arsenopyrite in equilibrium with the buffering phases (Sharp et al., 1985). Investigations into zoned arsenopyrite suggest that incorporation of Au, As, S, and Fe into the crystal lattice primarily reflects the composition of the mineralising fluid (Oberthur et al., 1997). The variation in Au, As, S, and Fe content of arsenopyrite crystals therefore result from changes in hydrothermal fluid composition. Thus, S-enriched and As-deficient arsenopyrite at Brewery Creek likely indicates that the hydrothermal fluid contained lesser amounts of As compared to systems that produce stoichiometric or As-enriched arsenopyrite and that S was in abundance. Increasing As content from core to rim of the arsenopyrite crystals also suggests that the fluid increased in As concentration as mineralisation progressed.

7.5 Isotopic constraints on fluid source

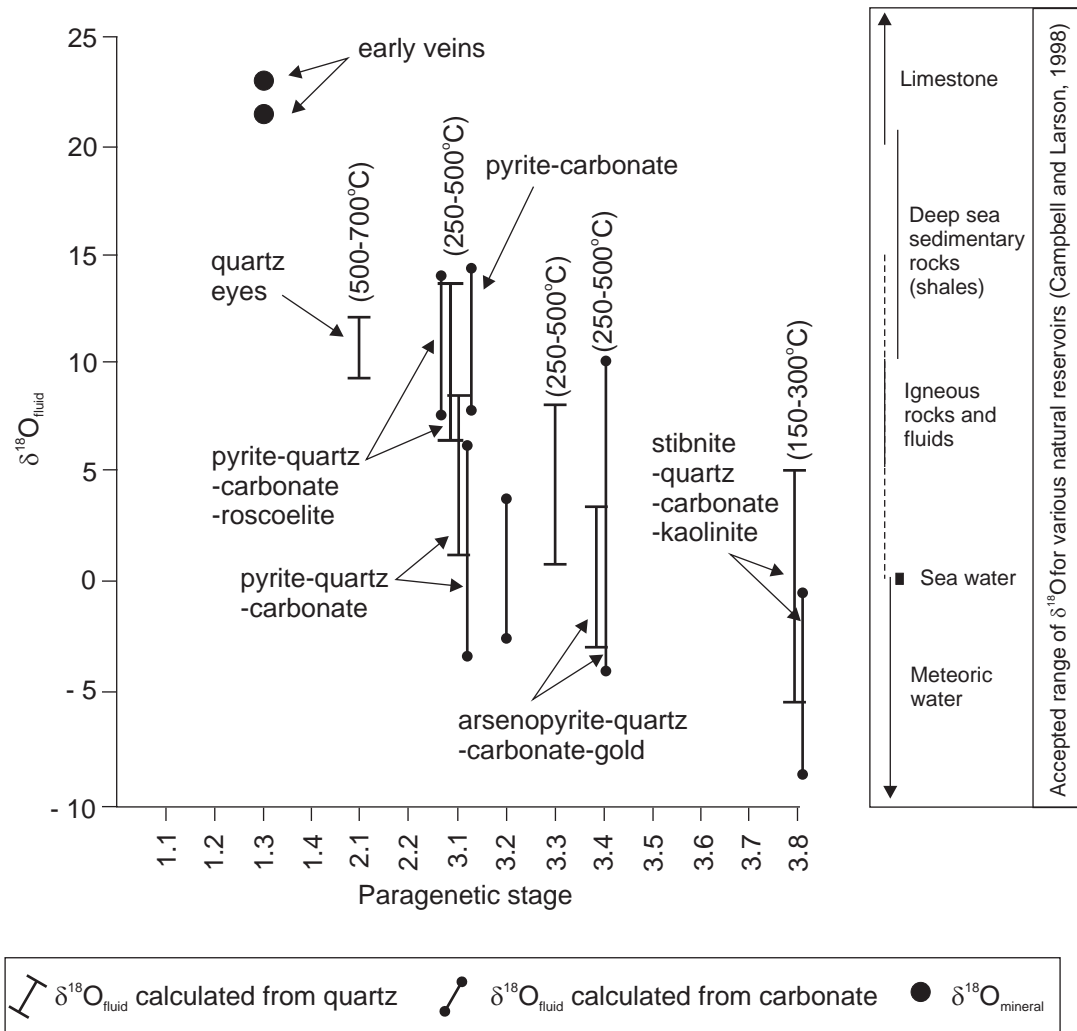
Comparison of calculated $\delta^{18}O$, $\delta^{13}C$, and $\delta^{34}S$ fluid values to the accepted isotopic ranges of natural reservoirs can provide constraints on the source of these components in hydrothermal fluids, which may in turn provide insights into the source of Au, As and

other elements of interest. Calculated $\delta^{18}\text{O}_{\text{fluid}}$ values of quartz and carbonate mineral separates and the $\delta^{18}\text{O}$ for various natural reservoirs are plotted on Figure 7.2. Quartz eyes from biotite monzonite sills gave $\delta^{18}\text{O}_{\text{fluid}}$ values of 9.6 ‰ to 11.8 ‰. These values are at the high end of typical magmatic values (5 -10 ‰, Campbell and Larson, 1998) and partially overlap with values recorded for representative sedimentary rocks. Goldfarb et al. (2004) attributed similarly high $\delta^{18}\text{O}$ of felsic igneous rocks at Donlin Creek to assimilation of crustal sedimentary rock into the primary magma. An analogous process is likely to have occurred at Brewery Creek as evidenced by xenoliths of carbonaceous shale contained within monzonite sills (Figure 3.10). Stephens (2003) also calculated higher $\delta^{18}\text{O}_{\text{fluid}}$ values for equivalent TPS rocks at Clear Creek.

Calculated $\delta^{18}\text{O}_{\text{fluid}}$ values of P-stage 3.1 vary from -4.4 ‰ at 250°C to 14.3 ‰ at 500°C. The data can be partitioned into two groups with pyrite-quartz-carbonate-roscoelite and pyrite-carbonate veins recording $\delta^{18}\text{O}_{\text{fluid}}$ values of 6.2 to 14.3 ‰ and pyrite-quartz-carbonate veins with $\delta^{18}\text{O}_{\text{fluid}}$ values of -4.4 to 8.5 ‰. The overlap between the $\delta^{18}\text{O}$ values of these veins is small despite the wide range of temperature that was used to estimate $\delta^{18}\text{O}_{\text{fluid}}$ values. This suggests that temperature is unlikely to be solely responsible for the variation in fluid isotopic values. Given that $\delta^{18}\text{O}_{\text{fluid}}$ values of the pyrite-quartz-carbonate-roscoelite and pyrite-carbonate veins are higher than the values calculated from quartz eyes hosted by monzonite sills it is likely that the O in these veins was derived from a mixed magmatic and crustal sedimentary source. This is consistent with the interpreted source of S (see below) and a possible source of V, as background levels of V, an element that is required to form roscoelite, are an order of magnitude higher in sedimentary rocks than igneous rocks (see chapter 5). The lower $\delta^{18}\text{O}_{\text{fluid}}$ values for pyrite-quartz-carbonate veins are consistent with a magmatic source.

$\delta^{18}\text{O}_{\text{fluid}}$ values for paragenetic P-stages 3.2 to 3.8 are generally lower than P-stage 3.1 and show an overall depletion trend from 11.1 to -8.7 ‰. A spread of 7 to 8 ‰ in the calculated $\delta^{18}\text{O}$ data would be consistent with quartz and carbonate precipitation from a single O reservoir over a temperature range of 150 to 500 °C. However, this does not explain the ~20 ‰ spread in $\delta^{18}\text{O}$ data from Brewery Creek and indicates that O was derived from more than one source. The only large reservoir with $\delta^{18}\text{O}$ values less than 0 ‰ is meteoric water. Therefore, a mixed magmatic and meteoric source of O is proposed for P-stages 3.2 to 3.8. The progressive depletion of $\delta^{18}\text{O}$ over time is

Figure 7.2 **Calculated δO^{18} fluid values from Brewery Creek compared with various natural reservoirs.** The values were calculated at the temperatures shown. The high δO^{18} mineral values for samples from two early stage veins indicate that the veins were formed from a fluid in equilibrium with sedimentary rocks. Quartz eyes from monzonite (P-stage 2.1) have values higher than those typically recorded for igneous rocks, which likely reflects the incorporation of sedimentary rock into the melt. Pyrite bearing quartz veins show a ~ 20 ‰ variation in isotope values that overlaps with typical magmatic and sedimentary values. Arsenopyrite and stibnite bearing veins record low positive and negative isotope values. Meteoric water is the only significant reservoir with negative values, indicating a mixed magmatic-meteoric source of O for these two stages. Note the overall decline in isotope values with time.



interpreted to correspond to an increase of meteoric water input into the hydrothermal system.

Carbon isotope data show a restricted range in $\delta^{13}\text{C}_{\text{fluid}}$ values of -8.7 to -2.5 ‰ (Figure 7.3). A spread of ~5 ‰ in the calculated $\delta^{13}\text{C}$ data would be consistent with carbonate precipitation from a single C reservoir over a temperature range of 150 to 500 °C. The calculated $\delta^{13}\text{C}$ values from Brewery Creek are equivalent to the accepted range of magmatic C (e.g. magmatic CO_2). Therefore a magmatic source of C is suggested for Brewery Creek. It should be noted that in most ore forming systems, fluids typically transport only a small quantity of C (<1 mole / kg H_2O) and C isotope values of the hydrothermal fluid are easily shifted by interaction with wall rocks and other fluids (Ohmoto, 1986). Therefore, the restricted range of C isotope values at Brewery Creek indicate that fluids derived from sedimentary rock and meteoric sources that contributed O and S (see below) to the hydrothermal system must have been C-deficient compared with the fluids derived from a magmatic source.

$\delta^{34}\text{S}_{\text{fluid}}$ values calculated from pyrrhotite, pyrite, arsenopyrite, and stibnite are plotted with the $\delta^{34}\text{S}$ for various $\delta^{34}\text{S}$ reservoirs on Figure 7.4. Pyrrhotite separated from biotite monzonite sills gave $\delta^{34}\text{S}_{\text{fluid}}$ values of 8.9 to 11.0 ‰. These values are higher than typical magmatic values (-2 to 5 ‰) and partially overlap with values recorded for representative sedimentary rocks (Ohmoto, 1986). Assimilation of crustal sedimentary rock that was implicated to explain higher than normal $\delta^{18}\text{O}$ values also accounts for elevated $\delta^{34}\text{S}$ values obtained from pyrrhotite hosted by monzonite.

P-stage 3.1 $\delta^{34}\text{S}_{\text{fluid}}$ values vary from -2.0 ‰ at 250°C to 19.6 ‰ at 500°C. Large $\delta^{34}\text{S}$ isotopic ranges can be achieved through a variety of mechanisms. A change in redox state and the presence of more oxidised fluids can result in significant S fractionation (Ohmoto and Goldhaber, 1997; Ohmoto and Rye, 1979). However, mineral assemblages and chemical reactions between biotite and pyrite suggest that the fluid is reduced (Chapter 6) and any fractionation would therefore be quite small. Furthermore, redox driven fractionation through magmatic processes is unlikely as pyrrhotite in monzonite sills, and in some instances a high component of black shale xenoliths in the sills, indicate that the intrusive rocks at Brewery Creek are reduced. Changes in temperature may also result in significant isotopic variation. However, $\delta^{34}\text{S}_{\text{fluid}}$ values are partitioned into two separate groups ($\delta^{34}\text{S}_{\text{fluid}}$ -2.0 to 6.5 ‰ and 12.0 to 19.6 ‰) that do not overlap despite values calculated over a large temperature range (Figure 7.4 a).

Figure 7.3 **Calculated $\delta^{13}\text{C}$ fluid values from Brewery Creek compared with various natural reservoirs.** The range bars represent the calculated composition of fluids between 250 and 500 °C for P-stages 3.1 to 3.4 and between 150 and 300 °C for P-stage 3.8. Note the very tight range in $\delta^{13}\text{C}$ values that is coincident with typical magmatic values.

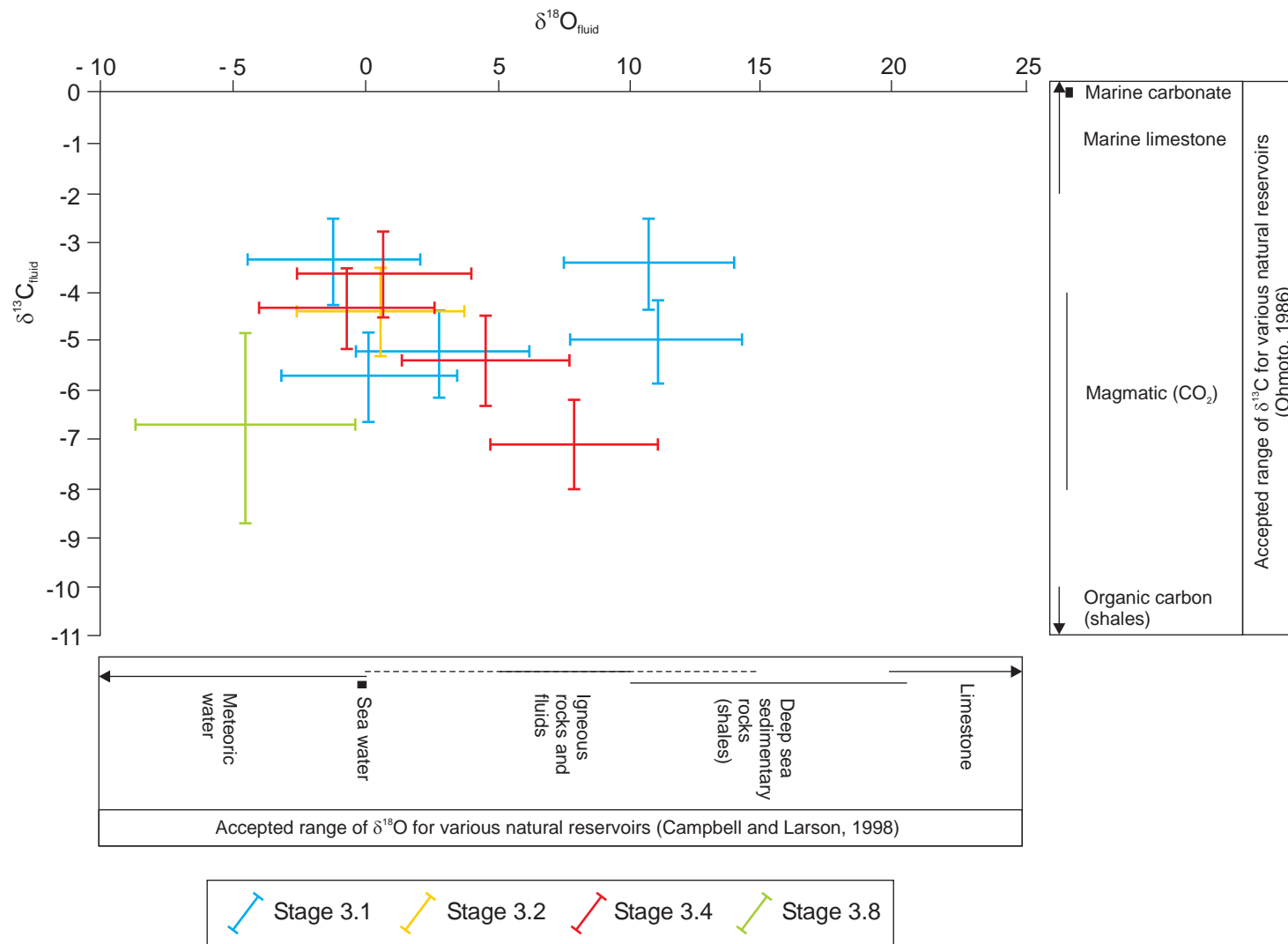
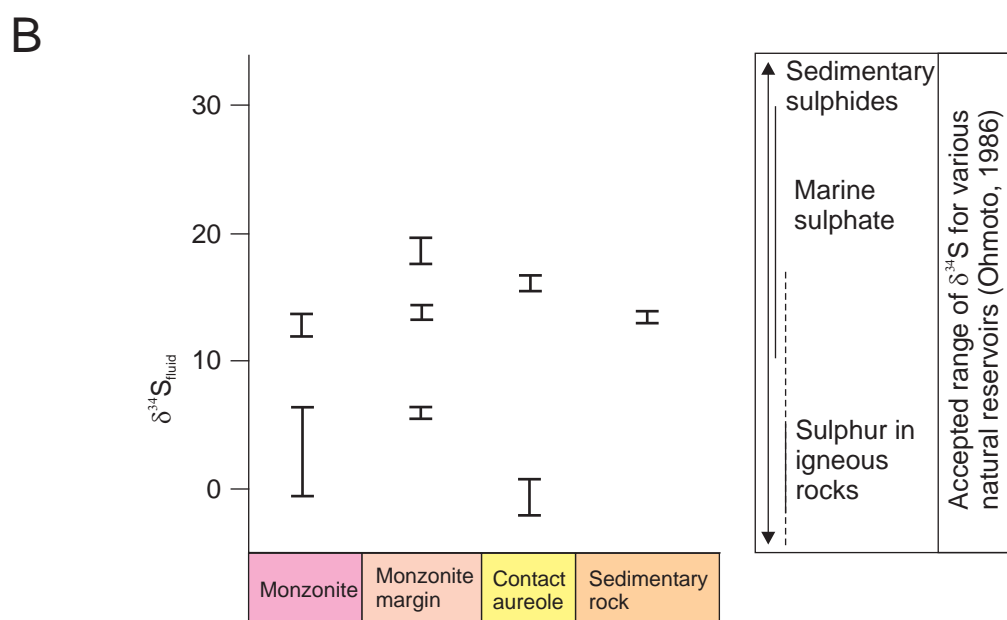
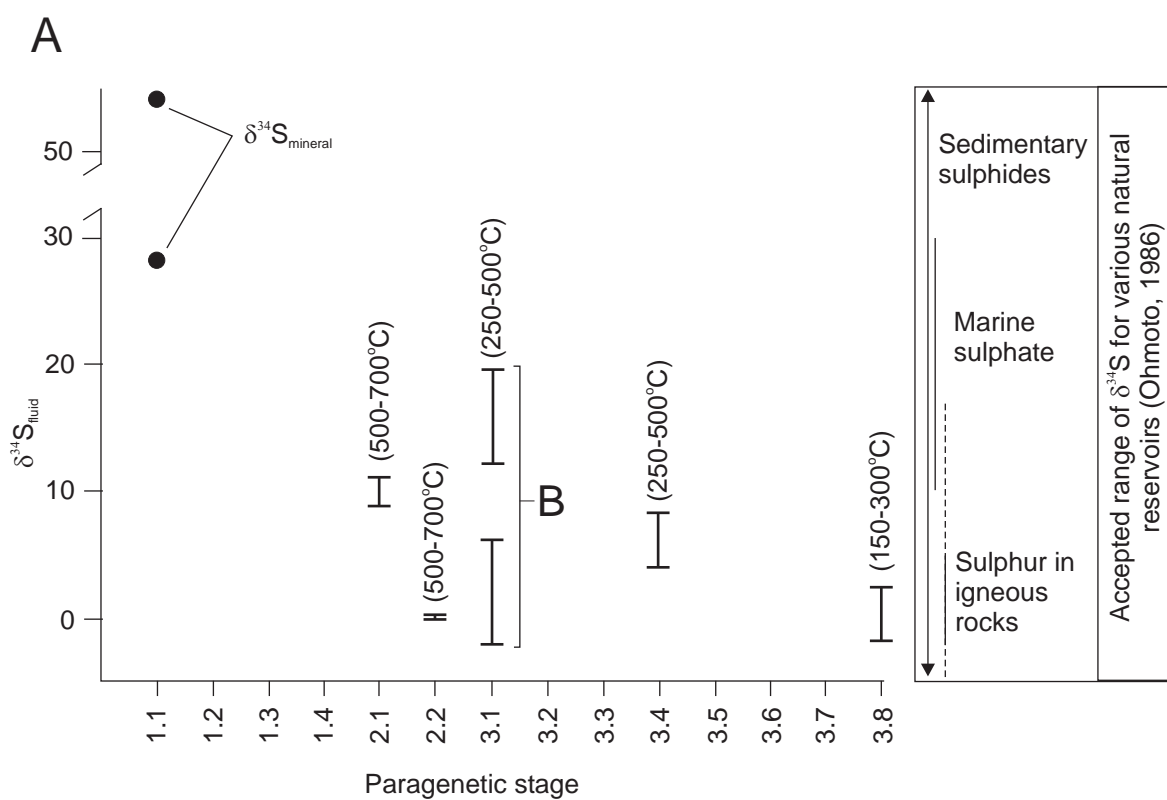


Figure 7.4 **Calculated $\delta^{34}\text{S}$ fluid values from Brewery Creek compared with various natural reservoirs.** The values were calculated at the temperatures shown. (A) A graph of all $\delta^{34}\text{S}$ fluid data. Pyrrhotite from monzonite (P-stage 2.1) shows values higher than those typically recorded for igneous rocks and likely reflects the incorporation of sedimentary rock into the melt. Pyrite bearing veins show a 20 ‰ variation in isotope values that are equivalent with both magmatic and sedimentary values. Arsenopyrite (P-stage 3.4) and stibnite (P-stage 3.8) bearing veins record S isotope values similar to those calculated for most igneous rocks. Note the overall decline in isotope values with time. Note also the $\delta^{34}\text{S}$ mineral values for two early stage samples pyrite. The high isotope values indicate that early pyrite has a sedimentary or marine origin. (B) $\delta^{34}\text{S}$ fluid plotted with respect to sample location. The graph shows that most of the high $\delta^{34}\text{S}$ values were obtained from pyrite close to the margin of monzonite or hosted by sedimentary rock.



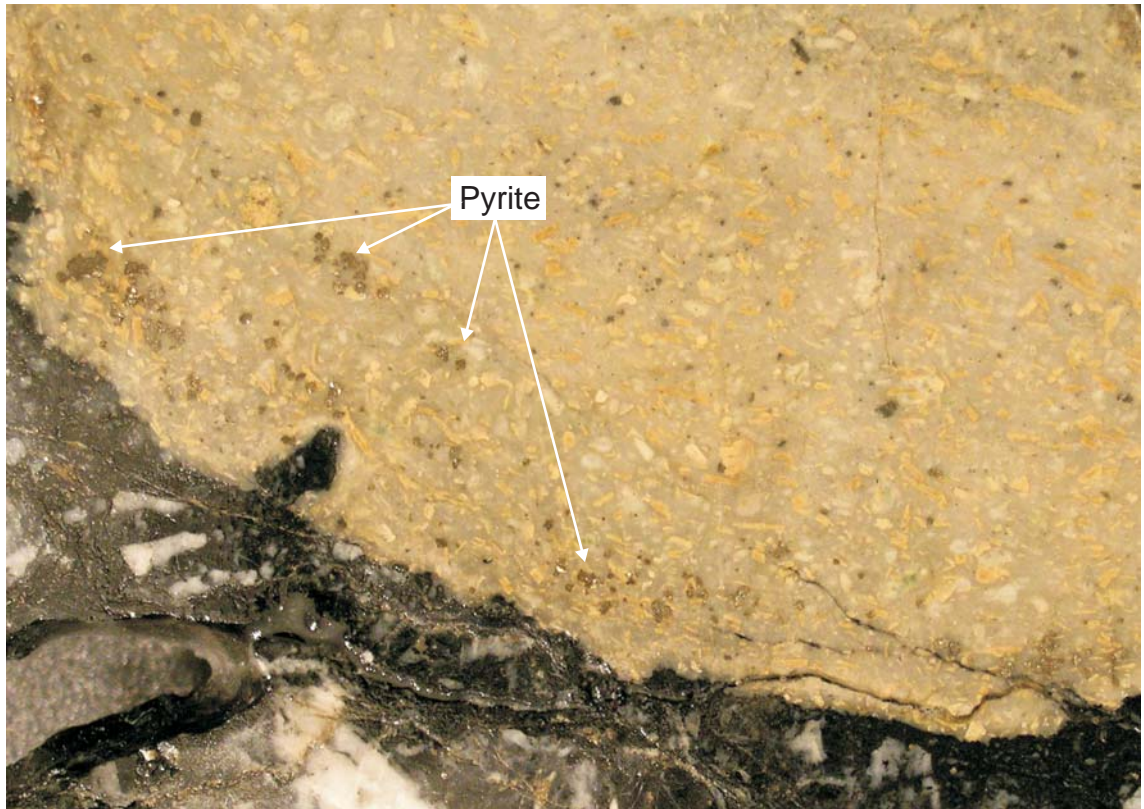
To resolve the source of S at Brewery Creek the data was plotted with reference to geological location such as pyrite hosted by a sill, at the margin of a sill, in the contact aureole and within sedimentary rock (Figure 7.4 b). The results show that the bulk of the $\delta^{34}\text{S}$ values $> 12\text{‰}$ are hosted in sedimentary rock or at the margin of the monzonite sills. Investigation of samples from the margin of sills shows that pyrite content increases toward the margin (Figure 7.5). Thus, the S in pyrite with calculated $\delta^{34}\text{S}_{\text{fluid}}$ values $> 11.0\text{‰}$ is probably partly derived from S in sedimentary rocks. Incorporation of sedimentary sulphur into monzonite sills could have occurred through sulphidation at sill margins (perhaps a consequence of convection associated with sill emplacement and associated leaching of S from sedimentary rocks) or via inclusion and assimilation of sedimentary rocks (e.g. Earn Group carbonaceous shale) as xenoliths in the monzonite sills or the precursor magma. $\delta^{34}\text{S}_{\text{fluid}}$ values -2.0 to 6.5‰ calculated from pyrite reflect a predominantly magmatic source of S.

Sulphur isotope values calculated for P-stages 3.4 and 3.8 are lower than those calculated for pyrrhotite from monzonite. Most hydrothermal fluids only transport only a small quantity of S (<1 mole / kg H_2O) and S isotope values of the hydrothermal fluid are easily shifted by interaction with wall rocks or S-bearing mineral precipitation (Ohmoto, 1986). Thus, the lower $\delta^{34}\text{S}_{\text{fluid}}$ values for stage 3.4 and 3.8 are likely sourced from the same reservoir as the pyrrhotite, which is consistent with a magmatic source of sulphur.

7.6 A genetic model for mineralisation at Brewery Creek

The isotope data documented above provide evidence for significant input of magmatic fluids into the mineralising system at Brewery Creek. The calculated fluid compositions are consistent with an initial mixed magmatic and crustal (sedimentary) fluid source that is replaced over time by a mixed magmatic and evolved meteoric fluid source. Furthermore, temperatures calculated for subsequent paragenetic stages decrease over time. These observations are most consistent with well-documented processes associated with magma emplacement, convection, and contact metamorphism. Thus a genetic model for mineralisation is described that is based on emplacement of felsic magma and subsequent cooling of the associated hydrothermal system (Figure 7.6). This model is supported by the spatial and temporal association of mineralisation at Brewery Creek to TPS igneous rocks that were demonstrated to be responsible for Au-mineralisation elsewhere in the Yukon and Alaska (e.g. Lang et al., 2000).

Figure 7.5 **A photo of the margin of a monzonite sill.** Note that the pyrite content increases toward the margin. This suggests sulphidation of the sill by fluids derived from the wall rocks.



0 1 2
Centimeters

The first stage in this genetic model is pluton emplacement and subsequent intrusion of monzonite sills into deformed Selwyn Basin and Earn Group stratigraphy. Crystallisation and thermal metamorphism occurred at temperatures of 500 to 700 °C. Monzonite sills that crop out along the Reserve Trend play an important role as host rocks for mineralisation but structural relationships indicate that they are not the direct source of metals, heat, or fluids. Thus, the presence of a source pluton at depth is implied. The nature of this pluton is unknown, however, the chemistry of TPS intrusions at Brewery Creek indicate that the source pluton is likely to be a reduced, alkalic to sub-alkalic, and metaluminous I-type intermediate to felsic intrusion.

Deformation at Brewery Creek and links to regional deformation were discussed in Chapter 3. Much of the early structural history is irrelevant to this model, however, normal reactivation on pre-existing thrust faults localised sill emplacement and mineralisation along what is now the Reserve Trend and must have played a key role in focussing magma and subsequent mineralising fluids. Thus, the down dip extension of thrust faults mapped at Brewery Creek were probably cut by a large magma chamber and subsequently acted as a pathway for exsolved magma and other fluids. E-W extension dominated the local structural regime during magma emplacement and extension is interpreted to have continued after the last sulphide-bearing veins were formed (Section 7.2).

The tectonic setting during the intrusion of middle Cretaceous igneous rocks in the Yukon, and therefore also at Brewery Creek, is poorly understood. Thompson et al. (1999) and Flannigan et al. (2000) suggest that the Tombstone plutonic suite was emplaced into continental crust in a back-arc or foreland setting well removed from convergent margins. Lang et al. (2000) concur with this assessment and further suggest that the distribution and geochemical characteristics of the Cretaceous intrusive rocks is consistent with their formation resulting from subduction related magmatism in a southwest facing continental magmatic arc. Most recently, Mair et al. (2006) suggested that middle Cretaceous igneous rocks were emplaced in a post-collisional, tensional regime. This model would accommodate the observed extension at Brewery Creek and thus emplacement of intrusive rocks and subsequent mineralisation at Brewery Creek most likely post-dated the major Jura-Cretaceous orogeny.

Figure 7.6 A genetic model for mineralisation at Brewery Creek. (A) Pluton emplacement and subsequent intrusion of monzonite sills into deformed Selwyn Basin and Earn Group stratigraphy. Structural relationships indicate that monzonite sills are not the main source of metals, heat, or fluids for mineralisation and thus, the presence of a source pluton at depth is implied. Reactivated thrusts mapped at Brewery Creek are interpreted to have acted as a pathway for magma and other fluids. E-W extension dominated the local structural regime during magma emplacement and extension is interpreted to have continued after the last sulphide-bearing veins were formed. (B) Pyrite-quartz-carbonate-roscelite-kaolinite mineralisation formed from a mixed magmatic and sedimentary source of fluids and produced disseminated mineralisation around steep veins and faults. The fluids that formed these veins likely followed the same structural pathways as the magma that formed the sills. (C) Structural constraints on vein formation indicate that the sills must have crystallised prior to being cut by veins. Petrographic evidence at Brewery Creek suggests that sedimentary S may have been incorporated into sills via sulphidation likely driven by convection (B and D). The precipitation of pyrite was controlled by sulphidation reactions as evidenced by pyrite preferentially replacing carbonate altered mafic phenocrysts (typically biotite) along mineral cleavage seams (E). The narrow range in calculated $\delta^{13}\text{C}_{\text{fluid}}$ suggests that the majority of C was derived from a magmatic source.

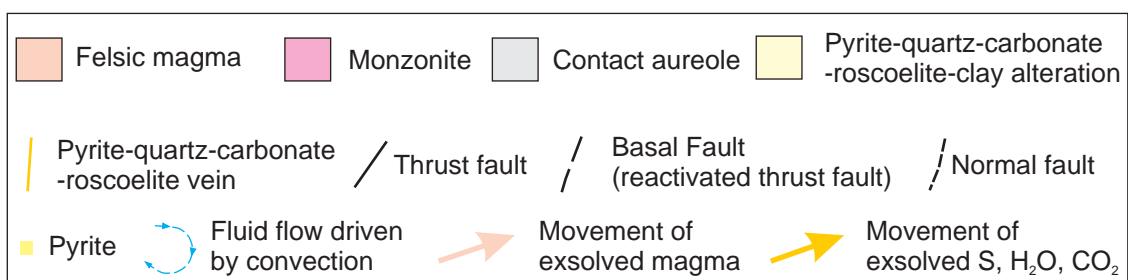
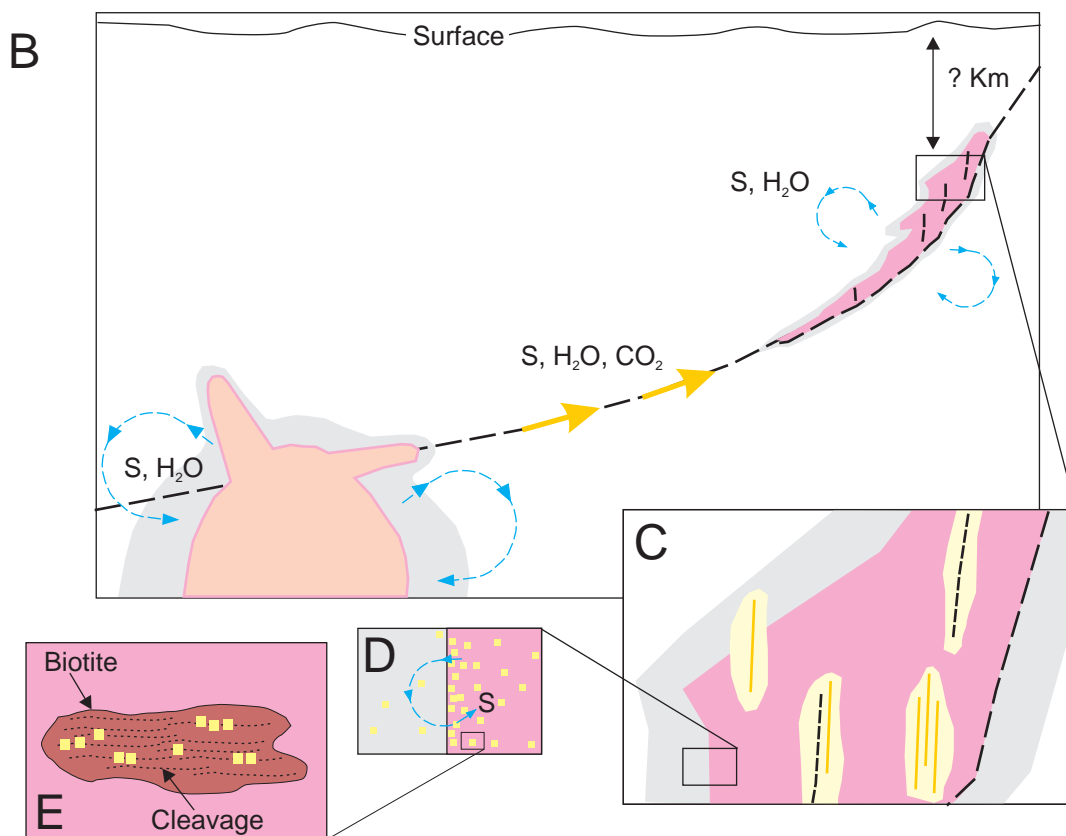
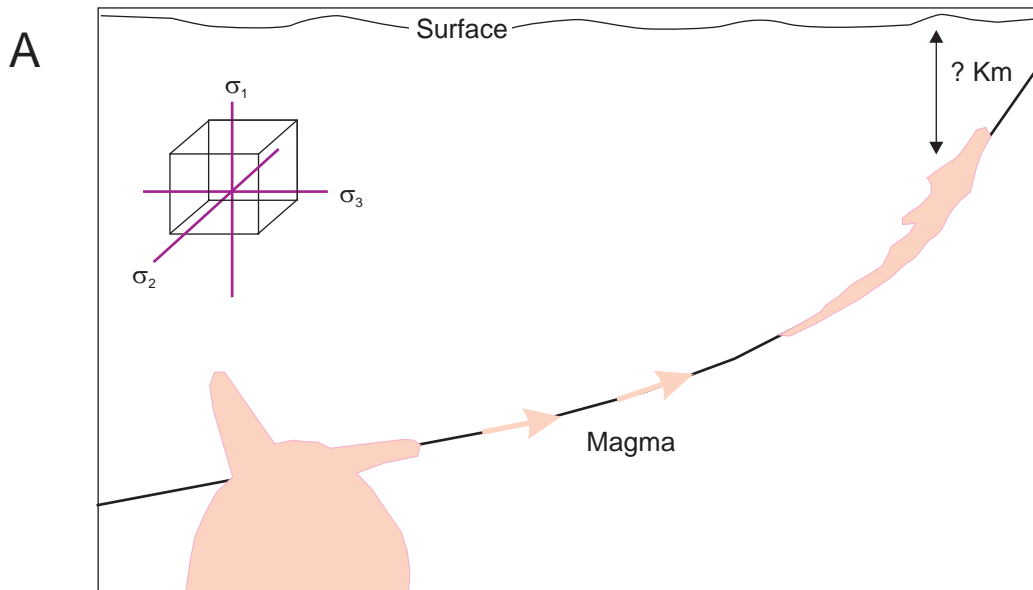
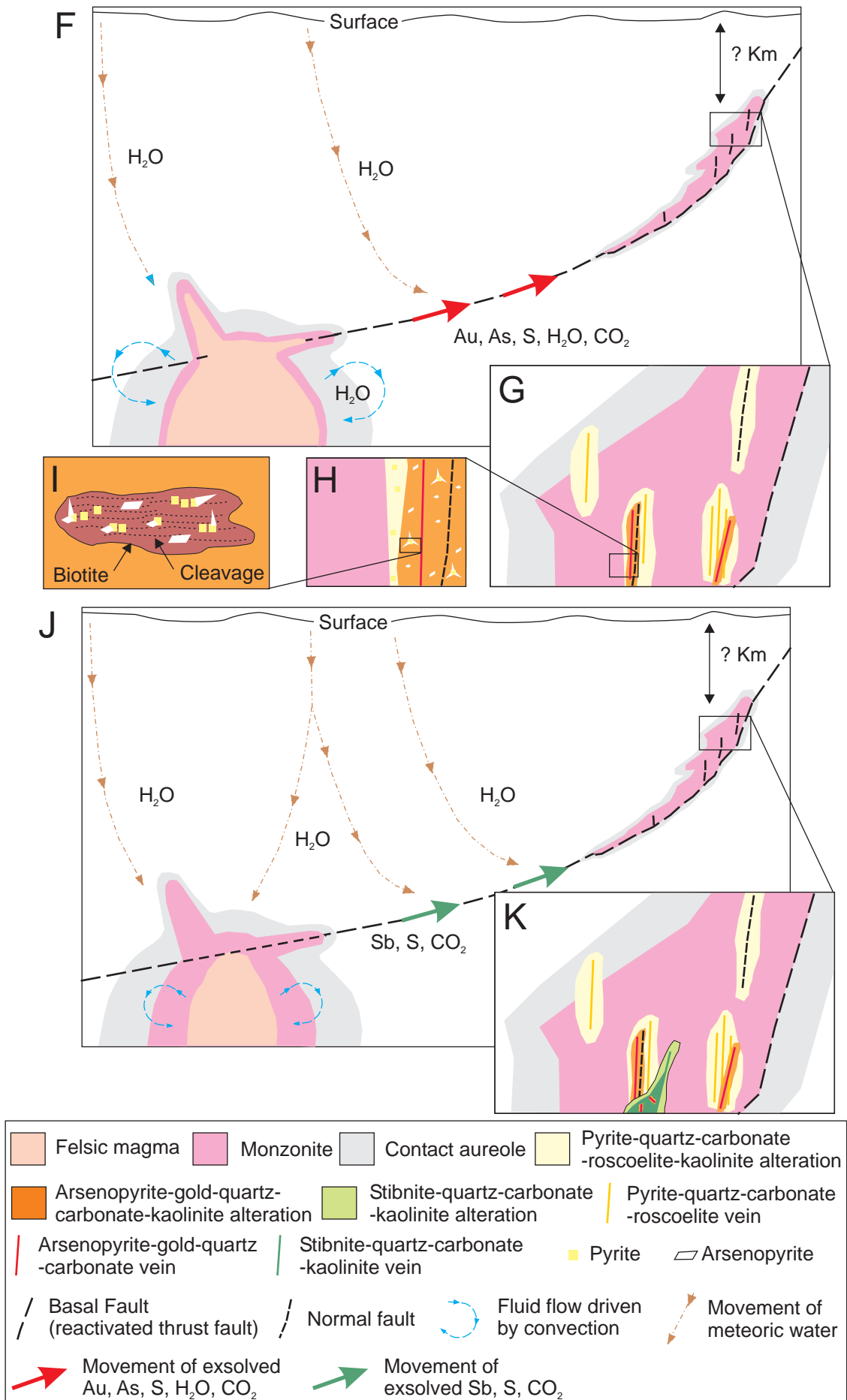


Figure 7.6 A genetic model for mineralisation at Brewery Creek (continued).

(F) P-stage 3.4 gold - arsenopyrite -carbonate - quartz – kaolinite mineralisation. Calculated O, C, and S fluid values for P-stage 3.4 indicate a dominantly magmatic source for C and S and a mixed magmatic and meteoric source for O. The absence of evidence for S input from sedimentary rocks and the mixed magmatic and meteoric signature of O implies that the hydrothermal system has evolved. This can be attributed to cooling and progressive crystallisation of the magma chamber at depth, which should limit magmatic fluid circulation and the amount wall rock S incorporated into the magma chamber. Incorporation of meteoric water would be aided by collapsing thermal gradients and percolation in an extensional structural regime. Veins associated with this stage are steeply dipping and cut P-stage 3.1 pyrite alteration (G). Arsenopyrite typically overgrows pyrite (H and I) indicating that arsenopyrite, and by association Au, precipitation was related to sulphidation reactions. If some of the S was sourced from pyrite then the early pyrite alteration should be considered an integral step in the mineralisation process at Brewery Creek. (J) P-stage 3.8 stibnite-quartz-carbonate-kaolinite mineralisation. Calculated O, C, and S fluid isotopic values for P-stage 3.8 indicate a magmatic source for C and S and a dominantly meteoric source for O. The presence of P-stage 3.8 mineralisation along the Reserve Trend suggests that fluids were likely focussed by the same faults that controlled sill emplacement. Stibnite-bearing veins are oriented sub-parallel to P-stage 3.1 and 3.4 veins (K) and therefore the extensional structural regime present during sill emplacement and Au-mineralisation was most probably active during P-stage 3.8.



Pyrite-quartz-carbonate-roscoelite-kaolinite (after muscovite or illite – see Chapter 4) mineralisation at temperatures of ~ 400 °C followed dyke and sill emplacement. The wide range of calculated fluid values for $\delta^{34}\text{S}$ and $\delta^{18}\text{O}$ indicate a mixed magmatic and sedimentary source of fluids. This is consistent with contact metamorphism and convection associated with cooling magma. Incorporation of sedimentary sulphur into monzonite sills could have occurred through sulphidation at sill margins or via inclusion and assimilation of sedimentary rocks as xenoliths in the monzonite sills or the precursor magma. A magmatic contribution to stage 3.1 fluids is also evidenced by the narrow range in $\delta^{13}\text{C}_{\text{fluid}}$ calculated from carbonate minerals in P-stage 3.1 veins that are consistent with a magmatic source.

The hydrothermal fluids exsolved from the magma chamber at depth to form P-stage 3.1 veins and alteration were reduced, CO_2 -rich and near neutral in pH. The precipitation of pyrite was the result of sulphidation reactions as evidenced by pyrite preferentially replacing carbonate altered mafic phenocrysts (typically biotite) along mineral cleavage seams. In this situation Fe in the wall rock, and specifically in mafic phenocrysts, has reacted with reduced S sequestered from the hydrothermal fluid. Sulphidation of monzonite is further supported by geochemical data (Chapter 5) that shows no significant increase in Fe concentration from unaltered to altered samples despite the obvious increase in Fe-sulphide content. The predominance of K-bearing illite and kaolinite relative to albite or Fe-Al silicates in alteration zones implies that the K/Na ratios were high and therefore the fluid was comparatively rich in K. Comparison of unaltered and altered samples clearly shows K addition and Na depletion (Chapter 5). Potassium-bearing clays likely formed through replacement of feldspars and as a direct result of sulphidation of biotite. Sodium loss can be directly attributed to destruction of plagioclase feldspars through carbonate alteration.

P-stage 3.1 was subsequently overprinted by P-stage 3.4 gold - arsenopyrite - carbonate - quartz - kaolinite. Pyrite and arsenopyrite were not observed to coexist because arsenopyrite was consistently observed as overgrowths on pyrite. Similarly, stibnite from P-stage 3.8 overprints arsenopyrite and pyrite but there is no evidence of equilibrium between these phases. Thus it appears that mineralisation occurred as a series of discrete events or pulses of fluid rather than evolution of a single fluid initially exsolved when P-stage 3.1 veins formed.

Calculated O, C, and S fluid values for P-stage 3.4 are restricted compared with P-stage 3.1 and are consistent with a dominantly magmatic source for C and S and a

mixed magmatic and meteoric source for O. The absence of evidence for S input from sedimentary rocks and the mixed magmatic and meteoric signature of O implies that the hydrothermal system has evolved. This likely reflects the cooling of the magma chamber at depth and associated collapse in thermal gradients that would reduce magmatic fluid circulation and therefore limit the amount wall rock S incorporated into the melt. The incorporation of meteoric water into the system would have been aided by favourable thermal gradients and percolation in an extensional structural regime.

The hydrothermal fluids responsible for Au-mineralisation are comparable in composition to P-stage 3.1 fluids (i.e. reduced, CO₂ rich and near neutral in pH). The precipitation of arsenopyrite was the result of sulphidation reactions analogous to P-stage 3.1 except arsenopyrite preferentially overgrows pyrite. This suggests that the Fe and potentially S in pyrite has reacted with As, and by association Au, sequestered from the hydrothermal fluid to produce arsenopyrite. It is uncertain how much S was carried by P-stage 3.4 hydrothermal fluids. Gold was likely transported as a bisulphide complex, however, far more sulphur would be required to form arsenopyrite than would be required to transport Au. If some (almost all?) of the S was sourced from pyrite then pyrite alteration should be considered an integral step in the mineralisation process at Brewery Creek.

The final stage of sulphide mineralisation at Brewery Creek was stibnite-quartz-carbonate-kaolinite (stage 3.8). Temperature estimates of between 150 and 300 °C were calculated from mineral pairs and fluid inclusions (Dunne, 1995). Calculated O, C, and S fluid isotopic values for P-stage 3.8 indicate a magmatic source for C and S and a dominantly meteoric source for O. The estimated temperatures and calculated isotope values are consistent with progressive crystallisation of the magma chamber, associated collapsing thermal gradients, and influx of meteoric water. Mineral assemblages indicate that hydrothermal fluids associated with P-stage 3.8 veins were most likely high in CO₂ and had a near neutral to moderately acidic pH. All stibnite is vein or breccia hosted and therefore precipitation is not controlled by sulphidation reactions. The common open space fill textures indicate that a drop in pressure, combined with temperature decrease, may be a feasible mechanism.

7.7 Classification of the Brewery Creek gold deposit

The Brewery Creek gold deposit has been variably classified by a number of authors. Diment (1995) cited the low sulphide content and Ag-As-Au-Hg-Sb geochemical signature to classify Brewery Creek as an adularia-sericite epithermal deposit. Decalcification and silicification in the North Slope zone led Poulsen et al. (1996) to discuss similarities between Brewery Creek and Carlin style mineralisation. Hart et al. (2002) partitioned gold mineralisation along the Tintina Gold Belt into three broad categories; intrusion-centred, shear-related, and epizonal. They classified Brewery Creek, Donlin Creek, and True North as epizonal in deference to a lack of clear genetic links with causative intrusions. The majority of recent studies have classified Brewery Creek as an intrusion-related gold deposit primarily based on temporal and spatial links with mid-Cretaceous intrusions, tectonic setting and geochemical signature (Thompson et al., 1999; Hart et al., 2000; Lang et al., 2000 a; Thompson and Newberry, 2000; Lang and Baker 2001). However, definitive links to magmatism were not established.

Carlin type gold deposits are characterised by carbonate dissolution, argillic alteration, sulphidation and silicification of calcareous sedimentary rocks (Hofstra and Cline, 2000). There is a broad spatial association between calc-alkaline subduction-related magmatism and mineralisation, however, no direct genetic links have been identified. Isotopic data suggests a mixed meteoric, metamorphic, and sedimentary fluid source (Hofstra et al., 1999). At Brewery Creek carbonate dissolution, argillic alteration, sulphidation and silicification of calcareous sedimentary rocks is present at the North Slope zone but mineralisation along the Reserve Trend is hosted by monzonite sills and carbonaceous rather than calcareous sedimentary rocks. There are also clear spatial, temporal, and genetic links with magmatism as evidenced by paragenetic, structural and isotopic data.

In Carlin deposits Au is typically hosted within arsenian pyrite and marcasite as sub-micron sized inclusions or in solid solution (Fleet and Mumin, 1997; Cline, 2000). Calcite, orpiment, realgar, quartz, stibnite, pyrite, marcasite, and barite are the most common open space filling minerals. Gold is similarly hosted by arsenopyrite and arsenian pyrite at Brewery Creek and calcite, quartz, stibnite and pyrite occur as vein fill. However, marcasite, orpiment, and realgar were not observed. The common late, low temperature opaline silica and chalcedony in Carlin deposits are absent at Brewery

Creek. The dominant geochemical signature of Carlin mineralisation (Au-As-Sb-Hg) and low base metal content is analogous to mineralisation at Brewery Creek and at both locations sulphidation of wall rock Fe is thought to be a key Au-depositional mechanism (Hofstra et al., 1991; Simon et al., 1999).

Low sulphidation epithermal deposits have been thoroughly documented, with the current understanding aided by deposit formation in active environments like the Broadlands-Ohaaki geothermal field in the Taupo Volcanic Zone, New Zealand (Browne, 1969; Henley and Ellis, 1983; Henley, 1985; White and Hedenquist, 1990, 1995; Hedenquist et al., 2000; Cooke and Simmons, 2000; Weissberg et al., 1979; Simmons and Browne, 2000). Low sulphidation epithermal deposits are characterised by quartz - adularia - carbonate - sericite alteration assemblage. Gold typically occurs as electrum in association with quartz and/or chalcedony plus lesser but variable amounts of adularia, calcite, rhodochrosite, illite or sericite, chlorite, pyrite, base metal sulphides, and silver sulfosalts. Common vein textures include lattice calcite or quartz, colloform and crustiform bands and comb quartz. Alteration and vein mineral assemblages are consistent with vein formation from a reduced, near-neutral pH, low salinity fluid and measured temperatures are generally less than 300°C. The waters that precipitate low sulphidation epithermal mineralisation have an isotopic signature that is consistent with a meteoric source for water and magmatic source for sulphur and carbon.

Mineralisation at Brewery Creek displays alteration assemblages, fluid geochemistry, and fluid sources that are typical of low sulphidation environments, however, several significant differences are apparent. Most notable is the lack of similar vein textures at Brewery Creek that typify epithermal environments and higher concentrations of CO₂ in the fluids that formed the veins. Appreciable base metal sulphides and silver sulfosalts that are common in low sulphidation deposits are absent at Brewery Creek.

Orogenic gold deposits are normally partitioned into Archaean and Phanerozoic deposits (Groves et al., 1998; Hagemann and Cassidy, 2000; Bierlein and Crowe, 2000). Phanerozoic orogenic deposits are characterised by Au-only mineralisation characteristically within veins of quartz with subordinate carbonate, feldspar, mica, pyrite, arsenopyrite and low base metal contents. Gold is typically free but may also be contained within arsenopyrite and arsenian pyrite (e.g. Ashley et al., 2000). These deposits are typically located proximal to major accretionary boundary structures in orogenic belts and commonly form in a compressive structural regime post-peak

metamorphism and deformation and pre-magmatism (Bierlein and Crowe, 2000). Some features of Phanerozoic deposits are comparable with mineralisation at Brewery Creek including a Au-As-Ag-Sb-Hg geochemical signature, low base metal content, significant CO₂ in the ore-forming fluid, and a sericite-carbonate-pyrite alteration assemblage. However, Brewery Creek differs from these deposits in plate tectonic and structural setting, wall-rock rather than vein-hosted gold, and most notably timing with respect to magmatism.

Geological and geochemical characteristics of the Brewery Creek deposit most closely resemble those described for intrusion-related gold systems (Lang et al., 1997, 2000; Thompson et al., 1999; Thompson and Newberry, 2000; Lang and Baker, 2001). Similarities between Brewery Creek and IRGS include (1) gold as a principal commodity, (2) a spatial, temporal and genetic association with metaluminous intrusions of intermediate to felsic composition, (3) the presence of carbonic hydrothermal fluids, (4) a reduced ore mineral assemblage that typically includes arsenopyrite, pyrrhotite and pyrite, and (5) a continental setting well inboard of inferred or recognized convergent plate boundaries. Features of IRGS that were not observed at Brewery Creek are (1) most of the gold deposits are sited either within a pluton or in the contact aureole, (2) a Au-Bi-Te-As geochemical signature, and (3) early feldspathic alteration. Thompson et al. (1999) and Lang et al. (2000) proposed a model for IRGS that highlights vertical and lateral zonation of ore environment and mineralisation styles with respect to a hypothetical central mineralising pluton (Figure 2.6). They state that the styles of gold deposits in IRGS are strongly influenced by depth of formation, host rock composition and the presence or absence of structures. Thus the differences between Brewery Creek and other IRGS may be accounted for by mineralisation at Brewery Creek occurring in a distal and/or shallow location with respect to the mineralising pluton. A shallow depth of mineralisation at Brewery Creek was also suggested by Baker (2002).

Within the Tintina Gold Belt, Brewery Creek strongly resembles Donlin Creek (Ebert et al., 2000; Goldfarb, et al., 2004). Both deposits are characterised by (1) felsic intrusive host rocks that cut interbedded greywacke and shale, (2) quartz-carbonate-illite-pyrite-arsenopyrite-stibnite veins and alteration associated with extensional fractures, (3) gold incorporated within arsenopyrite, (4) paragenetically late stibnite, and (5) extensive sulphidation and carbonatisation associated with mineralisation. However, Donlin Creek contains an order of magnitude more gold than Brewery Creek and measured

isotope values at Donlin Creek ($\delta^{34}\text{S}$ of -16 to -8 ‰; $\delta^{18}\text{O}$ of 11 - 18 ‰) contrast with those measured at Brewery Creek ($\delta^{34}\text{S}$ of 6 to 20 ‰; $\delta^{18}\text{O}$ of 8 to 14 ‰).

Goldfarb et al. (2004) suggest that the geological and geochemical features of Donlin Creek most closely resemble those associated with orogenic gold deposits. They cite the Ag-As-Au-Hg-Sb geochemical signature, Au/Ag ratio of 1 or higher, low base metal content, significant CO_2 , isotopically high oxygen, and alteration assemblage as features consistent with an orogenic model. However, they also state that the depth and temperature of mineralisation at Donlin Creek indicate high geothermal gradients that might support an intrusion-related gold deposit classification. Goldfarb et al. (2004) further describe a preferred genetic model that incorporates gold bearing fluids that have been sourced from devolatilisation of underlying sedimentary rock dominated terranes. Such a model is not appropriate for mineralisation at Brewery Creek as C, S and O isotopes preclude a metamorphic source of fluids.

7.8 Further exploration

Conceptual targets at Brewery Creek

There are several potential targets for further exploration Brewery Creek. These include:

- (1) **Down dip extension of the Reserve Trend.** The $> 20\text{Moz}$ Donlin Creek gold deposit is similar to Brewery Creek in structural setting, geochemical signature and mineral paragenesis and there is the potential for a comparable Au resource at Brewery Creek. The structural model outlined in this thesis suggests that mineralisation should diminish at depth. However, significant mineralisation at depth could be related to a change in the dip of the Basal fault (i.e. if the fault steepens) or if there is a flexure in the strike. Furthermore, the proposed Au precipitation mechanism (sulphidation) indicates that there are no depth constraints on mineralisation unlike boiling precipitation mechanisms.
- (2) **Parallel hydrothermal systems.** The mapped repetition of thrust faults indicates that there is the potential for a similar system hosted by other faults that trend sub-parallel to the Reserve Trend.

- (3) **Intersection of NE and E trending structures.** Mineralisation trends in the open pits at Brewery Creek indicate that both NE and E oriented structures are favourable for mineralisation. The intersection of these trends may result in the development of high-grade shoots. Furthermore, the mineralised NE oriented fault in Blue Pit indicates that NE striking structures (D-stage 6 faults) may be mineralised elsewhere on the property.
- (4) **Carlin style mineralisation in the Brewery Unit.** Poulsen et al. (1997) suggested that Au mineralisation at North Slope is comparable to Carlin style mineralisation and Viceroy explored for this style of mineralisation in the Steel Formation. The previously unrecognised Brewery Unit also has the potential to host Carlin Style mineralisation. Of particular note is that strongly decalcified siltstone crops out along the road to the Classic Zone.
- (5) **Au-skarn.** Minor tremolite - pyrrhotite - pyrite - arsenopyrite - Au skarn mineralisation has been documented in the Schooner Zone at Brewery Creek. This mineralisation is clearly associated with the monzonite sills that crop out through the centre of the property. Gold-skarn mineralisation could also be targeted where monzonite sills intersect the Brewery Unit and/or the Rabbitkettle Formation.
- (6) **Tintina-related Au mineralisation.** The proximity of Brewery Creek to the nearby Tintina Fault has prompted numerous questions about the role of this fault in localising mineralisation at Brewery Creek. This thesis has shown that the Tintina Fault is unlikely to have played a direct role in mineralisation along the Reserve Trend. However, mineralisation at the Classic Zone may be related to faults that were active during movement on the Tintina Fault. Thus, structures that trend sub-parallel to the Tintina Fault may host significant Au mineralisation.

Exploration parameters for Brewery Creek style mineralisation

There are several key differences between mineralisation at Brewery Creek and other previously described intrusion-related gold deposits. As such, it is important to describe exploration parameters for Brewery Creek style mineralisation. Key parameters include:

- (1) **Presence of TPS intrusive rocks.** The bulk of mineralisation along the Reserve Trend is hosted by TPS monzonite sills and a TPS syenite pluton hosts mineralisation at the Classic Zone. Identification of TPS intrusive rocks can provide a simple first pass exploration criterion for ranking follow-up work.
- (2) **Location outside the contact aureole.** The bulk of the Au mineralisation at Brewery Creek lies outside any significant contact metamorphic aureole. Much of the previous exploration in the Yukon has been centred on plutons and their aureole. Mineralisation at Brewery Creek suggests that explorers may extend their focus outside these areas.
- (3) **Geochemical signature.** The geochemical signature of mineralisation is Au-As-Sb \pm Ag-Pb. Overall, elevated As (> 1000 ppm) is the best indicator of Au > 1 ppm with high concentrations of Sb in intrusive rocks and elevated levels of Ag and Sb in sedimentary rocks providing further indication of Au. It is interesting to note that Brewery Creek was discovered through the investigation of Hg anomalies. Detailed geochemical investigations show that there is no clear link between Au and Hg. However, Hg levels at Brewery Creek are elevated and therefore any geochemical exploration program should also flag elevated Hg.
- (4) **Favourable structural setting.** Property- and mine-scale structures have played a key role in localising mineralisation to produce a mineable resource. E and NE oriented structures are preferentially mineralised at Brewery Creek. At Clear Creek the mineralised structures trend E and NW (Stephens, 2003; Stephens et al., 2004) indicating that the orientation of structures favourable for mineralisation may be controlled by both regional and local stress regimes. When investigating the mineralisation potential of structures it is important to consider if the structures were active and able to dilate during mineralisation. In addition, the presence of long-lived faults that possibly extend down dip for several kilometres is important, as these structures have the potential to access significant fluid reservoirs and focus mineralisation. Long-lived faults should be considered highly prospective if they have been intruded by TPS igneous rocks.

- (5) **Invisible gold.** Mineralisation at Brewery Creek is characterised by Au-bearing arsenopyrite and arsenian pyrite. Therefore traditional prospecting methods (i.e. gold panning) will not identify Brewery Creek style sulphide mineralisation and new deposits may be found in previously unworked areas.
- (6) **System footprint.** Any exploration strategy must account for the physical size of the deposit that they are looking for. Mineralisation along the Reserve Trend extends for more than 12 Km along strike but is at most 1 km wide and in some areas < 200 m wide.

7.9 Conclusions

This Ph.D. study has provided an extensive structural and geochemical investigation into the genesis of the Brewery Creek gold deposit. Numerous conclusions can be drawn from this work with the main points summarised below.

1. Palaeozoic sedimentary and volcanic rocks of the Selwyn Basin and the Earn Group and Cretaceous intrusions of the TPS underlie the Brewery Creek property. The stratigraphy includes rocks of the Rabbitkettle Formation, Menzie Creek volcanic unit (informal), Road River Group including the Duo Lake Formation and Steel Formation, Brewery unit (informal), and Earn Group. Outcropping lithologies are calcareous phyllite, basalt, dolerite, chert, calcareous sandstone, fossiliferous limestone, chert pebble conglomerate and variably carbonaceous sandstone, siltstone and shale.
2. The Early Devonian Brewery unit, previously unrecognised within the Selwyn Basin stratigraphy, is comprised of interbedded units of siltstone, chert, bioclastic limestone, and displays a distinctive banded appearance. The Brewery unit is interpreted to conformably overlie the Steel Formation and be unconformably overlain by the Earn Group.
3. A number of mid-Cretaceous intrusions crop out at Brewery Creek and are correlated with the TPS. Geochemical analysis indicates that these igneous rocks are reduced, alkalic, and metaluminous I-type intrusions that can be classified as monzonite, syenite, and hornblende gabbro. Monzonite was further

partitioned into quartz-biotite and biotite monzonite based on the presence or absence of quartz eyes.

4. Regional metamorphic minerals are not evident in most of the rocks at Brewery Creek. Contact metamorphic aureoles are present around most intrusive rocks but can be difficult to distinguish in the field. Where TPS intrusions cut rocks of the Steel Formation or Brewery unit distinct silicified and/or calc-silicate zones are developed and comprise grossular garnet, diopside, hedenbergite, wollastonite, sphene, scapolite, calcite, biotite, microcline, quartz, alkali feldspar, chlorite and rare tourmaline. Monzonite sills that intrude Earn Group rocks show little evidence of contact metamorphism. One occurrence of contact metamorphosed Earn Group shale immediately adjacent to a monzonite sill was found in drill core and contained a number of relict andalusite porphyroblasts.
5. Sedimentary and volcanic rocks that crop out at Brewery Creek have been multiply deformed and record a structural history that has been punctuated by several episodes of ductile and brittle deformation. Faults and folds of all scales are present, but there is poor development of cleavage or other micro-scale fabrics. The overall structure of the property is that of a NNE trending arch of thrust sheets. The rocks in each thrust sheet have been deformed into upright to steeply inclined, open to tight, variably NE-SW, E-W, NW-SE trending and plunging folds. Eight distinct structural events have been recognised at Brewery Creek and include from oldest to youngest NW trending folds (stage 1), SW vergent thrust faults (stage 2), km-scale folding (stage 3), km-scale thrusting (stage 4), NNE trending folding (stage 5), NE oriented faults (stage 6), normal faults (stage 7), and NW oriented strike slip faults (stage 8).
6. The bulk of the gold mineralisation at Brewery Creek occurs along a linear zone of intrusions and faulting termed the Reserve Trend. Mineralisation in this zone is hosted by TPS intrusions and sedimentary rocks of the Earn Group and can be partitioned into four broad paragenetic stages; (1) pre-TPS intrusion, (2) syn-TPS intrusion, (3) post-TPS intrusion, and (4) weathering. The pre-TPS intrusion stage encompasses sedimentary rock hosted disseminated and massive pyrite, carbonate veins and breccia, quartz veins, and stylolites. The syn-TPS intrusion stage comprises the emplacement of TPS intrusions and the development of contact aureoles. Gold mineralisation occurred post-TPS intrusion and this stage includes pyrite \pm quartz \pm carbonate \pm roscoelite veins,

quartz only veins, Au-bearing arsenopyrite \pm quartz \pm carbonate veins, several stages of brecciation and stibnite \pm quartz \pm carbonate \pm kaolinite veins. The mineralisation history at Brewery Creek is relatively simple and appears to be unidirectional with no evidence for repeated or alternating stages of sulphide deposition.

7. Correlation matrices and factor analysis describe a Au-As-Sb \pm Ag, Pb element correlation. This relationship was documented in all lithologies and in all open pits suggesting that there was only one major Au-mineralising event at Brewery Creek. Elevated As (> 1000 ppm) is the best indicator of Au > 1 ppm with high concentrations of Sb in intrusive rocks and elevated levels of Ag and Sb in sedimentary rocks providing further indication of Au.
8. Isocon analyses of geochemical data indicate that enrichment of CO_2 , K_2O , MnO , and SO_3 and depletion Na_2O characterises alteration. This element mobility can be directly correlated to pervasive carbonate, kaolinite (after muscovite or illite) and pyrite alteration of biotite and feldspars in monzonite sills. CaO and Fe_2O_3 are comparatively immobile, which suggests that the Ca and Fe required to form calcite and pyrite respectively was sourced from destruction of plagioclase and biotite.
9. LA-ICP-MS analysis of sulphide phases indicates that the highest Au concentrations are hosted by arsenopyrite crystals with lower but significant levels of Au also found in arsenopyrite overgrowths on pyrite and pyrite overgrown by arsenopyrite. Higher Au grades were found in wall rock arsenopyrite and arsenian pyrite than in vein hosted As-bearing sulphides.
10. Gold assay analysis and vein measurements from the open pits along the Reserve Trend highlight two distinct mineralised orientations; E and NE. These orientations are paralleled by a number of metre-scale, steeply dipping post-TPS faults and mineralisation is bound at depth by a moderately dipping, E-W striking normal fault, termed the Basal Fault.
11. Mineralisation occurred during extension. The Basal Fault is interpreted to represent a master fluid focussing structure developed in a site that was structurally prepared by earlier faulting (D-stage 4) and reactivated to produce normal dip-slip offset during extension. The smaller, variably oriented steeply

dipping faults would represent secondary structures that developed or reactivated (D-stage 6? and D-stage 7 faults) in response to movement along the Basal Fault and provided suitably oriented fluid pathways. The paucity of NE striking veins may be explained by mineralisation occurring in an extensional structural environment that contained a component of strike-slip.

12. Hydrothermal fluids associated with mineralisation were reduced, CO₂ rich and near neutral in pH. Gold was likely transported as a bisulphide complex and the predominance of Au-bearing wall rock arsenopyrite and arsenian pyrite emphasise the importance of sulphidation reactions as a Au precipitation mechanism. Rapid precipitation of arsenopyrite in non-equilibrium conditions may have further facilitated Au precipitation.
13. Isotope data provide evidence for significant input of magmatic fluids into the mineralising system at Brewery Creek. The calculated fluid compositions are interpreted to reflect an initial mixed magmatic and crustal (sedimentary) source that evolves to a mixed magmatic and meteoric fluid source.
14. The data presented in this thesis are consistent with a genetic model based on emplacement of felsic magma and subsequent cooling of the associated hydrothermal system. Exsolved fluids were focused by pre-intrusion structures into a favourable site for mineralisation that was distal from the source magma chamber. Therefore, Brewery Creek is interpreted to be an example of intrusion-related gold mineralisation in a distal setting relative to the mineralising pluton.



The End.....

REFERENCES

Abbott, J.G.

1993: Revised stratigraphy and new exploration targets in the Hart River area, southeastern Ogilvie Mountains. *In* Yukon Exploration and Geology, Exploration and Geological Services Division, Yukon, Indian and Northern Affairs Canada, pp. 13-23.

Abbott, J.G., Gordey, S.P., and Tempelman-Kluit, D.J.

1986: Setting of stratiform, sediment-hosted lead-zinc deposits in Yukon and northeastern British Columbia. *In* J.A. Morin (ed.), Mineral deposits of Northern Cordillera, Canadian Institute of Mining and Metallurgy, Special Volume 37, pp. 1-18.

Abbott, J.G., and Roots, C.F.

1992: Geological map of part of map sheets 116A/10 and 116A/11. Exploration and Geological Services Division, Yukon, Indian and Northern Affairs Canada, Open-File 1992-2, scale 1:50 000.

Abbott, J.G., and Roots, C.F.

1993a: Geological map of map sheet 116A/10. Exploration and Geological Services Division, Yukon, Indian and Northern Affairs Canada, Open-File 1993-7, scale 1:50 000.

Abbott, J.G., and Roots, C.F.

1993b: Geological map of Two Beaver Lake map area (116A/11). Exploration and Geological Services Division, Yukon, Indian and Northern Affairs Canada, Open-File 1993-8, scale 1:50 000.

Abercrombie, S.M.

1989: Petrology, geochronometry and economic geology: The Zeta tin-silver prospect, Arsenic Ridge, west central Yukon. Unpublished M.Sc. thesis, University of British Columbia, Vancouver, 226p.

Aitken, J.D., Cook, D.G., and Yorath, C.J.

1982: Upper Ramparts River (106G) and Sans Rapids (106H) map areas, District of Mackenzie. Geological Survey of Canada. Memoir 388, 48p.

Anderson, R.G.

1987: Plutonic rocks in the Dawson map area, Yukon Territory. *In* Current Research, Part A, Geological Survey of Canada, Paper 87-1A, pp. 689-697.

Argast, S. and Donnelly, T.W.

1987: The chemical discrimination of clastic sedimentary components. *Journal of Sedimentary Petrology*. Vol. 57, pp. 813-823.

Armstrong, R.L.

1988: Mesozoic and early Cainozoic evolution of the Canadian Cordillera. *Geological Society of America special paper* 218, pp. 55-92.

Asadi, H.H., Voncken, J.H.L., Kühnel, R.A., and Hale, M.

2000: Petrography, mineralogy and geochemistry of the Zarshuran Carlin-like gold deposit, northwest Iran. *Mineralium Deposita*, Vol. 35, pp. 656-671.

Arehart, G.B., Chrysosoulis, S.L., and Kesler, S.E.

1993: Gold and arsenic in iron sulphides from sediment-hosted gold deposits: implications for depositional processes. *Economic Geology*, Vol. 88, pp. 171-185.

Ashley, P.M., Creagh, C.J., and Ryan, C.G.

2000: Invisible gold in ore and mineral concentrates from the Hillgrove gold-antimony deposits, NSW, Australia. *Mineralium Deposita*, Vol. 35, pp. 285-301.

Bakke, A.A.

1995: The Fort Knox "porphyry" gold deposit: Structurally controlled stockwork and shear quartz vein, sulphide poor mineralization hosted by a Late Cretaceous pluton, east-central Alaska: In Schroeter, T.G., ed., Porphyry deposits of the northwestern Cordillera of North America: Canadian Institute of Mining and Metallurgy, Special Volume 46, p. 795-802.

Bakken, B.M., Hochella, M.F. Jr., Marshall, A.F., and Turner, A.M.

1989: High-resolution microscopy of gold in unoxidised ore from the Carlin Mine, Nevada. *Economic Geology*, Vol. 84, pp. 171-179.

Baker, T.

2002: Emplacement depth and carbon dioxide-rich fluid inclusions in intrusion-related gold deposits. *Economic Geology*, Vol. 97, pp. 1109-1115.

Baker, T., Mustard, R., Brown, V., Pearson, N., Stanley, C.R., Radford, N.W., and Butler, I.

2005: Textural and chemical zonation of pyrite at Pajingo: a potential vector to epithermal gold veins. *Geochemistry: Exploration, Environment, and Analysis*. Vol. 5, pp. 1-11.

Bamber, E.W., and Mamet, B.L.

1978. Carboniferous biostratigraphy and correlation, northeastern British Columbia and southwestern District of Mackenzie. *Geological Survey of Canada, Bulletin* 266, 65pp.

Barnes, H.L.

1979: Solubilities of ore minerals. In Barnes, H.L. (ed) *Geochemistry of hydrothermal ore deposits* 2nd edition. Wiley, New York, pp. 404-508.

Becker, U., Hochella, M.F., and Vaughan, D.J.

1997: The adsorption of gold to galena surfaces: calculation of adsorption/reduction energies, reaction mechanisms, XPS spectra and STM images. *Geochimica et Cosmochimica Acta*, Vol. 61, pp. 3565-3585.

Benning, L.G. and Seward, T.M.

1996: Hydrosulphide complexing of Au(I) in hydrothermal solutions from 150 to 400°C and 500 to 1500 bars. *Geochimica et Cosmochimica Acta*, Vol. 60, pp. 1849-1871.

Bhatia, M.R.

1983: Plate tectonics and geochemical composition of sandstones. *Journal of Geology*, Vol. 91, pp. 611-627.

Bierlein, F.P., Arne, D.C., McKnight, S., Lu, J., Reeves, S., Besanko, J., Marek, J., and Cooke, D.

1999: Wall-rock petrology and geochemistry in alteration halos associated with mesothermal gold mineralisation, central Victoria, Australia. *Economic Geology*, Vol 95, pp. 283-312.

Bierlein, F.P. and Crowe, D.E.

2000: Phanerozoic orogenic lode gold deposits. *Reviews in Economic Geology*, Vol 13, pp.221-244.

Blusson, S.L.

1971: Sekwi Mountain map area, Yukon Territory and district of Mackenzie. *Geological Survey of Canada, Paper* 71-22, 17p.

Boiron, M.-C., Essarraj, S., Sellier, E., Cathelineau, M., Lespinasse, M., and Poty, B.

1992: Identification of fluid inclusions in relation to their host microstructural domains in quartz by cathodoluminescence. *Geochimica et Cosmochimica Acta*, Vol. 56, pp. 175-185.

Bowen, N.L.

1928: The evolution of igneous rocks. Princeton University Press. 334 pp.

Boyle, R.W.

1979: The geochemistry of gold and its deposits (Together with a chapter on geochemical prospecting for the element). Geological Survey of Canada, Bulletin 280.

Breit, G.N.

1995: Origin of clay minerals associated with V-U deposits in the Entrada Sandstone, Placerville Mining District, southwest Colorado. *Economic Geology*, Vol. 90, pp. 407-429.

Brown, K.L.

1986: Gold deposition from geothermal discharges in New Zealand. *Economic Geology*, Vol. 81, pp 979-983.

Browne, P. R. L.

1969: Sulphide mineralisation in a Broadlands geothermal drill hole, Taupo volcanic zone, New Zealand. *Economic Geology*, Vol. 64, pp 156-159.

Bundtzen, T.K. and Miller, M.L.

1997: precious metals associated with Late Cretaceous-early Tertiary igneous rocks of southwest Alaska. *Economic Geology Monograph* 9, pp.242-286.

Cabri, L.J.

1992: The distribution of trace and precious metals in minerals and mineral products. *Mineralogical Magazine*, Vol. 56, pp. 289-308.

Cabri, L.J., Chryssoulis, S.L., de Villiers, J.P.R., Gilles Laflamme, J.H., and Buseck, P.R.

1989: The nature of invisible gold in arsenopyrite. *The Canadian Mineralogist*, Vol. 27, pp. 353-362.

Cabri, L.J., Newville, M., Gordon, R.A., Crozier, E.D., Sutton, S.R., McMahon, G., and Jiang, D.

2000: Chemical speciation of gold in arsenopyrite. *The Canadian Mineralogist*, Vol. 38, pp. 1265-1281.

Campbell, A.R. and Larson, P.B.

1998: Introduction to stable isotope applications in hydrothermal systems. In *Techniques in hydrothermal ore deposits geology*, Richards, J.P. and Larson, P.B. (eds.). *Reviews in Economic Geology*, Vol 10. pp. 173-193.

Campbell, R.B.

1967: Geology of Glenlyon map area, Yukon Territory. Geological Survey of Canada, Memoir 352, 92 p.+ maps

Cathelineau, M., Boiron, M-C., Holliger, P., Marion, P., and Dennis, M.

1989: Gold in arsenopyrite: crystal chemistry, location and state, physical and chemical conditions of deposition. *Economic Geology Monograph* 6, pp. 328-341.

Cathelineau, M., Boiron, M.C., Hollinger, P., Marion, P., and Denis, M.

1991: Hercynian gold-bearing quartz veins from western Europe. In Laderia, E.A. (ed), *Brazil Gold 91: The economics, geology, geochemistry and genesis of gold deposits*. Balkema, Rotterdam, pp. 115-119.

Cecile, M.P.

1982: The lower Palaeozoic Misty Creek Embayment, Selwyn Basin, Yukon and Northwest Territories; Geological Survey of Canada, Bulletin 335, 78p.

Cecile, M.P.

2000: The geology of the northeastern Nidderly Lake map area, east central Yukon and adjacent Northwest Territories. Geological Survey of Canada, Bulletin 553, 122p.

Cecile, M.P., and Abbott, J.G.

1992: Geology of the Nidderly lake map area, Yukon Territory – Northwest Territories. Geological Survey of Canada, Open File 2465, scale 1:250 000.

Chenery, S., Cook, J.M., Styles, M., and Cameron, E.M.

1995: Determination of three-dimensional distributions of precious metals in sulphide minerals by laser ablation microprobe-inductively coupled plasma-mass spectrometry (LAMP-ICP-MS). *Chemical Geology*, Vol. 124, pp. 55-65.

Cheng, Q., Agterberg, F.P., and Bonham-Carter, G.F.

1996: A spatial analysis method for geochemical anomaly separation. *Journal of Geochemical Exploration*, Vol. 56, pp. 183-195.

Chork, C.Y. and Salminen, R.

1993: Integrating a high breakdown option into discriminant analysis in exploration geochemistry. *Journal of Geochemical Exploration*, Vol. 48, pp 1-20.

Clauge, J.J.

1992: Quaternary glaciation and sedimentation. In: *Geology of the Cordillera Orogen in Canada*. Geological Survey of Canada, *Geology of Canada* no. 4, pp. 421-434

Clayton, R.N. and Mayeda, T.K.

1963: The use of bromine pentafluoride in the extraction of oxygen from oxides and silicates for isotopic analysis. *Geochimica et Cosmochimica Acta*, Vol. 27, pp. 43 – 52.

Clayton, R.N., O'Neil, J.R., and Mayeda, T.K.

1972: Oxygen isotope exchange between quartz and water. *Journal of Geophysical Research*, Vol. 77, pp. 3057 – 3067.

Cline, J.S.

2001: Timing of gold and arsenic sulphide mineral deposition at the Getchell Carlin-type gold deposit, north-central Nevada. *Economic Geology*, Vol. 96, pp 75-90.

Cook, N.J. and Chryssoulis, S.L.

1990: Concentrations of invisible gold in common sulphides. *The Canadian Mineralogist*, Vol. 28, pp 1-16.

Cooke, D.R. and Simmons, S.F.

2000: Characteristics and genesis of epithermal gold deposits. *Reviews in Economic Geology*, Vol 13, pp.221-244.

Cooke, D.R. and McPhail, D.C.

2001: Epithermal Au-Ag-Te mineralisation, Acupan, Baguio district, Philippines: Numerical simulations of mineral deposition. *Economic Geology*, Vol. 96, pp. 109-131.

Coplen, T.B., Kendall, C., Hopple, J.

1983: Comparison of stable isotope reference samples, *Nature*, Vol. 302, pp. 236 – 238.

Corbett, G.J. and Leach, T.M.

1998: Southwest Pacific rim gold-copper systems: Structure, alteration, and mineralisation. *Society of Economic Geologists special publication* 6, 237p.

Deer, W.A., Howie, R.A., and Zussman, J.

1992: *An Introduction to the Rock-Forming Minerals*. Longman Scientific and Technical, Essex, 696 pp.

Diment, R.

1996: Brewery Creek gold deposit. In *Yukon Exploration and Geology, 1995*, Exploration and Geological Services Division, Yukon, Indian and Northern Affairs Canada, p. 57-66.

Diment, R. and Craig, S.

1999: Brewery Creek gold deposit, central Yukon. *In* Yukon Exploration and Geology 1998, C.F. Roots and D.S. Emond (eds.), Exploration and Geological Services Division, Yukon, Indian and Northern Affairs Canada, p. 225-230.

Drummond, S.E. and Ohmoto, H.

1985: Chemical evolution and mineral deposition in boiling hydrothermal systems. *Economic Geology*, Vol. 80, pp 126-147.

Duncan, R.A., Russell, J.K., Hastings, N.L., and Anderson, R.G.

1998: Relationships between chemical composition, physical properties, and geology of the mineralised Emerald Lake Pluton, Yukon Territory. *In* Current Research 1998-A; Geological Survey of Canada, pp. 1-11.

Dunne, K.P.E.

1995: Brewery Creek preliminary fluid inclusion study - Report for Viceroy Exploration.

Ebert, S., Miller, L., Petsel, S., Dodd, S., and Kowalczyk, P.

2000: Geology, mineralisation and exploration at the Donlin Creek project, southwest Alaska. *In* Tucker, T.L. and Smith, M.T. (eds.), The Tintina Gold Belt: Concepts, exploration and discoveries. British Columbia and Yukon Chamber of Mines Cordilleran Round-up 2000. pp.99-114.

Flannigan, B., Freeman, C., McCoy, D., Newberry, R., and Hart, C.

2000: Palaeo-reconstruction of the Tintina Gold Belt, implications for mineral exploration. *In* The Tintina Gold Belt: concepts, exploration and discoveries. Special Volume 2. British Columbia and Yukon Chamber of Mines, Cordilleran Roundup, January 2000.

Fleet, M.E., MacLean, P.J., and Barbier, J.

1989: Oscillatory zoned As-bearing pyrite from strata-bound and stratiform gold deposits: and indicator of ore fluid evolution. *Economic Geology Monograph* 6, pp 356-362.

Fleet, M.E., Chrysosoulis, S.L., Maclean, P.J., Davidson, R., and Weisener, C.G. 1993: Arsenian pyrite from gold deposits: Au and As distribution investigated by SIMS and EMP, and colour staining and surface oxidation by XPS and LIMS. *The Canadian Mineralogist*, Vol. 31, pp. 1-17.

Fleet, M.E. and Mumin, A.H.

1997: Gold-bearing arsenian pyrite, marcasite and arsenopyrite from Carlin Trend gold deposits and laboratory synthesis. *American Mineralogist*, Vol. 82, pp. 182-193.

Fritz, W.H., Narbonne, G.M., and Gordey, S.P.

1983: Strata and trace fossils near the Precambrian-Cambrian boundary, Mackenzie, Selwyn and Wernecke Mountains, Yukon and Northwest Territories. *In* Current Research, Part B, Geological Survey of Canada, Paper 83-1B, p. 365-375.

Fritz, W.H., Cecile, M.P., Norford, B.S., Morrow, D., and Geldsetzer, H. J.

1991: Cambrian to Middle Ordovician assemblages. *In* H. Gabrielse and C.J. Yorath (eds.), Geology of the Cordilleran Orogen in Canada, Geological Survey of Canada, no. 4, P.151-218.

Gabrielse, H.

1967: Tectonic evolution of the northern Canadian Cordillera. *Canadian Journal of Earth Sciences*, Vol. 4, No. 2, pp. 271-298.

Gabrielse, H.

1976: Environments of Canadian Cordillera depositional basins; *In* Circum Pacific Energy and Mineral Resources, American Association of Petroleum Geologists, Memoir 25, pp. 492-502.

Gabrielse, H.

1985: Major dextral transcurrent displacements along the northern Rocky Mountain Trench and related lineaments in north central British Columbia. Geological Society of America Bulletin, v. 96, pp. 1-14.

Gabrielse, H. and Yorath, C.J.

1991: Geology of the Cordilleran Orogen in Canada. In: Geology of Canada, No. 4, Geological Survey of Canada.

Gabrielse, H., Blusson, S.L., and Roddick, J.A.

1973: Geology of Flat River, Glacier Lake, and Wrigley Lake map areas, District of Mackenzie and Yukon Territory. Geological Survey of Canada, Memoir 366, 153p.

Gaines, R.V., Skinner, H.C., Foord, E.E., Mason, B., Rosenzweig, A.

1997: Dana's new mineralogy: The system of mineralogy of James Dwight Dana and Edward Salsbury Dana, 8th Edition, Wiley, Chichester.

Gammons, C.H. and Williams-Jones, A.E.

1995: The solubility of Ag-Au alloy + AgCl in HCl/NaCl solutions at 300°C: New data on the stability of Au(I) chloride complexes in hydrothermal fluids. Geochimica et Cosmochimica Acta, Vol. 59, pp. 3453-3468.

Gao, Z.L. and Kwak, T.A.P.

1997: The geochemistry of wall rock alteration in turbidite hosted gold vein deposits, central Victoria, Australia. Journal of Geochemical Exploration, Vol. 59, pp. 259-274.

Genkin, A.D., Bortnikov, N.S., Cabri, L.J., Wagner, F.E., Stanley, C.J., Safonov, Y.G., McMahon, G., Friedl, J., Kersin, A.L., and Gamyranin, G.N.

1998: A multidisciplinary study of gold in arsenopyrite from four mesothermal gold deposits in Siberia, Russian Federation. Economic Geology, Vol. 93, pp. 463-487.

Gibson, D.W.

1975: Triassic rocks of the Rocky Mountain foothills and front ranges of northeastern British Columbia and west-central Alberta. Geological Survey of Canada, Bulletin 247, 42p.

Giesemann, A., Jager, H.J., Norman, A.L., Krouse, H.R., and Brand, W.A.

1994: On-line sulphur-isotope determination using an elemental analyser coupled to a mass spectrometer. Analytical Chemistry, Vol. 66, pp. 2816-2819.

Goldfarb, R., Hart, C., Miller, M., Miller, L., Garmer, G.L., and Groves, D.,

2000: The Tintina Gold Belt – a global perspective. In The Tintina Gold Belt: concepts, exploration and discoveries. Special Volume 2. British Columbia and Yukon Chamber of Mines, Cordilleran Roundup, January 2000.

Goldfarb, R.J., Ayuso, R., Miller, M.L., Ebert, S.W., Marsh, E.E., Petsel, S.A., Miller, L.D., Bradley, D., Johnson, C., and McClelland, W.

2004: The Late Cretaceous Donlin Creek gold deposit, southwestern Alaska: Controls on epizonal ore formation. Economic Geology, Vol. 99, No. 4, pp 643-671.

Golyshev, S.I., Padalko, N.L., and Pechenkin, S.A.

1981: Fractionation of stable oxygen and carbon isotopes in carbonate systems. Geochemistry International, Vol. 18, pp. 85-99.

Gordey, S.P.

1981a: Stratigraphy, structure and tectonic evolution of southern Pelly Mountains in the Indigo Lake area, Yukon Territory. Geological Survey of Canada, Bulletin 381, 44p.

Gordey, S.P.

1981b: Structure section across south-central Mackenzie Mountains, Yukon and Northwest Territories. Geological Survey of Canada, Open File 809.

Gordey, S.P.

1983: Thrust faults in the Anvil Range and a new look at the Anvil Range Group, south-central Yukon Territory. In Current Research, Part A, Geological Survey of Canada, Paper 83-1A, p. 225-227.

Gordey, S.P. and Irwin, S.E.B.

1987: Geology of Sheldon Lake (105J) and Tay River (105K) map areas; Geological Survey of Canada, Preliminary map, 19-1987.

Gordey, S.P. and Anderson, R.G.

1993: Evolution of the northern Cordilleran miogeocline, Nahanni map area (105I), Yukon and Northwest Territories. Geological Survey of Canada, Memoir 428, 214p. + maps.

Gordey, S.P., Abbott, J.G., and Orchard, M.J.

1982: Devonian-Mississippian (Earn Group) and younger strata in east central Yukon. In Current Research, Part B, Geological Survey of Canada, Paper 82-1B, p. 93-100.

Graham, A.D.

1973: Carboniferous and Permian stratigraphy, southern Eagle Plain, Yukon Territory, Canada. In Canadian Arctic Geology, J.D. Aitken and D.J. Glass (eds.). Geological Association of Canada and Canadian Society of Petroleum Geologists, Proceedings of the symposium on the Geology of the Canadian Arctic, pp. 159-180.

Grant, J.A.

1986: The isocon diagram: a simple solution to Gresens equation for metasomatic alteration. Economic Geology, Vol. 81, pp. 1976-1982.

Green, L.H.

1972: Geology of the Nash Creek, Larsen Creek and Dawson map areas, Yukon Territory (106D, 116A, 116B, and 116C (E1/2)), Operation Ogilvie. Geological Survey of Canada, Memoir 364, 157p. + maps.

Gresens, R.L.

1967: Composition-volume relationships of metasomatism. Chemical Geology, Vol. 2, pp. 47-55.

Griffin, W.L., Ashley, P.M., Ryan, C.G., Sie, S.H., and Suter, G.F.

1991: Pyrite geochemistry in the North Arm epithermal Ag-Au deposit, Queensland, Australia: A proton microprobe study. The Canadian Mineralogist, Vol. 29, pp. 185-198.

Groves, D.I., Goldfarb, R.J., Gebre-Mariam, M., Hagemann, S.G., and Robert, F.

1998: Orogenic gold deposits: A proposed classification in the context of their crustal distribution and relationship to other gold deposit types. Ore Geology Reviews, Vol. 13, pp. 7-27.

Hagemann, S.G. and Cassidy, K.F.

2000: Archean orogenic lode gold deposits. Reviews in Economic Geology, Vol. 13, pp. 9-68.

Hammond, N.Q. and Tabata, H.

1997: Characteristics of ore minerals associated with gold at the Prestea mine, Ghana. Mineralogical Magazine, Vol. 61, pp. 879-894.

Harman, H.H.

1976: Modern factor analysis (rev. 3rd edition). Chicago, Chicago University Press, 474 pp.

Hart, C.J.R., Baker, T., and Burke, M.

2000: New exploration concepts for country-rock-hosted, intrusion-related gold systems: Tintina Gold Belt in Yukon. In The Tintina Gold Belt: concepts, exploration and discoveries. Special Volume 2. British Columbia and Yukon Chamber of Mines, Cordilleran Roundup, January 2000.

Hart, C.J.R., McCoy, D.T., Goldfarb, R.J., Smith, M., Roberts, P., Hulstein, R., Bakke, A.A., and Bundtzen, T.K.

2002: Geology, exploration and discovery in the Tintina Gold Province, Alaska and Yukon. Society of Economic Geologists Special Publication 9, 2002, p.241-274.

Hedenquist, J.W.

1991: Boiling and dilution in the shallow portion of the Waiotapu geothermal system, New Zealand. *Geochimica et Cosmochimica Acta*, Vol. 55, pp.2573-2785.

Hedenquist, J.W., Arribas, R.A., and Gonzalez-Urien, E.

2000: Exploration for epithermal gold deposits. *Reviews in Economic Geology*, Vol. 13, pp. 245-277.

Henley, R.W.

1985: The geochemical framework of epithermal deposits. *Reviews in Economic Geology*, Vol. 2, pp. 1-24.

Henley, R.W. and Ellis, A.J.

1983: Geothermal systems, ancient and modern. *Earth and Planetary Science Reviews*, Vol. 19, pp. 1-50.

Hiyashi, K. and Ohmoto, H.

1991: Solubility of Au in NaCl- and H₂S- bearing aqueous solutions at 250-350°C. *Geochimica et Cosmochimica Acta*, Vol. 55, pp. 2111-2126.

Hofmann, B.A.

1991: Mineralogy and geochemistry of reduction spheroids in red beds. *Mineralogy and Petrology*, Vol. 44, pp. 107-124.

Hofstra, A. H., Leventhal, J.S., Northrop, H.R., Landis, G.P., Rye, R.O., Birak, D.J., and Dahl, A.R.

1991: Genesis of sediment hosted disseminated gold deposits by fluid mixing and sulphidation: Chemical-reaction-path modelling of ore depositional processes in the Jerritt Canyon district, Nevada: *Geology*, v.19, pp. 36-40.

Hofstra, A.H., Snee, L.W., Rye, R.O., Folger, H.W., Phinisey, J.D., Loranger, R.J., Dahl, A.R., Naeser, C.W., Stein, H.J., and Lewchuk, M.

1999: Age constraints on Jerritt Canyon and other Carlin-type gold deposits in the western United States – Relationship to mid-Tertiary extension and magmatism: *Economic Geology*, Vol. 94, pp. 769-802.

Hofstra, A.H. and Cline, J.S.

2000: Characteristics and models for Carlin-type gold deposits. *Reviews in Economic Geology*, Vol. 13, pp. 163 – 220.

Hollister, V.F.

1992: On a proposed plutonic porphyry gold deposit model. *Non-renewable resources*, Vol. 1, pp. 293-302.

Huston, D.L. and Large, R.R.

1989: A chemical model for the concentration of gold in volcanogenic massive sulphide deposits. *Ore Geology Reviews*, Vol. 4, pp. 171-200.

Huston, D.L., Sie, S.H., Suter, G.F., Cooke, D.R., and Both, R.A.

1995a: Trace elements in sulphide minerals from eastern Australian volcanic-hosted massive sulphide deposits: Part I. Proton microprobe analyses of pyrite, chalcopyrite and sphalerite, and Part II. Selenium levels in pyrite: comparison with $\delta^{34}\text{S}$ values and implications for the source of sulphur in volcanogenic hydrothermal systems. *Economic Geology*, Vol. 90, pp. 1167-1196.

Huston, D.L., Power, M., Gemmell, J.B. and Large, R.R.

1995b: Design, calibration and geological application of the first operational Australian laser ablation sulphur isotope microprobe. *Australian Journal of Earth Sciences*, Vol. 42, pp. 549-555.

Hyland, M.M. and Bancroft, G.M.

1989: An XPS study of gold deposition at low temperatures on sulphide minerals: Reducing agents. *Geochimica et Cosmochimica Acta*, Vol. 53, pp. 367-372.

Jean, G.E., and Bancroft, G.M.

1985: An XPS and SEM study of gold deposition at low temperatures on sulphide mineral surfaces: Concentration of gold by adsorption/reduction. *Geochimica et Cosmochimica Acta*, Vol. 49, pp. 979-987.

Jennings, D.S. and Jilson, G.A.

1986: Geology and sulphide deposits of Anvil Range, Yukon. In J.A. Morin (ed.), *Mineral deposits of the northern Cordillera*, Canadian Institute of Mining and Metallurgy, Special Volume 37, p.319-361.

Johan, Z., Marcoux, E., and Bonnemaïson, M.

1989: Arsenopyrite aurifère: mode de substitution de Au dans la structure de FeAsS. *C R Academic Science (Paris)*, Vol. 308, pp. 181-195.

Kaiser, H.F.

1958: The varimax criterion for analytical rotation in factor analysis. *Psychometrika*, Vol. 23, pp. 187 – 200.

Kishida, A. and Kerrich, R.

1987: Hydrothermal alteration zoning and gold concentration at the Kerr-Addison Archaean lode gold deposit, Kirkland Lake, Ontario. *Economic Geology*, Vol. 82, pp. 649-690.

Kretschmar, U. and Scott, S.D.

1976: Phase relations involving arsenopyrite in the system Fe-As-S and their application. *The Canadian Mineralogist*, Vol. 14, pp. 364-386.

Kuehn, C.A. and Rose, A.W.

1992: Geology and geochemistry of wall-rock alteration at the Carlin gold deposit, Nevada. *Economic Geology*, Vol. 87, pp 1697-1721.

Lambert, M.B.

1966: Geology of the Mount Brenner Stock, near Dawson City, Yukon Territory. Unpublished M.Sc. thesis, University of British Columbia, Vancouver, 64p.

Lang, J.R., Baker, T.

2001: Intrusion-related gold systems: the present level of understanding. *Mineralium Deposita*, vol. 36, p. 477-499.

Lang, J.R., Baker, T., Hart, C.J.R., Mortensen, J.K.

2000a: An exploration model for intrusion-related gold systems. *SEG newsletter*, January 2000, number 40.

Lang, J. (ed), Thompson, J., Mortensen, J., Baker, T., Coulson, I., Duncan, R., Maloof, T., James, J., Friedman, R., Lepitre, M.

2000b: Regional and system-scale controls on the formation of copper and/or gold magmatic-hydrothermal mineralisation. Final technical report, February 2000. The Mineral Deposit Research Unit, University of British Columbia.

Lang, J.R., Thompson, J.F.H., Mortensen, J.K., Baker, T., and Sillitoe, R.H.

1997: Intrusion-related Au mineralisation associated with lithophile elements; an under-recognized metallogenic association. Geological Society of America, 1997 Annual meeting, Abstracts with Programs, Vol. 29, pp. 358.

Laprenune, T.

1997: Brewery Creek composite testing metallurgical report. Internal company report by G and T Metallurgical Services Ltd, 10 p.

Lenz, A.C.

1972: Ordovician to Devonian history of northern Yukon and adjacent district of Mackenzie. Bulletin of Canadian Petroleum Geology, Vol. 20, No. 2, pp. 321-361.

Lindsay, M.J., Baker, T., Oliver, N.H.S., Diment, R., and Hart, C.J.R.

2000: The magmatic and structural setting of the Brewery Creek gold mine, central Yukon. In Yukon Exploration and Geology 1999, D.S. Emond and L.H. Weston (eds.), Exploration and Geological Services Division, Yukon, Indian and Northern Affairs Canada, p. 219 – 227.

Lindsay, M.J., Baker, T., Hart, C.J.R., and Oliver, N.H.S.

2001: The structural history and mineral paragenesis of the Brewery Creek gold deposit, Yukon Territory Canada. In 2001: A Hydrothermal Odyssey extended conference abstracts. P.J. Williams (ed). EGRU contribution Vol. 59, p. 118-119.

Lowenstern, J.B.

2001: Carbon dioxide in magmas and implications for hydrothermal systems. Mineralium Deposita, Vol. 36, pp. 490-502.

Maddox, L.M., Bancroft, G.M., Scaini, M.J., and Lorimer, J.W.

1998: Invisible gold: Comparison of Au deposition on pyrite and arsenopyrite. American Mineralogist, Vol. 83, pp. 1240-1245.

Mair, J.L., Hart, C.J.R., Goldfarb, R.J., O'Dea, M., and Harris, S.

2000: Geology and metallogenic signature of gold occurrences at Scheelite Dome, Tombstone gold belt, Yukon. In Yukon Exploration and Geology 1999, D.S. Emond and L.H. Weston (eds.), Exploration and Geological Services Division, Yukon, Indian and Northern Affairs Canada, p. 165-176.

Mair, J.L., Hart, C.J.R., and Stephens, J.R.

2006: Deformation history of the northwestern Selwyn Basin, Yukon, Canada: Implications for orogen evolution and mid-Cretaceous magmatism. GSA Bulletin, Vol 118, pp. 304 – 323.

Maloof, T.L., Baker, T., and Thompson, J.F.H.

2001: The Dublin Gulch intrusion-hosted gold deposit, Tombstone plutonic suite, Yukon Territory, Canada. Mineralium Deposita, Vol.36, pp. 583-593.

Marsh, E.E., Hart, C.J.R., Goldfarb, R.J., and Allen, T.L.

1999: Geology and geochemistry of the Clear Creek gold occurrences, Tombstone Gold Belt, central Yukon Territory. In Yukon Exploration and Geology 1998. Exploration and Geological Services Division, Yukon, Indian and Northern Affairs Canada, pp. 185-196.

Matsuhisa, Y., Goldsmith, J.R., and Clayton, R.N.

1978: Mechanism of hydrothermal crystallisation of quartz at 250 °C and 15 kbar. *Geochimica et Cosmochimica Acta*, Vol. 42, pp. 173 – 182.

Matthews, A. and Katz, A

1977: Oxygen isotope fractionation during dolomitisation of calcium carbonate. *Geochimica et Cosmochimica Acta*, Vol. 41, pp. 1431-1438.

McCoy, D.T., Newberry, R.J., Layer, P.W., DiMarchi, J.J., Bakke, A., Masterman, J.S., and Minehane, D.L.

1997: Plutonic-related gold deposits of interior Alaska. In Goldfarb, R.J. and Miller, L.D. (eds.) *Ore deposits of Alaska*. Society of Economic Geologists Monograph 9. pp. 151-190

McCrea, J.M.

1950: On the isotope chemistry of carbonates and a paleotemperature scale. *Journal of Chemical Physics*, Vol. 18, pp. 849-857.

Miyashiro, A.

1978: Nature of alkaline volcanic rock series. *Contributions to Mineralogy and Petrology*, Vol. 66, p.91-104.

Möller, P. and Kersten, G.

1994: Electrochemical accumulation of visible gold on pyrite and arsenopyrite surfaces. *Mineralium Deposita*, Vol. 29, pp. 404-413.

Möller, P., Sastri, C.S., Kluckner, M., Rhede, D., and Ortner, H.M.

1997: Evidence for electrochemical deposition of gold onto arsenopyrite. *European Journal of Mineralogy*, Vol. 9, pp. 1217-1226.

Mortensen, J.K., Murphy, D.C., Hart, C.J.R., and Anderson, R.G.

1995: Timing, tectonic setting and metallogeny of Early and Mid-Cretaceous magmatism in Yukon Territory. *Geological Society of America, Abstracts with programs*, v. 27, no. 5, p. 65.

Mortensen, J.K., Murphy, D.C., Poulson, K.H., and Bremner, T.J.

1996: Intrusion related gold and base metal mineralization associated with the Early Cretaceous Tombstone plutonic suite, Yukon and east-central Alaska. In *New Mineral Deposit Models of the Cordillera*, Short Course Notes, British Columbia Geological Survey and Northwest Mining Association, p. G1 – G11.

Mortensen, J.K., Hart, C.J.R., Murphy, D.C., and Heffernan, S.

2000: Temporal evolution of Early and mid-Cretaceous magmatism in the Tintina Gold Belt. In *The Tintina Gold Belt: concepts, exploration and discoveries*. Special Volume 2. British Columbia and Yukon Chamber of Mines, Cordilleran Roundup, January 2000.

Moss, R. and Scott, S.D.

2001: Geochemistry and mineralogy of gold-rich hydrothermal precipitates from the eastern Manus Basin, Papua New Guinea. *The Canadian Mineralogist*, Vol. 39, pp. 957-978

Mueller, A.G., Nemchin, A.A., and Frei, R.

2004: The Nevoria gold skarn deposit, Southern Cross greenstone belt, Western Australia; II, Pressure, temperature-time path and relationship to post-orogenic granites. *Economic Geology*, Vol. 99, pp. 453-478.

Mumin, A.H., Fleet, M.E., and Chrysosoulis, S.L.

1994: Gold mineralisation in As-rich mesothermal gold ores of the Bogosu-Prestea mining district of the Ashanti Gold Belt, Ghana: remobilisation of “invisible” gold. *Mineralium Deposita*, Vol. 29, pp. 445-460.

Murphy, D.C.

1997: Geology of the McQuesten River Region, Northern McQuesten and Mayo Map Areas, Yukon Territory (115P/14, 15, 16; 105M/13, 14). Exploration and Geological Services Division, Yukon Region. Bulletin 6. 95p. + maps.

Murphy, D.C., and Heon, D.

1994: Geological overview of Sprague Creek map area, western Selwyn Basin. *In* Yukon Exploration and Geology 1993: Exploration and Geological Services Division, Yukon, Indian and Northern Affairs Canada, p. 29-46.

Murphy, D.C., and Heon, D.

1995a: Geology and mineral occurrences of the Seattle Creek map area (115P/16), western Selwyn Basin. *In* Yukon Exploration and Geology 1994, Exploration and Geological Services Division, Yukon, Indian and Northern Affairs Canada, pp. 59-71.

Murphy, D.C., and Heon, D.

1995b: Geological map of the Seattle Creek map area, western Selwyn Basin, Yukon (NTS 115P/16). Exploration and Geological Services Division, Yukon, Indian and Northern Affairs Canada, Open File 1995-3 (G), scale 1:50 000.

Murphy, D.C., Heon, D., and Hunt, J.

1993: Geological overview of Clear Creek map area, western Selwyn Basin. *In* Yukon Exploration and Geology 1992: Exploration and Geological Services Division, Yukon, Indian and Northern Affairs Canada, p. 61-69.

Murowchick, J.B.

1992: Marcasite inversion and the petrographic determination of pyrite ancestry. *Economic Geology*, Vol. 87, pp. 1141-1152.

Murowchick, J.B. and Barnes, H.L.

1986: Marcasite precipitation from hydrothermal solutions. *Geochimica et Cosmochimica Acta*, Vol. 50, pp. 2615-2629.

Mustard, R.

2001: Granite-hosted gold mineralisation at Timbarra, northern New South Wales, Australia. *Mineralium Deposita*, Vol. 36, pp. 542-562.

Mycroft, J.R., Bancroft, G.M., McIntyre, N.S., and Lorimer, J.W.

1995: Spontaneous deposition of gold on pyrite from solutions containing Au (III) and Au (I) chlorides. I.A. surface study. *Geochimica et Cosmochimica Acta*, Vol. 59, pp 3351-3365.

Neumayr, P., Cabri, L.J., Groves, D.I., Mikucki, E.J., and Jackman, J.A.

1993: The mineralogical distribution of gold and relative timing of gold mineralisation in two Archaean settings of high metamorphic grade in Australia. *Canadian Mineralogist*, Vol. 31, pp. 711-725.

Newberry, R.J., McCoy, D.T., and Brew, D.A.

1995: Plutonic-hosted gold ores in Alaska: igneous vs. metamorphic origins. *Resource Geology Special Issue*, Vol. 18, pp. 57-100

Newberry, R.J.

2000: Mineral deposits and associated Mesozoic and Tertiary igneous rocks within interior Alaska and adjacent Yukon portions of the 'Tintina Gold Belt': a progress report. *In* Tucker, T.L. and Smith, M.T. (eds.) *The Tintina Gold Belt: concepts, exploration and discoveries*. British Columbia and Yukon Chamber of Mines Special Volume 2, pp.59-88.

Oberthür, T., Weiser, T., Armanor, J.T., and Chrysosoulis, S.L.

1997: Mineralogical siting and distribution of gold in quartz veins and sulphide ores of the Ashanti mine and other deposits in the Ashanti belt of Ghana: Genetic implications. *Mineralium Deposita*, Vol. 2, pp.2-15.

Ohmoto, H.

1986: Stable isotope geochemistry of ore deposits in Valley, J.W., Taylor, H.P., O'Neil, J.R., 1986. Stable isotopes in high temperature geological processes. *Reviews in Mineralogy* Vol. 16, 570pp.

Ohmoto, H. and Rye, R.O.

1979: Isotopes of sulphur and carbon. In Barnes, H.L. (ed), *Geochemistry of Hydrothermal Ore Deposits*, John Wiley and Sons, pp. 509-567.

Oliver, N.H.S., Valenta, R.K., and Wall, V.J.

1990: The effect of heterogeneous stress and strain on metamorphic fluid flow, Mary Kathleen, Australia, and a model for large-scale fluid circulation. *Journal of Metamorphic Geology*, Vol. 8, pp. 311-331.

Orchard, M.J.

1993: Report on conodonts and other microfossils. Geological Survey of Canada report number OF-1993-57.

Park, V.

1999: Brewery Creek project 1998 exploration progress report January 20, 1999. Viceroy Exploration (Canada) Inc. company report.

Peacor, D.R., Coveney, R.M., and Zhao, G.M.

2000: Authogenic illite and organic matter: The principal hosts of vanadium at the Mecca Quarry Shale at Velpen, Indiana. *Clays and Clay Minerals*, Vol. 48, pp. 311-316.

Pirajno, F.

1992: *Hydrothermal mineral deposits*. Springer-Verlag, Berlin, 709p.

Pflafer, G. and Berg, H.C.

1994: Overview of the geology and tectonic evolution of Alaska. In Pflafer, G. and Berg, H.C. (eds.) *The geology of Alaska: The geology of North America*, vol. G-1: Geological Society of America, Boulder, Colorado, pp. 989-1201.

Poulsen, K.H., Mortensen, J.K., and Murphy, D.C.

1997: Styles of intrusion related gold mineralization in the Dawson – Mayo area, Yukon. In *Current research, 1997-A*, Geological Survey of Canada, p.1-11.

Poulton, T.P. and Norford, B.S.

1995: *Palaeontological Report S-2-BSN-1995*. Geological Survey of Canada.

Reed, M.H. and Spycher, N.F.

1985: Boiling, cooling and oxidation in epithermal systems: A numerical approach. *Reviews in Economic Geology*, Vol. 2, pp. 249-272.

Rhys, D., DiMarchi, J., Smith, M., Friesen, R., and Rombach, C.

2003: Structural setting, style and timing of vein-hosted gold mineralisation at the Pogo deposit, east central Alaska. *Mineralium Deposita*, Vol. 38, pp. 863-875.

Ridley, J.

1993: The relations between mean rock stress and fluid flow in the crust, with reference to vein- and lode-style gold deposits. *Ore Geology Reviews*, Vol. 8, pp. 23-37.

Rollinson, H.R.

1996: Using Geochemical Data: Evaluation, Presentation, Interpretation. Longman, Essex, 352pp.

Ronacher, E., Richards, J.P., Villeneuve, M.E., and Johnston, M.D.

2002: Short life span of the ore forming system at the Porgera gold deposit, Papua New Guinea: laser $^{40}\text{Ar}/^{39}\text{Ar}$ dates for roscoelite, biotite and hornblende. Mineralium Deposita, Vol. 37, pp. 75-86.

Ronacher, E., Richards, J.P., Reed, M.H., Bray, C.J., Spooner, E.T.C., and Adams, P.D.

2004: Characteristics and evolution of the hydrothermal fluid in the north high-grade area, Porgera gold deposit, Papua New Guinea. Economic Geology, Vol. 99, pp. 843-866.

Roots, C.F.

1998: Cambro-Ordovician volcanic rocks in eastern Dawson map area, Olgilvie Mountains, Yukon. In Yukon Geology volume 2. Exploration and Geological Services Division, Yukon, Indian and Northern Affairs Canada, p.81-87.

Roots, C.F., Abbott, J.G., Cecile, C.F., and Gordey, S.P.

1995a: Bedrock geology of the Lansing Range map area (105N) east half, Hess Mountains, Yukon. Exploration and Geological Services Division, Yukon, Indian and Northern Affairs Canada, Open File 1995-7(G) and Geological Survey of Canada, Open File 3171, scale 1:125 000.

Roots, C.F., Abbott, J.G., Cecile, C.F., Gordey, S.P., and Orchard, M.J.

1995. New stratigraphy and structures in the eastern Lansing map area, central Yukon Territory. In Current Research 1995-A, Geological Survey of Canada, pp. 141-147.

Roth, B.

1994: XRD clay analysis from Brewery Creek. Unpublished company report. 15pp.

Savage, K.S., Tingle, T.N., O'Day, P.A., Waychunas, G.A., Bird, D.K.

2000: Arsenic speciation in pyrite and secondary weathering phases, Mother Lode gold district, Tuolumne County, California. Applied Geochemistry, Vol. 15, pp. 1219-1244.

Scaini, M.J., Bancroft, G.M., and Knipe, S.W.

1998: Reactions of aqueous Au^{1+} sulphide species with pyrite as a function of pH and temperature. American Mineralogist, Vol. 83, pp 316-322.

Selby, D., Creaser, R.A., Hart, C.J.R., Rombach, C.S., Thompson, J.F.H., Smith, M.T., Bakke, A.A., and Goldfarb, R.J.

2002: Absolute timing of sulphide and gold mineralisation: A comparison of Re-Os molybdenite and Ar-Ar mica methods from the Tintina Gold Belt, Alaska. Geology, Vol. 30, pp. 791-794.

Seward, T.M.

1973: Thio complexes of gold and the transport of gold in hydrothermal ore solutions. Geochimica et Cosmochimica Acta, Vol. 37, pp. 379-399.

Seward, T.M.

1989: The hydrothermal chemistry of gold and its implications for ore formation: Boiling and conductive cooling as examples. Economic Geology Monograph 6, pp. 398-404.

Seward, T.M.

1991: The hydrothermal geochemistry of gold. In Foster, R.P. (ed), Gold metallogeny and exploration. London, Blackie and Son, pp.37-62.

Seward, T.M. and Barnes, H.L.

1997: Metal transport by hydrothermal fluids. In Barnes, H.L. (ed), Geochemistry of hydrothermal ore deposits, 3rd edition. New York, John Wiley and Sons Inc. pp.435-486.

Sharp, Z.D., Essene, E.J., and Kelly, W.C.

1985: A re-examination of the arsenopyrite geothermometer: pressure considerations and applications to natural assemblages. The Canadian Mineralogist, Vol. 23, pp. 517-534.

Shriver, N.A. and MacLean, W.H.

1993: Mass, volume and chemical changes in the alteration zone at Norbec mine, Noranda, Quebec. Mineralium Deposita, Vol. 28, pp. 157-166.

Sillitoe, R.H.

1991: Intrusion-related gold deposits. In Foster, R.P. (ed) Gold metallogeny and exploration. Blackie, Glasgow, pp. 165-209.

Sillitoe, R.H.

1992: Gold and copper metallogeny of the central Andes – past, present, and future exploration objectives. Economic Geology, Vol 87, pp. 2205-2216.

Simon, G., Kesler, S.E., and Chrysosoulis, S.

1999: Geochemistry and textures of gold bearing arsenian pyrite, Twin Creeks, Nevada: implications for deposition of gold in Carlin type deposits. Economic Geology, Vol. 94, pp. 405-421.

Simon, G., Huang, H., Penner-Hahn, J.E., Kesler, S.E., and Kao, L.

1999: Oxidation state of gold and arsenic in gold-bearing arsenian pyrite. American Mineralogist, Vol. 84, pp. 1071-1079.

Simmons, S.F. and Browne, P.R.L.

2000: Hydrothermal minerals and precious metals in the Broadlands-Ohaaki geothermal system: Implications for understanding low sulphidation epithermal environments. Economic Geology, Vol. 95, pp. 971-999.

Smith, M.

2000: The Tintina Gold Belt: an emerging gold district in Alaska and Yukon. British Columbia and Yukon Chamber of Mines Special Volume 2, pp1-3.

Smith, M., Thompson, J.F.H., Moore, K.H., Bressler, J.R., Layer, P., Mortensen, J.K., Abe, I., and Takaoka, H.

2000: The Leise Zone, Pogo property: a new high-grade gold deposit in Alaska. British Columbia and Yukon Chamber of Mines Special Volume 2, pp131-134.

Spear, F.S.

1993: Metamorphic phase equilibria and pressure-temperature-time paths. Mineralogical Society of America Monograph Series. 799pp.

Spear, F.S. and Cheney, J.T.

1989: A petrogenetic grid for pelitic schists in the system $\text{SiO}_2\text{-Al}_2\text{-O}_3\text{-FeO-MgO-K}_2\text{O-H}_2\text{O}$. Contributions to mineralogy and petrology, Vol. 101, pp. 149-164.

Steele, I.M., Cabri, L.J., Gaspar, J.C., McMahon, G., Marquez, M.A., and Vasconcellos, M.A.Z.

2000: Comparative analysis of sulphides for gold using SXRF and SIMS. The Canadian Mineralogist, Vol. 38, pp. 1-10.

Stephens, J.R., Oliver, N.H.S., Baker, T., and Hart, C.J.R.

2000: Structural evolution and controls on gold mineralisation at Clear Creek, Yukon. In Yukon Exploration and Geology 1999, D.S. Emond and L.H. Weston (eds.), Exploration and Geological Services Division, Yukon, Indian and Northern Affairs Canada, p. 151-163.

Stephens, J.R.

2003: Structural, mechanical and P-T evolution of intrusion-related gold mineralisation at Clear Creek and Dublin Gulch, Yukon, Canada. Ph.D. thesis, James Cook University.

Stephens, J.R., Mair, J.L., Oliver, N.H.S., Hart, C.J.R., and Baker, T.

2004: Structural and mechanical controls on intrusion-related deposits of the Tombstone Gold Belt, Yukon, Canada, with comparisons to other vein-hosted ore-deposit types. Journal of Structural Geology, Vol. 26, p. 1025 - 1041.

Stoffregen, R.E.

1987: Genesis of acid sulphate alteration and Au-Cu-Ag mineralisation at Summitville, Colorado: Economic Geology, Vol. 82, pp.1575 – 1591.

Templeman-Kluit, D.J.

1970: Stratigraphy and structure of the Keno Hill quartzite in Tombstone River-upper Klondike River map areas, Yukon Territory (116B/7, B/8). Geological Survey of Canada, Bulletin 180, 102p. + maps.

Templeman-Kluit, D.J.

1979: Transported cataclasite, ophiolite and granodiorite in Yukon: evidence of arc-continent collision. Geological Survey of Canada, Paper 79-14, 27p.

Thompson, J.F.H. and Newberry, R.J.

2000: Gold deposits related to reduced granitic intrusions. Reviews in Economic Geology, Vol. 13, pp. 377 - 400

Thompson, J.F.H., Sillitoe, R.H., Baker, T., Lang, J.R., and Mortensen, J.K.

1999: Intrusion-related gold deposits associated with tungsten-tin provinces. Mineralium Deposita, Vol. 34, pp. 323 – 334.

Thompson, R.I.

1995: Geological compilation (1:250 000) of Dawson map area (116B, C) (northeast of Tintina Trench): Geological Survey of Canada, Open File 3223.

Thompson, R.I., Roots, C.F., and Mustard, P.S.

1990: Repeated Proterozoic passive margin extension influences on Late Cretaceous folding and thrusting in the southern Olgivie Mountains, Yukon. Geological Association of Canada, Program with Abstracts, v. 15, pp. 131.

Thompson, R.I., Roots, C.F., and Mustard, P.S.

1992: Geology of the Dawson map area (116B,C) (northwest of the Tintina Trench). Geological Survey of Canada, Open-File 2849, scale 1:50 000.

Tarnocai, C.A., Hattori, K., and Cabri, L.J.

1997: "Invisible" gold in sulphides from the Campbell mine, Red Lake greenstone belt, Ontario: evidence for mineralisation during the peak of metamorphism. The Canadian Mineralogist, Vol. 35, pp 805-815.

Watling, R.J., Herbert, H.K., and Abell, I.D.

1995: The application of laser ablation-inductively coupled plasma-mass spectrometry (LA-ICP-MS) to the analysis of selected sulphide minerals. Chemical Geology, Vol. 124, pp. 67—81.

Weissberg, B.G., Browne, P.R.L., and Seward, T.M.

1979: Ore minerals in active geothermal systems. In Barnes, H.L. (ed), *Geochemistry of hydrothermal ore deposits*, 2nd edition, New York, Wiley Interscience, pp. 738-780.

White, N.C. and Hedenquist, J.W.

1990: Epithermal environments and styles of mineralisation: Variations in their causes and guidelines for exploration. *Journal of Geochemical Exploration*, Vol. 36, pp. 445-474.

White, N.C. and Hedenquist, J.W.

1995: Epithermal gold deposits: Styles, characteristics and exploration. *Society of Economic Geologists Newsletter*, No. 23, pp. 1-13.

Windle, S.J. and Craw, D.

1991: Gold mineralisation in a syn-tectonic granite dyke, Sams Creek, northwest Nelson, New Zealand. *New Zealand Journal of Geology and Geophysics*, Vol. 34, pp. 429-440.

Wu, X. and Delbove, F.

1989: Hydrothermal synthesis of gold-bearing arsenopyrite. *Economic Geology*, Vol. 84, pp. 2029-2032.

Wu, X., Delbove, F., and Touray, J.C.

1990: Conditions of formation of gold-bearing arsenopyrite: a comparison of synthetic crystals with samples from Le Châtelet gold deposit, Creuse, France. *Mineralium Deposita*, Vol. 25, pp. S8-S12.

Yang, S., Blum, N., Rahders, E., Zhang, Z.

1998: The nature of invisible gold in sulphides from the Xiangxi Au-Sb-W ore deposit in northwestern Hunan, Peoples republic of China. *The Canadian Mineralogist*, Vol. 36, pp. 1361-1372.

Zhang, L.-G., Liu, J.-X., Zhou, H.B., and Chen, Z.-S.

1989: Oxygen isotope fractionation in the quartz-water-salt system. *Economic Geology*, Vol. 89, pp. 1643-1650.

Zheng, Y.-F.

1993: Calculation of oxygen isotope fractionation in anhydrous silicate minerals. *Geochimica et Cosmochimica Acta*, Vol. 57, pp 1079-1091.